Influence of top bar effect on corrosion behavior of reinforced concrete structure in case of chloride environment or concrete carbonation.

Thi Thu Trang Nguyen

To cite this version:

Thi Thu Trang Nguyen. Influence of top bar effect on corrosion behavior of reinforced concrete structure in case of chloride environment or concrete carbonation.. Civil Engineering. Université de Toulouse; Ecole Nationale Supérieure de Génie Civil, 2024. English. NNT : 2024TLSEI009 . tel-04758953

HAL Id: tel-04758953
https://theses.hal.science/tel-04758953v1

Submitted on 29 Oct 2024

HAL is a multi-disciplinary open access archive for the deposit and dissemination of scientific research documents, whether they are published or not. The documents may come from teaching and research institutions in France or abroad, or from public or private research centers.

L'archive ouverte pluridisciplinaire **HAL**, est destinée au dépôt et à la diffusion de documents scientifiques de niveau recherche, publiés ou non, émanant des établissements d'enseignement et de recherche français ou étrangers, des laboratoires publics ou privés.

Doctorat de l’Université de Toulouse

délivré en co-tutelle avec Ecole Nationale Supérieure de Génie Civil

préparé à l'INSA Toulouse

---

influence de l'effet de l'interface acier/béton (top-bar effect) sur la corrosion de structures en béton armé exposées en environnement de chlorures ou de carbonatation.

Thèse présentée et soutenue, le 4 juillet 2024 par

Thi Thu Trang NGUYEN

École doctorale

MEGEP - Mécanique, Energétique, Génie civil, Procédés

Spécialité

Génie civil

Unité de recherche

LMDC - Laboratoire Matériaux et Durabilité des Constructions de Toulouse

Thèse dirigée par

Raoul FRANÇOIS et Ngoc Tru VU

Composition du jury

Mme Myriam CARCASSES, Présidente, Université Toulouse III - Paul Sabatier
Mme Stéphanie BONNET, Rapporteure, Nantes Université
M. Trung Hieu NGUYEN, Rapporteur, Université de Génie Civil de Hanoi
Mme Valérie L'HOSTIS, Examinatrice, CEA Paris-Saclay
M. Anh Cuong HO, Examinateur, Université des Transports et Communications de Hanoi
M. Raoul FRANÇOIS, Directeur de thèse, INSA Toulouse
M. Ngoc Tru VU, Co-directeur de thèse, Université de Génie Civil de Hanoi

ACKNOWLEDGMENT

I would like to express my especially sincere appreciation to my supervisor, Prof. Raoul François at INSA-Toulouse. It was a great opportunity for me to work with him, a person who is always kind, enthusiastic and optimistic in life as well as has extremely profound scientific knowledge and skills. Without his guidance, support and encouragement, I would not have enough power to complete my work.

I would also like to express my warmest thanks to Ngoc Tru VU at HUCE, the co-director of my PhD thesis who gave me a precious chance to study in France, for having believed and kept motivated with me all the time.

I would also like to thank the engineers, technicians and office staff of laboratory LMDC for their assistance. Their warm support played an important role for my experiments to be completed.

I appreciate the help from Zhang Wulong and Lucas Hess. Thanks for your helps during my research.

The financial support from Van Phu Company in Vietnam for my study in France is acknowledged gratefully.

Finally, I deeply thank to my parents, my husband and my children for their love, support and sacrifices with me. I express many thanks also to you my brother and his family for their encouragement and assistance in France. You are always in my heart.

TABLE OF CONTENTS

LIST OF FIGURES

LIST OF TABLES

ABSTRACT

Reinforced concrete is known one of the most popular materials applied in construction. Nevertheless, after a period of time it can be corroded. Chlorides and carbonation are the main factors causing to corrosion in reinforced concrete structure. The thesis aimed to study the corrosion behavior of reinforcement concrete under carbonation or chloride environment, corresponding to the influence of top-bar effect, the cement type as well as artificial transverse crack or load-induced cracks.

In general, carbonation induced corrosion is usually studied from the point of view that it generates uniform corrosion. The first objective of the thesis is to study and quantified the part of macro cell corrosion in carbonated induced corrosion. According to the results of experiments in this part, corrosion rate in carbonated concrete reinforcement is likely to consider from the point of view of both uniform and macro cell corrosion, the latter one being strongly influenced by the ratio cathode/anode. In addition, the use of CEM III containing slag as addictive, allowed a reduction of macro cell corrosion.

The second part focuses on the influence of top-bar effect, on corrosion behavior in the case of carbonation induced corrosion and the presence of load induced crack. Macro cell corrosion current monitoring, using a steel coupon, was utilized in the experiment allowing the loss of mass as well as corrosion kinetic to be calculated. Corrosion mainly developed at the location of the pre-cracks. Due to the top-bar effect, upper bars were more corroded than bottom bars. Macro cell current corrosion of top bars was observed higher than bottom bars. Loss of steel mass calculated from macro cell current measurement corresponds to only to a small part of the total loss of mass determined by gravimetric measurement. Uniform corrosion appears to be the main phenomena.

The last part investigates the influence of top-bar effect in fibers concrete samples with or without artificial crack, on chloride induced corrosion. The top steel bars are more corroded than the bottom bars and the upper part of the top bar exhibit higher corrosion than the lower part. In presence of artificial crack, the top casting effect results that corrosion spreads along the surface of the steel bars. Corrosion also spreads along the top bar when there is no artificial crack, in a time not so different from the case of the presence of artificial crack. It confirms that top surface exposure and top bar effect are highly prejudicial for corrosion. By comparing the behavior with concrete without fibers, it appears that the addition of fibers in reinforced concrete leads to an increase of resistance to corrosion induced cracking.

For each part, experimental observations are coupled with numerical simulations to compare as well as demonstrate the experimental results.

Key words: reinforced concrete, carbonation induced corrosion, chloride induced corrosion, uniform corrosion, macro cell corrosion, top-bar effect, load-induced crack, artificial crack.

RÉSUMÉ

Le béton armé est un des matériaux les plus utilisés dans la construction. Néanmoins, après une période variable de fonctionnement, il peut se corroder. Les chlorures et la carbonatation sont les principaux facteurs provoquant la corrosion des structures en béton armé. La thèse a pour objectif d'étudier le comportement à la corrosion des armatures du béton sous environnement de carbonatation ou des chlorures, correspondant à l'influence du coulage à l'interface acier/béton (top-bar effet), du type de liant utilisé ainsi que d'une fissure transversale artificielle ou des fissures transversales induites par le chargement mécanique.

En général, la corrosion induite par la carbonatation est étudiée du point de vue d'un processus de corrosion uniforme. Le premier objectif de la thèse est d'étudier et de quantifier la présence de corrosion par macro pile (ou non uniforme) dans la corrosion induite par la carbonatation. Selon les résultats des expériences menées dans cette partie, le taux de corrosion dans les armatures de béton carbonaté est susceptible d'être considéré du point de vue simultané de la corrosion uniforme et macro pile, cette dernière étant fortement influencée par le rapport cathode/anode. De plus, l'application de CEM III utilisant des laitiers comme addictif a montré une réduction efficace de la corrosion non uniforme.

La deuxième partie se concentre sur l'influence de l'effet des défauts à l'interface acier/béton liés au coulage du béton (top-bar effet) sur le comportement à la corrosion dans le cas d'une corrosion induite par la carbonatation et de la présence d'une fissure induite par le chargement mécanique. Le suivi du courant de corrosion par macro pile, à l'aide d'un témoin métallique, a été utilisée dans l'expérience. La perte de masse ainsi que la cinétique de corrosion ont été calculées. La corrosion s'est développée principalement au niveau de la fissure induite par le chargement. En raison de l'influence de la qualité de l'interface acier/mortier, les barres supérieures étaient plus corrodées que les barres inférieures. Le courant de corrosion de macro pile mesurée sur les barres supérieures était plus élevé que sur les barres inférieures. La perte de masse de l'acier calculée à partir de la mesure du suivi de courant ne correspond qu'à une petite partie de la perte de masse totale déterminée par mesure gravimétrique. La corrosion uniforme semble ainsi être le phénomène principal.

La dernière partie étudie l'effet des défauts de coulage à l'interface acier/béton (top-bar effet) dans des échantillons de béton fibré avec ou sans fissure artificielle sur la corrosion induite par les chlorures. Les barres supérieures sont plus corrodées que les barres inférieures et la partie supérieure de la barre supérieure présente une corrosion plus élevée que la partie inférieure. En présence de fissures artificielles, le ''top-bar effet'' entraîne la propagation de la corrosion le long de la surface des barres d'acier. La corrosion se développe également le long de la barre supérieure lorsqu'il n'y a pas de fissure artificielle, dans un temps pas si différent du cas de la présence d'une fissure artificielle. Cela confirme que l'exposition aux chlorures de la surface supérieure et le « top-bar effect » sont très préjudiciables à la corrosion. En comparant le comportement avec un béton sans fibres, il apparaît que l'ajout de fibres dans le béton armé entraîne une augmentation de la résistance à la fissuration induite par la corrosion.

Dans chaque partie, les observations expérimentales sont couplées à des simulations numériques pour comparer et démontrer les résultats expérimentaux.

Mots clés : béton armé, corrosion induite par la carbonatation, corrosion induite par les chlorures, corrosion uniforme, macro pile, top-bar effet, fissure induite par le chargement mécanique, fissure artificielle.

GENERAL INTRODUCTION

Reinforced concrete is known as one of the most popular materials applied in construction thank to the excellent combination from compression strength of concrete and high tensile strength of steel bar. It is obviously most widely used in almost buildings, bridges as well as other structures in Vietnam. However due to exposure to such aggressive environments including carbonation or chlorides, reinforced concrete is sensitive to corrosion which leads to the reduction of mechanical performance during its lifetime, eventually triggering serious incidents or collapse of the structures. Unfortunately, Vietnam is a country where exist many “good condition” for aggressive factors causing corrosion. On the one hand, Vietnam owns a long coastline extending from north to south with over a length of 3260 km which facilities the chlorides induced corrosion. On the other hand, Vietnam is one of the most vulnerable countries to climate change and global warming. Emissions were estimated multiplied fivefold in the last 20 years. This led to the risk of carbonation induced corrosion to structures placed in populous cities with density of building. As a result, in-depth studies on the corrosion of reinforcement in concrete are necessary in order to analyze the behavior, evaluate the residual durability of the structures or giving solution to protect them from corrosion.

The main objective of the thesis is to study and give supplementary information concerning the response of reinforced concrete exposed to corrosion due to carbonation or chlorides. Additional points studied in the thesis are: the quantification of the ratio macro cell corrosion versus uniform corrosion, in carbonation-induced corrosion; the effect of load-induced cracks on carbonation-induced corrosion in case of “top bar effect”; the influence of “top bar effect” on chloride-induced corrosion, with or without artificial crack.

The presence of macro cell corrosion in carbonation-induced corrosion was hardly studied [1] in literature, and then be included in the thesis.

For carbonation-induced corrosion in presence of load-induced crack, Ghantous [2] in 2016 draws the following conclusion. After quick initiation at crack tip, there is a decrease in the corrosion kinetics with respect to time, and also there is also an absence of corrosion-induced cracks detection. Ghantous concluded that it can be predicted that structure sustainability will not be threatened by carbonation-induced corrosion deep in the crack. Nevertheless, this conclusion needs to be verified in case of presence of top-bar defects. Indeed, top bar defects would lead to a longer corroded zone from the crack tip and could lead to the appearance of corrosion-induced cracks before a significant decrease in corrosion kinetics.

For chlorides-induced corrosion in presence of cracks, the conclusions which can be drawn at this moment are more controversial. In the case of load-induced cracks, as studied and concluded by Hess in 2024 [3] the most important bias for the understanding of the corrosion process is the exact definition of the crack geometry at the steel concrete interface level and the resulting mechanical damage. To avoid this unknown of width of cracks at the SCI, Zhang [4]have performed his thesis with the use of artificial crack, where opening is constant from the concrete surface still the SCI. In this case, the artificial crack only plays a role of direct access for chlorides to SCI and allows to study the corrosion behavior in relation with the quality of interface, without any risk of healing or self-healing of the crack. The study of top bar defects and also the possible restriction of corrosion-induced cracking due to the presence of fibers in the concrete could then be studied.

In this thesis, the effect of top casting induced defects and cracks on the corrosion behavior were investigated. Both carbonation-induced corrosion and chlorides-induced corrosion were studied. If the macro cell predominant behavior is well established now for chlorides-induced corrosion, it was an open question concerning the carbonation-induced corrosion and was the subject of chapter 3. The effect of top-bar defects on carbonation-induced corrosion in presence of load-induced cracks was studied in chapter 4: it allows to complete the results concerning the presence of load-induced cracks on carbonation-induced corrosion already studied by Ghantous [2]. Finally, the presence of top bar defects associated with the use of concrete reinforced by fibers and the presence of artificial cracks was studied in chapter 5: it allows to study the possibility of anodic control of corrosion by increasing the confinement of corrosion products, and to complete the results from Zhang [4] concerning the effect of top bar defects associated with an artificial crack.

In the following, a brief description of each chapter in this thesis is given:

- The first chapter presents a literature review on both carbonation-induced corrosion and chlorides-induced corrosion. The effect of cracks, both load-induced cracks and artificial cracks are also reviewed in case of corrosion due to chlorides or carbonation.
- The second chapter describes the experimental program.

The remaining chapters going from the third one to the fifth one aim to present and discuss results:

- The third chapter is dedicated to discuss the part of uniform and macro cell corrosion in case of carbonation-induced corrosion.
- The chapter 4 discusses the influence of the top bar defects on the carbonation-induced corrosion in presence of load-induced cracks.

- The chapter 5 presents the corrosion results obtained in case of chloride-induced corrosion in presence of both top bar defects and artificial crack. The presence of fibers and their effects on corrosion and cracking control are discussed.

CHAPTER I. LITERATURE REVIEW

1. Introduction

When steel bars were embedded in concrete, they immediately receive the protection against corrosion. The concrete cover delays the time exposure to reinforcement bars from aggressive factors including carbonation and chloride ions. Also a highly alkaline pore solution derived from the hydration of cement (pH around 12.5-13) leads to form a thin, dense and passive film which limit the corrosion process at the steel surface to value below 0.1µA/cm^2 [5, 6]. However, in case of the presence of chlorides or carbonation the steel bars would become depassivated then active corrosion takes place causing the deterioration of the reinforced concrete structures. Several factors are related to facilitate the corrosion of steel bars and can be listed such as load-induced cracks, top bar effect and quality of steel concrete interface. This chapter focuses on the overall knowledge concerning the effect of these factors on corrosion behavior of concrete undergo carbonation and chloride contamination.

The following objectives include:

- Fundamental of corrosion of steel in concrete
- Carbonation induced corrosion in concrete
- Chloride induced corrosion in concrete
- Influence of crack on the corrosion of steel in concrete
- Influence of top bar casting of steel in concrete

1. Corrosion of steel in concrete

1.1. The process of corrosion of steel in concrete

Generally concrete protects steel bars from corrosion thanks to the high alkalinity in concrete when the pH of the pore solution is around 12.5-13. It is described in the Pourbaix diagram (Figure 1):

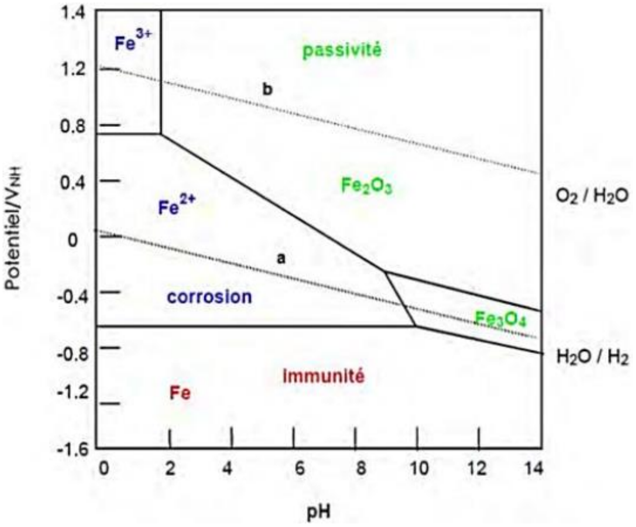

Figure 1 : Simplified E-pH Pourbaix diagram of iron in an aqueous medium under standard temperature and pressure conditions (T=25 °et P=1 atm [7]

It can be seen that the iron oxides Fe_3O_4 and Fe_2O_3 are species dominated in the interval value pH around 13 and steel bars are in passive form. This passivated film is a bilayer model consisting of the inner layer and the outer layer. The former was observed rich in Fe^{2+} oxides while the latter was rich in Fe^{3+} oxides and hydroxides [8-10]. In simulated alkali-activated fly ash the passive film was indicated with FeOOH-rich outer layer and FeO-rich inner layer [11]. The thickness of this thin protective layer was determined by value less than 10nm in different alkaline solution [12, 13], even around 3nm regardless of the electrolyte composition [8]. In the case of steel embedded with a cement matrix, it possessed a thickness about 10µm [14, 15]. The steel is protected by a passive film and dissolves at very low kinetic. The corrosion rate is less than 1µm/year [16, 17], even approximately 0.1 µm/year [2, 18]. However the passive film can be destroyed by the carbonation or chloride contamination[6, 18, 19].

Corrosion of steel in concrete is an electrochemical process and composed of four partial processes (Figure 2):

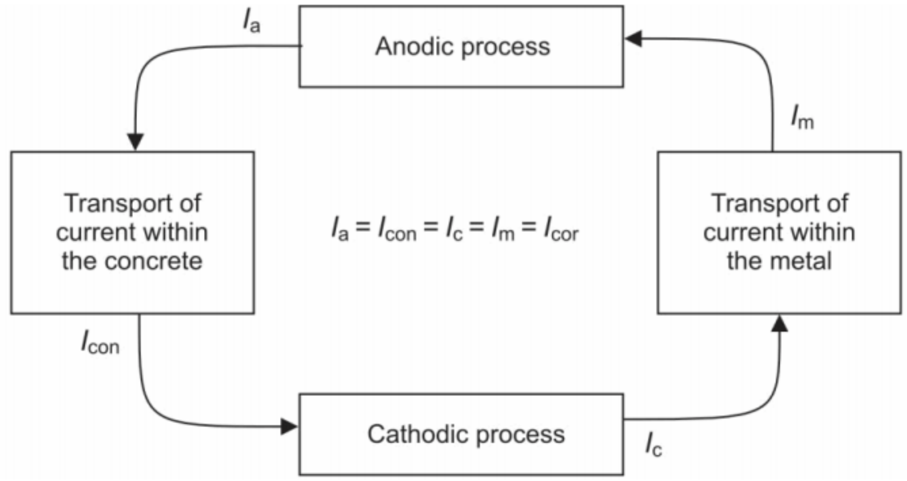

Figure 2 : Electrochemical mechanism of corrosion of steel in concrete [18]

- Anodic reaction:

This is the process from that iron was oxidized and electrons were liberated.

$$Fe \longrightarrow Fe^{2+} + 2e^-$$

- Cathodic reaction:

In the presence of oxygen, it consumes electrons to produces hydroxide and increase the alkalinity. The reaction will be:

$$O_2 + 2H_2O + 4e^- \longrightarrow 4OH^-$$

This reaction is the most frequent with atmospheric exposed concrete. The cathodic reaction is conditioned by oxygen availability determined by its diffusion kinetics through the cement matrix.

It could be noted that the cathodic reaction does not always corresponds to the reduction of oxygen, for example when the metal structure is buried in an anoxic soil which has poor oxygen. In that case the cathodic reaction can be the production of Hydrogen (it could also be the case in cathodic protection by impressed current).

- The transport of electron within the metal from anode to cathode.
- The transport of anions in the concrete from cathodic regions to anodic regions.

According to the different spatial locations of anode and cathode, corrosion of steel reinforcement in concrete structures can occur as uniform corrosion (anodic and cathodic zones are coincident) or galvanic corrosion (also known as macro cell, non-uniform or localized corrosion; anodic and cathodic zones are separated).

It should be noticed that in the point of view of the author of this thesis (and his supervisor) that the term of microcell which could be found in literature [20] is ambiguous and need clarification. Indeed, it corresponds in some case to uniform corrosion and in some case in small macro cell corrosion. The use of the term microcell to characterize small macro cell is not appropriate since whatever the distance between anodic and cathodic site, the corrosion process is the same. The use of microcell to indicate uniform corrosion would be then avoided in this thesis to eliminate confusion.

- Uniform corrosion: this means that the anodic (active steel) and cathodic (passive steel) zones are adjacent from one another. Each electron produced by an anodic reaction is consumed by a cathodic reaction. The Ohmic effect due to electrolyte resistance is inexistent and there is no current in the concrete [21]. In reinforced concrete, uniform corrosion could only exist in the case of corrosion-induced by carbonation, but is always coexisting with macro cell corrosion.
- Macro cell or Galvanic corrosion: this means that the anodic sites are distant from the cathodic ones: it could be adjacent and then sometimes up to a distance a few meters [22]. Electrons produced by anodic reaction could be consumed by cathodic reaction occurring somewhere else on the network of steel bars in concrete structure. The anodic and cathodic sites do not reach the same potential and there is presence of a corrosion current in sound concrete. Macro cell corrosion is consensually considered frequently induced by chlorides [19, 22-27] and is hardly considered in the case with carbonation induced corrosion. This case will be discussed further in this thesis.

Normally the steel bars in the concrete play the role of electron conductor and the pore solution in concrete acts as the conductor for the flow of ions. The corrosion rate in the concrete is negligible if presence of one in these conditions:

- The anodic current is slow (or passive control): when steel bars are passive, without the presence of aggressive factor such as carbon dioxide or chlorides.
- The cathodic process is slow (lack of oxygen or control of oxygen transport): when the diffusion of oxygen is slow or concrete is water-saturated.
- The resistance of concrete is high (or Ohmic control): when the exposed condition is low or dry relative humidity.

On the other hand, when the three conditions are present, the corrosion rate is high:

- The steel bar is depassivated
- Oxygen can reach the surface of steel
- Concrete resistivity is low.

Corrosion rate highly depends on the moisture in concrete. With high density concrete, corrosion rate could reach the maximum value when moisture content is equivalent to the equilibrium with a relative humidity ambiance of about 95% and a slightly higher relative humidity in the case of low-density concrete. Beyond this value (i.e concrete with high moisture content or near saturation), the electrochemical process is control by the cathodic process, the corrosion rate decreases with the increase of water content. Contrary, if concrete has lower moisture content, the corrosion rate depends of concrete resistivity.

Nevertheless, it should be noticed that even if the anodic site is in water-saturated concrete, the corrosion rate could be very important if there is somewhere a non-saturated cathodic zone: this is the case for partially submerged reinforced concrete pile [28, 29] for example.

The summary of corrosion rate related to different conditions is shown in Figure 3:

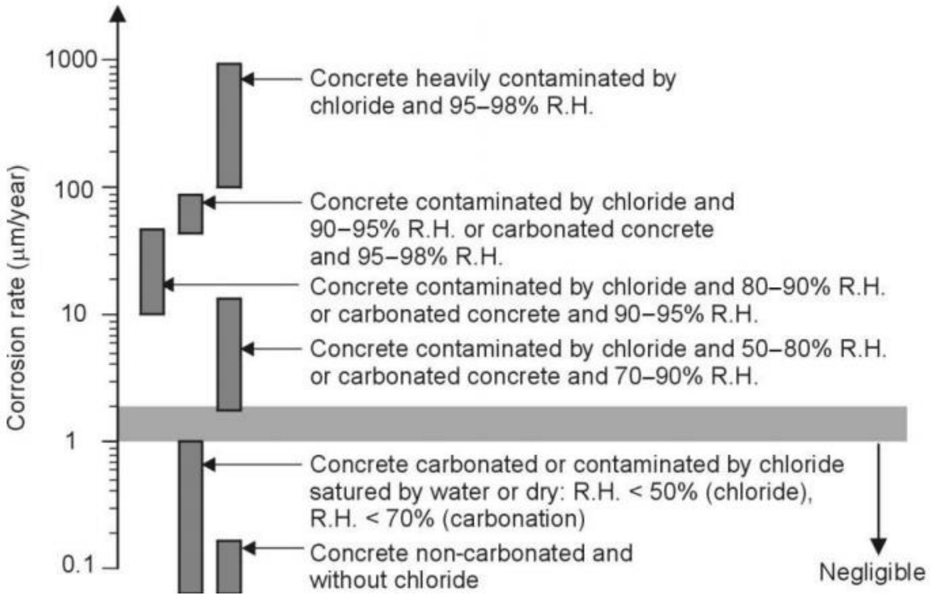

Figure 3 : Schematic representation of corrosion rate of steel in different concretes and exposures explosion [18]

1.2. Consequence of corrosion in concrete

The combination from irons oxidized and alkalinity can generate corrosion rust. Firstly, is the bright green ion (II) hydroxide:

$$Fe^{2+} + 2\,OH^{-} \longrightarrow Fe\,(OH)_2$$

This ion hydroxide then can consume oxygen and water results in ion (III):[18]

$$4\,Fe\,(OH)_2 + 2H_2O + O_2 \longrightarrow Fe(OH)_3$$

In reality, the precise composition of the corrosion product is not just only as in the chemical reactions above. It depends on some parameter such as oxygen concentration, pH value, temperature, carbonation, chloride contamination, etc… Additionally, the corrosion products lead the increase of volume of steel bars up to several times (1.8 to 6.2 times) [30, 31]. The expanding depends on the composition of chemical elements as in following Figure 4.

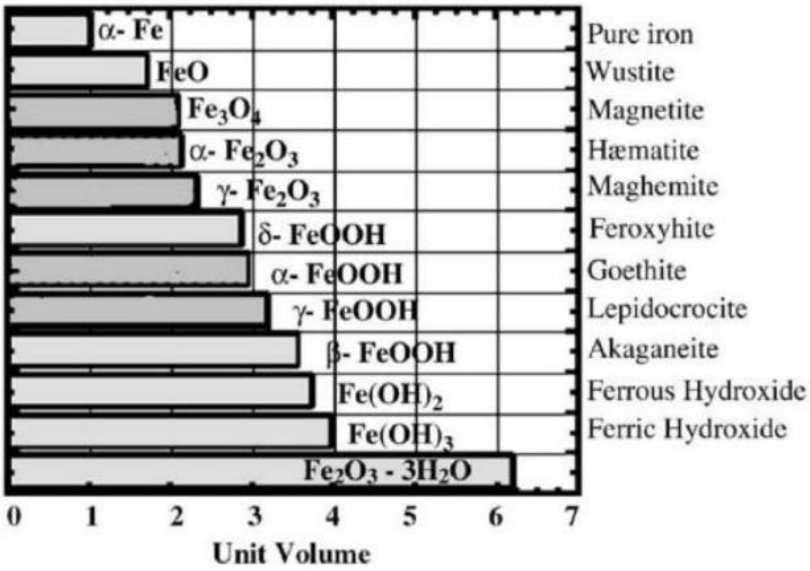

Figure 4 : Corrosion products and their expand factors [30]

At the beginning, a small amount of the rust may partly fulfill the pore in concrete without causing negative effect. However, when the volume is greater, there will be a pressure on the steel-concrete interface consequently generating cracks in the concrete cover and leading to a loss of bonding between steel and concrete as well as spalling and even delamination (Figure 5).

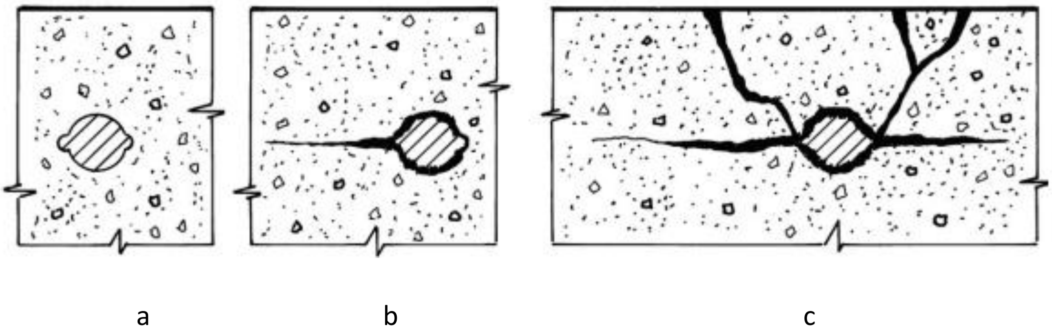

Figure 5 : Corrosion induced cracking of concrete(a. steel bar in the passive sate, b. internal crack within the concrete cause by rust growth, c. spalling of concrete by expansive rust products) [32]

On the other hand, the reduction of the cross section of steel bars lead to decrease the load-bearing capacity and to reduce the ductility of steel reinforcement.

2. Carbonation induced corrosion in RC

2.1. Carbonation of concrete

Carbonation process in reinforced concrete structures results from the ingress of atmospheric carbon dioxide in the concrete porosity. Carbon dioxide reacts with the hydrated cement paste and tends to neutralize the alkalinity of concrete and changes several characteristics of concrete including the microstructure of concrete, its mechanical performance, its transport properties and its water content.

Firstly, when carbon dioxide encountered concrete interstitial solution, it dissolved in the water then hydrating in the form of carbonic acid and followed by several reactions:

$$CO_2 + H_2O \longrightarrow H_2CO_3$$

$$H_2CO_3 + H_2O \longrightarrow H_3O^+ + HCO_3^- \text{ (pH is about 6.3)}$$

$$HCO_3^- + H_2O \longrightarrow CO_3^{2-} + H_2O \text{ (pH is about 10.3)}$$

For concrete made of Portland cement, the reactions between calcium hydrate in the cement paste and CO_2 can be written schematically as (Figure 6):

$$CaOH_2 \longrightarrow Ca^{2+} + 2OH^-$$

$$Ca^{2+} + CO_3^{2-} \longrightarrow CaCO^3$$

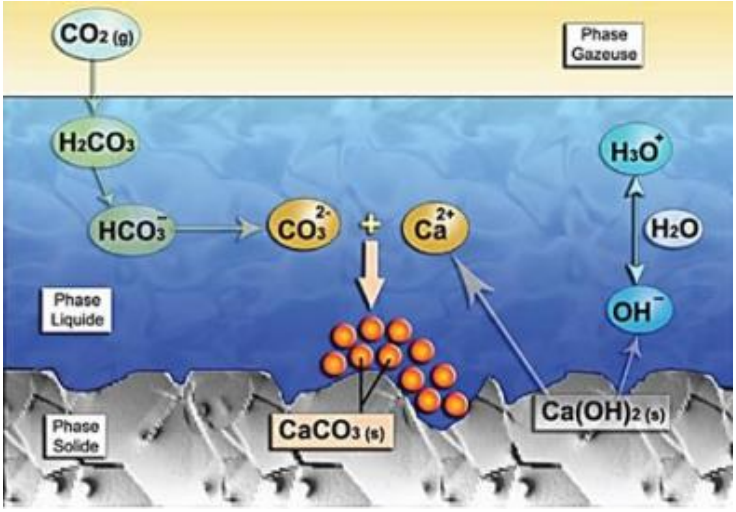

Figure 6 : Portlandite carbonation mechanism [33]

Also C-H-S can be carbonated as the equation below to form an amorphous structure which is similar to silica gel (Figure 7):

$$(CaO)_x - (SiO_2)_y\text{-}(H_2O)_z + xH_2CO_3 \longrightarrow xCaCO_3 + y\ SiO_2.tH_2O + (x\text{-}t\text{+}z)H_2O$$

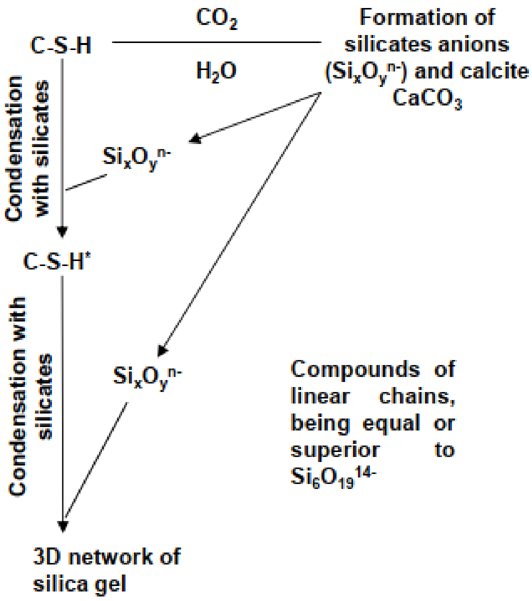

Figure 7 : C-S-H carbonation mechanism and formation of silica gel [34]

Additionally, there are other hydrates sensitive to carbonation such as hydrated calcium aluminates which result from the hydration of C_3A. However, the amount in conventional cementitious material contained moderate sulfate and/or aluminate is small (Table 1).

Composition of cement	Proportion (%)
C_3S	50-70
C_2S	15-30
C_3A	5-10
C_4AF	5-15

Table 1: Proportion of composition of clinker[35, 36]

The carbonation reaction firstly commences at the surface of the concrete. The rate of carbonation decreases in time and is affected by the diffusion of CO_2 according to Equation 1:

$$d=K\sqrt{t} \qquad \textit{Equation 1}$$

Where d is the carbonation front (mm) and t is the exposure time (year). The coefficient K can be determined thanks to a measure of the rate of carbonation for given concrete and environmental condition. Its value indicates the concrete quality. In case of poor concrete (which means highly porous concrete) or good concrete (concrete which has low porosity, well compacted and cured), K is more than 9 and less than 6, respectively. While average concrete (concrete which has medium porosity), K ranges from 6 to 9 [37].

Carbonation leads to several changes in reinforced concrete relating to the microstructure, the mechanical performance, the transport properties, the water content and the pH value. On the one hand, carbonation is found that it does not cause damage to the concrete itself and on the contrary, it can reduce the porosity in concrete then increase its mechanical properties [38]. Nevertheless, it can trigger some consequence to reinforced concrete structure. The drop of pH in interstitial solution promotes the depassivation process of embedded steel. Also, the modification of water transport because of carbonation[39] may influence to the oxygen concentration and the saturation degree in the concrete which directly affect the kinetic of corrosion in reinforced concrete.

2.2. Parameters influencing carbonation

The carbonation is a slow process. It would take several years for the carbonation front to reach to the steel bars. The rate of carbonation in concrete depends on several factors relating to environment and to the concrete itself.

2.2.1. Humidity

Relative humidity is an essential parameter influencing the carbonation rate. To accelerate the carbonation, it is indispensable the presence of water and CO_2. Both concrete which high RH and concrete with low RH, would hinder the chemical reactions. In case of high RH, CO_2 penetrates extremely slowly, even the diffusion rate can reach to value by zero if concrete is saturated. The diffusion of CO_2 is four orders of magnitude slower in aqueous than in the air phase [40]. On the other hand, in the case of low RH, the lack of water lead to inhibited the chemical reaction. The window for maximum rate of carbonation process is when the relative humidity ranges from 50 to 70% [41-43] (Figure 8):

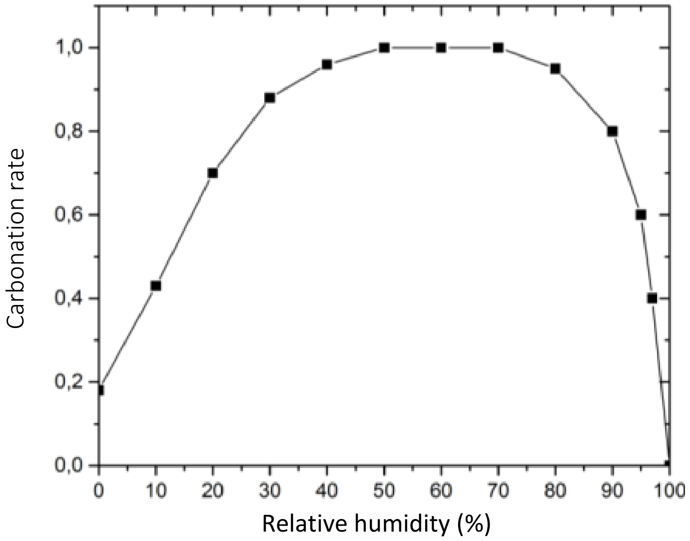

Figure 8 : Kinetics of the carbonation with respect to the relative humidity [44]

It should be noticed that CO_2 penetration is faster in dry concrete, as for example under a coating which protect the concrete from water and not for gas. As a result, a failure in the coating could lead to water penetration and then a deep carbonation front and high corrosion rate due to high water content. As a result, the 50-60% range of humidity is not always the worst environment.

2.2.2. CO_2 concentration

In natural conditions the content of CO_2 varies from 0.03% in rural environment to more than 0.1% in urban areas. Locally the concentration of carbon dioxide can reach higher concentration such as inside a motor vehicle tunnel. It is shown that the carbonation rate increases with the increasing of the content of CO_2 [18, 45, 46]. A week of exposure to content of CO2 by 4% indicates a similar penetration of carbonation of concrete which exposed one year to natural environment of carbon dioxide [47]. Numerous researches show that there is almost no change in the microstructure due to carbonation for content of CO_2 up to 4%. Even for 100% CO_2 under increased pressure, T. K. H. Al-Kadhimi et al offered the idea that it leads to the same microstructural as natural carbonation [48]. However, there are several contradictions. Castellote et al. hold the point of view that more than 3% of CO_2 gives results that do not represent the natural carbonation [45]. Ghantous indicated that the high carbon dioxide concentration probably leaded to a high carbonation shrinkage permitting a greater penetration length than the damaged one [2]. In this study, CO_2 ingresses from load induced cracks to reach the Steel Concrete Interface (SCI). Some researchers observed the similar reaction or phenomenon from the case of lower CO_2 [49-51]. Low CO_2 concentration (i.g by value 3-4%) was recommended to use in accelerated carbonation testing [2, 52, 53] [54, 55].

2.2.3. Temperature

The effect of temperature is still not really clear. In general, an increase in temperature will also increase the carbonation rate [43, 56]. When the temperature rises, transport properties and ion diffusion increase due to the thermal – activation according to Arrhenius law and the water evaporation. Nevertheless, several publications indicated that the solubility of the hydrates reduces as the increase of temperature, leading to the reduction of kinetics of carbonation in concrete. Both antagonist phenomena lead to an optimal temperature [57, 58] for carbonation process. In [52], reaction temperature of 20°C, 40 °C, 60 °C, 80 °C and 100 °C were applied and it was observed that the CO_2 content increased with the increase of temperature up to 60 °C following a decrease of CO_2 content despite the thermal activation. In [53], an increase of the temperature from 20 °C to 80 °C, leads to carbonation depth multiplied by 3.9.

2.2.4. Parameters related to concrete

Apart from several factors from the environment above, following factors related to concrete also influence to carbonation rate.

- Cement type:

Concrete's capacity to fix CO_2 is proportional to the alkalinity in its cement paste. In Portland cement, major of the mass of the original cement is composed of CaO. With blended cement, the ratio of CaO is lower, consequently leading to a lower $Ca(OH)_2$ content in the hardened cement paste which can result to an increase of carbonation rate in concrete. Indeed the carbonation rate of blended cement has been found a factor of 2-4 times higher than for Portland cement [59, 60]. Nevertheless, in blended cement, penetration of carbon dioxide may be slowed down because of smaller size of pores in case of blended cement which lead to lower porosity.

- Water/cement ratio:

The reason is that the permeability of concrete has huge influence on diffusion of carbon dioxide and thus on the carbonation rate. Some research showed that the higher w/c ratio, the higher the permeability and porosity [61, 62]. In particularly, a few of authors applied high w/c ratio by 0.9 or 1.0 to enhance the transport properties and the carbonation process in order to research carbonation induced corrosion [63, 64]. In fact, in high w/c, a large quantity of water evaporates facilitate carbon dioxide approach the concrete pores. On the other hand, in low w/c (by providing high cement contents) the cement density decreases the porosity in concrete then slow down the penetration of CO_2.

- Curing duration:

Curing is an effective method to ensure the maturity as well as minimize the defaults of concrete including the high porosity which facilitates the penetration of carbon dioxide. After some first hours casting, concrete may be subjected to desiccation Therefore curing reduces the amount of water which will be evaporated from concrete after casting. It was indicated that the longer duration of curing, the higher the compressive strength is which means the porosity decrease resulting a higher carbonation resistance [65].

The concretes with longer curing before exposing to carbonation gave a lower carbonation depth than the one with short period of initial curing [65]. With concrete owning low w/c, one of its objects to slow down the carbonation rate can only be achieved if concrete is well cured. In the case of concrete with blended cement, if being cured properly, the carbonation depth can be significantly limited (Figure 9).

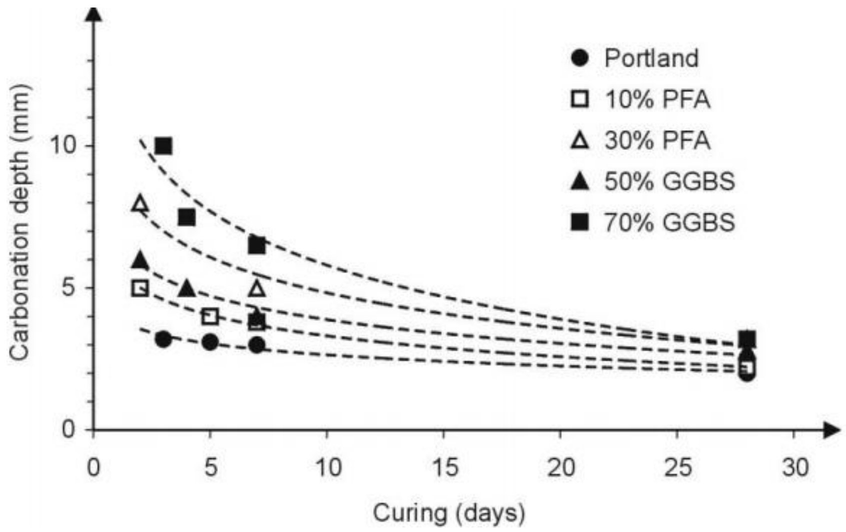

Figure 9 : Influence of curing on the depth of carbonation for different cement pastes of Portland cement and blended cements with fly ash and ground granulated blast furnace slag [18]

2.3. Corrosion rate in carbonation-induced corrosion

In case of carbonation, due to chemical reactions taking place in concrete structure the pH in the pore solution can reduce below 9 causing the depassivation of reinforcements. Once reinforcement is depassivated and if water and oxygen are present, corrosion takes place. On the one hand usually, carbonation-induced corrosion is considered as uniform corrosion. Corrosion rate in carbonation induced corrosion is mainly influenced by several parameters related to environment and concrete. On the other hand, carbonation-induced corrosion could also be considered owning galvanic part. In the latter case corrosion rate is assumed that it depends mainly on cathode/anode ratio, concrete resistivity as well as highly depends on steel- concrete interface and pre-existing oxides layer contributing at the surface of the reinforcement [1, 66].

2.3.1. Parameters from environment influencing the uniform corrosion rate

- Exposure condition (relative humidity and wet/dry cycling):

Angst et al. observed a general increase of corrosion rate with higher the relative humidity in the environment [41]. It is similar to this picture above (Figure 10) which show corrosion rate in carbonate concrete as a function of relative humidity.

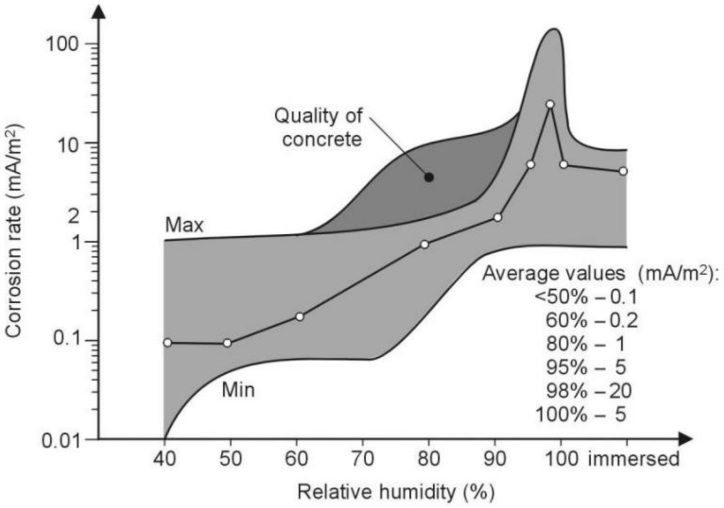

Figure 10 : Maximum and minimum values of corrosion rate in carbonated concrete as a function of environmental humidity [18]

If placing in the same graph it is easy to observe a different relationship of corrosion rate and carbonation rate with relative humidity (Figure 11).

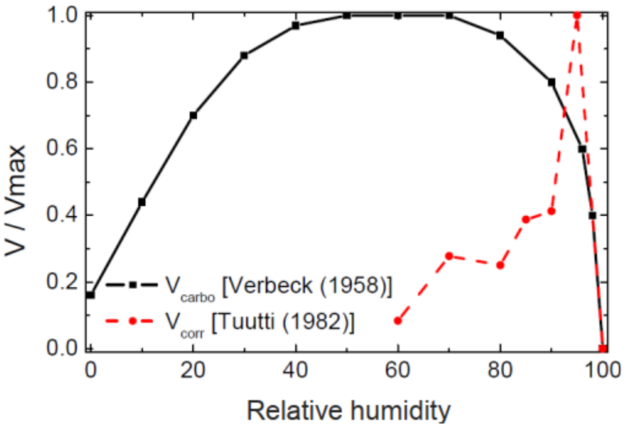

Figure 11 : Kinetics of corrosion and carbonation with respect to relative humidity [67]

In the interval of relative humidity about 60% where carbonation rate reaches the maximum value, the corrosion rate is considered negligible and vice versa. Many researchers agree that water saturated is the worst aggressive condition for carbonation-induced corrosion when RC structure is submitted to wetting-drying period of low humidity following high humidity. Indeed corrosion rate could be two to four times higher in case of high humidity (corrosion rate could be from 0.38-1.76µA/cm^2 if relative humidity by 95-100% and from 0.75-7 µA/cm^2 if sample was partly immersed or immersed [41]). For the experiments with carbonated sample in this thesis, they will either immersed in water or suffering wetting-drying cycles.

- Temperature:

In general there is a higher corrosion rate at higher temperature [41]. However, relation between temperature and corrosion rate in case of carbonation-induced corrosion indicated some dissimilarity.

In [56] the test was carried out in condition of 15% CO_2 concentration and temperature by 20°C, 30°C and 40°C and the author had the same conclusion. Nevertheless in [2] performing the experiments with 3% CO_2 concentration and temperature by 20°C and 40°C Ghantous concluded that the same corrosion rate was found under these two temperatures because the drying phase at 40°C generates a higher concrete resistivity restricting to the galvanic corrosion process. Temperature is indicated to play a role only in environments with high relative humidity [68].

2.3.2. Parameters related to characteristics of reinforced concrete influencing the uniform corrosion rate

- Water to cement ratio:

The increase of w/c reduce the strength of concrete and increase its porosity leads to a high diffusivity of oxygen and facilitates the penetration of aggressive agents as carbon dioxide [69, 70]. On the contrary, a general trend is that there is a drop of corrosion rate if w/c decreases. For example a reduction of 2.5 times was observed when w/c decrease from 0.8 to 0.55 [41]. However, the significant influence was found at high relative humidity.

- Cement type:

Majority of researchers agree that the corrosion rate of reinforcement increases for clinker replaced binders [71-75]. Concrete made with Portland showed the lowest corrosion current density was confirmed in [68]. The increase of corrosion rate varies to exposure conditions. It gets the most significant in case of partially or fully immersed conditions (Figure 12).

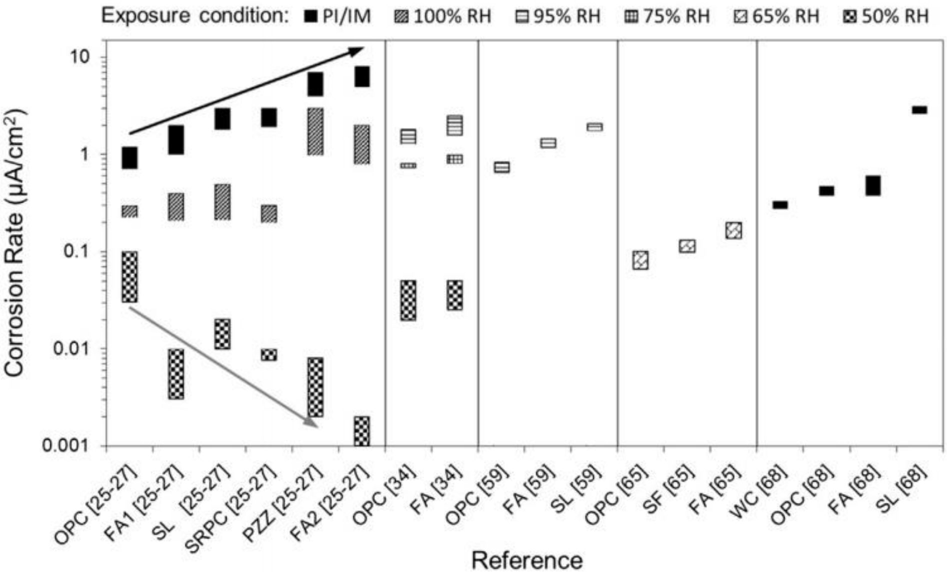

Figure 12 : Corrosion rate value with concrete made with different binders in different exposure conditions [41]

- Concrete resistivity:

This is the interest of several researchers. In their research in term of corrosion rate and resistivity, authors signify a relationship between them. Most of them carried out the measurement form the point of view that corrosion in carbonation-induced corrosion is uniform type. In uniform form, corrosion rate is necessary independent from resistivity, but a relationship between resistivity and corrosion kinetic is generally assumed [76]. According to [77] generally, a decrease in concrete resistivity leads to a drop of corrosion rate. Nevertheless it is not the case in saturated concrete where the corrosion is still small despites a low resistivity and under the cathodic control [78, 79]. Also, the correlation of resistivity and corrosion rate should be linked to other factor such as the cement type, the cause of corrosion, moisture state, etc…

- Cracks:

Cracking is an unavoidable problem in concrete structure and its influence on corrosion process is always concerned. In the presence of cracks, it is clear that corrosion commences at the crack tips which can promote the penetration of carbon dioxide, following the depassivation of steel bar. Whatever crack widths allow carbon dioxide to expose the steel concrete interface starting the corrosion and spreading the interface [80, 81]. The time to depassivation decrease in the presence of cracks and relates to several factors such as micro climate, concrete cover and deposits within the crack [82].

Regarding the influence of cracks on successive phase of corrosion in carbonation-induced corrosion, several researches were mentioned to it. In [83] propagation of corrosion may be favored by pre-cracks. In [19] the authors indicated no link between cracks and propagation phase of corrosion, but the two-phase model by Tuutti [84] (which includes the initiation and propagation phase) needs to be completed by a four phase model (which includes incubation, initiation, induction and propagation phase) in case of cracked concrete. For carbonation-induced corrosion, Tuutti [82] proposes such a four-phase model indicating that there is repassivation at the crack tip which leads to a dormant phase of corrosion (or induction phase). Such behavior was also described by François [85] for carbonation-induced corrosion but also for chloride-induced corrosion. As a result, after steel bar is being depassivated the corrosion reaches high value during initiation following slowing down to a negligible current because of a blockage at the crack tips induced by corrosion products as being indicated in [2]. During this dormant phase corrosion rate does not depend of crack opening. Also, it is independent to the crack orientation and rain duration.

Further study on influence of crack will be mentioned in the following part of the thesis.

2.3.3. Macro cell corrosion rate

There are a few references in literature concerning the corrosion rate corresponding to the macro cell corrosion in carbonation-induced corrosion [1, 66, 86]. For parameters related to the environment, there is no reason that the influence could be different from the case of uniform corrosion. For parameters related to reinforced concrete, there is a strong influence of the following parameters on the macro cell corrosion rate:

- Resistivity: because it is a part of the macro cell process. It should be noticed that resistivity is different in cathodic areas (non-carbonated) than in anodic areas (carbonated).

- Ratio Cathode/Anode: in case of carbonation-induced corrosion, this ratio could be quite limited (around 1 or 2).

- Cracks: in case of load-induced cracks, there is necessary a high C/A ratio, since the anodic site is small, which could lead to increase the macro cell corrosion rate.

- Steel – concrete interface is known to play an important role to reinforcement corrosion. This one was even evaluated more essential to corrosion of steel bar than the surface crack width [2]. The presence of defects between steel and concrete highly influences the macro cell corrosion current [1]. The macro cell current could be up to 3 times higher in case of existence steel concrete interfacial default. Corrosion layer appears to be non–uniform at the steel surface and more corrosion products were also observed in space between the aggregate and the steel bar [87]. Steel bar with the pre-existing oxides being cleaned results to a higher value in both macro cell and uniform corrosion current.

3. Chloride-induced corrosion of steel bars in concrete

Among the dangerous factors to corrosion in reinforced concrete, chloride is always the most mentioned parameter [88-91]. Different from the corrosion due to carbonation, corrosion by chloride contamination takes place if the chloride content closed to the surface of steel bar reaches a given threshold value or critical chloride content.

The source of chlorides can come from the concrete composition or/ and from the environment (exogeneous chlorides and endogeneous chlorides).

- Chloride from the environment (exogeneous chlorides): this external source can be marine environment with different level of contamination or structures where chloride-bearing de-icing salts were used in wintertime, or industrial environment, or swimming pool …. [92-94]
- Chloride from the concrete composition (endogeneous chlorides): endogenous chlorides could be in water, additives, admixtures, aggregates and cement. According to EN 206, the limitation of chloride content in the cement are 0.2-0.4% chloride ions by mass of binder for reinforced and 0.1-0.2% for pre-stressed concrete. The adding of chlorinated additives, sea water or

aggregates polluted by chlorides is forbidden now, however, this problem could be encountered in several structures built in the past.

Chlorides are mainly fixed to the cement matrix by physical absorption on C-S-H but also by chemical reaction with hydrates.

3.1. Local depassivation of steel

Chloride can induce damages to the passive film of steel bars, leading to localize corrosion. The failure of the passive film of reinforcement is assume to be managed by 3 mechanisms which could be concomitant.

- Mechanism of adsorption (chemical and physical): the physical mechanism of adsorption of chlorides on the surface of the passive film increases the transfer of ferrous and ferric ions towards the interstitial solution of concrete. According to the chemical mechanism, chloride dissolved the passive film. The 2 mechanisms can take place individually or interact (Figure 13, Figure 14).
- Penetration mechanism: Chloride penetrates through the defects of the passive film up to the metal/ passive film interface. Steel will be in contact with chlorides forming ferrous ion Fe^{2+}. This latter combine hydroxyl ions OH^- generate ferrous hydroxide $Fe(OH)_2$ which is not stable and form Fe_3O_4 or Fe_2O_3. The expanding up to above 6 times of these products can cause cracking in the passive film (Figure 15).
- Mechanism of failure of the film by electrostriction: the passivation layer can be destroyed under the influence of electrostriction due to the superficial tension of the oxide layer triggered by the adsorption of chloride (Figure 16).

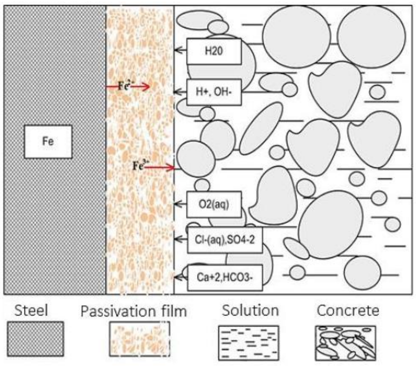

Figure 13 : Physical adsorption of chlorides at the surface of the passivation film [95]

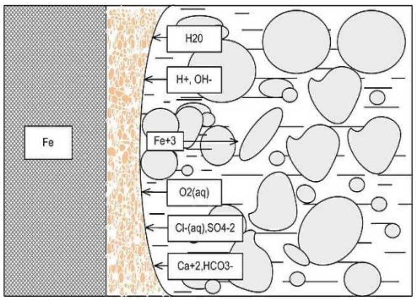

Figure 14 : Chemical adsorption leading to the dissolution of the passivation film [95]

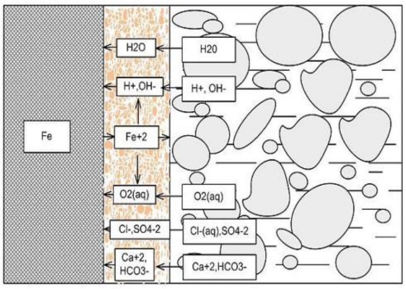

Figure 15 : Diffusion of chlorides through the passivation film [95]

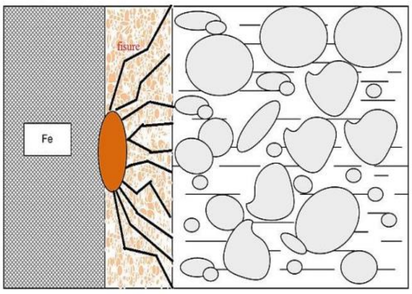

Figure 16 : Cracking of the passive film induced by the formation of oxy-hydroxide [95]

3.2. Mechanism of chloride ingress and binding in concrete

The mechanism of chloride is different from un-cracked concrete to cracked concrete because of a combination of chloride ingress in concrete porosity and in crack in the latter case.

3.2.1. Chloride transport in un-cracked concrete

The penetration of chloride in un-cracked concrete is managed by 3 mechanisms including convection, diffusion and permeation [94, 96].

- Convection: the chloride transport is caused by a difference in moisture content. In non-saturated concrete, water containing chloride ions moves towards zones with lower moisture content due to surface tension in the capillary pores.
- Diffusion: ionic transport is driven by a concentration difference in various zones. Chloride ions move from higher concentration zone to the lower zone. This process is most effective when the concrete is fully saturated.
- Permeation: the movement of chloride ions is under a difference in hydraulic pressure in various zones.

3.2.2. Chloride binding in concrete

Once chloride has penetrated in concrete, a portion of them is bound physically or chemically by cement hydration product. The chloride binding in concrete is the interaction between the porous concrete matrix and chloride ions. This process has influence on corrosion in concrete [97]. Firstly, the reduction of the free chloride content can reduce the probability of corrosion. Secondly, the removing of chloride from the diffusion flux can slow down the chloride ingress. Thirdly, this leads to formation of Friedel's salt in a less porous structure then affect the transport of chloride ions [98].

The chlorides in concrete can be expressed either the chloride concentration in pore solution (free chloride) or the total chloride content in the concrete (including free and bound chlorides). In generally only the chloride ions dissolved in pore solutions is believed to generate corrosion. However, study of chemical aspects of binding show that bound chloride may also affect corrosion risk because some of the bound chlorides may be released at altered conditions (i.e the increase of temperature above 55°C [99], the drop of pH [90, 100] or by sulfate attack or carbonation of the hardened concrete paste [92]). It can be seen that theoretically, only free chlorides are considered to initiate corrosion. Therefore, free chloride is preferably used to express chloride threshold. The free chlorides concentration in the porosity can be calculated by Equation 2:

$$Free[Cl] = \frac{FreeCcrit_m.\rho}{p_w} = \frac{FreeCcrit_b.C_b}{P_w} \qquad \text{Equation 2}$$

Where:

- P_w is the water porosity (%)
- ρ is the theoretical density of material (mortar or concrete)
- C_b is the binder content (kg/m^3 of material)
- $FreeCcrit_m$, $FreeCcrit_b$ are the free critical chloride content per weight of material (mortar or concrete) expressed in %/wt. material and per weight of binder expressed in %/wt. binder respectively.

Chloride binding depends on many parameters [101] including chloride concentration [102], the cement composition [103] or supplementary in cementitious materials [104].

3.2.3. Chloride threshold initiating corrosion

This is a fundamental condition to the chloride-induced corrosion in concrete. Once reaching a critical concentration of chloride, the passive film is locally broken which leads to initiation of corrosion. This critical chloride content depends on numerous factors. Major of them are the concentration of hydroxyl ions in the pore solution, the potential of the steel and the presence of voids at the steel- concrete interface. Other factors that have influence on chloride threshold are also concerned such as the temperature, the composition of cement, the composition or surface roughness of the steel reinforcement, or the polarization with anodic and cathodic current.

Commonly chloride threshold is expressed by these following ways [27, 105] (it should be noted that total chloride content or free chloride content can be found):

- Weight of binder or concrete (aggressive species is total chloride content)
- Weight of binder or concrete or as a concentration of chloride in the interstitial solution (aggressive species is free chloride)
- $[Cl^-]/[OH^-]$ ratio (aggressive species is free chloride ion concentration)
- $[Cl^-]/[H^+]$ ratio

The precise value of chloride threshold is still various, ranging up to three orders of magnitude. Angst et al. in [105] resumed that the total chloride expressed by weight of cement vary from 0.04% to 8.34% and free chloride ion concentration range from 0.01 to 45 if it is expressed by $[Cl^-]/[OH^-]$ ratio. Nygaard and Geiker [106] found chloride threshold (expressed as total chloride content) in the range from 0.52 to 0.74 /mass of binder. Such interval value is also often found in [100]. The critical threshold is found by a value of 0.8% /weight of cement with a standard deviation 0.2 % for concrete made with Portland in [107]. Related to this type of cement a wide range of Ccrit value over years is found. The variety of chloride threshold value is derived from the physicochemical factors in material, the testing methodology or inherent stochastic processes in corrosion progress [91]. Among these sources of variability of Ccrit, applying appropriate technique and focusing on steel concrete interface should be highly considered.

Recently Chalhoub et al. have developed a new experimental protocol which allows determine chloride threshold values initiating corrosion and study the corrosion current during the propagation phase also [108].

3.2.4. Chloride transportation in cracked concrete

Not similar to the ingress on chlorides in un-cracked concrete, chloride transportation in cracked concrete is the combination of chloride penetration in concrete and in cracks [109]. Chlorides penetrate along cracks in two phases. In the first phase, convection is the major mechanism. Chlorides ingress is under capillary suction or water convection. In the second phase, the penetration is governed by diffusion in cracks and under concentration gradient. There are numerous characteristics of cracks that influence chloride penetration. Crack density, crack orientation, crack depth, crack width and self-healing of cracks will be mentioned in detail in section 4.

3.3. Corrosion rate

Corrosion induced by chloride in concrete is localized (or galvanic or macro cell) corrosion. The passive film on the surface of steel bar is destroyed locally acting as anode which is spatially separated to cathode. The corrosion level corresponding to corrosion rate and penetration rate is traditionally ranged in this Table 2 below resulting from the work of the RILEM TC 154 EMC committee:

I_{corr}(µA/cm^2)	V_{corr}(mm/y)	Corrosion level
≤ 0.1	≤ 0.001	Negligible
0.1-0.5	0.001-0.005	Low
0.5-1	0.005-0.01	Moderate
>1	>0.01	High

Table 2: Range of corrosion level according to corrosion rate and speed of penetration[110]

Nevertheless, the actual corrosion rate in chloride-induced corrosion appears in reality to be higher than the value report in Chalhoub et al. [111] measure corrosion current density in the order of 50-200 µA/cm^2 before the appearance of the corrosion-induced cracks. As reported by François [112] it is necessary to review completely the method to evaluate corrosion current densities which need to evaluate the real size of anodic site.

The observation of localized corrosion induced by chloride in concrete indicated a more remarkable corrosion progress on the length of the rebar than in depth [112]. There are several influenced factors on corrosion current related to material, environment and geometry. Some of them may interact and result influence together to corrosion rate.

3.3.1. Factors related to material

- Electrical resistivity:

This parameter expresses its ability to withstand the transfer of charge and is one of major influential factors for corrosion kinetics in reinforced concrete. In presence of chloride, the electrical resistance of concrete decreases as chloride ions increase which lead to increase the corrosion density. However it will not be valid in the case of totally immersed structure where the corrosion rate is small despite a low resistance [77, 113] because in this case corrosion rate is under cathodic control. Electrical resistivity of concrete depends on several factors related to material (such as water binder ratio, cement type…), environment condition (such as chloride content, humidity, temperature…)

- Binder type:

It is clear besides Portland cement (PC), different cements with supplementary cementitious materials (SCM) such as Blast Furnace Slag (BFS), Fly Ash (FS), Silica Fume (SF) is more and more applied. These types of cement were indicated to impact on corrosion kinetics. SCMs modify both pore solution chemistry and environment surrounding the steel which can lead to reduce the corrosion rate [114, 115]. In the same research, the author ranked the corrosion rate in ascending order according to

SCMs application as SH (75% BFS) < TR (50% PC+43% BFS+7% SF) < SM(50% BFS) < 30% FA < SL (25% BFS) < 7% SF < PC and SM < FA < SF < PC with samples owning cover depth by 4cm and 2cm respectively as well as crack width of 0.2mm and 0.7mm for each of the binder types. Blended cement is observed better against to chloride induced corrosion than PC in [116] due to an increase in resistivity in blended cement which comes from interaction in pore structure. Ranking between corrosion rate and various substitute level of SCMs as follows PC > 5% SF > 20% FA > 40% FA > 40% BFS > 60% BFS > 60% FA > 80% BFS > 10% SF was assessed in [117]. Generally in a given set conditions in terms of humidity, temperature and provided corrosion has initiated, the higher resistivity of blended cements bring a lower corrosion in comparison to Portland cement, yet it is not totally with the case by Arya and Xu in [118]. Implement the measurement with samples in different cement type under different chloride content, the rank of corrosion density is FA >SF >S > PC for 1% addition of chloride but is FA > PC > S > SF for 3% addition of this chemical element. In a different research [119] the authors studied on Portland limestone cement partially replaced with 5%, 10%, 15% and 20% of metakaolin and they found a reduction of corrosion rate with the higher addition of metakaolin. In addition several researches on the relation of application geopolymer concrete (GPC) and its impaction on corrosion also proposed a similar conclusion that geopolymer can hinder effectively corrosion in reinforced steel [120-123] rather than OPC concrete because GPC was exhibited higher resistance to chloride ingress and steel corrosion than the other.

- Cover thickness:

The influence of cover depth of concrete on corrosion rate is obvious while putting together with other parameters for example binder type, crack width and concrete quality. Thicker cover of concrete can reduce the diffusion rate of oxygen remarkably. In the case the concrete is not water-saturated it was observed that cover depth generated no influence to corrosion rate by Raupach in [124]. Related to the effect of cover depth to corrosion rate under binder type, Scott and Alexander studied various binder type with 2 value of cover by 20 and 40mm [114]. The result is that an increase of cover depth performed a reduction of corrosion rate by more than half was measured with PC sample but it is not the case with SCMs samples. Model proposed by Otieno et al. [125] suggests that the worst scenario for the highest effect on corrosion rate is when a low cover depth links to a high crack width. The collaboration of concrete cover and crack thickness influenced remarkable on corrosion is confirmed in [126]. An appropriately selected cover depth plays an important role in protect steel from corrosion.

3.3.2. Factors related to environment

- Chloride content:

Chloride concentration has a significant influence on the corrosion rate. Even, it is was evaluated the strongest effect on corrosion rate than other factors followed by cement type, steel type and water concrete ratio [116]. Higher corrosion current was measured under a development of chloride content [113, 118, 127, 128]. The reason is that conductivity of concrete increases with the increments of chloride content and also there is combination between chloride ions and ferrous ions to form a water-soluble product that can ameliorate corrosion progress. The electrochemical properties of steel at anodic sites are influenced by chloride concentration modifying the iron anodic Tafel coefficient and, subsequently, the kinetics of corrosion [129].

- Temperature:

Commonly it is confirmed in several research that the corrosion current of reinforcement increases with a rise of temperature. The trend can be seen clearly if the other factors are held unchanged. The fact is that temperature varies can lead other parameter which can influence to corrosion rate alter also. According to [130] the influence of temperature should be considered with moisture availability. In the study of Otsuki [131] the author investigated specimens with temperature by 20°C, 30°C, 40°C and relative humidity of 60% and found that the rate of diffusion of Cl^-, O_2 and macro cell corrosion increased as the temperature was increased. Sample by Michel et al in [132] were subjected to different temperature by 1°C, 15°C, 25°C, 35°C and 50°C expressed considerable higher value of corrosion rate at above 85% RH than at 75% RH. The result was explained thank to Arrhenius equation with a moisture dependent activation energy about 10kJ/mol by RH 75% and 3-4 times higher at above RH 85%. In the research [133], the author investigated with wide range of temperature (10, 20, 30, 40 and 50°C) ,relative humidity from 55% to 95%. The conclusion was that corrosion rate increase when temperature increases under both resistance and cathodic reaction control due to a drop of resistivity of concrete under higher temperature.

- Relative humidity:

This parameter is usually studied together with other influenced factors to corrosion density like temperature, chloride concentration electrical resistivity or binder type … in order to evaluate the impact on corrosion rate. In [134] no clear relation between relative humidity and corrosion rate was found due to their interaction with each other or the complex dependency of these two factors could best be related to changes of electrical resistivity of concrete as in [135]. In case of concrete with chloride contaminated corrosion rate increases with both humidity and temperature. Therefore, it is not reasonable to consider these two parameters separately. Correlation of humidity and chloride was presented by author in [136]. Corrosion current is moisture dependent with a maximum in the interval 91-97% depending on chloride content. At higher concentration the maximum rate is at the lower end of the interval whereas the maximum value is at the higher end of the interval in the case lower chloride content.

3.3.3. Factors related to geometry

- Cathode - anode ratio:

An increase of corrosion rate can correspond to higher value of cathode anode ratio was found in several research and once again was confirmed in another recent study [137]. In [138] a change by 3 to 4 times of cathode/anode ratio results only a growth about 30% of corrosion current due to the effect of the spreading resistance surrounding anodic sites. Additionally, the cathode/anode ratio and corrosion current were found strongly related to resistivity of concrete especially at very high resistivity, where the current density showed a remarkable decrease. Or in the research [139] a similar correlation between cathode/anode area ratio up to 190 and galvanic corrosion was observed yet the rate of increase decreased as the cathode anode ratio increased. Chalhoub et al. also investigated the relationship of corrosion current with cathode/anode ratio in [27] where the authors applied a large range of cathode anode ratio up to 2950 and found the equal result. There is a limitation of mobilized cathodic surface above which the impact of cathode becomes negligible.

- Cathode - anode distance:

In term of geometric parameters and corrosion rate in concrete, cathode anode distance is considered one of the most influenced factors. Generally the corrosion current decrease if the distance between cathode and anode increase [139]. The authors effectuated the test with a 4m long beam and also found a significant current contributed to the most distant cathode. The throwing power of the anode was indicated exceeding a distance of one meter which is similar to the observation in [140]. Additionally, the throwing power of anode is under the quality of concrete or in the other word is the resistivity of concrete. With an increasing distance of cathode by 70cm with the specimens owning 1.5m in length and a anode in the middle as description in [141], a fall by 3 times of current density was measured with the furthest cathode. Chalhoub et al. [29] studied the effect of cathode anode distance by using a 10 m long reinforced beam and found the macro cell corrosion current can be provided by cathode at large distance from the anode and closer cathode receive more current. Also, was found the influence of resistivity on the repartition of macro cell current.

4. Influence of crack on the corrosion of steel in concrete

The presence of cracks in reinforced concrete is unavoidable due to an exceeding of its tensile capacity induced by structural loads, a volume change of concrete (shrinkage or temperature change …) or expansive pressure inside the concrete (such as from chemical attack or freezing damage …).

Among related causes generated crack above, except load-induced crack, the rest can be mitigated using a proper mixture design, placement, compacting, finishing and curing technique.

Once appearance of crack, it generates significant effects to the de-passivation of steel bars by providing favorable conditions exposure for aggressive factors (chloride and carbon dioxide) to reinforcement and influence corrosion process. The penetration of these factors is under several crack properties such as crack width, crack depth, crack frequency, crack orientation and capacity of seal-healing in location of crack. Both several influenced characteristics of cracks and effect of crack to corrosion process will be discussed.

4.1. Effect of several crack characteristics on penetration of aggressive specimens

4.1.1. Crack width

The role of crack width is that to provide such a favorable condition for the diffusion of chloride as well as penetration of carbon dioxide in concrete specimens exposed to chloride or carbonation.

In the case chloride induced corrosion, chlorides are described to penetrate both across sound concrete and along crack path as in Figure 17.

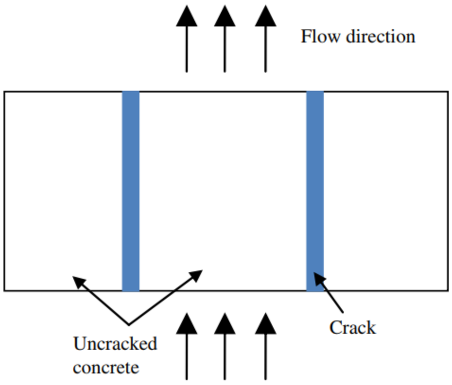

Figure 17 : two phase parallel model for diffusion in cracked concrete [142]

In the same research, the author proposed an equation to determine the equivalent diffusion coefficient of cracked concrete which indicated a proportional of diffusion coefficient and crack width. That chloride penetration increases with an increase of crack width was supported by several researchers. By investigating the samples with varying crack width from 0.1-0.4mm, it was observed a diffusion coefficient increase from 24 times to 145 times in comparison to un-cracked concrete in [143]. However, it was also indicated a critical crack width below which no significant chloride diffusion takes places, reduces or even no occurs. As an observation by Ismail et al. in [144] no chloride diffusion occurring perpendicularly to the crack path, below the crack width of 0.03mm was reported. Additionally some studies proposed that there is no correlation between crack width and chloride diffusion in reinforced concrete such as [145] with crack width up to 0.5 mm and [146] width crack width in the range 0.2-0.3 mm. In general, impact of crack width on chloride ingress has been received conflicting results which were resumed in a recent study [147]. In a recent study Hess[3] show that whatever the crack width (measured using X-Ray Tomography), in the range 20-100 µm, chloride can penetrate quickly in cracks to induce corrosion.

In the case of carbonation-induced corrosion, the fact that the carbonation depths increase with the increase in crack width is also indicated in many studies based on varying widths. Author in [148] investigated carbonated concrete samples made with different types of cement including OPC, PFA and GGBS and found that the crack width increase the depth of carbonation for all concrete samples. L. E. Sullivan-Green in [149] confirmed that the relationship between crack width and carbonation penetration is linear. Some other authors built modeling to forecast the depth of carbonation considering crack width. Kwon and Na in [150] suggested an equation exhibited relation of carbonation depth with crack with a ranging from 0.1 and 0.2 mm in cracked concrete. The proposed model by A. S. Al-Ameeri et al. in [151] with a range of crack widths from 0 and 0.35mm expressed the influence of crack width and also considered the impact of externally affected factors such as temperature and relative humidity. On the contrary Alahmad et al. [80] shows that there is no threshold limit in crack opening for carbonation: whatever the crack width, crack path is fully carbonated and CO_2 reached the reinforcement to induce corrosion.

4.1.2. Crack depth

Crack depth is also a critical parameter which impacts the chloride ions penetration depth in concrete. In [146] the authors studied specimens with different crack depth of 5, 10, 15, 20 mm. It was found that as crack depth increases the chloride penetration increase and the longer duration the test, the more pronounced the effect is. Another study by Stitmannaithum et al. [152] on effect of crack depth to chloride penetration with different water cement ratios confirmed the trend of increasing the chloride ions diffusion when crack depth increase and also observed the independence of the tendency with W/C.

4.1.3. Crack frequency

Crack frequency or crack density is the number of cracks per specific length. The general tendency is that chloride penetration increases with the growth of crack frequency. It can be understood because more quantity of crack will supply more pathways for chloride ions to concrete matrix.

In a study, Konin et al. [153] evaluated the effect of parameters on chloride ingress in concrete. It was observed that an increase in micro-cracking density in concrete, lead to higher chloride ions penetration. The same trend was also found in [154] where the author applied freeze/thaw cycles to create cracks and a steady-state flow to measure the chloride diffusion. The result was that the chloride migration rate increased by 2.5 times after 31 cycles, 4.3 times after 61 cycles and 7.9 times after 95 cycles where generated crack density was measured by 0.46, 0.61 and 0.77 per millimeter respectively compared to the initial specimens. In [155], it was found that the water and acid soluble chlorides concentration increase with increasing crack density of concrete under a non-steady state diffusion and this correlation can be described as a linear function.

4.1.4. Self-healing

Self-healing is the capacity of concrete to heal its crack itself under proper conditions. Self-healing of cracks is observed to be able to reduce the permeability of cracked concrete, the chloride ingress or water transport.

The precipitation of calcium carbonate crystal $CaCO_3$ from reaction of free calcium hydroxide and calcium oxide in cement matrix with atmospheric CO_2 or the presence of ettringite and brucite in sea water can promote the mechanisms self- healing in the case of small crack width (i.e ≤ 0.5mm as investigated in [156], ≤ 0.1mm in the case high performance concrete as observed in [157] or up to approximately 0.2mm in the case of fiber reinforced cementitious composites (FRCC) as studied in [158]).

Reinhardt and Jooss found a huge reduction of water flow rate due to the self-healing of the crack in [157] after 300h of flow test at three dimensions width of crack by 0.05, 0.1 and 0.15mm in specimens tested. Nishiwaki et al. in [158] investigated and reported the evaluation of recovery of the water tightness regarding some types of fiber and highlighted the dependence self-healing on crack width.

Jacobsen et al in their research [154] reported both a decrease of chloride mitigation rate by 28-35% in the self-healed concretes and an increase of penetration time compared to newly cracked concrete.

4.2. Effect of crack on the corrosion process

4.2.1. Corrosion process in cracked concrete

Crack was shown to accelerate chloride penetration [159-164] as well as carbonation [80, 164]. It is clear that corrosion begins at the location of crack tips especially on those sites where crack is closer to rebar [19, 165].

Crack concrete was investigated to reduce time of corrosion initiation in comparison to un-cracked concrete. Possible effects of crack on the service life of reinforced concrete can be described in followed Figure 18 and Figure 19 based on a classical model by Tuutti [84].

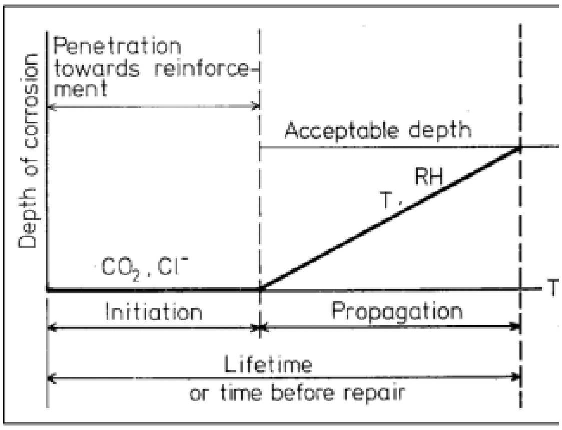

Figure 18 : Schematic sketch of steel corrosion sequence in concrete

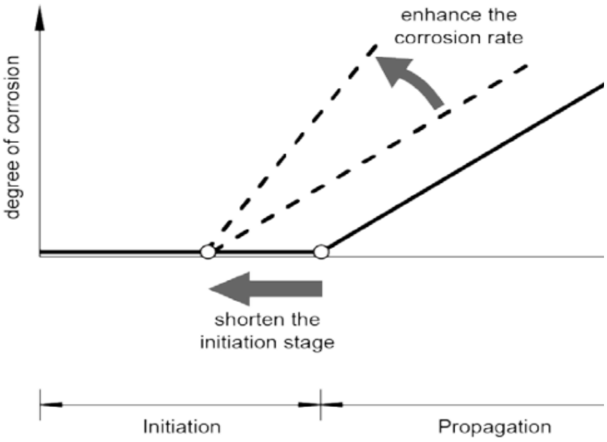

Figure 19 : Possible effect of crack on service life of RC (the dashed line corresponds to cracked concrete and the solid line corresponds to un-cracked concrete) [166]

According to the model, corrosion process consists of two phases (initiation phase and propagation phase). The initiation phase is a period time for penetration of aggressive factors e.g CO_2 or Cl^- to the concrete cover but reinforcing steel is still passive. The second phase begins once de-passivation occurs until an acceptable maximum damage. However, this is not suitable for cracked concrete. Here was proposed a four phase model by Francois et al [167] in which corrosion process is divided into four phases including incubation, initiation, induction and propagation phase (Figure 20). It should be noticed that the four-phase model proposed by François et al. corresponds to all scenario of corrosion (carbonation or chlorides), on the contrary Tuutti propose such a four-phase model only for carbonation-induced corrosion.

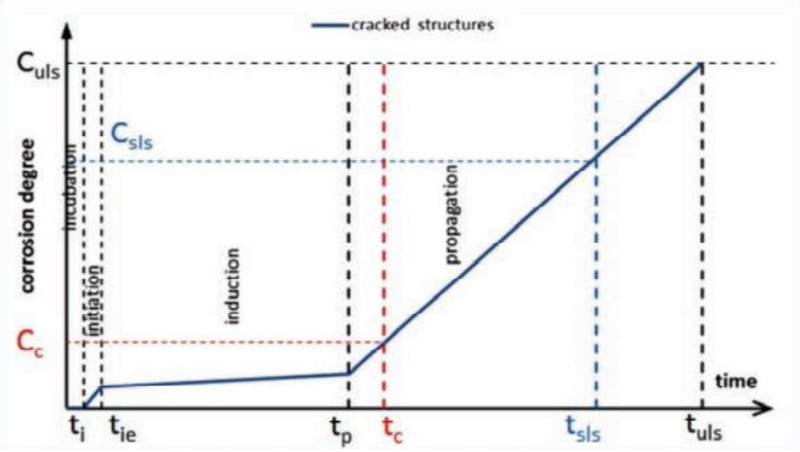

Figure 20 : Description of four phase corrosion process [167]

- Incubation phase:

During this phase (t_i) the aggressive agents can easily access in concrete through crack path resulting damage to passive film on the steel bar around the crack whatever its width. t_i is short (could be a few days) and negligible with respect to the cycle life of RC structures.

- Initiation phase:

This phase starts from t_i to t_{ie} at which corrosion products are formed then could heal the crack path and slow down the increase of corrosion. Others healing processes could be involved, such as self-healing of formation of deposits such as calcium carbonate. Duration of this phase is also short and may be overlooked in term of service life.

- Induction phase:

This phase is following the initiation phase. During the induction phase the corrosion development is slow down low due to corrosion rust filling the crack or others healing processes. The duration is linked to the time for aggressive species to penetrate through the concrete cover to reach the reinforcement and then depends on the exposure conditions. In this phase, the corrosion products do not generate corrosion induced cracking, because the pre-cracking acts as an expansion tank.

- Propagation phase:

The propagation phase starts at t_p when the carbonation front encounters reinforcement or critical chloride threshold is reached in un-cracked zone. After a given time, first corrosion-induced cracks are formed at t_c and corresponds a local corrosion rate C_c. The corrosion process develops to reach service limit criteria of structure, corresponds to time t_{SLS} and corrosion C_{SLS}. The end of service life is associated with a time t_{ULS} and corrosion C_{ULS} is reached.

In fact, the two-phase model is still often referenced. However, it is clear that the four-phase model can introduce more complete information to corrosion process in the case of cracked concrete. From perspective of four-phase model, the initiation of the two-phase model corresponds to the first three phases of the former.

4.2.2. Corrosion initiation in cracked concrete

When studying corrosion initiation in cracked concrete, one important difficulty is the duration of the experiments. Indeed, based on the 4-phases model of François et al. [167], the real initiation period should correspond to 3-phases: incubation-initiation-induction. If the duration of the experiment is too short, then the conclusions concerning the initiation of corrosion could be related to only incubation, or to incubation following by initiation, but probably never to incubation-initiation-induction which could be only studied in long term experiments.

Nevertheless, because there is a lack of use of the four-phase model in the literature, the initiation process will be described in the following based on the two-phase model, which means that initiation is the phase which begins after incubation (referred as propagation in Tuutti model).

The corrosion initiation process is known to depend on the penetration of chloride or carbon dioxide along the crack path. This relationship is under numerous of studies and most of them hold the point of view that cracking of concrete leads to a potentially faster penetration of these harmful substances therefore accelerating the corrosion initiation. This is obviously reasonable because cracks provide pathways for the ingress resulting a speeding up to damage of passive film on steel bar by chloride penetration or carbonation.

De Schutter in [168] indicated that the main factors are the crack width and the crack depth and the influence is significantly higher for chloride than carbon dioxide penetration. In his research was exhibited a tentative formula to quantify these effects. Wider surface crack widths could result to much faster initiation (incubation in case of four-phase model) than relative smaller ones was mentioned in [163]. However, the author suggested that it is more appropriate to consider crack width and concrete cover ratio as a suitable parameter. The similar influence of crack and corrosion initiation was introduced in [169, 170] yet the difference is no existence of correlation between crack width and corrosion. The perspective to support the correlation between crack and corrosion initiation can also be found in lots of other research [169, 171-175]. According to Jaffer et al. in [172],it was observed that corrosion occurred only at intersections of reinforcement with cracks in the concrete and there was no corrosion in any location of the steel that was not adjacent to a crack. Both chloride and carbonation induced corrosion commence and develop for a few millimeters surrounding the reinforcements (corresponding to damage zone induce at the creation of load-induced crack [176]) and at its intersection with the pre-existing crack.

4.2.3. Corrosion propagation in cracked concrete

The impact of cracks to corrosion initiation has received a general consensus from the scientific community while the influence of this factor to corrosion propagation is still in debate. As mentioned previously, the effect of cracks on corrosion needs to be studied according to a 4-phases model and not according to the usual 2-phases model suitable for un-cracked concrete. The influence of crack on reinforcement corrosion could be a function of several crack characters which will be discussed in the following.

- Effect of crack width

The influence of this parameter and corrosion propagation has been received numerous attentions of researchers and it exhibits different points of view also.

On the one hand, crack width is considered to accelerate the propagation corrosion process. This perspective can be found in such studies as [160, 177-179]. Sahmaran and Yaman [177] concluded that as the crack width increased, corrosion rate increased. In the research, the authors observed the impactions on both initiation and propagation with a growth of chloride diffusion and higher mass loss of reinforcements in the case higher crack width. The remarkable effective impact is reported when crack width value is more than 0.135mm. Otieno et al. [160, 178] supported the influence of crack width to corrosion propagation. It must be noticed that such results are based on so-call “accelerated corrosion” by anodic impressed current, which do not correspond to the real process of localized corrosion of steel in concrete where both anodic and cathodic sites are present on a same rebar. Concrete samples with different binder, different water binder ratio, different crack width (0.4mm, 0.7mm and incipient cracks) and two concrete cover (20 and 40mm) were applied in the experiments. A proportional corrosion rate to the increase of crack width for a given binder type and water cement ratio was presented. Le et al. show an increasing of corrosion rate with variety cracks applied in the study [179] in the order of un-cracked < 0.2 mm < 0.3 mm < 0.4 mm < 0.5 mm.

On the other hand, many research reported little effect [180] or no effect on corrosion rate in propagation phase [81, 171, 175, 181-184]. Mohammed et al. in their study [184] performed the experiment in 13 weeks. After 4 week of exposure NaCl 3.5% solution no relationship between crack width and corrosion rate was observed in cracked samples. The presence of crack should be considered rather than the role of crack width. Series long-term studies by François et al. [181-183] indicated that crack widths generate no influence on the development of reinforcement corrosion. The 3m concrete beams were exposed to salt fog and under sustained loading. In the case of 12 years old beam [181, 182] it was found that long term corrosion is independent of the widths of cracks (for widths less than 0.5 mm) or by the cracks themselves. In the case of 1 year old beam [183] the similar result that there was no correlation between corrosion propagation and crack width was also mentioned.

It can be seen that all the studies above are related to chloride induce corrosion. Few of the scarce studies mentioned the influence of crack on corrosion propagation phase are by Dang et al. in [81, 83] or Ghantous et al. in [2] . However, no correlation of crack width and corrosion propagation was found. In study by Ghantous it was observed an induction period less than 180 days whatever the crack widths (Figure 21).

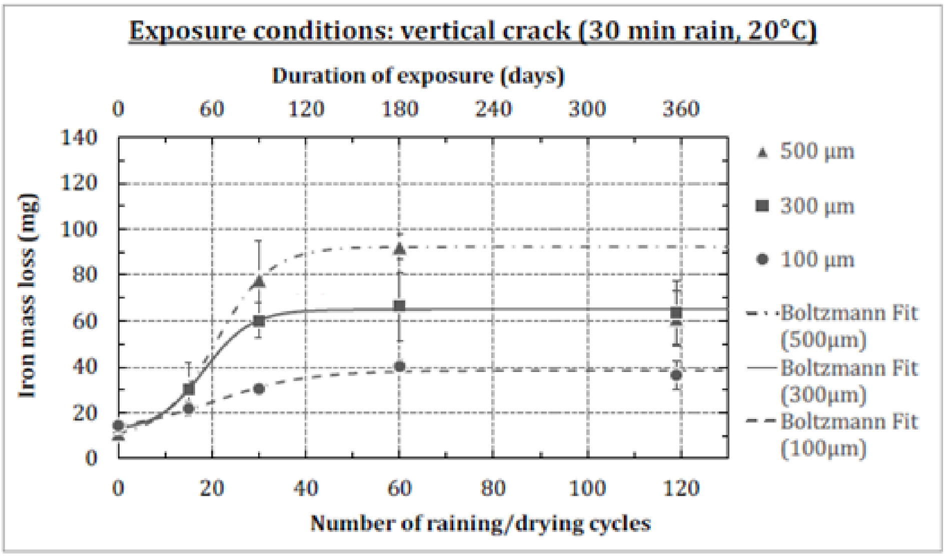

Figure 21. Loss of mass in specimens having different crack opening [2]

- Effect of crack frequency

The correlation of crack frequency or crack density and corrosion rate received some different points of view.

According to Arya et al in [118] the smaller the crack density the smaller the weight loss of reinforcement. The authors proposed a hypothesis that it might be more effective to impede corrosion by limiting the crack density rather than by controlling surface crack width. The study utilized beams containing 0, 1, 4, 8, 12, 16, and 20 parallel sided cracks with the same sum total width of 2.4mm. All the samples had the same trend result except beams with 20 cracks which can be explained by crack self-healing.

In another study [185], Blagojevic investigated concrete beams with different concrete cover by 20, 30 and 40mm and crack quantity of active crack by 9, 8 and 6 respectively. Each beam had total crack width of 0.15mm. The author indicated that corrosion rate reduced as crack density decreased and concrete cover increased.

On the contrary, in Schieβl and Raupach in [186] it was observed a decrease of corrosion rate when crack frequency increased. In the case that frequency reduce a half, the corrosion rate doubled. It was suggested that increase crack frequency resulted cathode area decrease, then the corrosion rate reduced.

- Effect of crack orientation

In term of the orientation with respect to reinforcement, crack in concrete is classified as longitudinal (or coincident) for cracks which are parallel to main steel bar and transverse (or intersecting) for cracks which are perpendicular to the reinforcement. The transverse crack type is common in concrete, however, for corrosion longitudinal crack type is considered to have more significant impact on corrosion rate because it provides reinforcement more favorable exposure to aggressive factors [187]. In a study [188], Poursaee and Hansson carried out the measurement in concrete prism in presence of longitudinal and transverse cracks and they found a higher corrosion current density with the first type of crack than the second type of the same crack width by 0.1mm.

- Effect of crack self-healing

The observation of this phenomenon and its positive influence on corrosion rate can be found in numerous researches [166]. Crack self-healing is considered to lead the corrosion reduce even reach a negligible level. Besides crack width, type of loading (e.g. static vs. dynamic), binder type or exposure conditions may affect self-healing.

Mohammed et al. [156] carried out a study with 15 years old concrete beams made with different binder type and exposed to marine environment. Self-healing was supposed to occur irrespective of the cement types in crack width ≤ 0.5mm at which also exhibited tendency of lower current density (0.1-0.5 $\mu A/cm^2$). More corrosion was measured at location of healed crack size of 0.5mm than crack size ≤0.4mm which was expected that self-healing had assisted to reduce or stop corrosion process.

Evidence of influence of self-healing on corrosion rate was presented in a study by Otieno et al. [160]. There was a period of time in the experiment with incipient and 0.4mm cracked samples that corrosion rate reduced was observed in the research. This was expected to relate to crack self- healing which is considered to occur in widths less than 0.4mm.

5. Effect of top bar effect on the corrosion of steel in concrete

The steel-concrete interface (SCI) is known to significantly influence corrosion of reinforced concrete exposed to chloride and carbon dioxide. Due to improper stability of fresh concrete, some defects can be formed when casting and compacting of concrete. In reinforcement structure with multi steel layers, upper bars (according to casting direction) exhibit more defects than the others. In this case SCI defects are linked to a phenomenon which is well-known: “top-bar effect”. The main SCI defects include the presence of air bubbles or entrained air, voids beneath the steel bar due to the phenomenon of settlement and bleeding of fresh concrete and mechanical de-bonding of the SCI which can be seen in Figure 22.

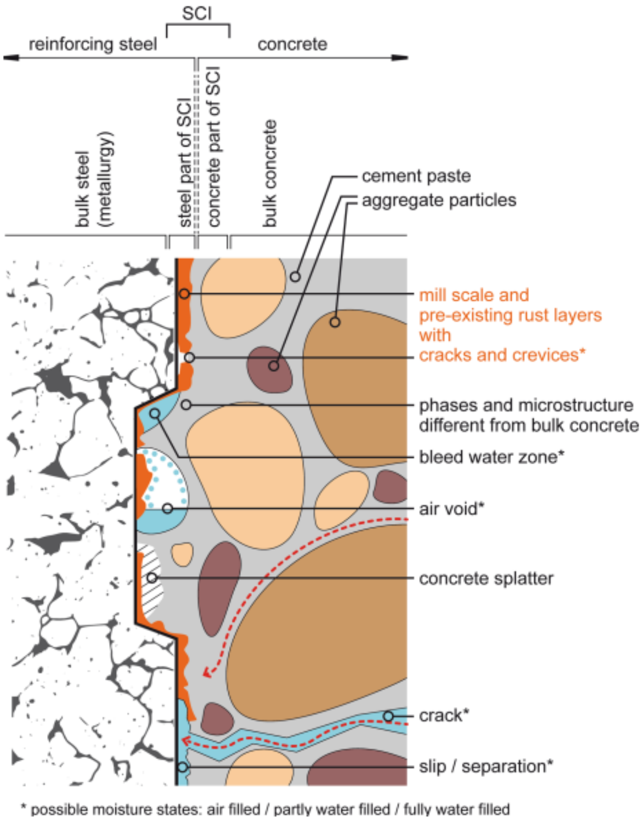

Figure 22 : Schematic illustration of selected characteristics at the steel-concrete interface [189]

5.1. Main characteristics of steel concrete interface related to top-bar effect

Steel concrete interface consist of steel part and concrete part. The former includes mill scale, pre-existing rust layer and passive film on the steel surface while the latter includes cement hydration products, air void, crack, water bleed zone and separation… Due to the top-bar effect some SCI defects are generated at the bottom interface of steel concrete. Top-casting defects can be divided into air voids and bleed water voids/zone (Figure 23 and Figure 24).

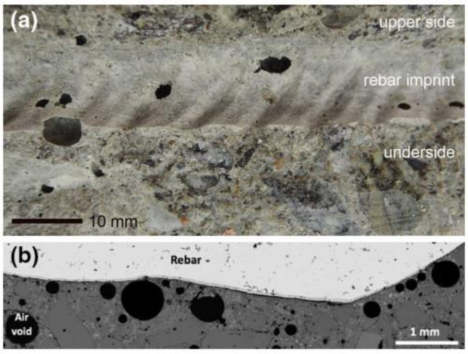

Figure 23 : Air voids at the SCI [189]

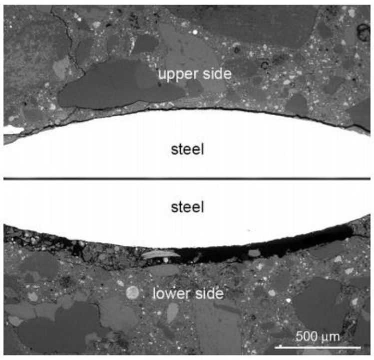

Figure 24 : Bleed water zone at the SCI [189]

- Air voids at the SCI: (Figure 23)

Air voids are generated during concrete compaction and air bubbles can adhered to the surface of bars or can be trapped beneath the horizontal surface of rebar. Air voids initially are not filled by water. These bubbles can have different sizes and shapes which result into two classifications: entrained voids or entrapped voids.

Entrained voids are small bubbles (typical diameter of 50µm) and have normally a near spherical shape. Only a minor part of these spherical voids is in contact with the steel surface and only a very small portion of these air voids can be observed at SCI after steel bar is extracted. Entrapped voids have diameter more than 1mm and irregular shape depended on the contour of surrounding environment.

- Bleed water zone and voids at the SCI: (Figure 24)

Segregation, settlement, and bleeding of fresh concrete can form this type of voids. In the study by Mohammed et al [190] the presence of these voids was only found in the bottom part of horizontal bar. These defects were observed increasing with the depth of concrete under the steel. When the height is more than 15cm they can appear at the bottom side of the steel bar [191]. However this phenomenon exists for all the bars even those positioned above a shallow height of concrete, but the defect is microscopic in this case [19] : i.e. invisible [3]. Nevertheless, according to the concrete composition, quite significant gap such as 100–200 µm wide as reported in [189].

Settlement may cause empty voids at the underside of reinforcement steel in concrete, but a thin layer of paste may adhere onto the rebar surface. Bleed water zone may be mistaken with air voids. Nevertheless, bleed water voids have a more elongated nature or crescent shape and are thereby able to achieve a greater loss of contact area with the rebar surface compared with air voids. Additionally, bleed water voids initially are water filled and can be subjected to wetting-drying.

In terms of defects due to bleeding and settlement of fresh concrete, Söylev and François [191] divide them into macro defects and micro defects. Both have the similar origin but macro defects can be easily identified using video-microscopy but micro defects exhibit no identified visual inspection.

5.2. Influence of steel concrete interface on initiation corrosion

Numerous researches about relation of SCI and corrosion process hold the view that it is a key parameter to corrosion initiation. Characteristics of SCI are considered to have strong influence on initiation of chloride-induced corrosion, even more than several well-known parameters such as w/b ratio and cement type [192] and those have been suggested to be focused in research community [91]. Defects at steel concrete interface facilitate the ingress of aggressive factors along the re-bars resulted accelerate corrosion process.

The influence of top-bar defects on corrosion initiation will be discussed with the role of air voids and the role of bleeding zone.

- Air voids:

The presence of air voids was found to strongly affect the critical chloride threshold [193, 194]. A decrease in air voids content at SCI corresponds to an increase of critical chloride threshold then a decrease of the risk the corrosion initiation of reinforcement (Figure 25, Figure 26).

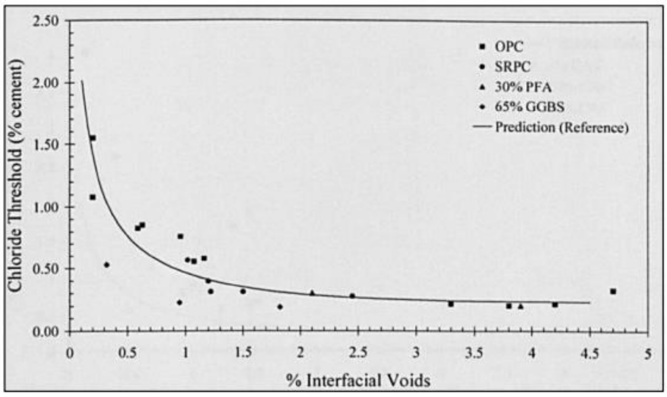

Figure 25: Effect of cement binders on chloride threshold level [194]

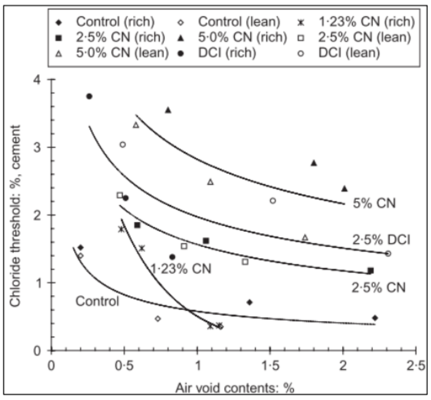

Figure 26: Chloride threshold level as a function of air void content [193]

According to [194-197] corrosion initiation is considered to occur mainly at the location of air voids while no correlation was found as in [198, 199]. The role of air voids probably is influenced by other conditions such as the moisture of the concrete.

- Bleeding zone:

The size of settlement and bleeding zones increase with the height of concrete under the reinforcements: these defects are always located at the bottom side of steel bar rather than at the top side. An example of top casting defects can be seen in [200] where Söylev and François discussed the SCI defect with the height of concrete section (Figure 27). The influence of defects on corrosion process was indicated in [191] by the same authors. It was observed that macro defects have a direct effect on corrosion while micro defects have no significant effect on corrosion.

The gap/voids was observed on the surface of the lower side of steel bar in [201]. In seawater environment, the author found that those defects are the locations of immediately corrosion after casting concrete with seawater.

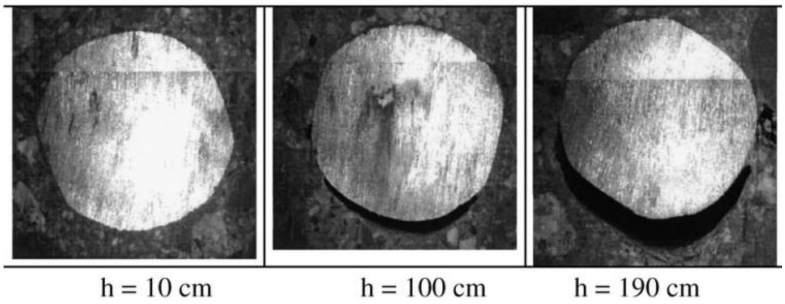

Figure 27: Three sections at 10, 100 and 190 cm of height, respectively, at video-microscope with an enlargement of X25 magnification [200]

Castel et al. in [202] highlighted the role of steel concrete quality to predict the corrosion initiation. As the reported result, even when all the chloride content at steel bar exceeded the maximum usual threshold for corrosion initiation, the corrosion mainly took place on steel bar with top-bar effect defects. Chloride threshold is necessary to corrosion initiation but not sufficient parameter to forecast corrosion onset.

Vidal et al. in [203] carried out the experiments with 17 years old reinforced concrete beam and found the same conclusions: the presence of voids (de-bonding) at the interface can be a determinant factor to assist corrosion initiation as well as reduce the initiation period corrosion process.

Steel concrete defects seems remarkably reduce the chloride threshold in concrete. In a study [204], Zhang et al. compared chloride content for corrosion onset with steel in the presence of top casting defects and without defects in a 110cm wall in height composing 10 horizontal steel placed along the height. Interfacial defects due to bleeding and settlement was found increase against the height of wall (Figure 28).

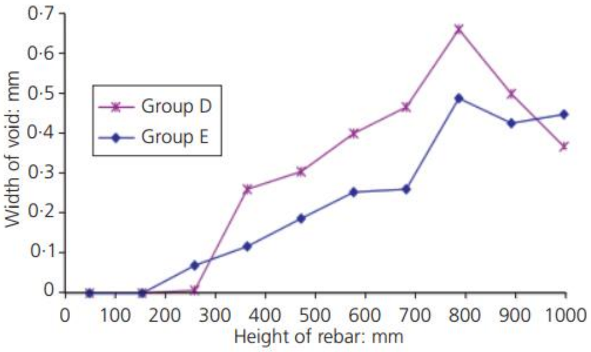

Figure 28: Width of the interfacial defects plotted against height of rebar in the high concrete members [204]

The chloride content was measured from 0.5-0.8% of cement mass for rebar with defects while the value was 0.8-0.9% for specimens without defects. Similarity, Zhang et al. in [205] found that corrosion mainly initiated at the bottom side of the rebar despite a higher chloride profile at the top side. This may be explained by the lack of the buffering capacity formed by cement hydration or no protection by concrete cover due to top casting defects.

Related to carbonation-induced corrosion, the influence of top-bar effect was observed by Ghantous in [2] .The author used specimens cut from a slab concrete with 15cm in height, 55 cm in length and two reinforcements layers which can highlighted the effect of casting direction (Figure 29).

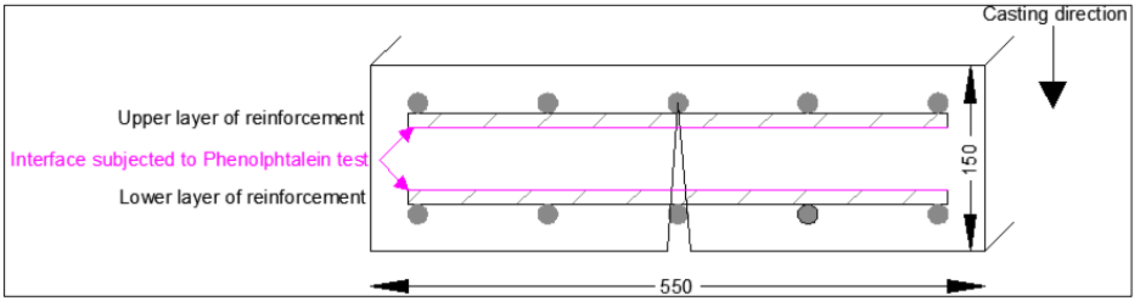

Figure 29: Schematic representation of the steel/concrete interfaces localization subjected to the phenolphthalein test (concrete slab) [2]

Carbon dioxide was found spreading along the entire length of the lower side of the upper steel bar while remaining limited on the upper side of the lower steel bar. Defects due to top-bar effect occurring on the bottom part of the upper bar are considered to facilitate the carbon dioxide penetration even with the presence of a thinner crack than on the bottom steel bar. In [53], Timhadjelt showed a similar observation with a great longer carbonation length appearing on the top steel than on the bottom steel (Figure 30). Additionally, a higher corrosion was measured on the top steel bar rather than bottom steel bar despite the unfavorable ratio C/A.

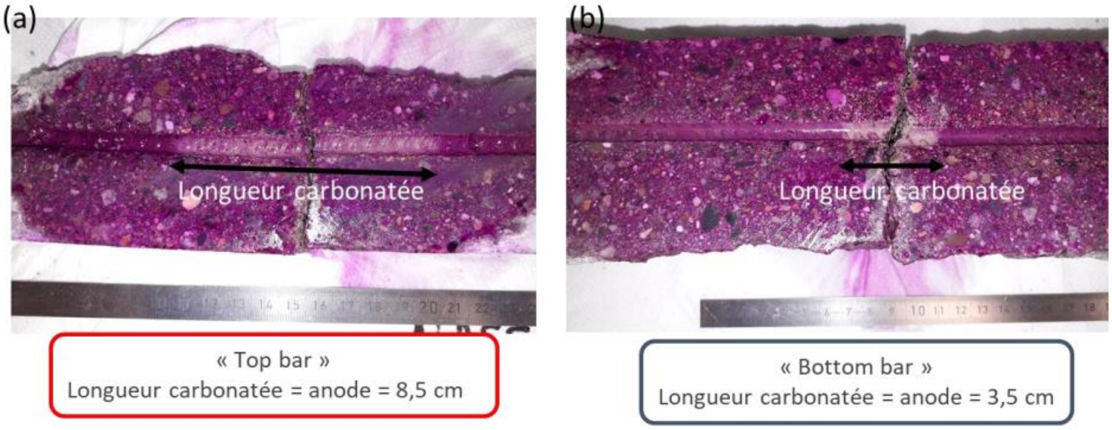

Figure 30: Schematic representation of the steel/concrete interfaces localization subjected to the phenolphthalein test [53]

5.3. Influence of steel concrete interface on propagation corrosion

If the perspective that gaps in SCI due to top-bar effect facilitates corrosion initiation receive consensus as well as attention from a lot of researchers the concern on corrosion propagation are still limited.

Majority of the researches mentioned this issue with respect of chloride-induced corrosion. In [182], François and Arliguie observed the development of corrosion occurring at steel concrete interface of poor quality due to bleeding. Four reinforced concrete 3-meter-long beams divided into group A and B suffered salt environment for 12 years were investigated in term of measurement the growth of corrosion-induced cracks due to the increase in the volume of rust product. Prior to loading, pre-cracks were only recorded on the upper surface of beam in group B, which group had lower concrete cover, due to bleeding of concrete. As observed over time, it was seen that corrosion-induced cracks mainly appeared and increased at the zone of top-casting reinforcement. These pictures below (Figure 31, Figure 32, Figure 33 and Figure 34) described and compare the development of crack of one beam in each group. It is clear that top-bar effect can accelerate the propagation corrosion.

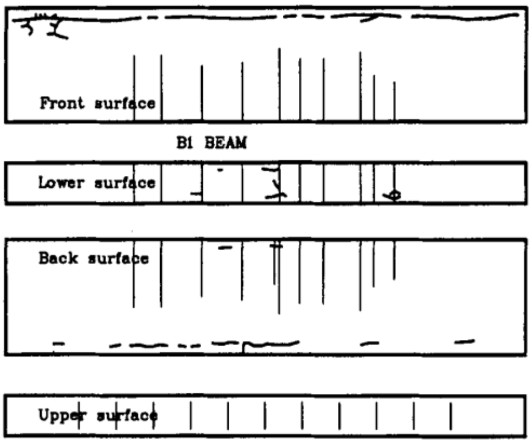

Figure 31 : Cracking map after 7 years (B1) [182]

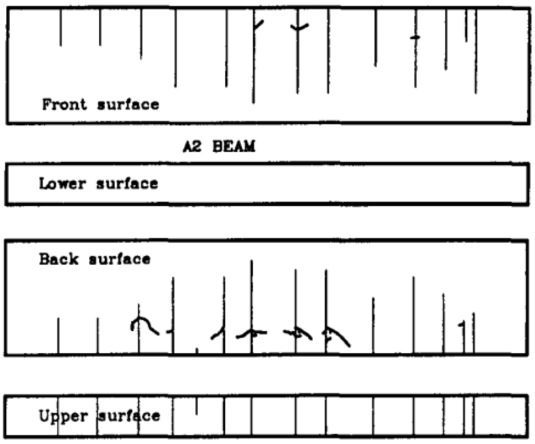

Figure 32: Cracking map after 7 years (A2) [182]

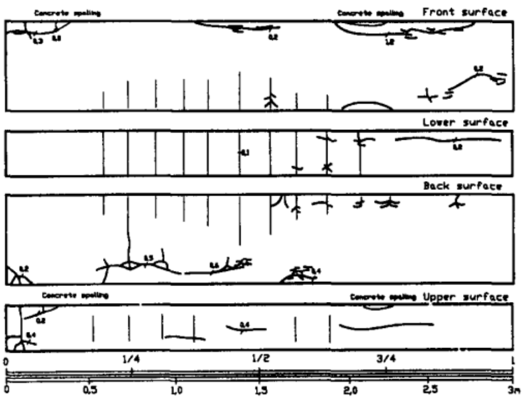

Figure 33: Cracking map after 11 years (B1) [182]

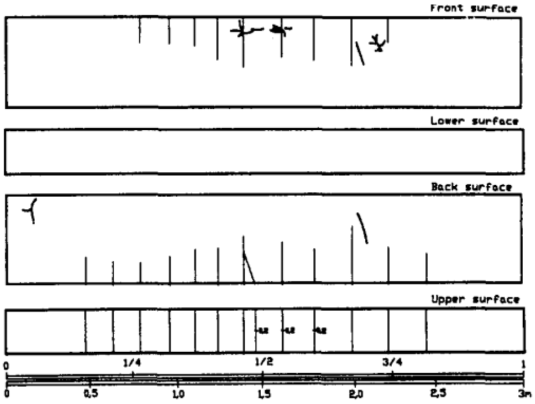

Figure 34: Cracking map after 11 years (A2) [182]

In [202, 203] the SCI quality and corrosion in 14 years old and 17 years old beams with the similar exposure to salt environment were investigated. Corrosion was always found rather on the bottom side of steel bar with regard to casting direction and the horizontal upper bar of stirrups. The bleeding of concrete played an important role to generate interface de-bonding resulting to an early corrosion propagation of the reinforcements.

In [169, 206], relation of steel concrete interface damage caused by top casting effect and corrosion process in reinforcement concrete under sustained loading was studied. Casting induced damage causes a lower interface quality which results in different corrosion state to reinforcement despite the same cover thickness. Steel bars which exhibits SCI defects due to top-bar effect can be in active corrosion state while the others which are not affected by defects, can be in passive state as observing by Yu et al. in [169]. The statement that top-bar effect has significant influence on corrosion development is again confirmed in [206].

In [205], Zhang et al. reported a comparison about propagation corrosion in reinforced concrete beam in presence of top-bar effect defects and without top-bar effect defects. The important role of SCI defects to corrosion process is then highlighted. The results, in the case with no presence of SCI defects, showed a weak level of corrosion and show that corrosion start on steel bar at the closer exposure side to chloride. While in the case of SCI defects, corrosion was likely to commence from the bottom side of upper steel bar and spread around perimeter of the bars when crack induced by corrosion appeared. The influence of top casting defects on corrosion process was no longer once the corrosion degree reached a threshold value.

Related to carbonation-induced corrosion, few researches mentioned the influence of top-bar effect defects and propagation corrosion. One of those is a study by Nasser et al. [1] to investigate steel concrete interface defects on macro cell current in carbonated concrete. A wall with dimension 100x250x1100mm was casted. Due to top casting effect, some defects were observed in some top steel bar while steel bars located at the bottom part showed perfect steel concrete bond. After that 6 small cube concrete with embedded steel bar were extracted and then exposed to carbonation process.

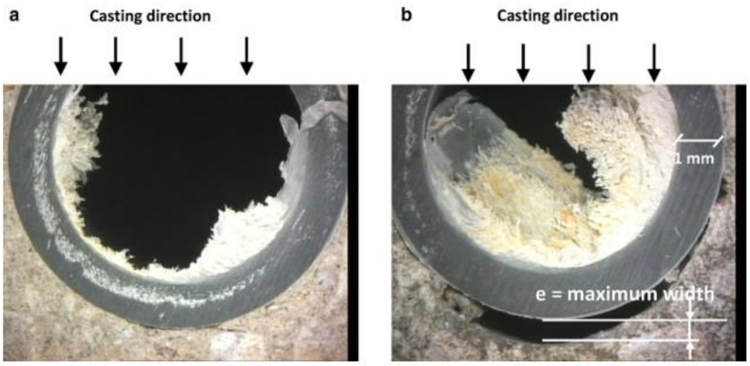

Figure 35: Observation of steel concrete interface (a- steel bar at the bottom, b-steel bar at the top) [1]

The macro cell corrosion current measured expressed a significant higher value in steel bar with defects in compared to steel bar without defects, up to 3 times. Then, the macro cell current decreased versus time probably due to more iron oxides formed at the interface. However, the value in steel with defects remains higher than the other.

Other study concerning the study of SCI in carbonation-induced corrosion is [83] where the authors used ring-shaped mortar samples in the experiments. It was found a thicker layer of corrosion products at the lower surface of steel bars than in the upper location and also the corrosion rate in the lower half-surface of the reinforcement steel is greater than that in the upper half of the reinforcement steel surface. This can be explained by presence of voids related to casting direction. The similar observation can be found in the study by Ghantous [2]. Corrosion is more developed along the lower surface of the upper reinforcement than the lower part of the lower steel bar. The lower part of the upper steel bar shows the highest corrosion thickness. Here is also confirmed the role of steel concrete interface more significant than the surface crack width.

6. Conclusion

Conclusions of literature review:

A shown in the literature review, there is some lack of knowledge concerning the following points:

- Carbonation-induced corrosion is hardly considered in two complementary aspects: uniform and non-uniform (or localized or macro cell). Indeed, almost all the researches done and published on carbonation-induced corrosion considered that it corresponds to uniform corrosion. On small laboratory samples, this is mostly the case, but on real reinforced concrete structures where reinforcing bars framework include both transverse and longitudinal bars and possible multi-layers, macro cell process is suitable to superpose to uniform process. A chapter of the thesis will be dedicated to this study.

- The use of blended cement which reduced the amount of clinker and then the amount of Portlandite in the hardened concrete is mostly considered to be detrimental for carbonation-induced corrosion. Indeed, the pH buffering effect of Portlandite is reduced with the use of blended cement. Nevertheless, this aspect of the problem is not sufficient to characterize the durability of concrete versus carbonation -induced corrosion. As a result, some blended cement as the CEM III using slag as additives, lead to higher resistivity which is highly beneficial to reduce the non-uniform part of corrosion current. This point is studied in the thesis.

- Carbonation-induced corrosion in presence of pre-cracks (such as load-induced cracks) appears to follow the 4-phases corrosion diagram initially described by Tuutti in 1982 [84] and also proposed by François and Arliguie [167] i.e. after a short period of corrosion initiation at crack location, corrosion is dormant (induction phase) due to the “healing” of cracks due to corrosion products. Ghantous et al. [175] have confirmed this 4-phases process. Nevertheless, there is still an open question which is the influence of large voids along the reinforcement as it could be induced by top-bar effect: i.e. the increase of bleeding and settlement in relation with the height of casting concrete below the re-bars. A chapter of the thesis will be dedicated to this study.

- Effects of pre-cracks on chloride-induced corrosion are more controversial than the case of carbonation-induced corrosion. There is a major ambiguity on the effect of the duration of experiments on the conclusions of the results. Indeed, in the 4-phases corrosion diagram proposed by François and Arliguie. [167], the change between the initiation phase and dormant phase could be not reach if the duration of experiments is too short. Moreover; the influence of top-bar effect is also an important issue for chloride-induced corrosion. Pre-cracking when it is due to loading is accompanied by damage at Steel Concrete Interface. To separate the effect of this mechanical damage from the defects at SCI due to top-bar effect, a study of the effect of artificial cracks is done in one chapter of this thesis.

CHAPTER II. EXPERIMENTAL PROGRAM

1. Introduction

In this chapter the material and experimental method of specimens concerning the thesis are presented. Some details of the experimental programs related to studying on carbonated and chloride induced corrosion are described in the following sections.

Firstly, the stage of the process is to prepare the specimens for the suitable experiment (1). To dedicate to the tests related to crack certain concrete samples were controlled cracking (2). The specimens were subjected to aggressive conditions (3). For studying corrosion, the cracked samples were exposed to wetting/drying cycles (4). The general process of specimens is presented in Figure 36.

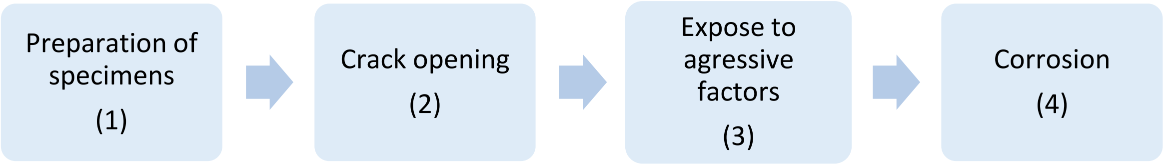

Figure 36. Process of specimens

(1) Include the specimens for carbonation induced corrosion or chloride induced corrosion.
(2) This step is subjected to specimens dedicating to the test concerning to carbonation induced corrosion or chloride induced corrosion in presence of pre-cracking.
(3) Include the accelerated carbonation or exposing to chloride environment.
(4) Include the wetting exposure following to the drying.

2. Experiments corresponding to carbonated induced corrosion

In order to study carbonation induced corrosion, several concrete samples were utilized in the measurement. These are extracted from a series sample in an experimental campaign by Chahoulb [27].

2.1. Description of the cathode samples

Cylindrical cathodes (Figure 37) and a reinforced concrete wall (Figure 38) were used in the measurements.

The cylindrical cathode samples had a diameter of 110mm, a height of 220 mm and a cover of 5.2 cm. One Fe 500 steel bar with 6 mm diameter ribbing was embedded at the center of the cathode. Three lengths of steel bar were utilized including 10 mm, 50 mm and 160 mm. The upper and lower part of each steel bar was welded with an electrical wire.

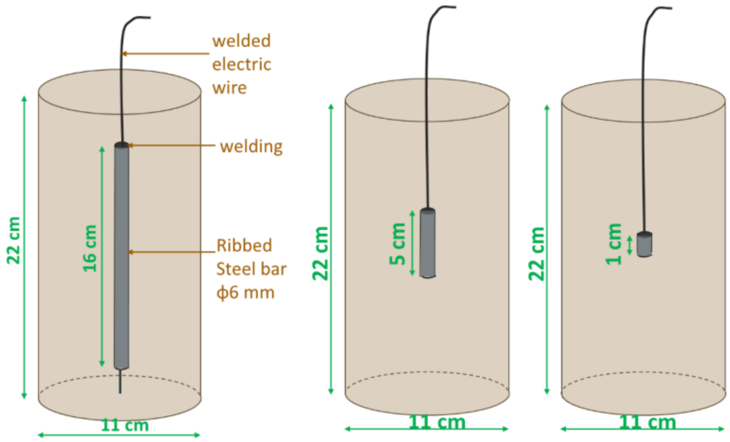

Figure 37. Dimension of cathode samples adopted from [27]

The reinforced concrete wall had dimensions 75x20x100 cm and contained 10 horizontal Ø 12 mm bars 70 cm in length and 8 vertical Ø 12 mm bars having lengths of 102 cm and 5 cm emerging from the concrete. The steel bar network was completely electrically disconnected but could be electrically connected externally thanks to a connection box. After demolding a PVC pipe containing a sodium hydroxide solution was connected to the wall with silicone. The pipe must be supported for 1 to 2 days to allow the silicone to dry and to make sure the connection is completely sealed.

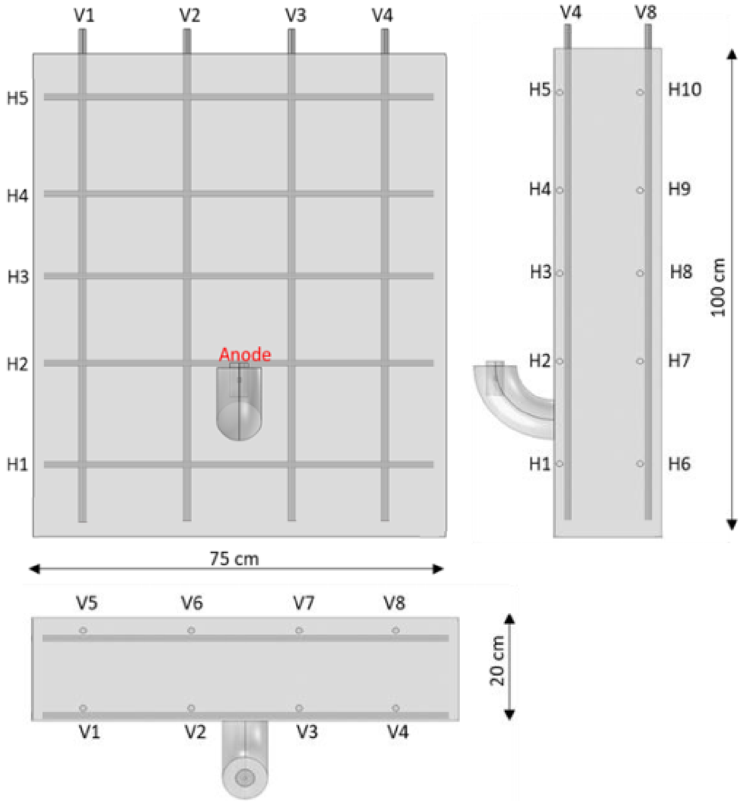

Figure 38. Dimension of concrete wall adopted from [27]

2.2. Description of the anode samples

The anode samples (Figure 39) were cylindrical with dimensions Ø= 33 mm and h= 70 mm, having one steel bar with a diameter of 6 mm and a height of 10 mm embedded at the center.

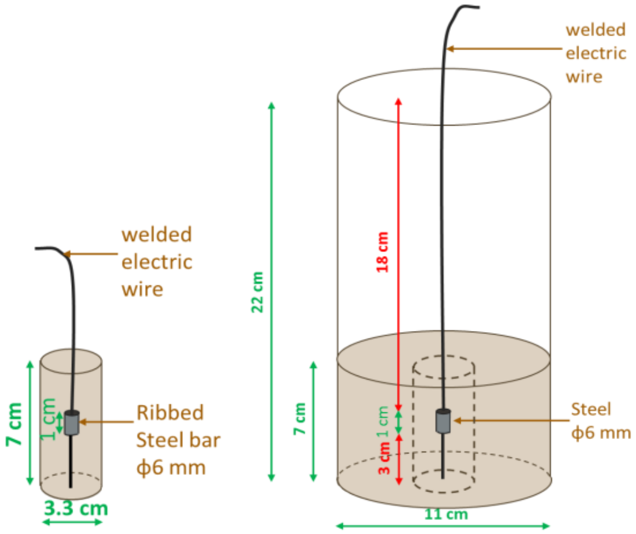

Figure 39. Dimension of anode samples adopted from [27]

Anode concrete samples were casted as cylindrical concrete specimens with a diameter of 110 mm instead of 33 mm and a height of 70 mm were made because of the size of aggregates. After curing, the final anode (ϕ 33 x h 70 mm) was extracted from the cylindrical specimen by coring. Electrical wires were welded to the upper and lower side of the steel bar. These anodes were carbonated before applying in the following test.

2.3. Material

For the cathodes and anodes, three concrete formulations, used in Perfdub Project (https://www.perfdub.fr/), (B1-15L-049, B3-041 and B3-15L-051) were used in this study. Their compositions are given in Table 3.

Constituents	B1-15L-049	B1-15L-049	B3-15L-051
Cement	280 kg/m^3 (CEM I 52,5 N CECP2 NF)	380 kg/m^3 (CEM III A 52,5 L CE PM-ES-CP1 NF)	280 kg/m^3 (CEM III A 52.5 L CE PM-ES-CP1 NF)
Sand	818 kg/m^3	830 kg/m^3	818 kg/m^3
Gravel	957 kg/m^3 (6-20 SC)	309 kg/m^3 (4-11.2 All SCL) 696 kg/m^3 (11.2-22.4 All SCL)	957 kg/m^3 (6-20 SC)
Water/cement	0.58	0.41	0.6
Water/ binder	0.49	0.41	0.51

Table 3. Formulation of the concrete

The reinforced concrete (RC) wall was made with CEM I cement and water/cement ratio of 0.55. Table 4 presents the formulation of concrete wall.

Constituents	Mass (kg/m3)
Cement (CEM I 52.5 N CE CP2 NF)	350
Sand (0/4R ALL SIL CE)	700
Gravel (4/10 SR ALL SIL CE)	1100
Water	195

Table 4. Formulation of the concrete wall

2.4. Accelerated carbonation of the anodes

After curing, the anodes were stored in an oven for 14 days at 45^{o}C followed by 7 days at 20^{o}C and a relative humidity of 65%. The samples then were subjected to carbon dioxide concentration of 50% in a climate chamber. Carbonation front was controlled with Phenolphthalein test in 3 control samples during the carbonation process.

3. Experiments corresponding to carbonation induced corrosion in presence of pre-crack

In order to study the influence of top-bar effect on carbonated induced corrosion process, five small concrete beams were utilized.

3.1. Descriptions

The laboratory tests are usually performed on centimetric scale specimens. However, it is important to carry out some experiments on representative samples of the real reinforced concrete structures. This is why the beams with dimensions of 150x150x550 mm with two layers of steel bars (Figure 40) were cast. Each of them was reinforced with two layers of steel bars of 6 mm in diameter including two steel bars embedded on the upper and two steel bars on the lower side, respectively. Two shorter steel bars were placed in the middle of the left and right sight of the specimens acting as the control bar in the following measurements. Electrical wires were welded to the reinforcement as well as the reference bars in the measurement of corrosion current. The concrete cover depth was 32 mm. The casting direction is from top bars to bottom bars. This casting direction aims to study the defects of steel concrete interface due to fresh concrete settlement and bleeding (top-bar effect).

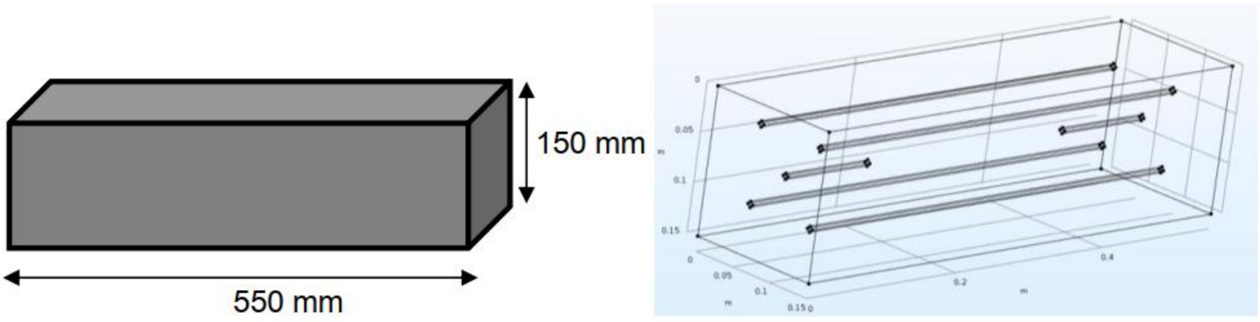

Figure 40. Description of the beams

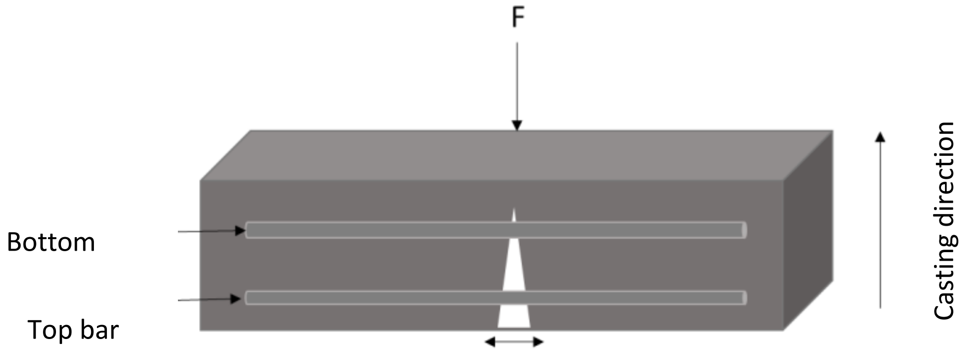

Figure 41. 3-points bending test

After curing the specimens were pre-cracked by three point bending test (Figure 41). In order to control the crack opening, a Linear Variable Differential Transformer (LVDT) was placed where the crack was expected to appear). At the beginning, the load is increased slowly until cracking starts. Then, by performing loading/unloading cycles and by increasing the maximum applied load from one cycle to another, the residual crack opening (that is to say after unloading) increases. Therefore, the crack opening could be controlled and a range of crack opening could be obtained.

The specimens were exposed to accelerated carbonation before being utilized in following test. During the period of measuring corrosion current, the beams were applied wetting/drying cycle each day.

3.2. Material

The following tables (Table 5, Table 6) present the chemical composition of cement and concrete composition, respectively.

SiO_2	Al_2O_3	Fe_2O_3	TiO_2	MnO	CaO	MgO	SO_3	K_2O	Na_2O	P_2O_5	S^{-2}	Cl^-
20.34	4.53	2.47	-	-	65.35	1.01	3.38	0.14	0.13	0.08	<0.01	<0.01

Table 5. Cement composition (%)

Constituents	Mass (kg/m^3)
Sand (NF EN 196-1)	1543
CEM 1 52.5R (Le Teil)	514
Water	257

Table 6. Concrete mix

3.3. Carbonation process

- Descriptions of the process:

The carbonation process of specimens was generated in a carbonation climatic chamber according to the plans of another carbonation chamber implemented by Drouet [58] which is describes as following:

- A climatic chamber Vötsch VC3 0060 of 600 liters (Figure 42): which can continuous control the temperature and relative humidity. The standard deviations in the temperature and in the relative humidity are respectively equal to 0.05˚C and 0.2%.
- A SIEMENS cabinet of analysis and control (Figure 43): which regulate the carbon dioxide rate inside the climatic chamber. This cabinet consists of a CO_2 analyzer (measure by absorption of infrared radiation) and a regulation system (pumps and servo-electro

valves). Gas is continuously sampled from the climatic chamber and analyzed by the analyzer. If the CO2 concentration inside the climatic chamber drops below the set value, the regulation system injects CO_2 inside the climatic chamber in order to maintain the required carbon dioxide pressure. The standard deviation detected in the CO_2 pressure value is equal to 0.05% for an operating range from 0 to 100%.

Figure 42. Climatic chamber

Figure 43. Siemens cabinet of CO2 analysis and control

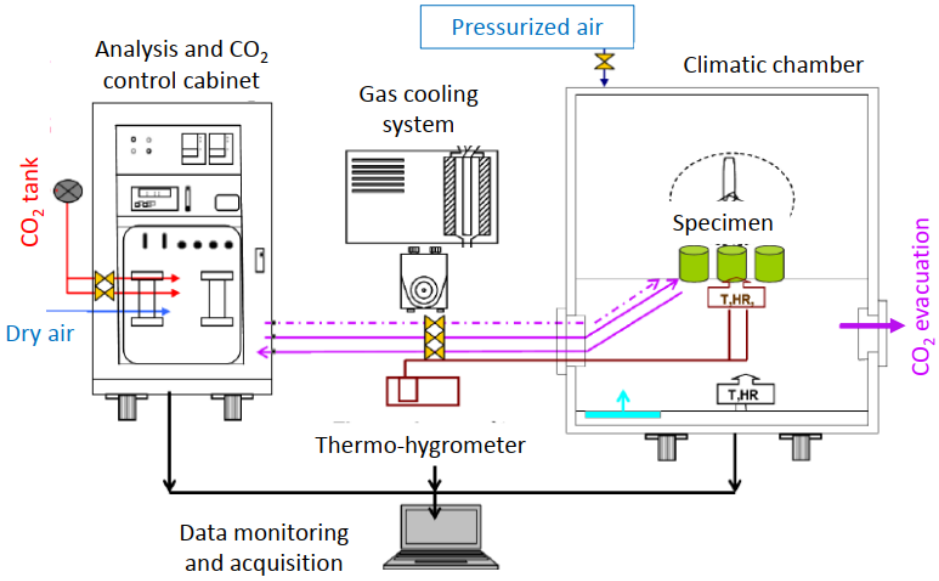

Figure 44. Schematic of the carbonation system[58]

The accelerated carbonation conditions were chosen as following:

- The carbon dioxide concentration was 3%. This is considered a suitable concentration which offers a compromise between the duration of the experiments and the representative to the natural carbonation [52, 207].

- The temperature and relative humidity were 25^{o}C and 55%, respectively. These are the conditions which obtain the maximum carbonation rate [42, 207].

3.4. Exposure environment

The wetting/drying cycles was performed each day by means of a device (Figure 45).

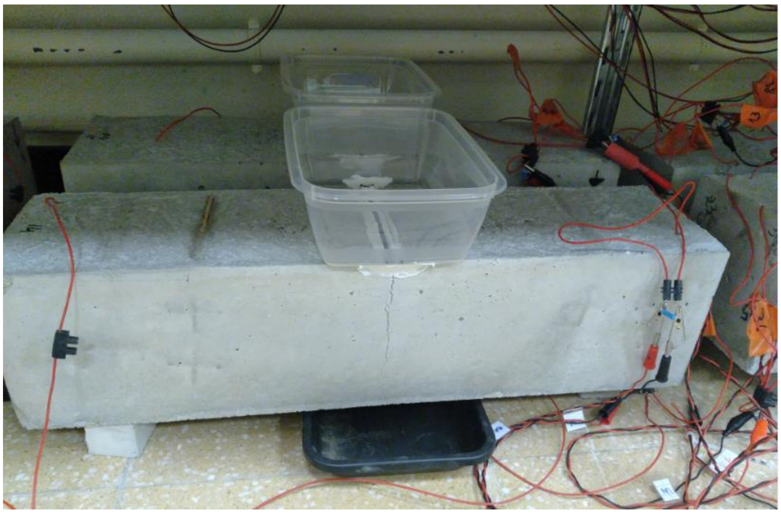

Figure 45. Device generates wetting/drying cycle and measure macro cell current

4. Experiments corresponding to chloride induced corrosion in presence of pre-crack

In order to research the influence of top-bar effect on chloride induced corrosion process, twelve reinforced concrete blocks which were named type G3 blocks were cast.

4.1. Descriptions

As presented in Figure 46, the G3 samples have the dimensions of 280x210x150 mm. Each specimen contains 5 embedded main steel bars of 12mm in diameter and a stirrup of 6 mm in diameter. Four of main bars were fixed at the corner of the stirrup and one was placed at the center playing a role of the steel coupon in the macro cell current measurement. Electrical wires were welded to the end of the main bars to measure the macro cell current between the steel coupon and the main bars in the concrete block. Each corner of the stirrups was covered by insulting material to exclude the affection of stirrup on the corrosion of main bars. The purple arrow signified the casting direction.

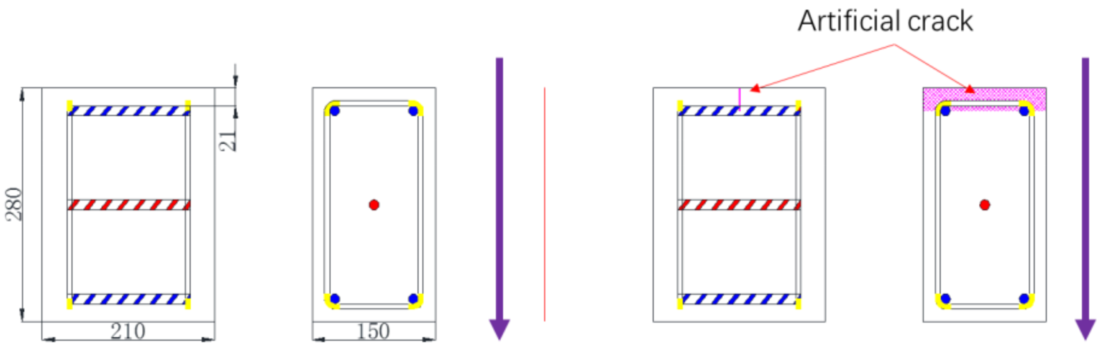

Figure 46. Description of G3 concrete block

The twelve concrete blocks were divided into two groups of 6 samples. In one group, an artificial crack with 1mm in width and 27 mm in depth was created in the location of midcourt line on the top surface of each specimen. In order to obtain the artificial crack, a shim was fixed at the middle location of the steel frame work before casting concrete and was removed after initial setting of concrete. However, no artificial crack was applied to the concrete block of the other group. In each group, there were 3 samples in which each main bar is connected to a wire while in the 3 other samples, all four steel bar were simultaneously connected to a wire.

4.2. Material

Table 7 and Table 8 provide the chemical composition of cement and concrete composition, respectively. The water/cement ratio was finely adjusted to obtain a slump of 70 mm.

SiO_2	Al_2O_3	Fe_2O_3	CaO	MgO	SO_3	Na_2O
21.4	6.0	2.3	63.0	1.4	3.0	0.5

Table 7. Cement composition (%)

Mix composition	Size	Mass (kg/m^3)
Portland cement OPC (high performance)		435
Water		217.5
Rolled gravel	5-15 mm	726.19
Sand	0-5 mm	895.28
Fiber (Dramix 65-35)		58.5

Table 8. Concrete proportion

4.3. Exposure environment

After curing the specimens were exposed to chloride environment. The exposure condition was always wetting and drying cycles and experienced in a wooden chamber. Each cycle was included two days of wetting followed by five days of drying. During the wetting period all the samples were exposed to salt fog environment (35g/L of NaCl, equivalent to the concentration of seawater) thank to four spray nozzles at each upper corner of the chamber. The door was opened during the drying period. The temperature was the same as the natural outdoor environment of southwest France, with monthly average temperature ranging from 5.1^{o}C to 21.3^{o}C .The monthly average relative humidity varied from 50% to 84%.

CHAPTER III. UNIFORM AND MACRO CELL CORROSION IN CARBONATION INDUCED CORROSION

1. Introduction

Recently, concern about carbonation-induced corrosion has increased due to the need to lower emissions released to the environment [208-210]. However, a change of clinker content to reduce CO2 emission could lead to concrete exhibiting lower resistance against the carbonation process. Among the binder substitutes available, slag is a supplementary cementitious material that is currently in favor [76, 211, 212]. One part in this chapter will compare the carbonation induced corrosion occurring when cement with high clinker content is used and when a high percentage of the clinker is replaced by ground granulated blast furnace slag.

Numerous researchers are of the opinion that carbonation-induced corrosion occurs in uniform or generalized corrosion [75, 212-218]. However, there are several alternative opinions. According to [76], in real structures, corrosion caused by carbonation may be localized. In [66], Castel and Nasser indicate that galvanized corrosion (or macro cell corrosion) in carbonated concrete structures seems higher than uniform corrosion. This phenomenon is also described by François et al. in [19].

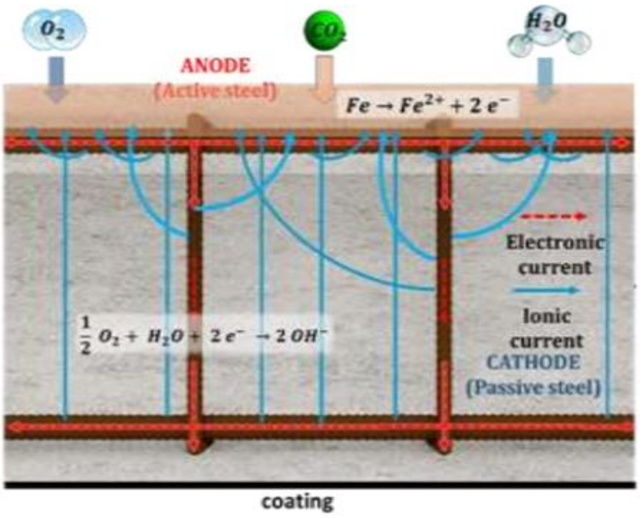

Figure 47. Schematic Illustration of macro cell corrosion due to carbonation: when the carbonation front reaches the first layer of the reinforcement layout, the other layers of steel bars, which are still passive and located in the un-carbonated zone act as a cathode.

As schematically shown in Figure 47, when the carbonation front reaches the first layer of the rebars, there is a strong macro cell coupling between the other layers of the reinforcement, including the stirrups, which are still in un-carbonated concrete that is quite saturated due to the distance to the concrete surface. The corrosion of the first layer then results from a coupling between a uniform corrosion and macro cell corrosion. Unlike the corrosion products formed during chloride-induced corrosion, those of carbonation-induced corrosion are not fluid, so the pressure on the concrete cover will be high. It could lead to the premature appearance of corrosion-induced cracks, which are inaesthetic, may reduce the bond between reinforcing steel and concrete, and may lead to delamination and thus to safety problems for the public.

In the chapter, the corrosion in carbonated concrete will be also studied from the points of view of both galvanized corrosion and uniform corrosion. It is important to better understand the relative proportions of macro cell corrosion and uniform corrosion in the early process of corrosion in real carbonated reinforced concrete structures.

2. Materials and method

2.1. Materials

Three concrete formulations (B1-15L-049, B3-041 and B3-15L-051) were used in this study. Their compositions are given in Table 9 and Table 10. These 3 concretes are studied in a French Project called Perfdub (https://www.perfdub.fr/) which aims to study concrete performance according to durability indicators. It corresponds to industrial concrete compositions used on site, but the W/B ratio is almost the same (i.e. 0.5) for the CEM I concrete (B1-15L-049) and one CEM III concrete (B3-15L-051). The 2nd CEM III concrete allows study the influence of a lower W/B ratio (0.41).

	B1-15L-049	B3-041	B3-15L-051
Cement type	85% CEM I 52.5N + 15% Betocarb GY	100% CEM III A 52.5L	100% CEM III A 52.5L+ 15% Betocarb GY
Slag %	0	64	64
Clinker %	97	36	36
C3S %	68	68	68
C2S %	11	11	11
C3A %	10	10	10
C4AF %	8	8	8
Vitreous Slag %	98.7	98.7	98.7
(CaO+MgO)/SiO2		1.3	1.3
(CaO+MgO+SiO2)%		83.6	83.6
Limestone filler Betocarb GY CaCO3 (%)	95	95	

Table 9. Silicate and aluminate compositions of cements and GGBS slag compositions

	Mass of constituents in kg/m^3		
Concrete formulations	B1-15L-049	B3-041	B3-15-051
Sand	818	830	818
Gravel	957	1005	957
Cement	280 (CEM I)	380 (CEM III A)	280 (CEM III A)
Limestone filler	50 (Betocarb HP Gy)	0	50 (Betocarb HP Gy)
Binder C_b	330	380	330
Plasticizer	1.6 (SIKA Techno 348)	4.6 (Optima 372)	2.1 (OMEGA 144)
Effective water	163	155	169
Theoretical density ρ	2315	2390	2320
Apparent density	2090	2280	2130
Measured density at 28d	2319	2349	2332
Mbp %	14.25	15.9	14.22
Slump (mm)	160	170	190
water/cement	0.58	0.41	0.60
Water/binder	0.49	0.41	0.51
Paste volume (L)	320	300	329

Table 10. Composition of concrete formulations.

The steel bars used in this study were cold rolled ribbed steel bars with diameters of 6 mm and 12 mm, manufactured by Fimurex, France. No treatment was applied to the rebar and the presence of a non-uniform layer of mill scale on the surface was observed. This surface state, also called “As Received”, is one of the most popular types for steel bars.

2.2. Characterization tests

Table 11 presents the results of several characterization tests which were performed on these 3 concretes.

Concrete formulations	Strength Fc28 (MPa)	Porosity pw (%)	Resistivity (Ω.m)
B1-15L-049	40	16.3	69
B3-15L-051	41	17.2	267
B3-041	74	11.4	718

Table 11. Characterization tests results of the concrete formulations.

Water porosity tests were carried out according to standard NF P18-459. It was found that the water porosity of concrete B3-15L-051 at 90 days was slightly higher than that of B1-15L-049 at 28 days and that the porosity of B3-041 was much lower than that of B1-15L-049 and B3-15L-051 due to the lower w/b ratio of this formulation.

The average values of electrical resistivity of all the mixes with the coefficient of variation (CV) were tested in the French Perfdub project [108]. It can be seen that slag cement formulations (B3-041 and B3-15L-051) present higher resistivity than the concrete without slag (B1-15L-049), B3-041 having a higher resistivity than B3-15L-051 due to its lower w/b ratio.

2.3. Preparation of samples

The samples were based on the test protocol with separation of the cathode and anode derived by Chalhoub et al. [111]. However, the anodes were involved in the process of carbonation instead of chloride contamination.

2.3.1. Cathode samples

Cylindrical cathodes and a reinforced concrete (RC) wall were used in the research.

The cylindrical cathode samples had a diameter, Ø, of 110 mm, a height, h, of 220 mm and a cover of 5.2 cm (Figure 48). One Fe 500 steel bar with 6 mm diameter ribbing was embedded at the center of the cathode. To verify the influence of the cathode/anode ratio, 3 lengths of steel bar were utilized: 10 mm, 50 mm and 160 mm. After casting and demolding, the cathode samples were placed in a wet curing room (relative humidity = 95%). Cylindrical cathodes allowed cathode/anode ratios of 1, 5 and 16 to be tested.

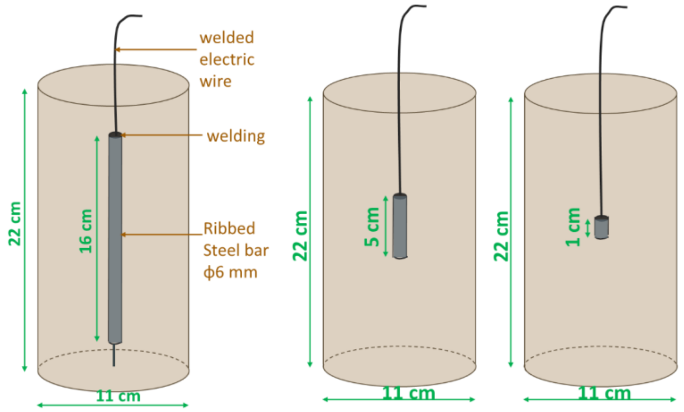

Figure 48. Cathode samples

The RC wall had dimensions 75x20x100 cm and contained 10 horizontal Ø 12 mm bars 70 cm in length and 8 vertical Ø 12 mm bars having lengths of 102 cm and 5 cm emerging from the concrete (Figure 49). The steel bar network was completely electrically disconnected but could be electrically connected externally thanks to a connection box. During the measurement of the macro cell current, the anode was immersed in NaOH solution contained in a PVC pipe firmly sealed outside the wall. Reinforced concrete wall was used to test cathode/anode ratios (C/A) from 750 to 2200. The RC wall was made with ordinary concrete: CEM I cement and w/b ratio of 0.55. The electrical resistivity was recorded 110 Ωm at 90 days. The RC wall has a different mix composition because it is used only to test high C/A ratios.

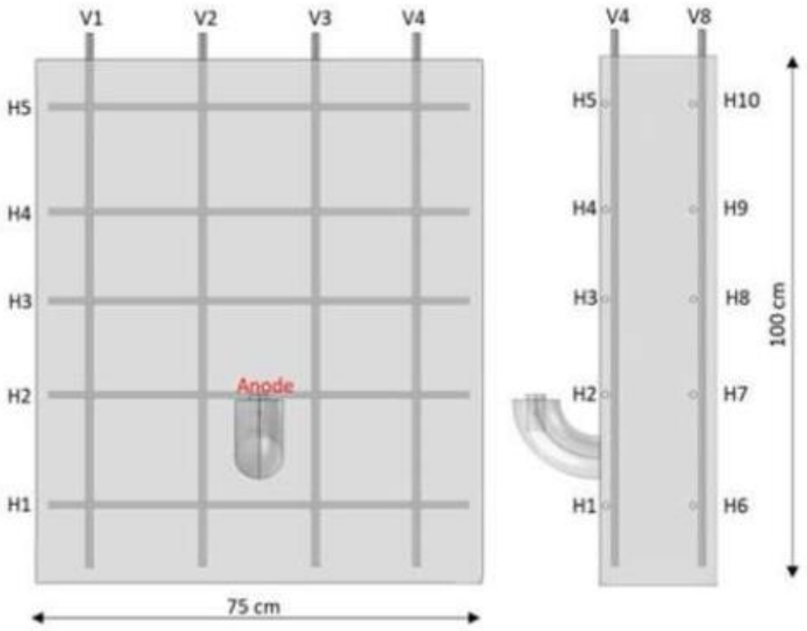

Figure 49. Wall sample

2.3.2. Anode samples

The anode samples were cylindrical with dimensions Ø= 33 mm and h= 70 mm, having one steel bar with a diameter of 6 mm and a height of 10 mm embedded at the center (Figure 50). These samples were carbonated before being utilized in the following tests.

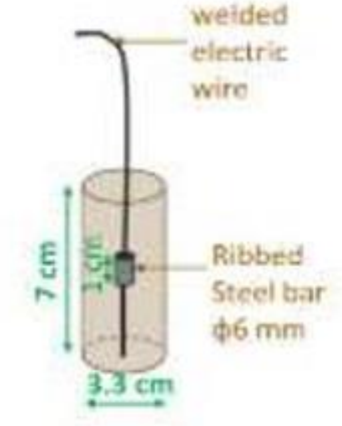

Figure 50. Anode sample

2.3.3. Anode carbonation process

After 8 weeks of wet curing, the anodes were stored in an oven at controlled temperature of 45°C and constant relative humidity of 25% during 14 days, followed by 7 days at 20°C and 65% relative humidity. The contamination of the anodes with carbon dioxide was carried out in a 65% relative humid chamber with 50% of CO2. The choice of 50% of CO2 was done in accordance to NF XP P18-458 standard, this method was used in the first part of French Perdub project. The percentage of CO2 is very high and it could have an effect on the length of steel concrete interface carbonated from a crack as shown by Ghantous et al. [207]. Nevertheless, here the goal is to fully carbonated the anode sample, and not studied the progress of the carbonation front. Then, results will allow compare the corrosion rates of the 3 concretes.

The carbonation depth was measured with phenolphthalein solution. After spraying with this solution, if the concrete is observed to be purple, its pH is higher than 9. The pH is from 8 to 9 when the concrete becomes pink and is below 8 when no change of color is observed. The aim was to obtain complete carbonation of the anode samples. For each formulation, 3 control specimens (without reinforcements) 40 mm in diameter and 70 mm in height were extracted from specimens 110 mm in diameter and 220 mm in length by coring. These test pieces were placed under the same conditions of attack (carbonation chamber) as those intended to reveal the progress of the carbonation front.

The complete carbonation of the anode samples was quite long especially for the B3-041 concrete with the lower W/B ratio. The end of the carbonation process was decided at 100d, 200d and 250d respectively for the 3 concretes B1-15L-049, B3-15L-051 and B3-041.

2.3.4. Corrosion process

After complete carbonation of the anode samples, checked according to the control samples, they were placed in tap water for 48 hours to induce full capillary suction to reach the re-bar and lead to the onset of corrosion. The corrosion onset was checked by both a potential drop greater than 200 mV and the existence of macro cell current when connected to a cathode.

2.4. Measurement of currents

The methods chosen for the assessment of corrosion under uniform current and galvanized current were Polarization resistance and a Zero resistance ammeter (ZRA), respectively. All the electrochemical experiments were performed at a constant temperature of 20oC in a controlled room.

2.4.1. Measurement of the uniform current

The measurement of the current was based on RILEM TC 154-EMC [110]. This is a non-destructive electrochemical method to obtain the corrosion current density. The corrosion rate was calculated by means of the Stern-Geary formula (Equation 3):

$$i_{corr} = \frac{B}{R_p}(\mu A)$$

Equation 3

The value of 26 mV is recommended for constant B in cases where steel is in an active state [30]. For the anode used in the test, the dimension of the steel is very small and the concrete totally carbonated. Corrosion can be considered uniform and the corrosion current can therefore be calculated by means of Equation 4:

$$i_{corr} = \frac{I_{corr}}{S}(\mu A / cm^2)$$

Equation 4

Where S is the surface area of the steel embedded in the anode. With the anodes used in the test, S= 1.88 cm2.

The LPR technique gives an “apparent” response including both the polarization resistance Rp and the Ohmic resistance Re. The calculation of Re was achieved by a potentiostatic step of 30 mV to calculate the instantaneous response corresponding to the Ohmic behavior (see Figure 51 and Figure 52).

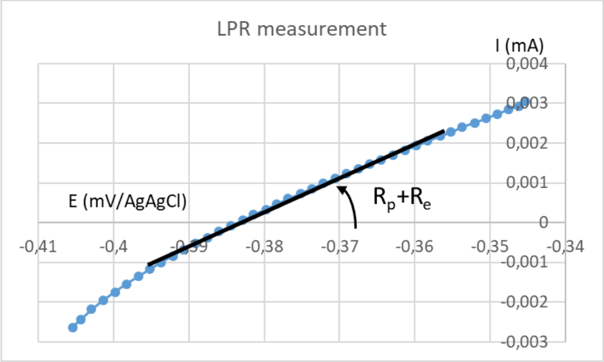

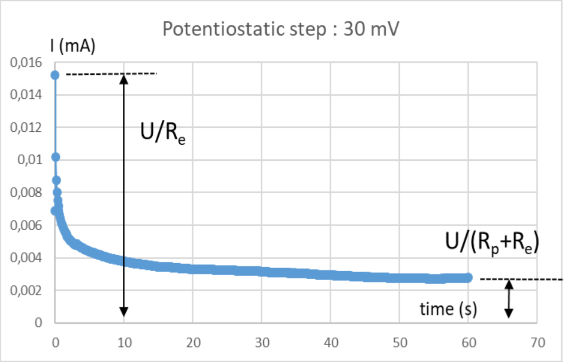

Figure 51 : example of LPR test on B1-15L-049 sample

Figure 52 : example of potentiostatic test on B1-15L-049 sample

2.4.2. Measurement of the macro cell current

The anode and cathode samples were connected by a Potentiostat controlled by EC lab Software using the electrochemical technique to measure the galvanized current between them (Figure 53). The measurement of the current was set up in 24 hours. The anodes were totally immersed in water during the test.

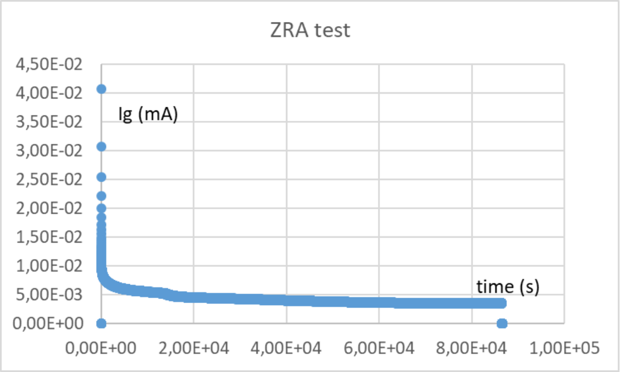

Figure 53 : Example of macro cell current measurement by ZRA technique for B1-15L-049 concrete

Cathode permutation was used to study the impact of cathode/anode ratio by changing the size of the cathode. Cylindrical cathode corresponding to a ratio of 1, 5 and 16 were used. In addition, the anode samples were coupled a concrete wall to obtained larger C/A ratio (varying from 750 to 2200).

2.4.3. Measurement of electrical resistivity of carbonated samples

The approach used to measure the resistivity of carbonated sample consisted in using the electrical resistance obtained during the potentiostatic tests of steel reinforced specimens (from the instantaneous responses at the polarization step such as shown in Figure 52 and converting it into electrical resistivity by inverse numerical modeling. In others words, a numerical model was involved to assess the specimens geometrical factor, linking resistance and resistivity. The protocol is defined in Chalhoub et a.[129].

3. Results and discussions

3.1. Electrical resistivity of carbonated samples

Table 12 presents the average value of electrical resistivity of the 3 concretes after full carbonation and the carbonation duration of the samples when tested. It can be seen that CEM III formulations (B3-041 and B3-15L-051) present higher resistivity that the CEM I concrete (B1-15L-049), B3-041 having the higher resistivity than B3-15L-051 due to its lower w/b ratio.

Concrete formulations	Resistivity (Ω.m)	Carbonation duration (day)
B1-15L-049	240	100
B3-15L-051	800	200
B3-041	2000	250

Table 12. Resistivity of carbonated samples

The resistivity of the 3 concretes after carbonation is about 3 times higher than non-carbonated concretes. In both cases, the measurement was achieved on saturated materials. The result is in agreement to previous researches [219, 220].

3.2. Uniform corrosion current

The corrosion current densities measured according to LPR tests for the 3 different concretes are shown in Figure 54, Figure 55 and Figure 56. For each concretes, four samples are tested (S-1 to S-4 for B1-15L-049 and B3-15L-051; or S-2 to S-5 for B3- 041 concrete).

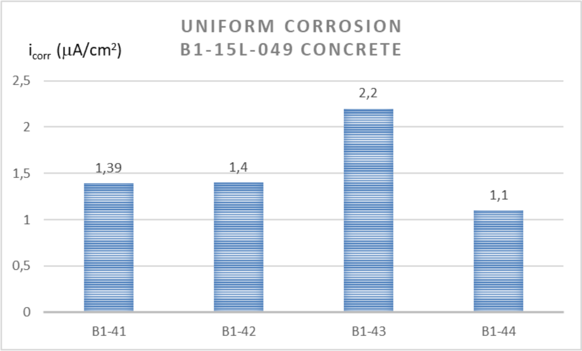

Figure 54. Concrete B1-15L-049 – uniform current density

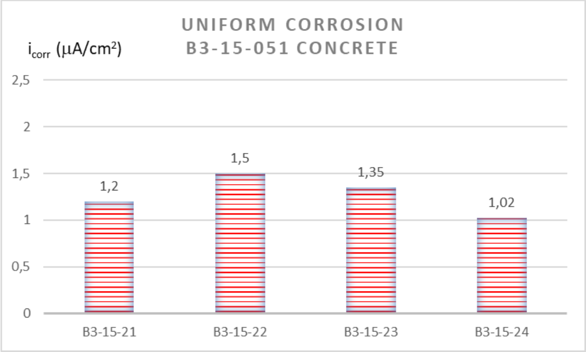

Figure 55. Concrete B3-15-051 – Uniform current density

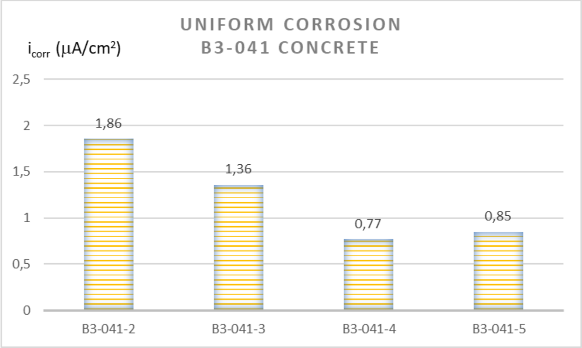

Figure 56. Concrete B3-041 – uniform current density

A significant dispersion can be seen between the different anodes of the same concrete group. The difference in terms of uniform current does not change very much from one concrete composition to another. Despite a significant difference in resistivity for the 3 concretes, the uniform current densities are in the same order of magnitude about 1.5 µA/cm^2. The porosities of the 3 concretes B1-15L-049, B3-15L-051 and B3-041 are respectively 16.3%, 17.2% and 11.4%. The absence of effect of porosity on the uniform corrosion current is probably linked to the high moisture environment involved in the test protocol [41].

3.3. Macro cell corrosion current

The macro cell corrosion current, expressed as macro cell current density by using the anode surface area, between the 4 anodes of each group connected to a cathode of the same group are shown in Figure 57, Figure 58 and Figure 59. The cathode used is the one with a C/A ratio of 16.

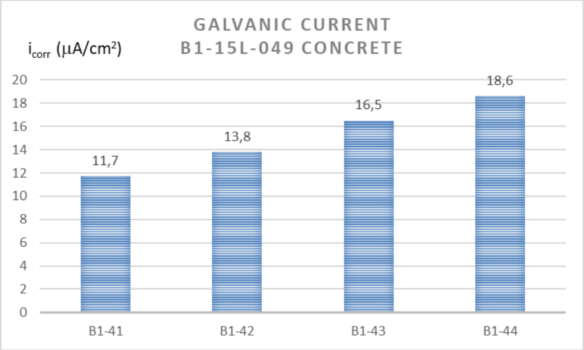

Figure 57. Concrete B1-15L-049 – macro cell current density

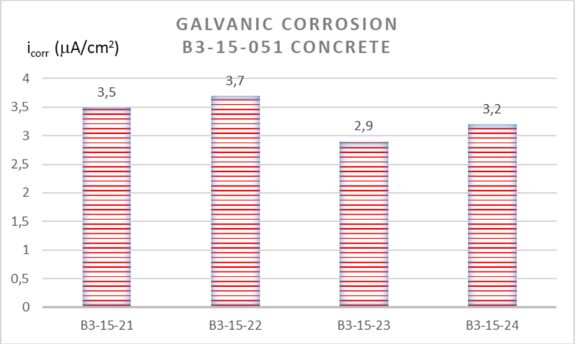

Figure 58. Concrete B3-15-051 – macro cell current density

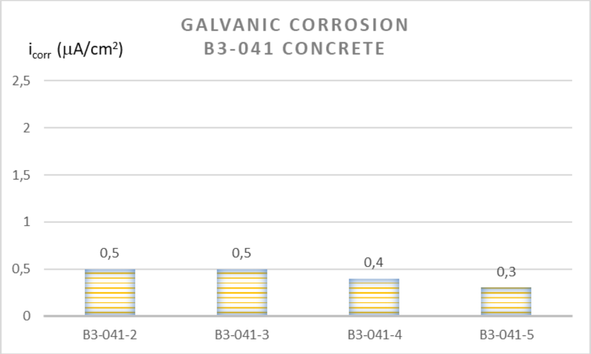

Figure 59. Concrete B3-041 – macro cell current density

It can be seen that the differences in macro cell current density between the different anodes of the same group of concretes are not very large but, on the contrary, there is a large difference in terms of macro cell current density between the different concrete compositions. The effect of concrete resistivity in the case of macro cell corrosion is thus highlighted.

When dealing with macro cell corrosion process, the effect of resistivity of concrete is linked to both anode and cathode. At anode location the resistivity is higher than at cathode location. Nevertheless, for a given concrete, a higher resistivity at anode corresponds also to a higher resistivity at cathode. As a result, the macro cell current in case of CEM III concretes (B3-041 and B3-15L-051) is significantly lower than CEM I concrete (B1-15L-049), B3-041 having the lower macro cell current density than B3- 15L-051 due to its lower w/b ratio.

3.4. Macro cell current in relation to the Cathode to Anode ratio (C/A)

When dealing with carbonation-induced corrosion, the Cathode to Anode ratio (C/A) is not as high as in the case of chloride-induced corrosion, because a significant surface area of reinforcing steel is depassivated by the motion of the carbonation front. In the case of two layers of reinforcing steel, the ratio could be estimated to have a value of 1. In the case of a multi-layer structure or structure with a very dense reinforcement layout, such as can be found in a nuclear power plant, the ratio could be higher - but probably less than 10. It should be noticed that in case of pre-cracked concrete (load-induced cracks or others causes), the carbonation front could reach quickly the steel bar at crack tip and then induced corrosion initiation with a high C/A ratio.

Nevertheless, to compare the effect of the C/A ratio on the macro cell current density with that of chloride-induced corrosion as shown by Chalhoub et al. [111], the B3-041 anodes were connected to different cylindrical cathodes with C/A ratios varying from 1 to 16, and then to a reinforced concrete wall with a C/A ratio varying from 750 to 2200. The same CEM I concrete cathode as used by Chalhoub et al. [111] was connected to the different anodes of the 3 groups of concrete. This experiment does not correspond to a practical case since on-site the anode and cathode are obviously made with the same concrete. Because the tendency was the same, it was chosen to only show the B3-041 results. It gives information on the control process due to the resistivity of the cathode and the effect of C/A ratio.

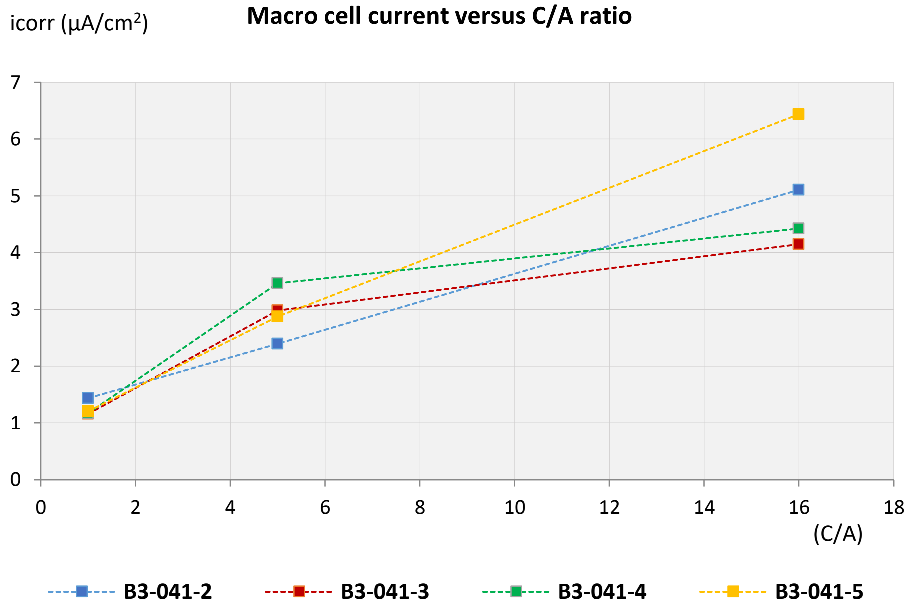

Figure 60. Macro cell current density vs C/A ratio (1 to 16)

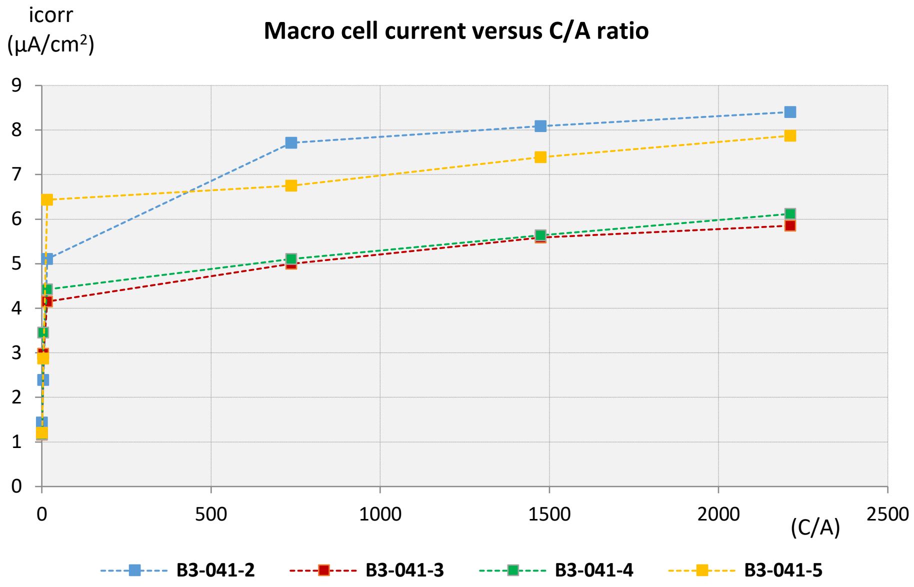

Figure 61. Macro cell current density vs C/A ratio up to 2200

From the results plotted on Figure 60, it can be seen that the macro cell current for a C/A ratio of 16 is varying between 4 and 6.4 μA/cm^2, with an average value of 5 μA/ cm^2, which could be compare with Figure 59 where the average value is 0.425 μA/ cm^2. As a result, by changing the concrete at the cathode from CEM III concrete (B3-041) (resistivity of 718 Ωm) to the CEM I concrete from the wall (resistivity of 110 Ωm), the macro cell current measured is more than 10 times higher. It confirms that the macro cell corrosion process is on Ohmic control.

The effect of C/A ratio on macro cell current is shown in Figure 60 and Figure 61. For low C/A ratios, it seems that the current density is quite proportional to the ratio but, for high C/A ratios, the behavior tends to become asymptotic. These results are similar to those found by Chalhoub et al. [111] when dealing with chloride-induced corrosion. Effect of C/A is well-known for macro cell current in chloride- induced corrosion as shown by Warkus and Raupach [138], but usually not considered in carbonation induced corrosion. Because the increase in electrical resistivity reduces the mobilizable Cathode- Anode distance [221, 222], a high resistivity concrete can limit the macro cell process in case of structures with dense reinforcement lay-out.

3.5. Influence of resistivity of concrete on corrosion current

For uniform corrosion process, the resistivity involved is the one after carbonation which is higher than the initial one. Figure 62 shows the effect of the resistivity of concrete on the uniform current density in carbonation-induced corrosion. Resistivity was measured in saturated conditions corresponding to the corrosion test.

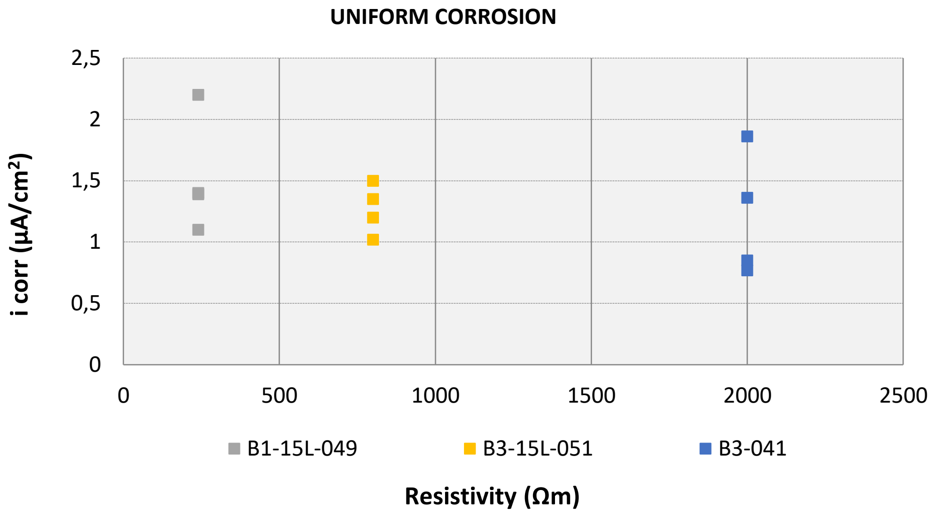

Figure 62. Influence of resistivity on the uniform current density

Resistivity of the 3 carbonated concretes B1-15L-049, B3-15L-051 and B3-041 were respectively 240, 800 and 2000 Ohm.m as shown in Table 12. The results plotted in Figure 62 do not show a clear influence of concrete resistivity on uniform current. This result is quite logical since, in a uniform corrosion process, anodic and cathodic sites are at the same location, so neither anodic nor cathodic current is supposed to be influenced by the concrete resistivity. This indicates that the uniform corrosion rate of steel in carbonated concrete is not under Ohmic control as found by Stefanoni et al. [41]. Nevertheless, many studies have shown a negative correlation between corrosion rates and the resistivity of concrete for carbonation induced corrosion [76, 77, 216, 217, 223-225].

For macro cell corrosion process, both resistivity before and after carbonation are involved in cathodic and anodic process respectively.

Figure 63 and Figure 64 indicate the effect of resistivity of concrete on the macro cell current density measured both after carbonation and before carbonation.

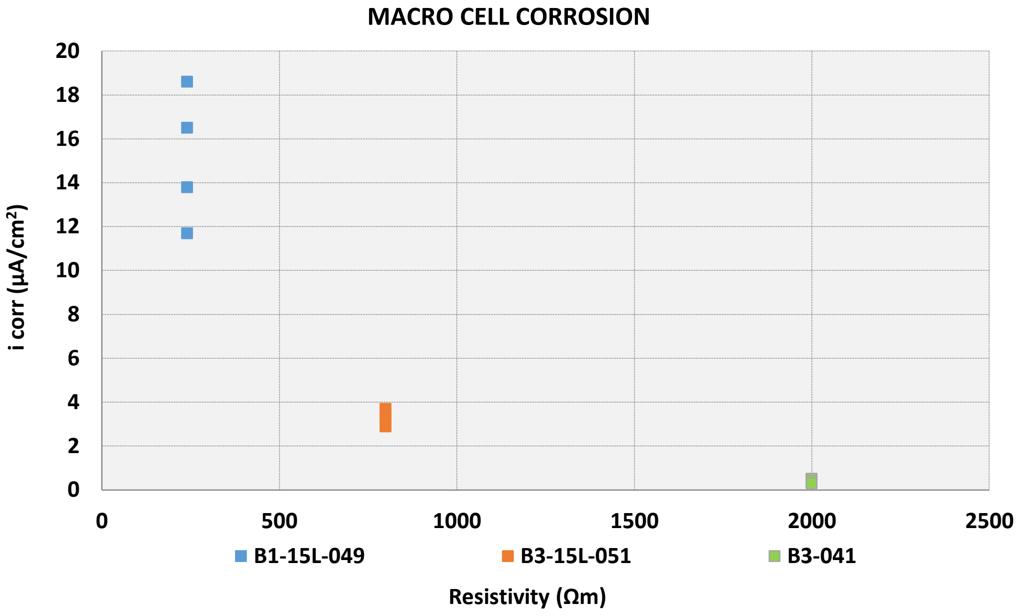

Figure 63. Influence of resistivity on the macro cell current density (for a C/A ratio of 16)

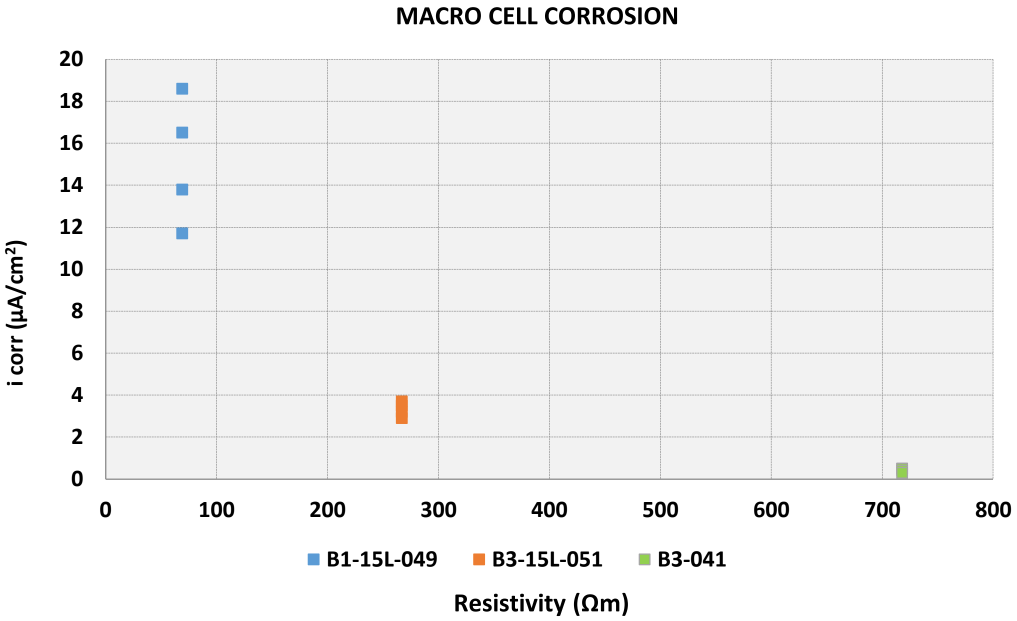

Figure 64. Influence of resistivity on the macro cell current density (for a C/A ratio of 16)

The results plotted in Figure 63 show a huge effect of resistivity of the concrete on the macro cell current. Here again, this result is quite logical since the ionic current flowing in the concrete is affected by the concrete resistivity and the distance between the anode site and the cathode. It should be noticed that the cathodic process corresponds to a non-carbonated concrete where the resistivity is lower than the one used in the Figure 63. Nevertheless, the use of the resistivity of sound concrete in abscissa of Figure 63 will not change the tendency because the changes in resistivity before and after carbonation are almost the same for the 3 concretes tested.

The use of CEM III cement in concrete, which significantly increases the resistivity of the concrete, is thus shown to reduce the macro cell part of the corrosion current in real structures with multi- layer reinforcements.

Indeed, Figure 63 shows that macro cell current density for B1-15L-049 concrete is about 5 times higher than B3-15L-051 concrete for a quite identical w/b ratio of respectively 0.49 and 0.51 resulting in a quite identical water porosity of respectively 16.3%, 17.2%. This result clearly shows an impact of the cement type on the corrosion rate of carbonated concrete.

Moreover, when the two CEM III concretes (B3-15L-051 and B3-041) are compared, the corrosion current density is significantly lower for the B3-041, which has the lowest resistivity due to a lower w/b. This result clearly confirms the impact of w/b ratio on the macro cell current density.

3.6. Numerical simulation of macro cell corrosion

This section is dedicated to the Numerical simulation to study macro cell corrosion is relation to the resistivity of concrete closed to the anode, the resistivity of concrete closed to the cathode, the value of the cathodic Tafel coefficient and the ratio C/A.

The numerical simulation was based on the Finite Element Method (FEM) using The COMSOL Multiphysics software (Figure 65).

The numerical simulation was governed by the local Ohm's law (Equation 5) and electric charge conservation (Equation 6).

$$i = -\frac{1}{\rho}\nabla E$$ Equation 5

$$\nabla i = 0$$ Equation 6

Where:

- E is the potential field (V)
- i is the local current density vector (A/m^2)
- ρ is the electrical resistivity (Ω.m)

The steel–concrete interface for both active and passive steel was modeled according to the Butler–Volmer kinetics with their respective parameters as presented in Equation 7 and Equation 8:

$$I_{corr,a} = i_{corr,a}\left(\exp\left(\frac{\log(10)(E_a - E_{corr,a})}{\beta_{a,a}}\right) - \exp\left(\frac{-\log(10)(E_a - E_{corr,a})}{\beta_{c,a}}\right)\right)$$ Equation 7

$$I_{corr,\mathrm{p}} = i_{corr,\mathrm{p}}\left(\exp\left(\frac{\log(10)(E_p - E_{corr,\mathrm{p}})}{\beta_{a,\mathrm{p}}}\right) - \exp\left(\frac{-\log(10)(E_p - E_{corr,\mathrm{p}})}{\beta_{c,\mathrm{p}}}\right)\right)$$ Equation 8

Where:

- $I_{corr,a}$ and $I_{corr,p}$ (A/m^2) are the corrosion currents following through the steel concrete interface for active and passive steel, respectively.
- $i_{corr,a}$ and $i_{corr,p}$ (A/m^2) are the corrosion current density values at active steel and passive steel, respectively.
- E_a and E_p (V) are are polarization potential for both steel rebars, respectively.
- $E_{corr,a}$ and $E_{corr,p}$ (V/ref) are the corrosion potential values at active steel and passive steel, respectively.
- $\beta_{a,a}$ and $\beta_{a,\mathrm{p}}$ (V/dec) are the is the anodic Tafel slope at active steel and passive steel, respectively.
- $\beta_{\mathrm{c},a}$ and $\beta_{\mathrm{c,p}}$ (V/dec) are the is the cathodic Tafel slope at active steel and passive steel, respectively.

The final electrochemical parameters used in the numerical simulation are presented in Table 13.

Concrete formulation	$E_{corr,p}$ (V)	$i_{corr,p}$ (A/m^2)	βa,p (V/dec)	βc,p (V/dec)	$E_{corr,a}$ (V)	$i_{corr,a}$ (A/m^2)	βa,a (V/dec)	βc,a (V/dec)	Rhoa (Ωm)	Rhoc (Ωm)
B1-15L-049	-0.15	0.00015	0.4	0.1	-0.5	0.05	0.125	0.136	240	69
B3-15L-051	-0.15	0.00015	0.4	0.22	-0.5	0.05	0.125	0.136	800	267
B3-041	-0.15	0.000015	0.4	0.25	-0.5	0.05	0.125	0.136	2000	718

Table 13. Electrochemical parameters and materials parameters

Indeed, the values of cathodic Tafel coefficient βc,p and the current density at cathode $i_{corr,p}$, appears to be in relation with the type of cement and the W/B ratio. The others electrochemical parameters are kept constant. As a result, we consider that anodic process in not dependent of cement type and W/B ratio as it was supposed in Chalhoub work [27] .On the contrary, because cathodic reaction involved oxygen reduction, the availability of oxygen in term of porosity at SCI interface, linked to W/B ratio, and in term of oxygen consumption, linked to the presence of sulfur (CEM III cement) would be different for each concrete. Cathodic parameters are then adjusted for each concrete formulation.

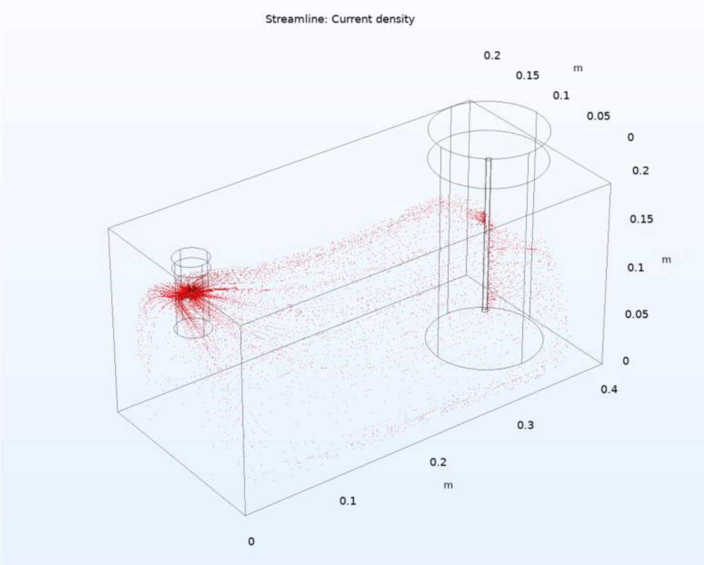

Figure 65. Modeling of anode and cathode in COMSOL

Firstly, we will do some numerical simulation to see the impact of electrochemical parameters of the corrosion current density. Indeed, Chalhoub [27] have shown that the cement type could have an influence of the cathodic reaction and especially on the cathodic Tafel coefficient.

Secondly, the influence of resistivity at anode or cathode will be tested. Indeed, resistivity has a significant impact of the macro cell current density. Both effect of resistivity at the anode or at the cathode are tested.

Finally, the effect of C/A ratio is tested. Indeed, in case of carbonation induced corrosion, the ratio C/A is not as high as it is the case for chloride-induced corrosion.

3.6.1. Effect of the value of Tafel cathodic coefficient: βc,p

To study the effect of βc,p coefficient on the macro cell corrosion current, it is first assumed that cathodic corrosion current density $i_{corr,p}$ is in relation with the W/B ratio. Then $i_{corr,p}$ is considered to be the same for B1-15L-049 and B3-15L-051 concrete while it is considered that $i_{corr,p}$ decrease with the decrease of W/B.

As a result, the $i_{corr,p}$ is kept the value of 0.00015 A/m2 with B1-15L-049 and B3-15L-051 while the value is 0.000015 A/m^2 with B3-041. Then we make numerical simulations with βc,p varying between 0.1 and 0.3. Figure 66 gives information of the effect of changing the value of βc,p.

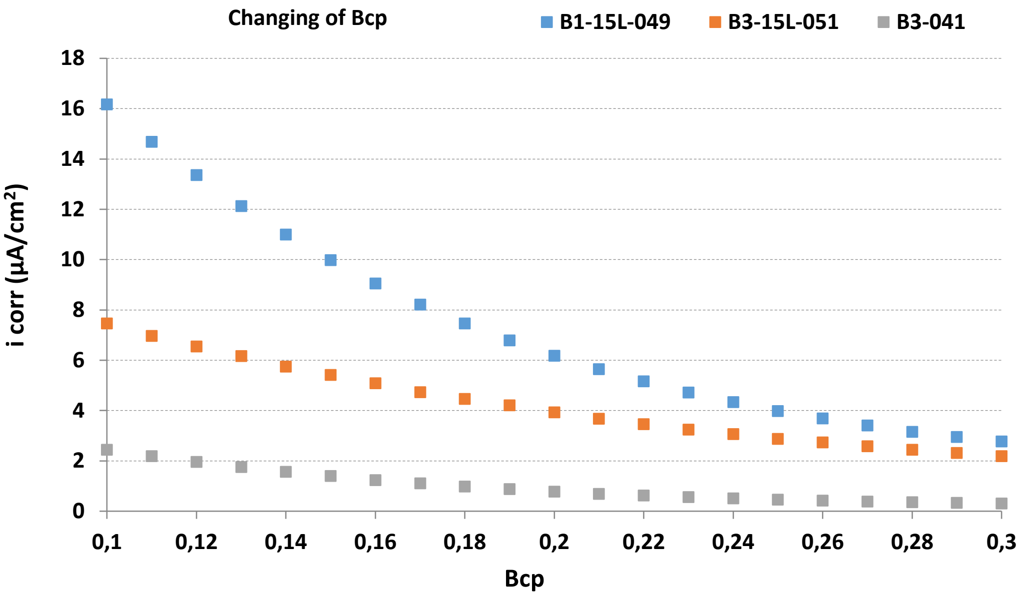

Figure 66. Changing the value βc,p

Figure 66 shows the effect of the cathodic Tafel coefficient on the macro cell current corrosion in the case of a C/A ratio of 16, which corresponds to the experimental results at the beginning of the chapter. From Figure 66, it appears that βc,p coefficient has a huge impact of the macro cell corrosion current. From this parametric study, we can see that it is necessary to have a value of βc,p =0.1 for B1-15L-049 concrete to be able to fit with the experimental results: i.e. a macro cell current density around 16µA/cm^2 (Figure 57). Concerning the B3-15L-051 concrete, it appears that the value of βc,p = 0.22 is suitable to fit the experimental results: i.e. a macro cell current density below 4µA/cm^2 (Figure 58). And finally, for the B3-041 concrete, it is necessary to adjust the βc,p =0.25 to fit the experimental results: i.e. a macro cell current density below 0.5µA/cm^2 (Figure 59).

The change in cathodic Tafel coefficient according to the type of cement and porosity is coherent with the results from Chalhoub [27]. Chalhoub used βc,p = 0.115 for CEM I concrete and found that βc,p could varied between 0.113 to 0.240 for CEM I cement with a high amount of slag in substitution of cement (80%) (Figure 67). In our results, we found that 0.22 and 0.25 values need to be used for respectively B3-15L-051 and B3-041, which corresponds to the interval of values found by Chalhoub.

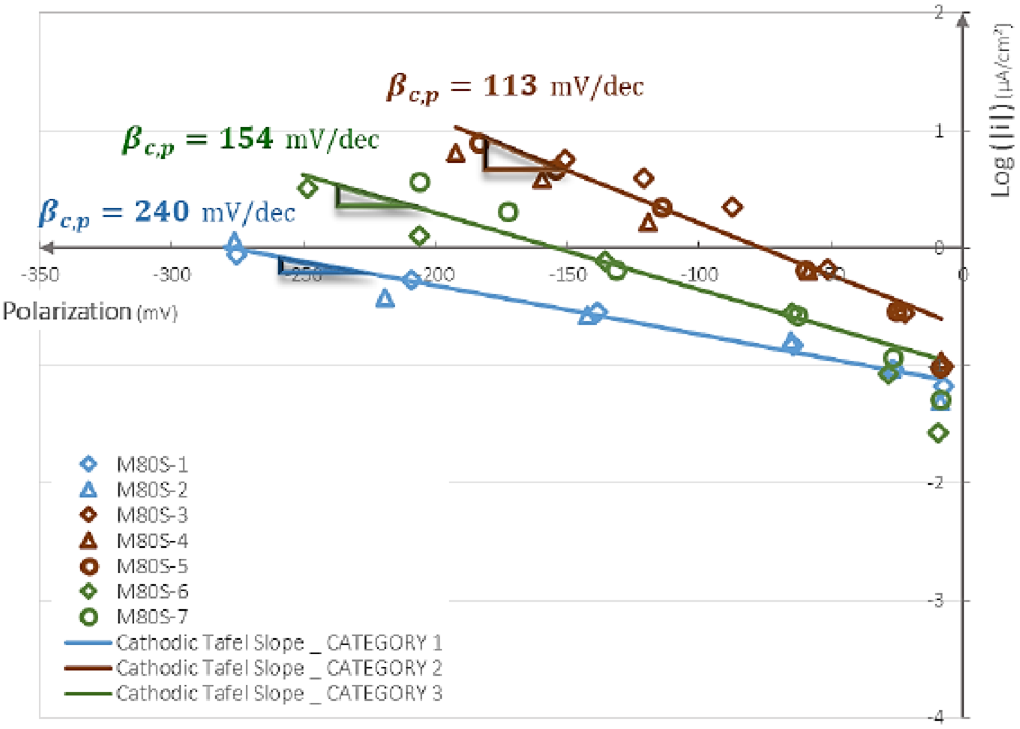

Figure 67 : Cathodic Tafel coefficient according to the availability of oxygen in case of binder with 80% of slag and 20% of CEM I. (From Chalhoub [27])

In the macro cell process, both anode and cathode are involved. In the case of carbonation-induced corrosion, there is not only the electrochemical parameters which could have an influence but also the resistivity. Indeed, anode is necessary in carbonated zone and will exhibit and higher resistivity than cathode, which is necessary in the non-carbonated zone in the case of macro cell current study.

3.6.2. Macro cell corrosion current in relation to resistivity at the Anode or at the Cathode

Following is the change of resistivity at anode and cathode in simulation. This aims to evaluate the influence of resistivity on macro cell corrosion.

Case of changing the resistivity of anode with B1-15L-049 concrete is shown in Figure 68.

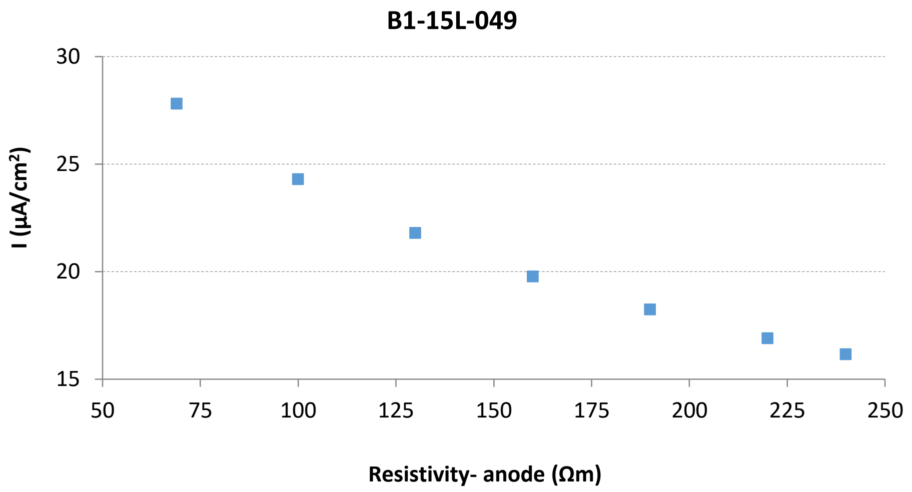

Figure 68. Changing in resistivity of the anode in B1-15L-049

From Figure 68, it appears that resistivity at anode as an important effect on the macro cell current corrosion. For B1-15L-049 concrete, the decrease in macro cell current corrosion corresponds to 50% reduction between the non-carbonated value (69 Ω.m) of resistivity and the carbonated one (240 Ω.m).

Case of changing the resistivity of cathode with B1-15L-049 concrete is shown on Figure 69.

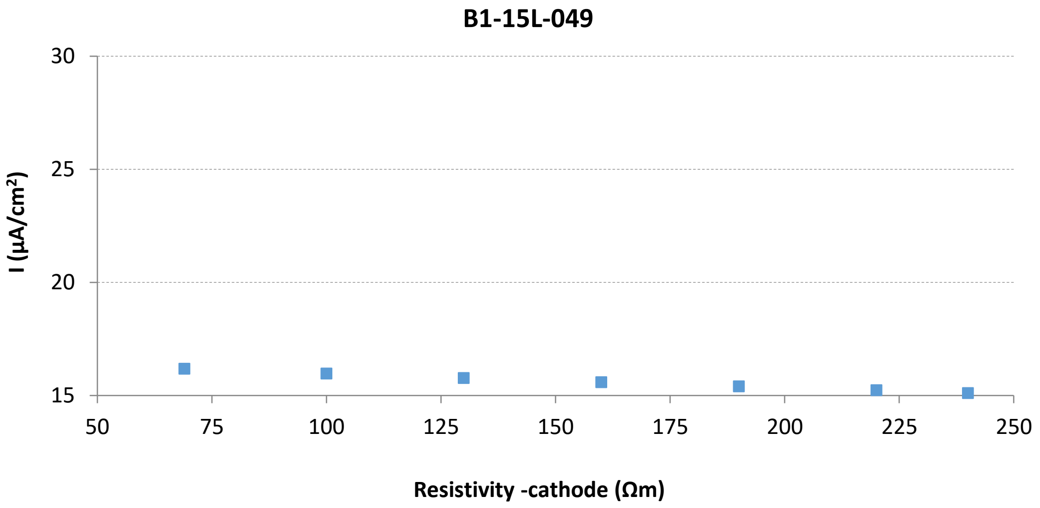

Figure 69. Changing in resistivity of the cathode in B1-15L-049

From Figure 69, it appears that resistivity at cathode do not play a significant role on the macro cell current corrosion. For B1-15L-049 concrete, the macro cell current corrosion is almost constant between the non-carbonated value of resistivity and the carbonated one.

Case of changing the resistivity of anode with B3-15L-051 concrete, is shown Figure 70.

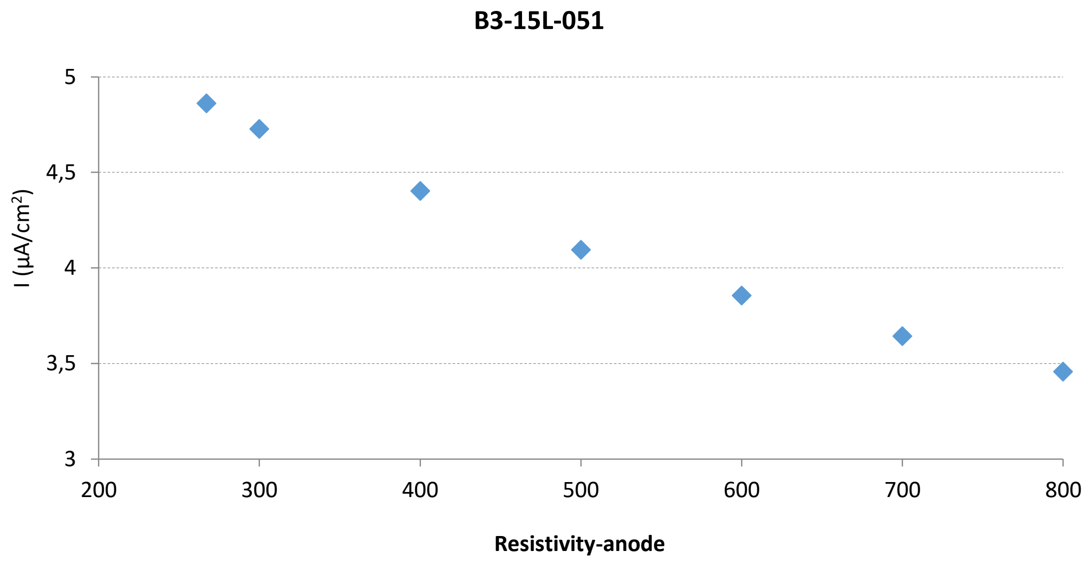

Figure 70. Changing in resistivity of the anode in B3-15L-051

From Figure 70, it appears that resistivity at anode as an important effect on the macro cell current corrosion. For B3-15L-051 concrete, the decrease in macro cell current corrosion corresponds to 1.5 times between the non-carbonated value of resistivity (267 Ω.m) and the carbonated one (800 Ω.m).

Case of changing the resistivity of cathode with B3-15L-061 concrete is shown on Figure 71.

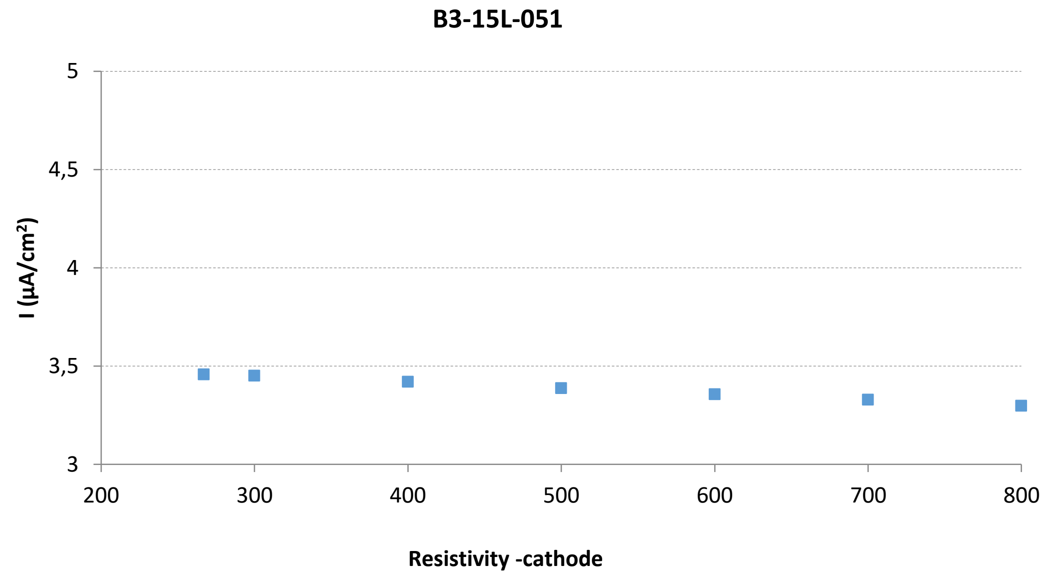

Figure 71. Changing in resistivity of the cathode in B3-15L-051

From Figure 71, it appears that resistivity at cathode do not play a significant role on the macro cell current corrosion. For B1-15L-049 concrete, the macro cell current corrosion is almost constant between the non-carbonated value of resistivity and the carbonated one.

Case of changing the resistivity of anode with B3-041 concrete is shown on Figure 72.

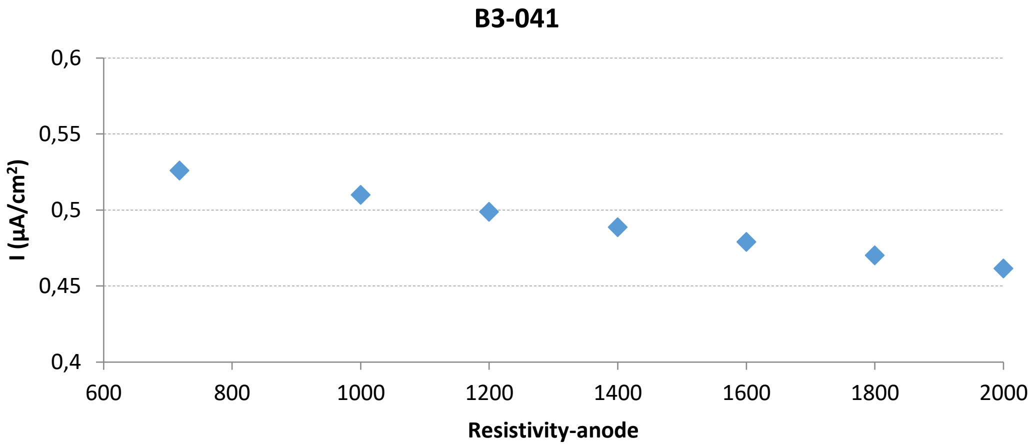

Figure 72. Changing in resistivity of the anode in B3-041

Case of changing the resistivity of cathode with B3-041 concrete is shown on Figure 73.

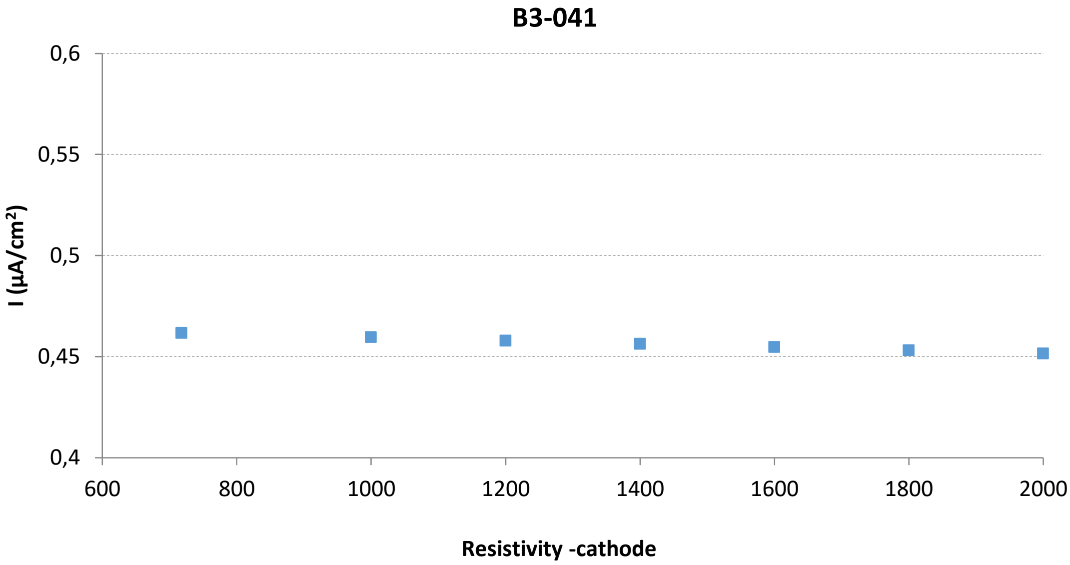

Figure 73. Changing in resistivity of the cathode in B3-041

From Figure 72 and Figure 73 , it appears that resistivity at anode is more important effect on the macro cell current corrosion. For B3-041 concrete, it was recorded a decrease in macro cell current corrosion between the non-carbonated value of resistivity (718 Ω.m) and the carbonated one (2000 Ω.m).

From Figure 73, it appears that resistivity at cathode do not play a significant role on the macro cell current corrosion. For B3-041 concrete, the macro cell current corrosion is almost constant between the non-carbonated value of resistivity and the carbonated one.

It was observed that the change of resistivity in anode have a huge impact on the macro cell current corrosion which is not the case at cathode.

From the results of numerical simulation, it allows to highlight why it is important to modify the cathodic Tafel coefficient according to the change in W/B ratio. Indeed, increasing the resistivity at the cathode does not allow to reduce the macro cell corrosion current. As a result, it is necessary to change the cathodic Tafel coefficient to take into account the more difficult access to oxygen for cathodic reactions in the case of lower porosity at the SCI.

3.6.3. Macro cell corrosion current in relation to cathode-anode ratio (C/A)

Experimental results on macro cell corrosion current were investigated with a C/A ratio of 16. While it could be the case in case of cracked concrete when depassivation occurs quickly at crack tip, the on-site C/A in non-cracked area would be not so high. Indeed, because the carbonation front is quite regular along the concrete surface, carbonation would depassivate a large part of the reinforcement and then lead to C/A ratio closed to a value of 2 is the reinforcement layout is made of 2 layers.

To investigate the influence of C/A ratio, the length of the cathode was input with several values: 1cm, 5cm, 10cm, 13cm and 16cm leading to the C/A ratio range from 1 to 16. Figure 74 exhibited the relation between macro cell current and C/A ratio.

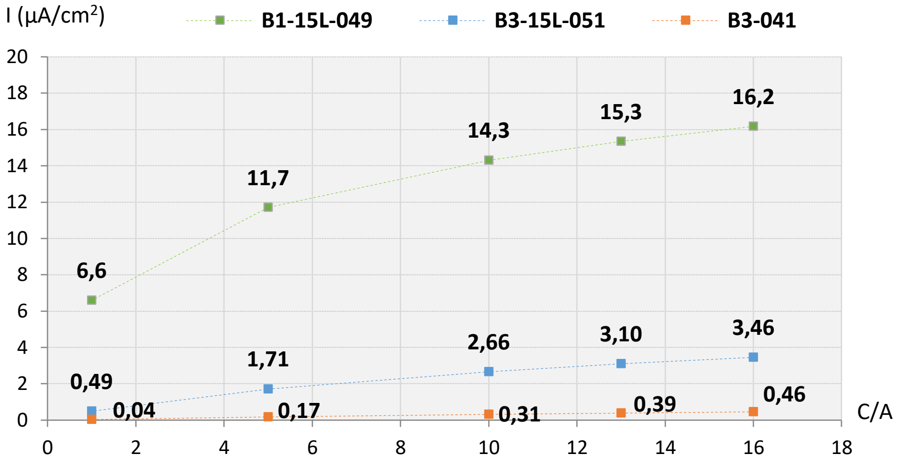

Figure 74. Macro cell corrosion vs cathode-anode ratio

From Figure 74, it appears C/A ratio plays a significant role in the macro cell corrosion process.

Figure 74 shows also the effect of C/A ratio on the macro cell corrosion current. It appears clearly that the change in C/A ratio do not correspond to a linear law. Many factors could be involved in this nonlinear process. First of all ,we can think, as show in Chalhoub [222] at the effect of the cathode-anode distance whereas most distant part of cathode received a limited amounts of current. Nevertheless, in the numerical model and also in the experimental process, the cathode-anode distant is constant for all cathodes since it corresponds to the cover of concrete which is constant for cathode specimens.

As a result, if it is not an ohmic effect since the anode-cathode distance is the same, then it could be attributed to the nonlinear behavior in both cathodic and anodic current response to a polarization.

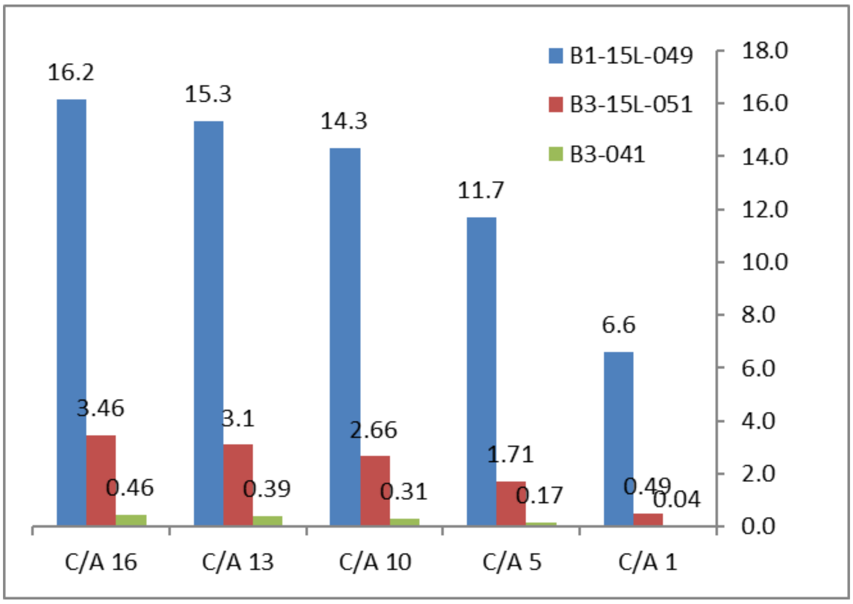

Figure 75 : macro cell current versus the C/A ratio for the 3 concretes studied

From Figure 75, it is clear that the resistivity at anode plays a significant role on the macro cell current whatever the C/A ratio. For B1-15L-049 concrete, the macro cell current for C/A =1 is 13.5 times higher than B1-15L-051 concrete and 165 times higher than B3-041.

Finally, Figure 76 shows the relative change in macro cell current when the C/A ratio change for the 3 studied concretes.

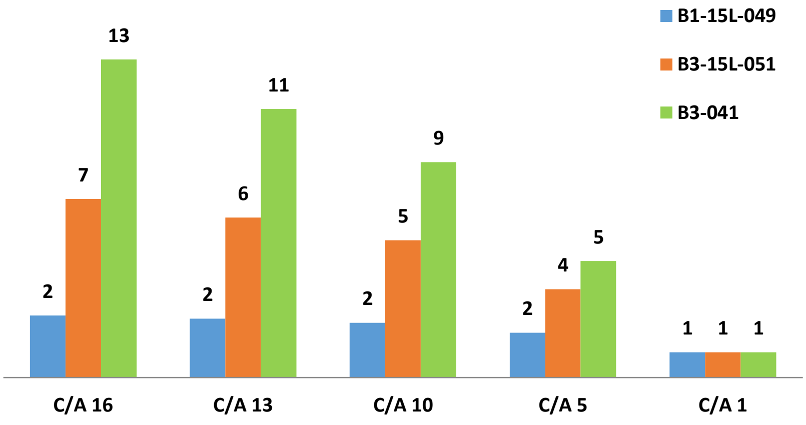

Figure 76: Relative change in macro cell current versus C/A ratio for the 3 concretes studied

From Figure 76, it appears that C/A ratio have a more important relative effect when the resistivity at the anode is high, which could be a non-intuitive result. Indeed, for B3-41 concrete with the higher resistivity at anode (i.e. 2000 Ohm.m), there is an increase in macro cell current of 13 times when the C/A ratio increase from 1 to 16. On the contrary, for B1-15L-049 concrete with the lower resistivity at anode (240 Ohm.m), the increase in macro cell current is only 2 times when C/A ratio increase from 1 to 16.

Finally, if we compare the uniform current recorded experimentally with the macro cell current calculated in case of C/A ratio= 1 (Figure 77, Figure 78 and Figure 79); it appears that the uniform current is higher in case of important resistivity (case of B3 concrete). For B1-15L-049 with the lower resistivity, macro cell corrosion current is still higher to uniform one.

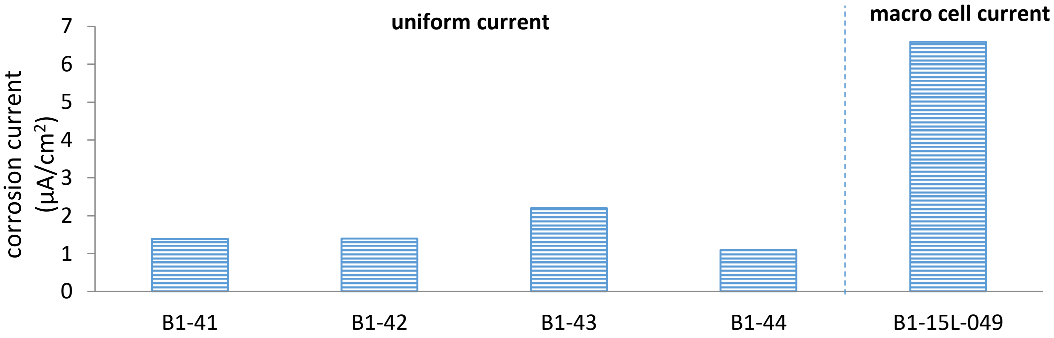

Figure 77. Compare the uniform current recorded experimentally with the macro cell current calculated in case of C/A ratio= 1 (B1 concrete)

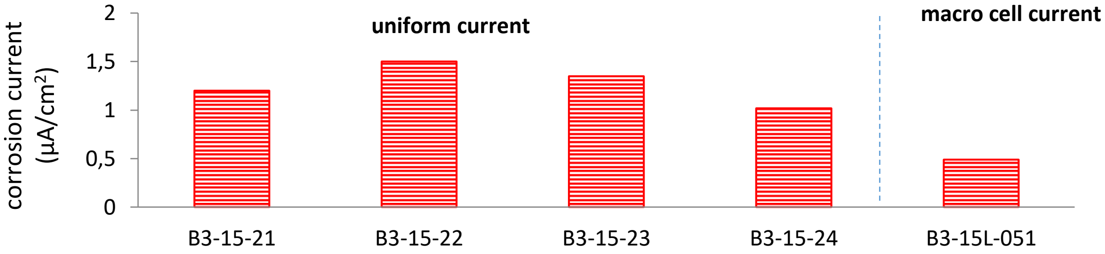

Figure 78. Compare the uniform current recorded experimentally with the macro cell current calculated in case of C/A ratio= 1 (B3-15L-051)

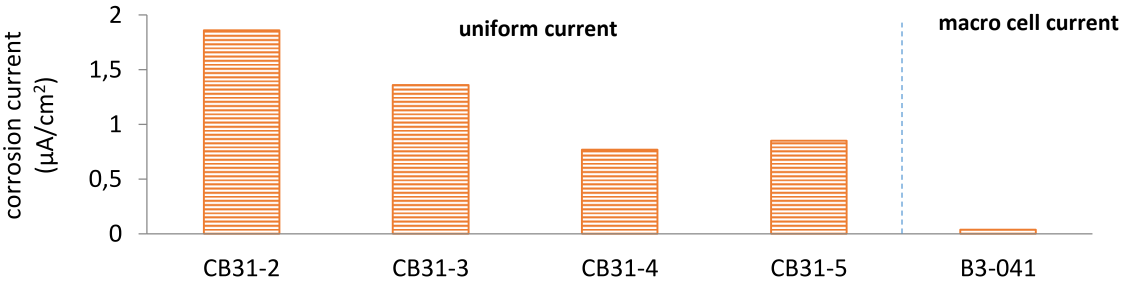

Figure 79. Compare the uniform current recorded experimentally with the macro cell current calculated in case of C/A ratio= 1 (B3-041)

4. Discussion

The main object of the study was to investigate the two aspects of corrosion involved in the carbonation of real multi-layer reinforced concrete structures: uniform corrosion and macro cell corrosion. Three different industrial concretes actually used on site were tested: a CEM I and two CEM III. CEM III concrete is nowadays the most common concretes currently used for reinforced concrete structures. Indeed, using CEM III allows the emission of CO_2 into the atmosphere to be reduced and also leads to higher resistivity concretes, which are considered to be more durable. Nevertheless, the resistance of CEM III to carbonation is currently considered to be lowered when the amount of clinker is reduced [60] so the use of CEM III in high-carbonate environments could be questionable.

It should be reminded that the carbonation process is not studied: only the corrosion rate is measured after full carbonation of the steel concrete interface.

From this study, it is possible to highlight some points of discussion. The possibility of carbonation-induced corrosion should be considered with both uniform and localized or macro cell corrosion, rather than with only uniform corrosion. Indeed, real reinforced concrete structures use multi-layers reinforcement framework which lead to the co-existence of passive and depassivated layers during the corrosion process.

4.1. Corrosion rate

The uniform corrosion rate found in this study is about 1.5 $\mu A/m^2$. For the results of this limited study, the uniform corrosion rate is quite constant whatever the type of cement used and whatever the w/b ratio.

The macro cell corrosion rates found in this study are varying between 15.5 $\mu A/cm^2$ (average value for B1- 15L-049), 3.3 $\mu A/cm^2$ (average value for B3-15L-051) and 0.5 $\mu A/cm^2$ (average value for B3-41). Nevertheless, it corresponds to a high C/A ratio (16).

In practice, in case of a situation with two layers of steel reinforcement, where one is in carbonate and one not, the C/A ratio will be reduced (C/A =1), then the macro cell corrosion rate will be reduced. As a result, the macro cell corrosion rates found in this study are varying between 6.6 $\mu A/cm^2$ (for B1- 15L-049), 0.49 $\mu A/cm^2$ (for B3-15L-051) and 0.04 $\mu A/cm^2$ (for B3-41).

The macro cell corrosion current appears to be highly dependent of the resistivity at anode site. The use of low W/B ratio and CEM III cement will lead to weak macro cell corrosion and possibly neglected macro corrosion current if compare to uniform one.

Nevertheless, in practice, there is also the possibility to have high C/A ratio: for example, for corrosion in pre-cracked concrete (load-induced cracks, shrinkage cracks etc..) where the carbonation front reach quickly the rebar at crack tip. Some local lack of concrete cover could also lead to high C/A ratio since the carbonation front reach only a small area of steel bar at the cover defect. In case of high C/A ratio, the macro cell corrosion rate could be significant and could not be neglected. As a result, the use of high resistivity concrete leads to reduce the corrosion rate, by anodic effect, ohmic effect and also because the mobilizable cathode surface decrease with the increase in resistivity.

4.2. Concrete resistivity before and after carbonation

Carbonation on concrete leads to a significant increase in resistivity of about 3 times. For the concretes tested the increase in resistivity seems more important when initial resistivity is lower. Such result was also found in [220].

Uniform corrosion rate does not depend on resistivity. For macro cell corrosion process, the cathodic reaction occurs in sound concrete zone (non-carbonated) then the resistivity value which needs to be considered is the one before carbonation. It is the case when dealing with durability indicator for concrete, such as in the French Perfdub project: indeed, the concrete resistivity corresponds to the value of sound concrete before carbonation.

4.3. Corrosion environment

In this study, the Relative Humidity RH% at anode corresponds to saturated conditions. Such saturated conditions could be found on-site, when for example a RC wall or RC floor initially exposed to dry environment during many years is exposed to water leakage due for example to a damage in roof waterproofing. Moreover, as shown in a review by Stefanoni et al. [41] the contact with water is the most aggressive conditions in term of carbonation-induced corrosion.

5. Conclusion

- The uniform corrosion rate does not depend of the concrete resistivity. (Resistivity in this research varies from 69 to 718 Ωm before carbonation and from 240 to 2000 Ω.m after carbonation)
- The macro cell corrosion rate is highly dependent of the resistivity.
- On-site corrosion rate, which is the sum of the uniform part and the macro cell part, is then likely to depend of the resistivity of concrete.
- The macro cell corrosion rate is highly dependent of the C/A ratio. In practice, C/A ratio could be limited or important. In the case of local defects or presence of cracks, the macro cell part of corrosion rate could be the most important contribution to the total corrosion rate. Without

local defects, the uniform corrosion current is suitable to be the more important part of corrosion process. During a corrosion diagnosis on a reinforced concrete structure, it is then important to take into both local and global phenomena.

- The use of CEM III concrete, which corresponds to high resistivity concrete, leads to a significant limitation in the macro cell corrosion rate on-site.

CHAPTER IV. EFFECT OF TOP-BAR CASTING ON CARBONATION-INDUCED CORROSION IN CONCRETE IN PRESENCE OF LOAD-INDUCED CRACKS

1. Introduction

This chapter aims to study the effect of top-bar casting to carbonation-induced corrosion process in presence of load-induced cracks. It deals also with the influence of time of wetness on the part of macro cell current involved in the process of corrosion.

First of all, the detailed material and method related to experiments are introduced. This leads to several results in the following and the discussion. Finally, conclusions are drawn.

2. Materials and methods

2.1. Process of specimens

The process is illustrated as following (Figure 80).

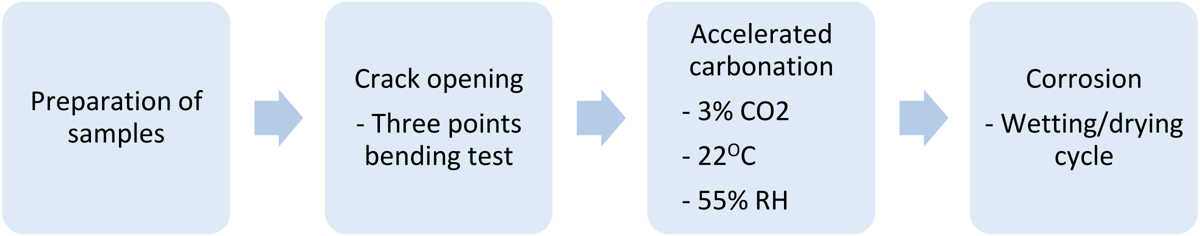

Figure 80. Process of reinforced concrete beams

Five concrete beams with dimensions of 150x150x550 mm were prepared. It corresponds to the same design as the one used by Timhadjelt [53]. Each sample contained two layers of steel bars of 6mm in diameter and 500 mm in length, including two rebars on the top and two rebars at the bottom. The concrete cover depth was 32 mm. Two control bar 100 mm in length were placed in the central including one on the left side and one on the right side of the concrete block. The main steel and control bars were firmly positioned in a special mold with four thin small and pre-perforated wooden plates (Figure 81).

Figure 81. Photo of the special mold for casting concrete beam

Two electrical wires (the red line) were welded to upper steel bar (including CH202-top, CH203-top, CH206-top, CH208-top and CH209-top) and the same connection was applied to the bottom steel bars (named CH201-bottom, CH204-bottom, CH205-bottom, CH 207-bottom and CH210-bottom) in each specimens named Ref 1, Ref 2, Ref 3, Ref 4 and Ref 5, respectively. One side of each control bar was also link to an electrical wire (the black line). The top bars and control bar were connected to a resistor calibrated for the measuring of cathodic corrosion current.

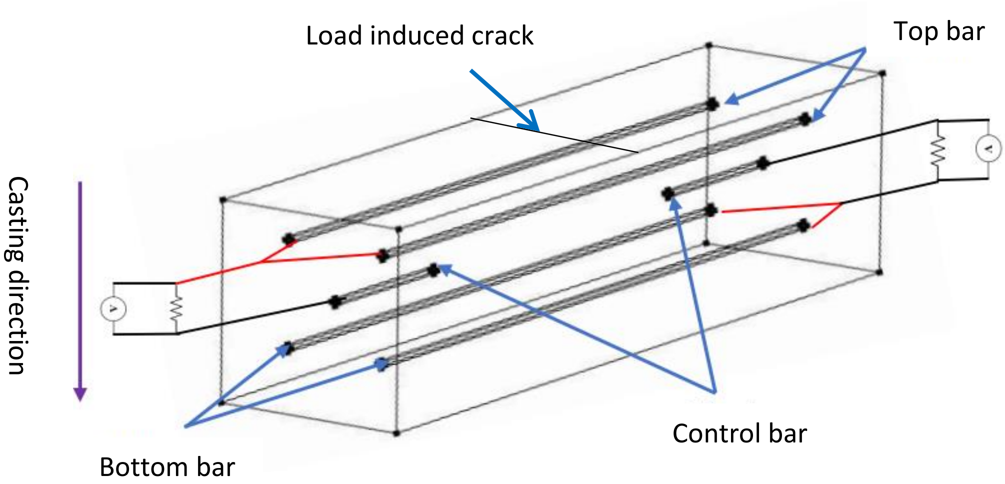

Figure 82. Description of the concrete beam

The casting direction was subjected from the top steel bar to the bottom steel bar as shown in Figure 82.

After casting and curing, the reinforced concrete blocks were subjected to crack opening by using three points bending test (Figure 83). Loading was applied in the middle of the specimens. Cracks were elaborately controlled during the test. Cracked samples were pre-conditioned before carbonation.

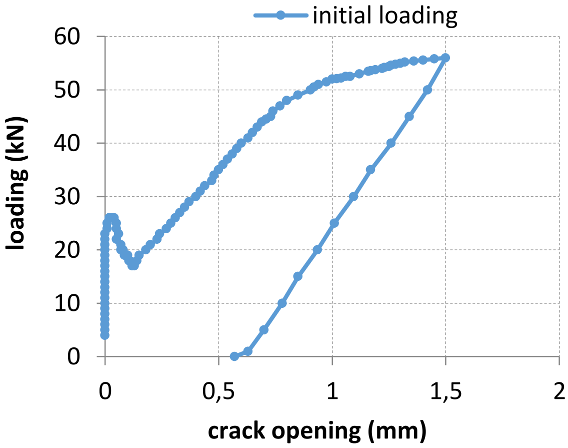

Figure 83 : cracking process in 3 points-loading

The environmental conditions for accelerated carbonation were chosen at temperature of 25^{O}C and relative humidity of 55% which was indicated to obtain the maximum carbonation rate [42, 207]. The carbon dioxide concentration was chosen by 3% which both represents the natural carbonation phenomenon and leads no significant change in the hydrates [52, 207].

After carbonation the specimens were subjected to the corrosion by wetting/drying cycles. In the experiment, five beams (named Ref 1-5) were applied including the two ones (named Ref 3 and Ref 4) were recorded corrosion current in about half a year and the three others (named Ref 1, Ref 2 and Ref 5) were carried out in more than one year (Figure 84).

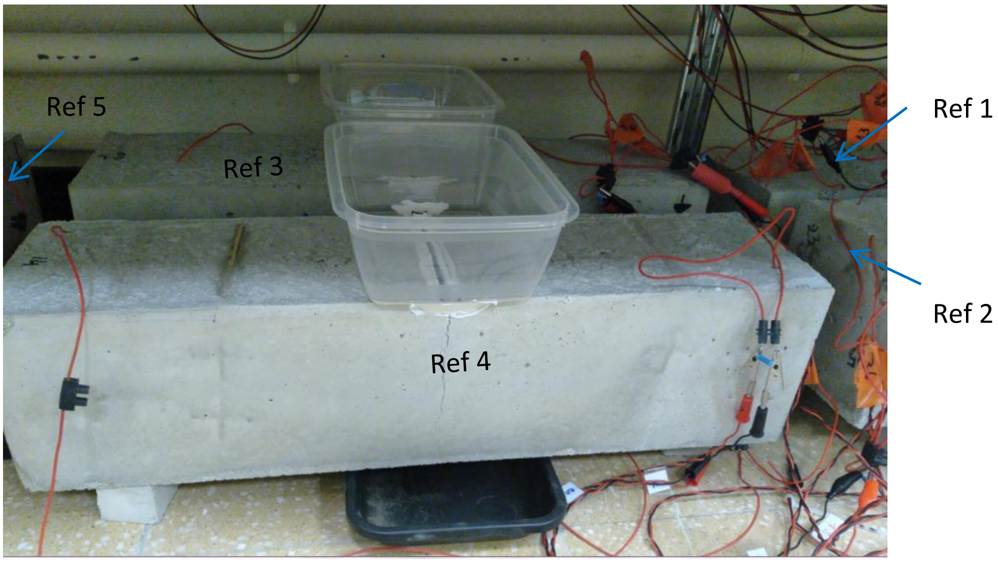

Figure 84. Figure of specimens in TP room

2.2. Material

2.2.1. Concrete

The formulation of the small beams is summarized in Table 14.

Materials	Quantity (kg/m^3)
CEM1 52.5R (Le Teil)	514
Sand (NF EN 196-1)	1543
Water	257
Water/cement	
0.5	

Table 14. Composition of mortar formulation

2.2.2. Reinforcement

Steel used in the research was steel as received without any treatment at the surface.

The description of specimens is summarized in Table 15.

Specimens	Steel bar and position	Duration of the test
Ref 1	CH201-bottom	380 days
	CH202-top	
Ref 2	CH203-top	380 days
	CH204-bottom	
Ref 3	CH205-top	160 days
	CH206-bottom	
Ref 4	CH207-top	160 days
	CH208-bottom	
Ref 5	CH209-top	380 days
	CH210-bottom	

Table 15. Summary of specimens

2.3. Methodology of corrosion analysis

The methods for examining corrosion are included visual inspection, gravimetric measurement and macro cell corrosion current monitoring.

2.3.1. Visual inspection

The object of this step is in order to determine the carbonated interface length and corrosion products length. The concrete blocks firstly were cut into smaller parts (Figure 85). Each prismatic sample contained a top or a bottom bar. Afterward the smaller specimens were split into two parts before extracting the reinforcement. Here the visual inspection was carried out to measure the length of corrosion products distribution along the steel bar. For each samples the corroded length appearing on the upper and lower part of steel bar corresponding to the casting direction was measured.

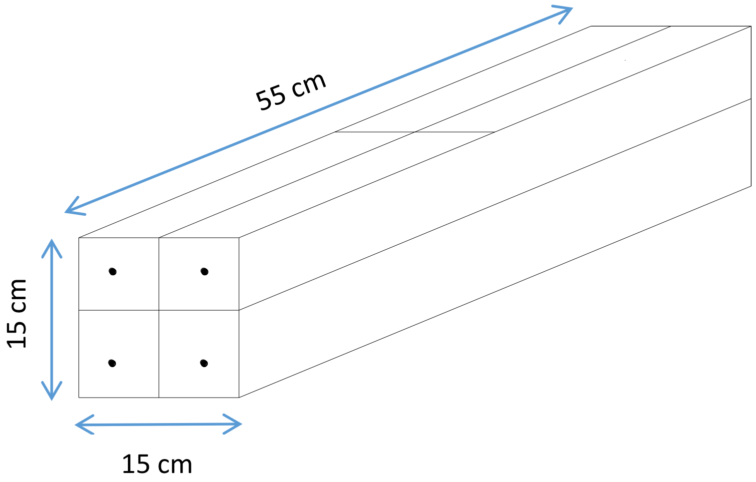

Figure 85. Illustration of position of the smaller prisms

2.3.2. Gravimetric measurement and corrosion kinetics estimation

2.3.2.1. Gravimetric measurement

After being extracted from the concrete, the reinforcements were carefully cleaned to remove the corrosion products attached to the steel. Then the loss of mass was measured. The reinforcement was weighed utilizing a balance with a precision of 0.01 g. The difference between the initial and final mass (which means the mass before and after being treated, respectively) expressed the steel mass loss (Δm). This value permits to estimate the corrosion kinetics.

2.3.2.2. Corrosion kinetics estimation

The corrosion product layer in carbonation induced corrosion is supposed to be homogenous and the thickness of the steel lost (T_{sl}) could be considered uniform along the corroded length (L_{sl}) on the surface corroded (S_{sl}). Therefore the volume of steel loss (V_{sl}) is determined (Equation 9). S_{sl} is calculated using Equation 10 knowing diameter of steel bar by 6 mm. The volume of steel loss (V_{sl}) is defined in Equation 11 using the loss of mass and density of steel by 7860 kg/m^3 (ρ_s). Then the thickness of steel loss could be obtained from the Equation 12.

$$V_{sl} = S_{sl} \times T_{sl} \;\; (m^3) \qquad \text{Equation 9}$$

$$S_{sl} = 18.85 \times L_{sl} \;\; (m^2) \qquad \text{Equation 10}$$

$$V_{sl} = \frac{\Delta m}{\rho_s} \;\; (m^3) \qquad \text{Equation 11}$$

$$T_{sl} = \frac{\Delta m}{\rho_s \times S_{sl}} \;\; (m) \qquad \text{Equation 12}$$

The kinetics of corrosion then is calculated as this following equation:

$$\text{Corrosion kinetics} = \frac{Tsl}{corrosion\ duration}\ x\ 12\ (\mu m/year) \qquad \text{Equation 13}$$

2.3.3. Corrosion current monitoring

As illustrated in Figure 82, the two top bars and a steel coupon were connected to a resistor calibrated and the voltage (V) across the resistor is read. The value of resistance (R) was known leading to calculate the current corrosion by using the Ohm's law (Equation 14):

$$I_{measured\ current} = \frac{V}{R} \qquad \text{Equation 14}$$

The resistance of the shunt is low (150 Ω) compared to the resistance of the steel coupon and do not modify the corrosion current received by the steel coupon (the result will be introduced in following section). However this value does not represent to the total macro cell corrosion current and it is necessary to modify using a ratio between the total electrical charge and the measured current (Equation 15, Equation 16).

$$_{total\ electrical\ charge} = \text{ratio} \times i_{\ measured\ current} \qquad \text{Equation 15}$$

$$\text{Ratio} = \frac{I\ total\ electrical\ charge\ (simulation)}{I\ simulation} \qquad \text{Equation 16}$$

For this, The COMSOL Multiphysics software, based on the Finite Element Method (FEM) was utilized to obtain this value. The numerical simulation was governed by the local Ohm's law (Equation 17) and electric charge conservation (Equation 18).

$$i = -\frac{1}{\rho}\nabla E \qquad \text{Equation 17}$$

$$\nabla i = 0 \qquad \text{Equation 18}$$

Where:

- E is the potential field (V)
- i is the local current density vector (A/m^2)
- ρ is the electrical resistivity (Ω.m)

The steel–concrete interface for both active and passive steel was modeled according to the Butler–Volmer kinetics with their respective parameters as presented in Equation 19 and Equation 20.

$$I_{corr,a} = i_{corr,a}\left(\exp\left(\frac{\log(10)(E_a - E_{corr,a})}{\beta_{a,a}}\right) - \exp\left(\frac{-\log(10)(E_a - E_{corr,a})}{\beta_{c,a}}\right)\right) \qquad \text{Equation 19}$$

$$I_{corr,\mathrm{p}} = i_{corr,\mathrm{p}}\left(\exp\left(\frac{\log(10)(E_p - E_{corr,\mathrm{p}})}{\beta_{a,\mathrm{p}}}\right) - \exp\left(\frac{-\log(10)(E_p - E_{corr,\mathrm{p}})}{\beta_{c,\mathrm{p}}}\right)\right) \quad \text{Equation 20}$$

Where:

- $I_{corr,a}$ and $I_{corr,p}$ (A/m^2) are the corrosion currents following through the steel concrete interface for active and passive steel, respectively.
- $i_{corr,a}$ and $i_{corr,p}$ (A/m^2) are the corrosion current density values at active steel and passive steel, respectively.
- E_a and E_p (V) are are polarization potential for both steel rebars, respectively.
- $E_{corr,a}$ and $E_{corr,p}$ (V/ref) are the corrosion potential values at active steel and passive steel, respectively.
- $\beta_{a,a}$ and $\beta_{a,\mathrm{p}}$ (V/dec) are the is the anodic Tafel slope at active steel and passive steel, respectively.
- $\beta_{\mathrm{c},a}$ and $\beta_{\mathrm{c,p}}$ (V/dec) are the is the cathodic Tafel slope at active steel and passive steel, respectively.

The loss of mass can estimated using this equation:

$$\Delta_m = \frac{C \times M_{Fe}}{2F} \quad \text{Equation 21}$$

Where:

- Δm is the loss of mass
- C is cumulative charge
- M_{Fe} is the atomic molar mass of the Fe^{2+} ion (55.844 g/mol)
- F is Faraday's constant (96500 C x mol^{-1})

C is calculated as following:

$$C = \sum_{i=0}^{i=j} I_{current} \times (t_i - t_{i-1}) \quad \text{Equation 22}$$

Where:

- t_i and t_{i-1} is time interval
- $I_{current}$ is the measured value from current monitoring (µA)

2.3.3.1. Measurement for electrical resistance

The measurement for electrical resistance is based on the method described in RILEM TC 154-EMC [226].Each specimen sliced is located between 2 stainless steel grids which are connected to the terminal of the ohmmeter Omega Ω. Wet sponge is also placed between the sliced concrete and the grids during the measurement. This is to promote electrical coupling. The ohmmeter displays the average value of electrical resistance obtained. The electrical resistance is then transformed into electrical resistivity which is calculated as follows:

$$\rho = R\, x \frac{S}{L} \qquad \text{Equation 23}$$

Where:

- ρ is the electrical resistivity of the material (Ω.m)
- R is the measured electrical resistance (Ω)
- S is the section of the sample (m2)
- L is the length of the sample (m)

2.3.3.2. Electrochemical parameters for the model

Based on the result obtained in Chapter 3, the electrochemical parameters used in the numerical simulation are presented in Table 16. The values of parameters correspond to the ones of sample B1 since it is a CEM I cement.

Corrosion parameter	Active steel	Passive steel
E_{corr} (V)	-0.5	-0.15
i_{corr} (A/m^2)	0.015	0.001
β_a(V/dec)	0.125	0.4
β_c (V/dec)	0.136	0.15
Rho (Ohm.m)	425	

Table 16. Electrochemical parameters

The resistivity was measured at the end of the study and corresponds to a value of 425 Ohm.m, which is quite high but corresponds to a relatively unsaturated specimen due to the dry environment: storage in the lab without wetting (only in the crack path). Nevertheless, a parametric study will be presented to see the effect of the resistivity on the corrosion current: between 50 Ohm.m to 500 Ohm.m.

2.3.3.3. Geometry of the model

The loaded induced crack is modeled through a virtual crack represented by the volume between two planes. It is important to model the load-induced crack to be able to have a good representation of the macro cell corrosion current in the sample. Indeed, due to the lower resistivity (or higher conductivity) of water in comparison with the concrete, the crack path (when filled by water) is a preferential path for ionic current.

As a result, a comparison is proposed between a numerical model with or without crack.

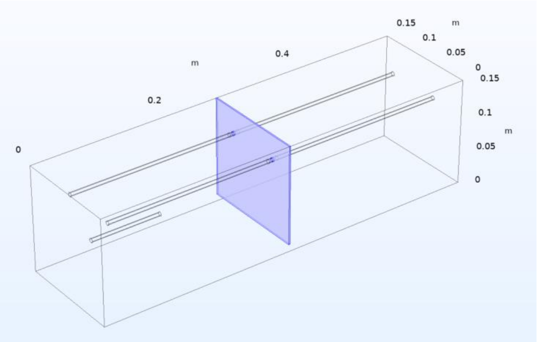

Figure 86 : numerical model with crack filled by water

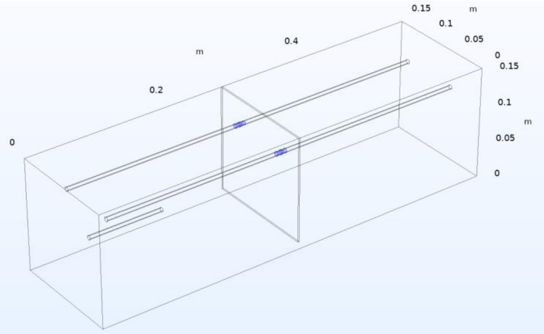

Figure 87 : numerical model without crack

Figure 86 shows the model with a crack which is simulated by two parallel planes. Figure 87 shows the model without crack.

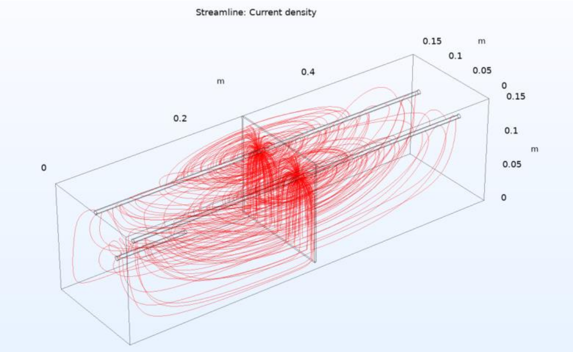

Figure 88 : numerical model with crack filled by water

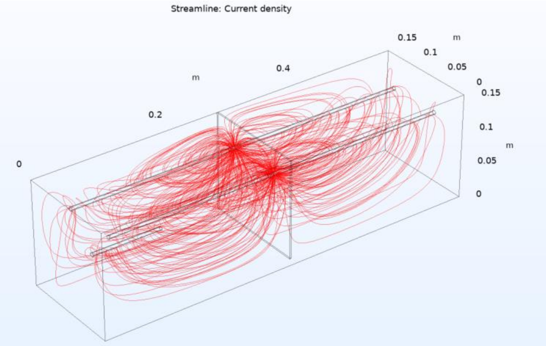

Figure 89 : numerical model without crack

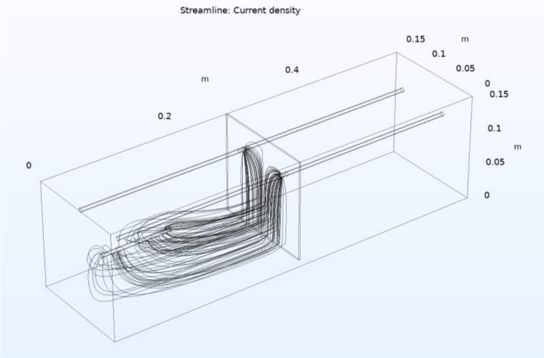

Figure 90 : numerical model with crack filled by water

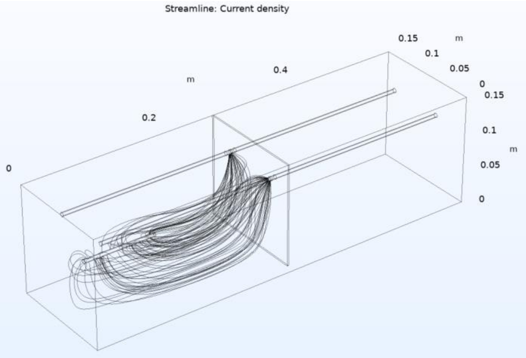

Figure 91 : numerical model without crack

In the presence of crack filled by water, there is a preferential path for ionic current which could distribute more easily in the concrete volume as show in Figure 88, Figure 89, Figure 90 and Figure 91.

3. Results and discussion

3.1. Visual inspection

3.1.1. Measuring the carbonation at steel concrete interface

Phenolphthalein pH indicator test was used to determine the carbonated length. After the carbonated sample was split into two parts, it was sprayed on the concrete surface with a solution of phenolphthalein. The change of color on the surface indicated the level of carbonation. In carbonated zone (pH<9-10) the color is observed colorless while in non-carbonated zone (pH>9-10) the color becomes purple.

3.1.2. Top bar effect

These following figures exhibit the photographs of the tested interface after spraying phenolphthalein solution and measuring the carbonated length. Each specimen included two tops and two bottom bars and their names were completed by number 1 or 2, to separate the steel bar in the visual inspections as well as gravimetric measurement.

Concrete beam Ref1:

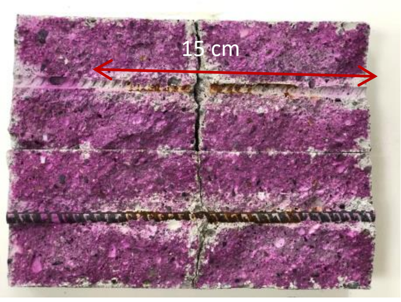

Figure 92. Carbonation of sample CH202-top-1

Carbonated length of the upper part is 15 cm.

Corrosion length is 9.5 cm

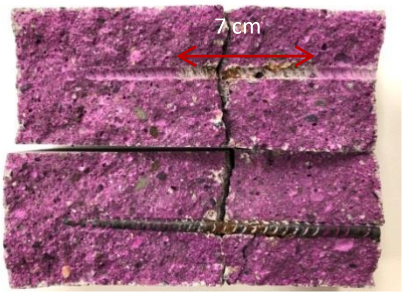

Figure 93. Carbonation of sample CH201-bottom-1

Carbonated length of the upper part is 7 cm.

Corrosion length is 5 cm

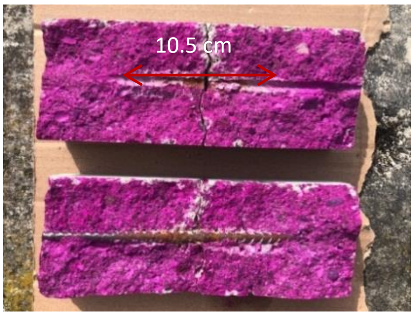

Figure 94. Carbonation of sample CH202-top-2

Carbonated length of the upper part is 10.5 cm.

Corrosion length is 10 cm

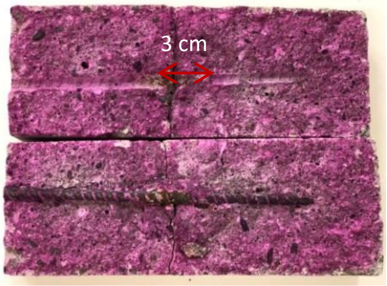

Figure 95. Carbonation of sample CH201-bottom-2

Carbonation of the upper part is 3 cm.

Corrosion length is 2.5 cm

Concrete beam Ref2:

Figure 96. Sample CH203-top-1 after being split

Carbonated length of the upper part is 8 cm.

Corrosion length is 7 cm

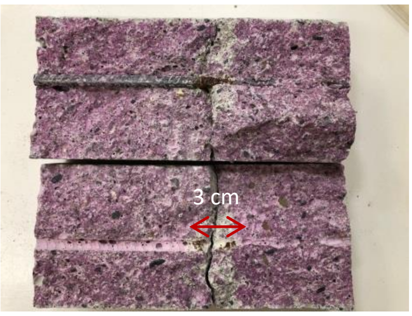

Figure 97. Carbonation of sample CH204-bottom-1

Carbonated of the lower part is 3 cm.

Corrosion length is 2.5 cm

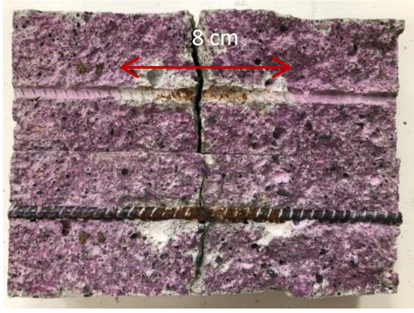

Figure 98. Carbonation of sample CH203-top- 2

Carbonated length of the upper part is 8 cm.

Corrosion length is 7 cm

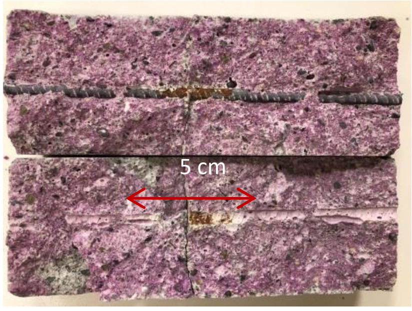

Figure 99. Carbonation of sample CH204-bottom-2

Carbonated part of the lower part is 5 cm.

Corrosion length is 3.5 cm

Concrete beam Ref 3:

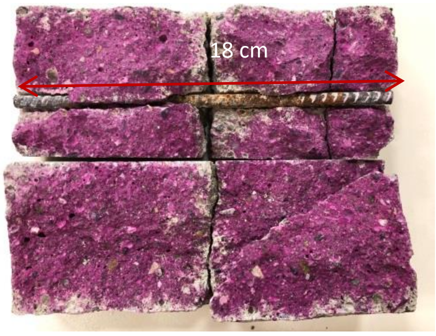

Figure 100. Carbonation of sample CH206- top-1

Carbonated length of the lower part is 18cm.

Corrosion length is 15.5 cm.

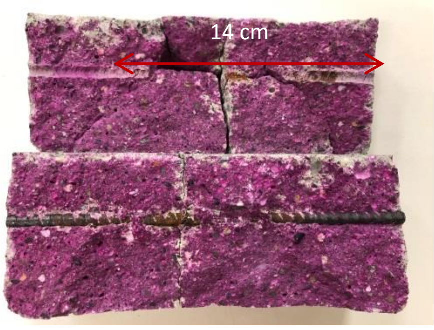

Figure 101. Carbonation of sample CH205- bottom-1

Carbonated length of the upper part is 14cm.

Corrosion length is 11.5 cm.

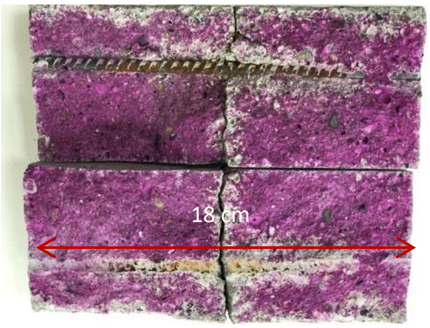

Figure 102. Carbonation of sample CH206- top-2

Carbonated length of the lower part is 18cm.

Corrosion length is 11.5 cm.

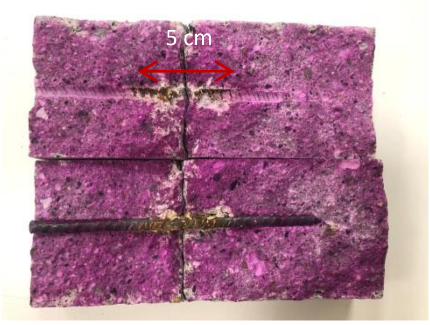

Figure 103. Carbonation of sample CH205- bottom- 2

Carbonated length of the upper part is 5 cm.

Corrosion length is 5 cm.

Concrete beam Ref 4:

Figure 104. Carbonation of sample CH208- top- 2

Carbonated length of the upper part is 7 cm.

Corrosion length is 10 cm.

Figure 105. Carbonation of sample CH207- bottom- 1

Carbonated length of the upper part is 3 cm.

Corrosion length is 3 cm.

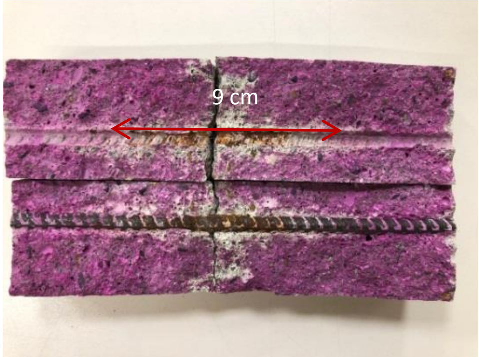

Figure 106. Carbonation of sample CH208- top- 1

Carbonated length of the upper part is 9 cm.

Corrosion length is 9 cm.

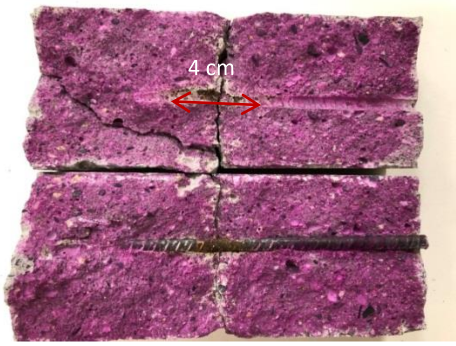

Figure 107. Carbonation of sample CH207- bottom- 2

Carbonated length of the lower part is 4 cm.

Corrosion length is 4 cm.

Concrete beam Ref 5:

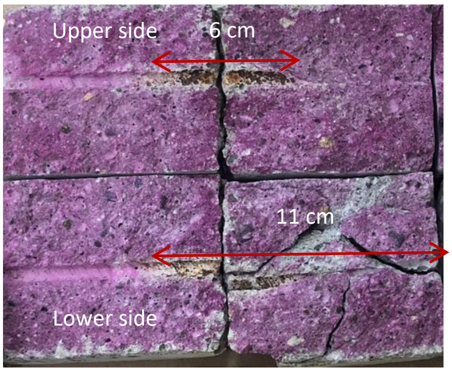

Figure 108. Carbonation of sample CH209- top- 2

Carbonated length of the upper part is 6 cm.

Carbonated length of the lower part is 11 cm.

Corrosion length is 7 cm.

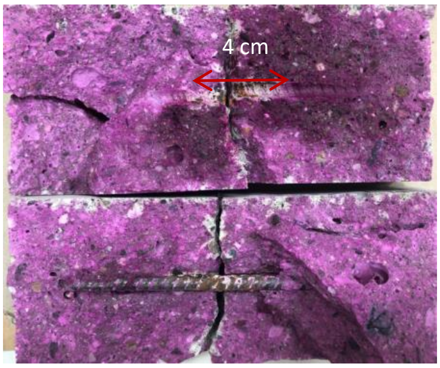

Figure 109. Carbonation of sample CH10- bottom- 2

Carbonated of the upper part is 4 cm.

Corrosion length is 4 cm.

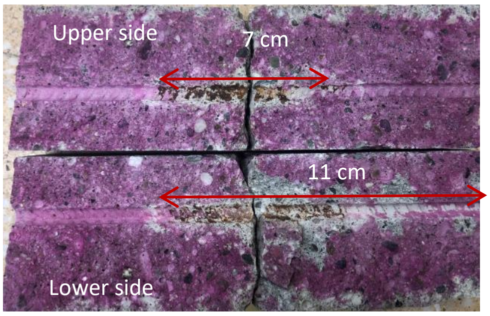

Figure 110. Carbonation of sample CH209- top- 1

Carbonated length of the upper part is 7 cm.

Carbonated length of the lower part is 11 cm.

Corrosion length is 7 cm.

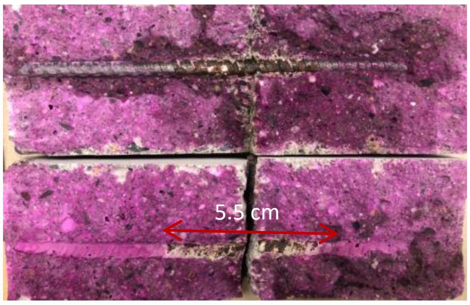

Figure 111. Carbonation of sample CH210- bottom- 1

Carbonated of the lower part is 5.5 cm.

Corrosion length is 5.5 cm.

The length of carbonation and corrosion are presented in these following charts (Figure 112 and Figure 113).

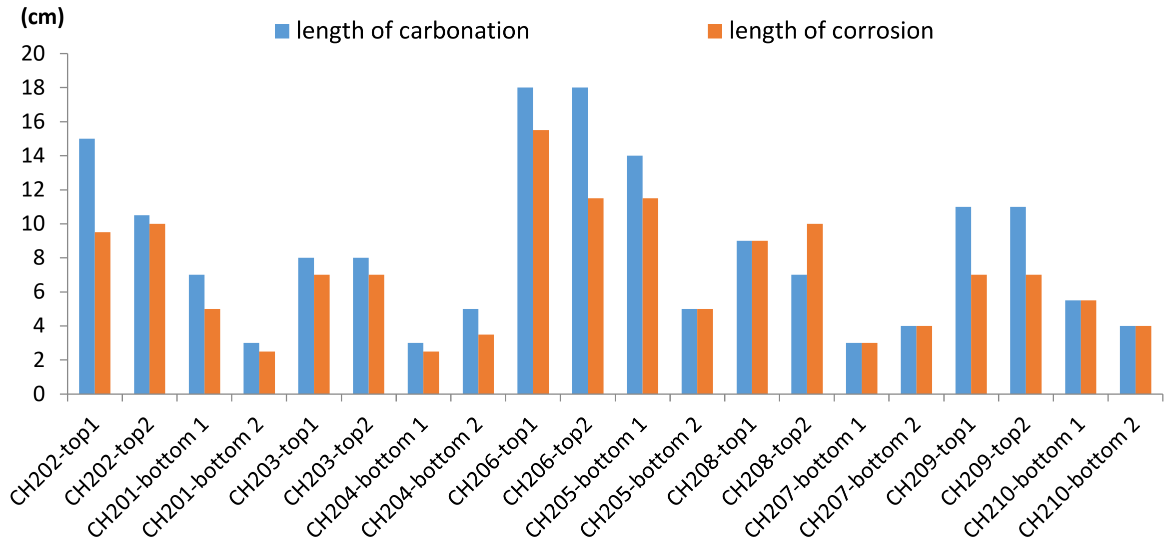

Figure 112. Carbonation and corrosion length in the steel bars

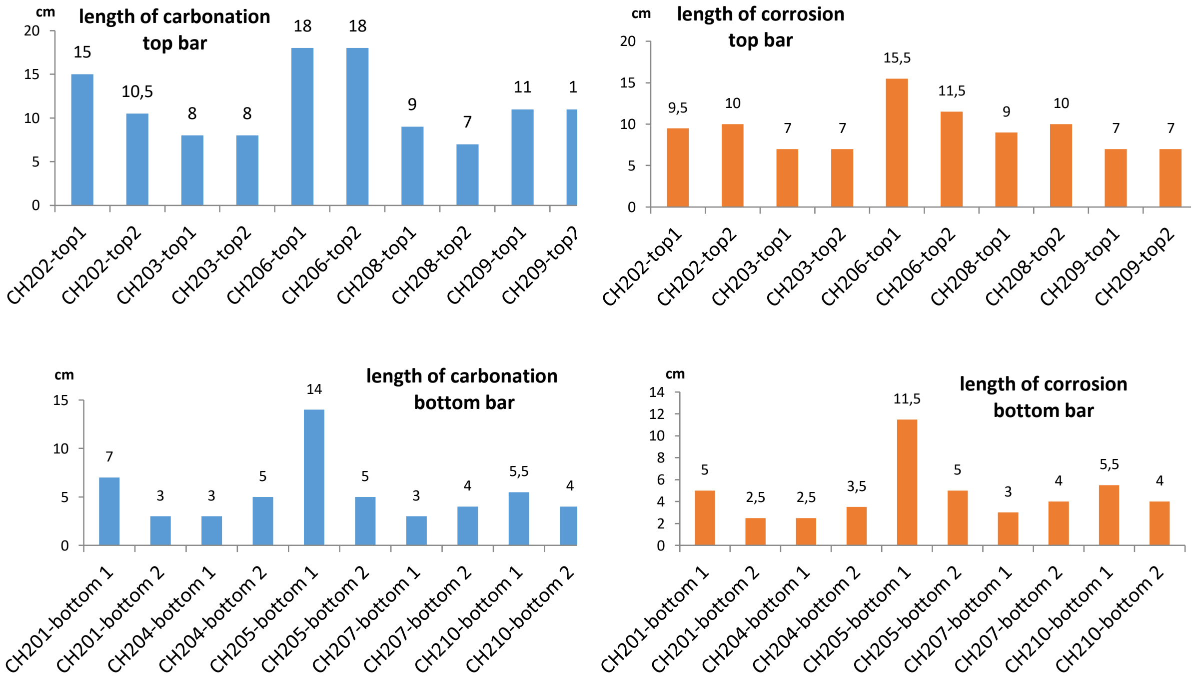

Figure 113. Length of carbonation and corrosion in the case of top bar and bottom bar

These figures show that the length of carbonation measured in the top bar is general much higher than the carbonated length in the bottom bar with all the concrete beams. This is suggested that more carbon dioxide spread along the top bars than along the bottom bars. The same observation was also found in other researches [2, 53]. In addition, if we take a look at the upper and lower side of one reinforcement, it was found a higher carbonation length along the lower side than along the upper side, for example the case ref 5 (Figure 114). During the three points bending test, the width of crack on the upper side was bigger than on the lower side or in the other words there was more mechanical damage on the upper surface than on the lower surface. Nevertheless, the carbonated length was recorded longer in the bottom side than in the top side. This is due to the top bar effect. The reason is that the settlement and water bleeding caused to the presence of defects and voids in the lower of steel bar which facilitate the propagation of carbon dioxide. Also is a difference in porosity at the steel concrete interface between top and bottom part of the bar [41].

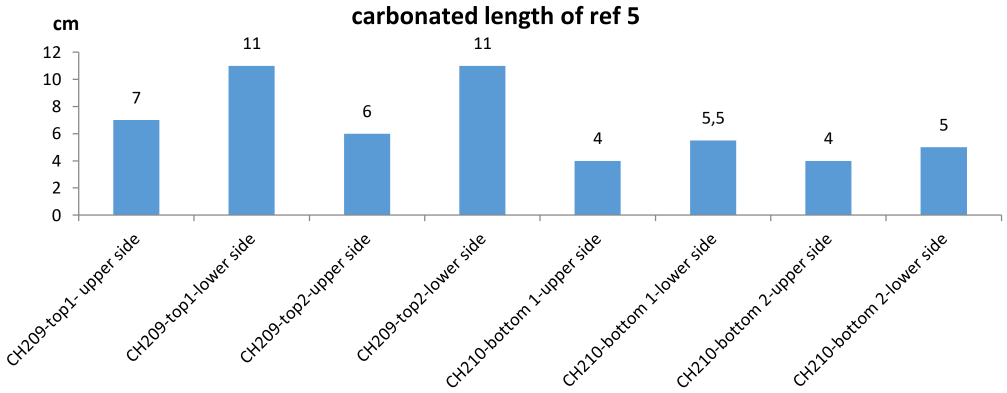

Figure 114. Carbonated side length of ref 5

It is also noted that in the three points bending test, the width of mechanical crack was greater with the upper steel bars than with the lower steel bars, which results a more significant mechanical damage in the steel concrete interface of the upper rebar than in the surface of the lower rebar. In addition, the concrete beams were in the same condition of preparing as well as experiments process. Indeed, the widths of crack obtained are in the range from 500 to 570µm. This should have leaded to a similar carbonation length with the group of top bars and group of bottom bar. However, it is not the case. For example the carbonated length on the lower side of upper reinforcements in Ref 3 (Figure 100, Figure 102) was found about 1.5 times higher in compare to the lower side of upper steel bars in ref 5 (Figure 108, Figure 110). This means that the steel concrete interface is more likely to play an essential role in this case. A higher quality of surface corresponds to a lower of carbonated length. Indeed, if we observe the samples containing longer carbonation track, for example ref 1 (Figure 92) and ref 3 (Figure 102) it can be seen a high density of void defects in the location of carbonated concrete.

When recording the presence of corrosion products, the corrosion length of upper steel bar was found always higher than the value of lower rebar. With bottom bar, the corrosion length is from 1.5 cm to 5.5 cm except a steel bar in concrete ref 3 (Figure 101) with a higher value (11.5cm). Corrosion existed in the location of carbonated concrete. Nevertheless, corrosion was also found even when the concrete had not completely carbonated in ref 4 (Figure 104).

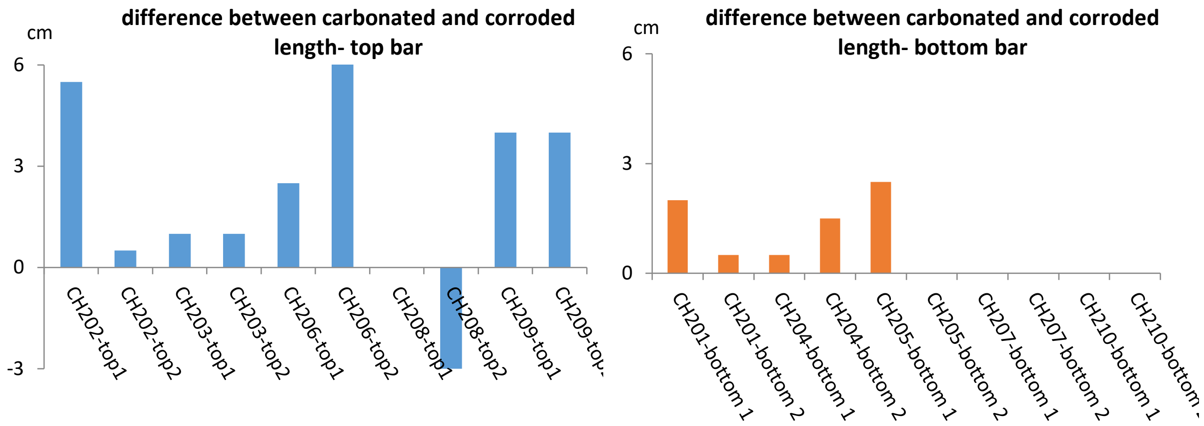

Figure 115. Difference between carbonated length and corroded length

It is worth noting that there is an important difference in carbonated length between top and bottom bars as seen on ref 3 sample (Figure 116 and Figure 117). But it is also interesting to notice than in the case of top bar there is also a penetration of carbonation front perpendicularly to the bar direction (Figure 116). This result is significant of a more porous concrete and also an easier access to CO_2 along the steel concrete interface.

Figure 116 : Carbonation along top bar for ref 3 sample

Figure 117 : Carbonation along bottom bar of ref 3 sample

3.2. Gravimetric measurement

At the end of the experiments, the loss of mass of steel bars was determined from gravimetric measurement.

- In the case of samples with measurement duration of 160 days:

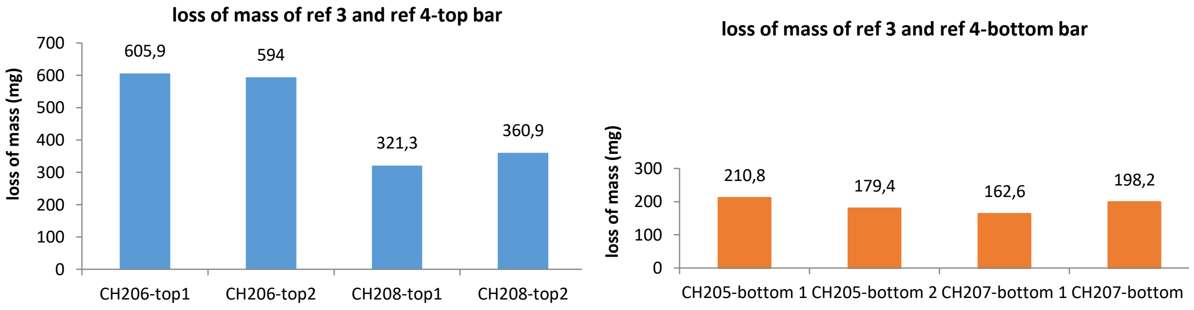

Figure 118. The loss of mass of ref 3 and ref 4

- In the case of samples measurement duration of 380 days:

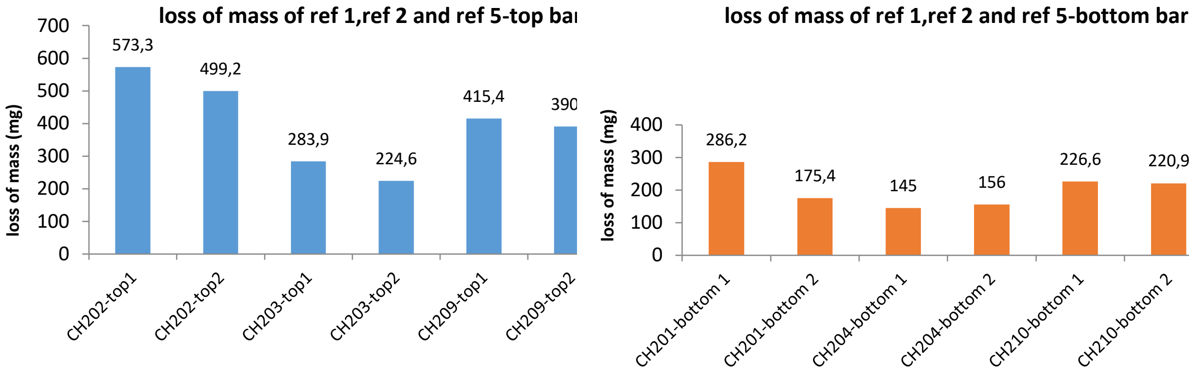

Figure 119. The loss of mass of ref 1, ref 2 and ref 5

From Figure 118 and Figure 119, it appears that the loss of mass measured by gravimetric are not very different according to the duration of the experiments (160 or 380 days). In fact, the difference between the loss of mass of 2 samples, ref 3 and ref 4 is around twice for duration of 160 days, and the difference between ref 1 and ref 2 is also around twice for duration of 380 days. On the contrary, there is almost no difference between ref 1 and ref 3 in loss of mass, despite duration, respectively, of 380 and 160 days. As a result, the scatter between 2 samples could be comparable to the effect of a double duration of aging. On one way, it confirms that corrosion has a part of stochastic process, and on other way, it would be difficult to draw conclusions by comparing the behavior of all samples.

3.3. Corrosion current monitoring

The numerical simulation is used, firstly, to validate the use of the value of the shunt resistance to measure the macro cell current. Then secondly, the numerical simulation will be used to calculate the ratio between the macro cell current measured by the steel coupon versus the total macro cell corrosion current. Finally, the effect of drying of the path crack will be also studied numerically.

3.3.1. Numerical simulation to validate the use of the shunt resistance for the measurement of the cathodic corrosion current of the steel coupon

To validate the use of the shunt resistance, a parametric study is done. Firstly, with different values of length of anode site on both rebar, where the different length included 13.2mm, 26.5mm, 53mm, 106mm, 160mm and 212mm. Secondly, different resistivities of concrete are tested since the resistivity is an aging characteristic.

The concrete resistivity was measured at the beginning and at the end of the test.

At the beginning of the test, the resistivity is around 150 Ω.m and increase according to the aging of the specimen due to the exposition in dry condition. At the end of the test, because of the environmental condition, i.e. exposure in the lab without any wetting, the resistivity of concrete is high > 400 Ω.m.

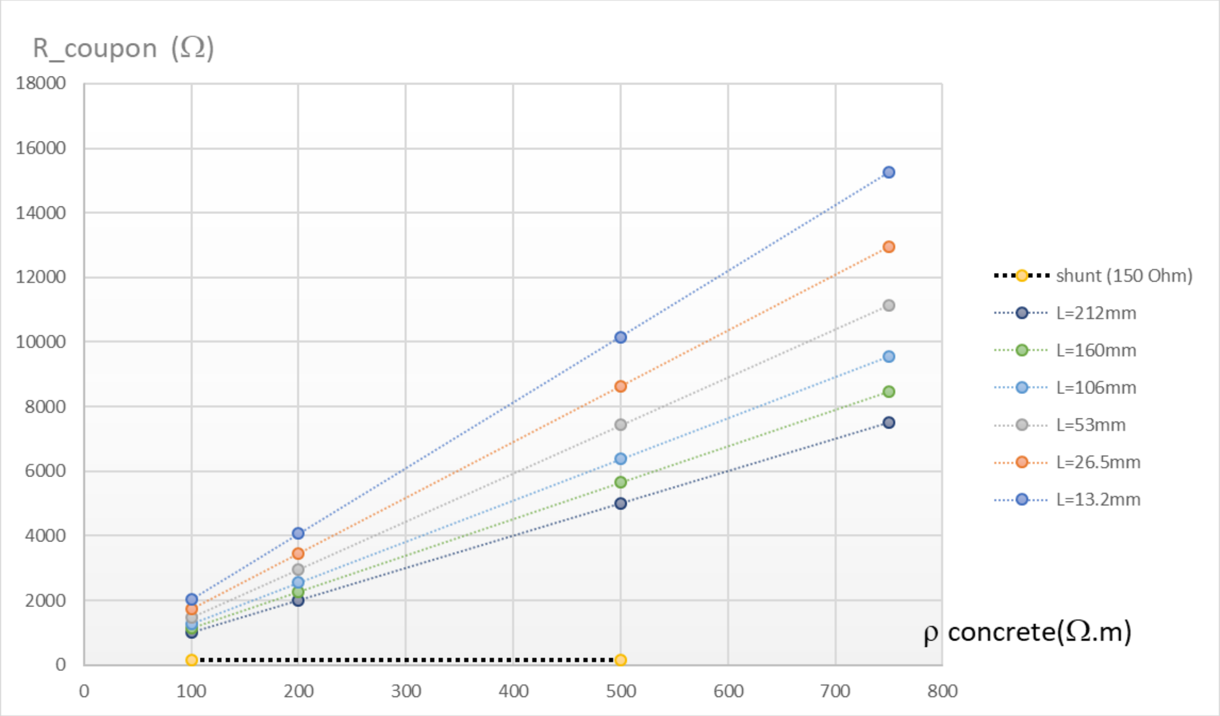

Figure 120. Evolution of the electrical resistance of the metallic coupon in relation to the concrete resistivity and for 6 different lengths of the anodic site.

The electrical resistance of the metallic coupon is increasing linearly with the concrete resistivity. The electrical resistance of the metallic coupon decreases when the anodic site length increase (Figure 120). On the contrary and obviously, the electrical resistance of the shunt is constant (150 Ω).

For a low concrete resistivity, the ratio between the steel coupon resistance and the shunt resistance is higher than 10 for a length of anodic site below 50 mm. With the increase in resistivity with time, the ratio increase. As a result, even for a length of anodic site of 212 mm, the ratio between the coupon resistance and the shunt resistance is higher than 28 for a concrete resistivity of 425 Ohm.m (Figure 121).

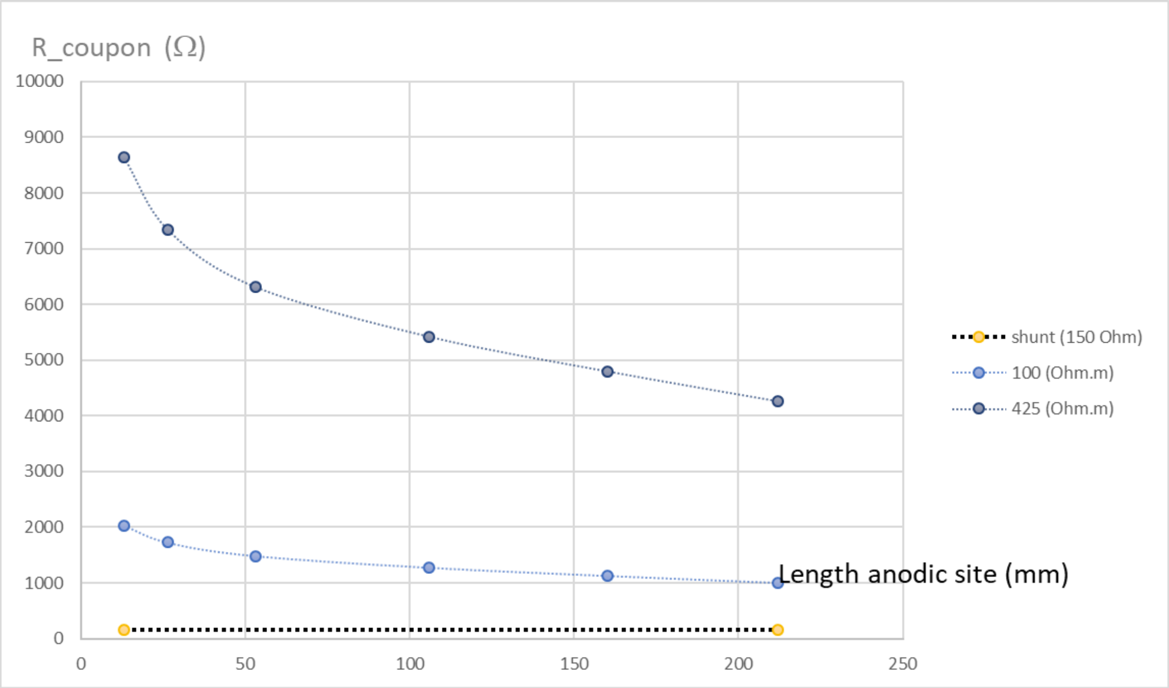

Figure 121: Evolution of the electrical resistance of the metallic coupon in relation to the length of the anodic site

It appears that the resistance of the shunt used to measure the cathodic current between the metallic coupon and the anodic site, is always neglectable according to the electrical resistance of the metallic coupon. It is always at least below 10 %, even at the beginning of the test.

As a result, the part of macro cell measured by the metallic coupon is not affected by the value of shunt resistance used in the experimental protocol.

3.3.2. Numerical simulation to calculate the ratio between the parts of macro cell cathodic current measure by the steel coupon over the total macro cell current

The effect of the presence of the crack or not in the modeling is studied. The length of the anodic site is also studied since it changes the value of C/A ratio.

3.3.2.1. Comparison between corrosion current with or without the presence of the crack in the model

The comparison between the corrosion current in case of the presence or not of the crack path is studied for only one anodic site length: 13.2 mm.

For an anodic length of 13.2 mm, the corrosion current for a concrete resistivity of 425 Ohm.m is 65 % higher in the case of the presence of crack than without crack: 83 µA vs 47 µA. Because of the preferential path for ionic current in case of the presence of a crack filled by water, there is an increase in the corrosion current for a given size of the anodic length (Figure 122). Because of this important difference between sound concrete and cracked concrete, it is decided for the following modeling to take into account the crack path, which is supposed fill by water. The effect of drying will be studied later.

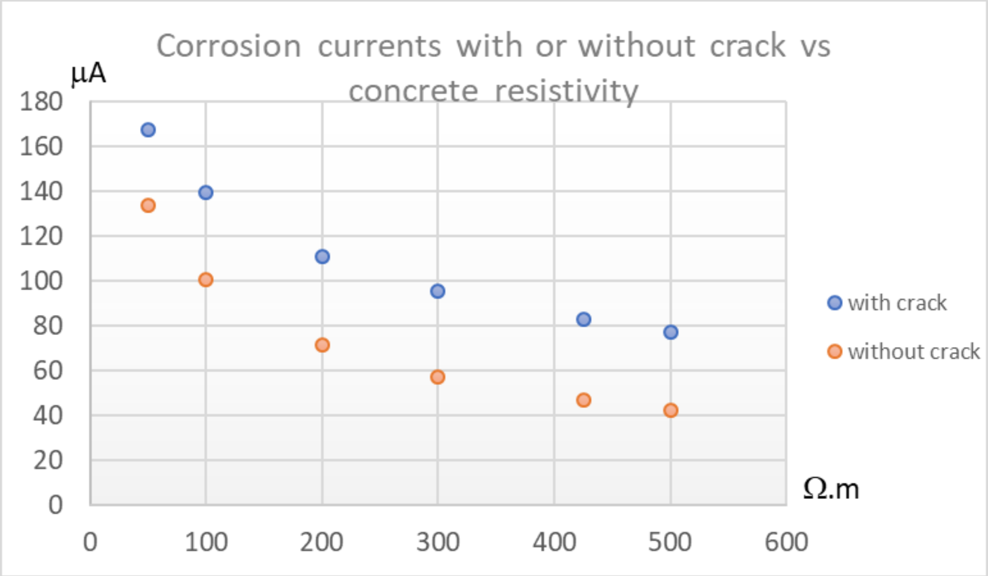

Figure 122 : Difference in corrosion current between the model with or without crack filled by water for an anodic length of 13.2 mm

3.3.2.2. Influence of the length of the anodic sites on the corrosion current and the ratio between the total corrosion current and the cathodic part of current measured of the steel coupon

The size of the anodic site depends of the location of the rebar: top or bottom part of the concrete sample according to the casting direction.

Experimental results show a large set of values for the size of the anodic site. To be able to calculate the total corrosion current based of on the measurement of the cathodic current on the steel coupon, it is necessary to study the effect of the size of anodic length of the corrosion current and on the ratio between total corrosion current and cathodic part of current measured of the steel coupon.

Different sizes of the anodic site are studied: 13.2 mm; 26.5 mm, 53 mm; 106 mm, 160 mm, 212 mm and 477 mm.

- Effect of resistivity on the corrosion current and the ratio k between the total corrosion current over the cathodic current measured by the steel coupon.

Concrete resistivity has a huge impact of the macro-cell corrosion current. This is not a linear variation because of the non-linearity of electrochemical response. Figure 123 and Figure 124 show, respectively, the decrease in total macro cell corrosion current or in cathodic current recorded by the metallic coupon in relation to the increase in concrete resistivity.

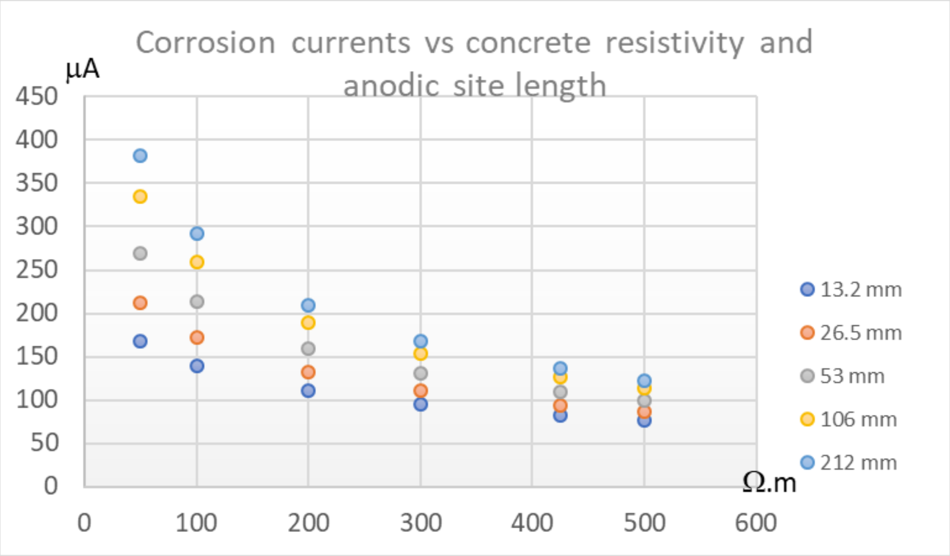

Figure 123 : Evolution of the total corrosion current in relation to the resistivity of concrete

It is interesting to notice that the value predicted by the numerical model for the cathodic current measured by the steel coupon (Figure 124): about 5 µA for a resistivity of 425 Ohm.m is quite comparable with the peak value of the sample "CH205" (Figure 125), which means that the model, without any fitting coefficient, is able to catch the macro-cell corrosion behavior of carbonated samples when the crack path is filled by water.

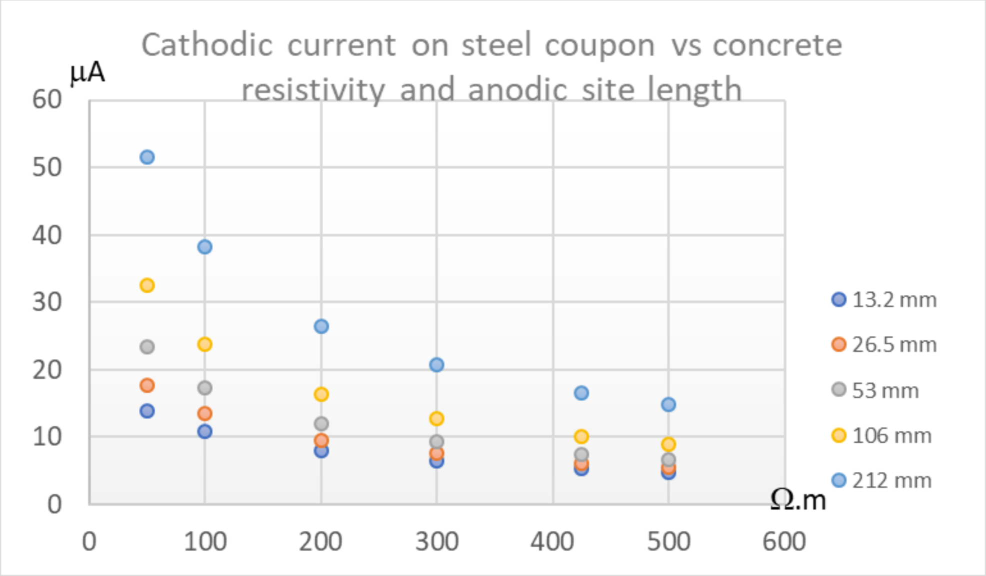

Figure 124 : Evolution of the cathodic current measured by the steel coupon in relation to the concrete resistivity

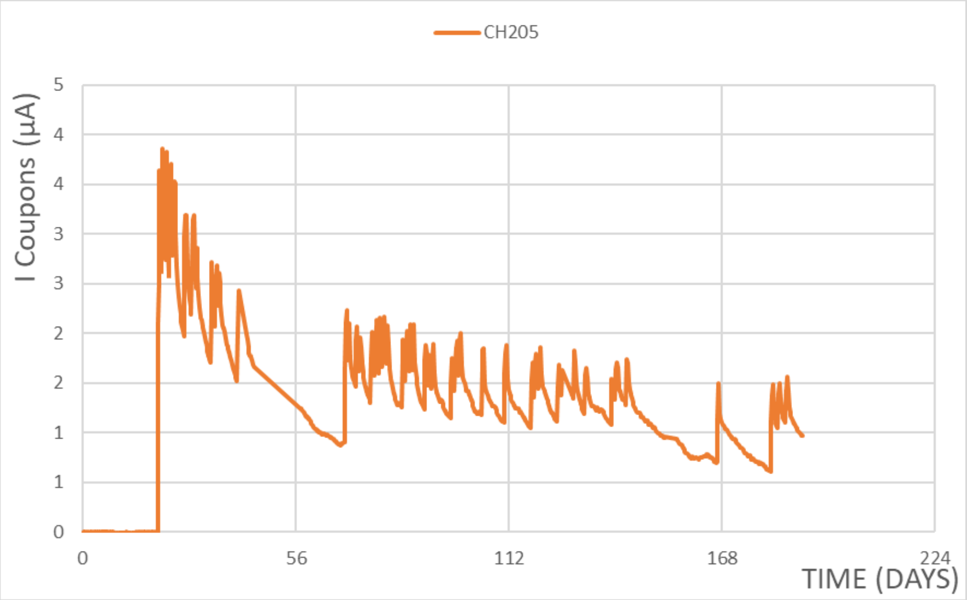

Figure 125 : Experimental cathodic current variation versus time for sample (CH205)

It is possible to calculate the ratio k between the total macro-cell corrosion current over the cathodic part measured by the steel coupon. It appears clearly on Figure 126 that the k coefficient is impacted by the resistivity and increases when resistivity increased.

For the resistivity measured at the end of the testing, the k coefficient appears to be closed to 15 for the lower length of anodic site. When the length of anodic site increase, the k ratio decreases to reach a value of 8.

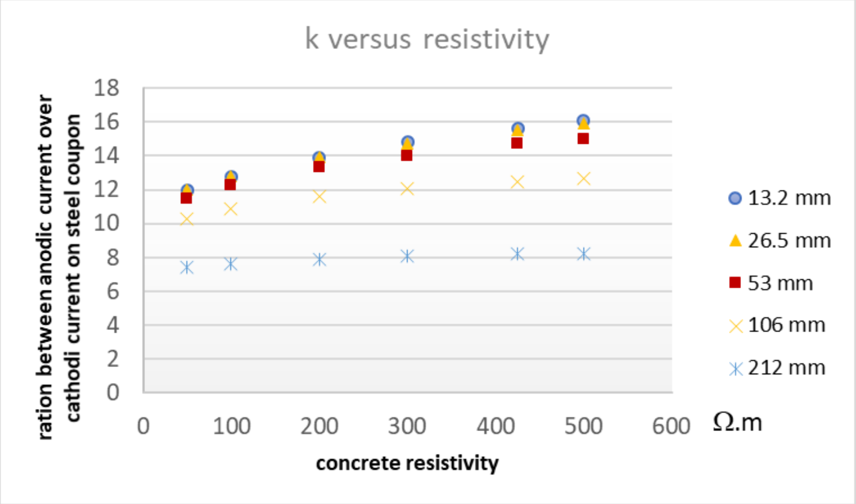

Figure 126 : evolution of the ratio k between total macro-cell current and cathodic part measured by the steel coupon in relation to resistivity for different anodic size

- Effect of anodic size length on the corrosion current and the ratio k between the total corrosion current over the cathodic current measured by the steel coupon.

The size of the anodic length has an influence of the k ratio between the total macro-cell current over the cathodic part measured by the steel coupon, since it changes the ratio C/A (Cathode/Anode).

Figure 127 shows the evolution of k coefficient according to the length of anodic site. The k ratio decreases when anodic sites size increase because of the reduction of the C/A ratio. It is quite interesting to notice that there is no effect of the presence of a crack or not in the k evolution.

The k evolution versus the anodic site length is quite important and the change in k coefficient will be taken into account to predict the total corrosion current for the different samples tested: bottom or top bars.

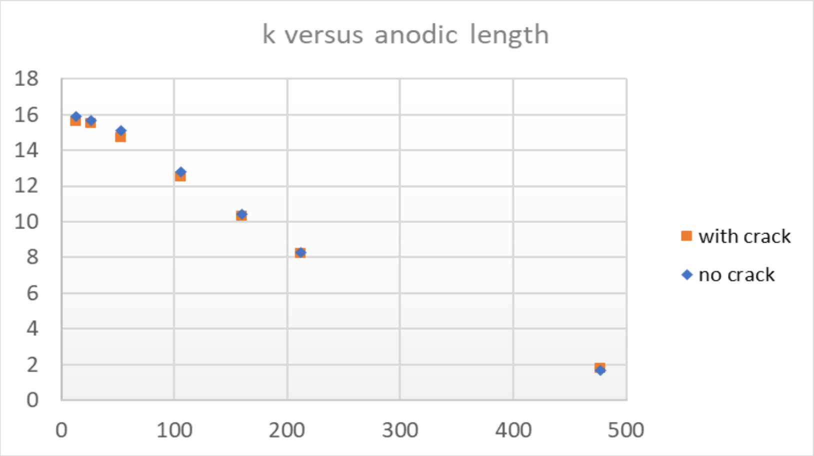

Figure 127 : evolution of k ratio in relation to the anodic length

As a result, the experimental macro cell corrosion current will be calculated with the following k ratio which is extrapolated from Figure 127 as in following Table 17:

Steel bar	Anodic length (cm)	k ratio
CH202- top-1	9.5	12.8
CH202- top-2	10	12.7
CH201-bottom-1	5	14.8
CH201- bottom-2	2.5	15.5
CH203- top-1	7	14
CH203-top-2	7	14
CH204-bottom-1	2.5	15.5
CH204- bottom-2	3.5	15.3
CH206- top-1	15.5	10.5
CH206- top-2	11.5	12.2
CH205- bottom-1	11.5	12.2
CH205-bottom-2	5	14.8
CH208- top- 1	9	13.3
CH208- top- 2	10	12.7
CH207- bottom- 1	3	15.4
CH207- bottom- 2	4	15.3
CH209- top- 1	7	14
CH209- top- 2	7	14
CH210- bottom- 1	5.5	14.7
CH210- bottom- 2	4	15.3

Table 17. K coefficient of steel bar

3.3.2.3. Macro-cell current during the drying of the load-induced crack

During the measurement of the cathodic current on the steel coupon, it appears that a peak value is followed by a decrease with time, and then a new peak appears for the following wetting to the crack path as shown on Figure 125 and Figure 130.

An example of zoom around on peak is also proposed in Figure 128 : it appears clearly that after wetting there is an instantaneous increase in macro cell current, then follow by a kind of plateau, then a very progressive decrease which could be attributed to the drying process in the crack path. It is worth noting that the plateau is longer in case of bottom bar where the crack path is smaller than the drying process would take more time. A similar observation could be found in [227] and authors propose that the current decay could followed an exponential behavior. The curved was fitted (Figure 129) by applying this equation proposed in [227]:

$$I=I_0 \times e^{-at} \qquad \text{Equation 24}$$

Where:

- I_0: the peak macro-cell current
- a: constant (0.012 for 40% RH and 0.006 for 75% RH)

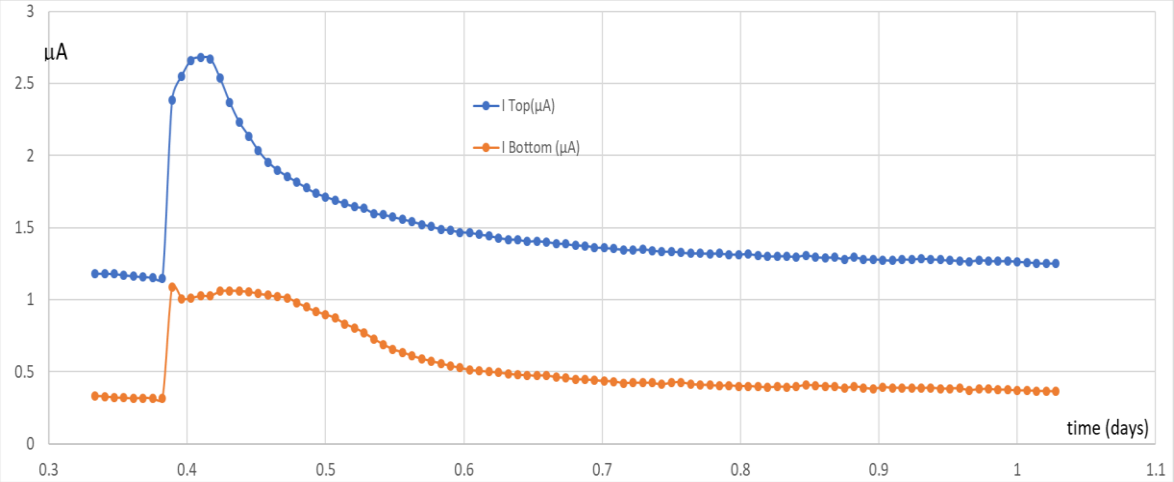

Figure 128 : Macro cell current around a peak for both top and bottom bars on less than 1 day

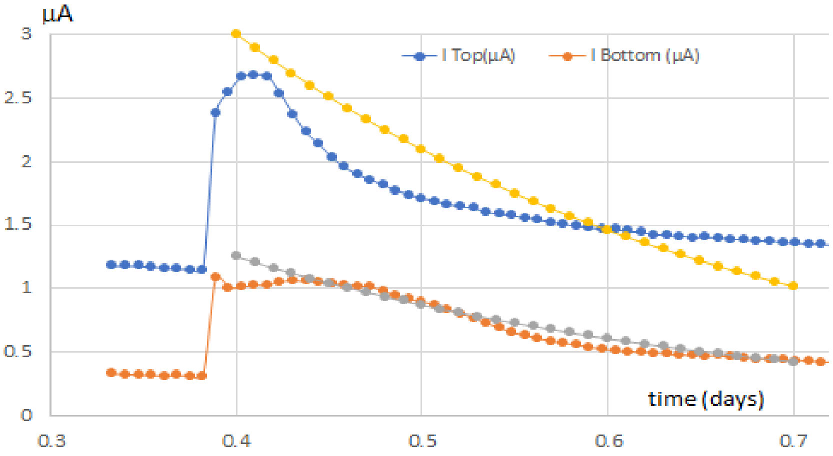

Figure 129. Fitting the curve of current

To have a better understanding of this phenomenon, a modeling of the desaturation of the crack path, after wetting, in relation to time is proposed.

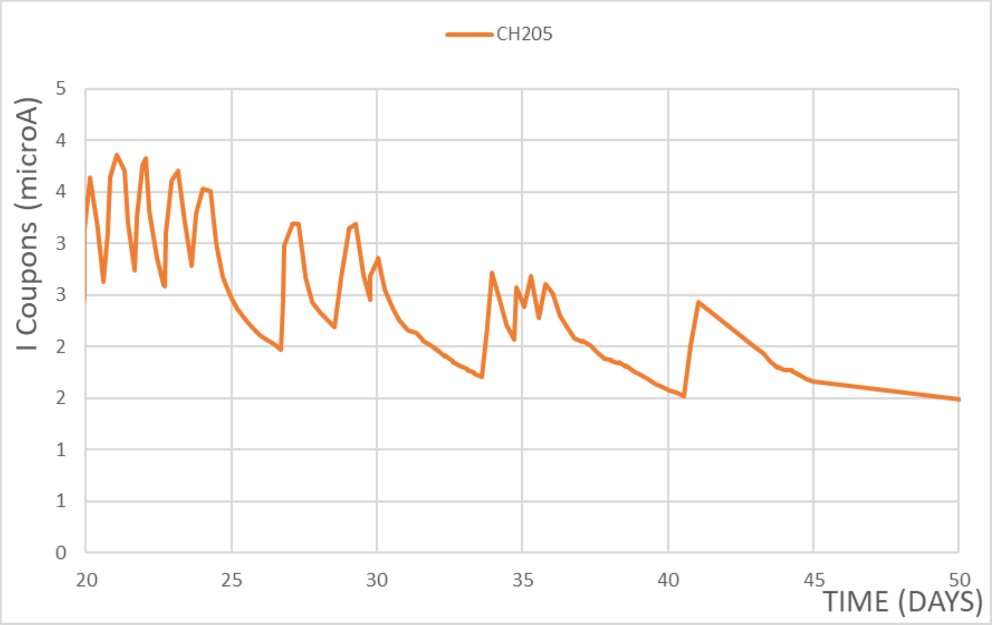

Figure 130 : Evolution of the cathodic current measured by the coupon as a function of time: each wetting corresponds to peak value.

The numerical calculation of the effect of drying in crack path is only done for one layer of rebar since there is no difference for the modeling approach between top and bottom bars: the crack path is modeled by two parallel surfaces.

We consider that the desaturation of the crack is less pronounced at the vicinity of the steel bar due to the fact that the crack path is change closed to the rebar. Indeed, as shown by x-Ray tomography in [3] the main crack is divided in a set of smaller cracks closed to the rebar (branching due to the presence of ribs on the rebar). As a result, the desaturation of smaller cracks is delayed in comparison with a large crack.

The model consists than to reduce the size of the crack filled by water in the vicinity of crack as shown in Figure 131.

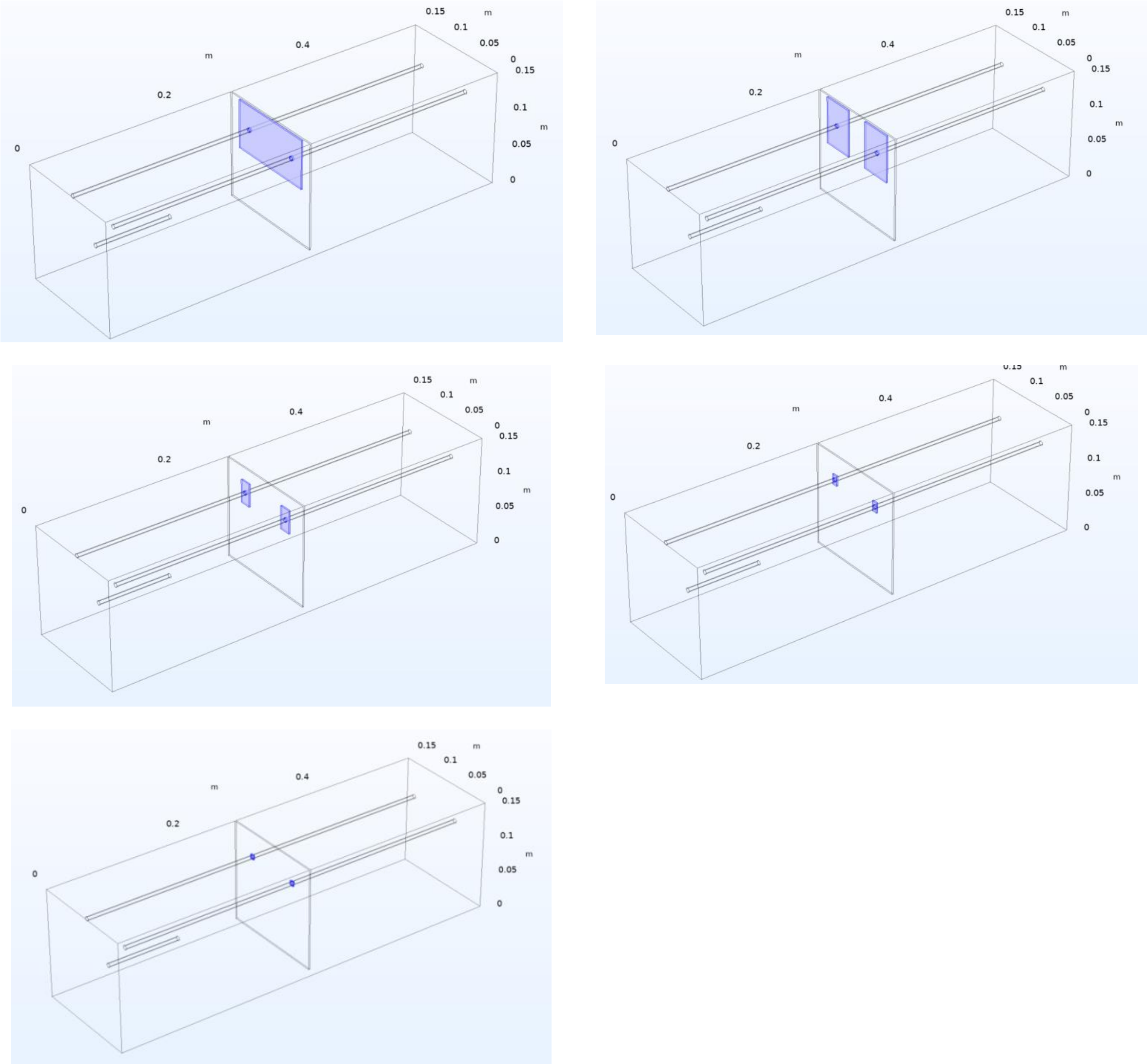

Figure 131 : progressive drying of the crack versus time

The reduction of the size of the crack surface filled with water reduced the availability of spreading ionic current in the sample as shown in Figure 132 for the total corrosion current, or in Figure 133 for the cathodic current measured by the steel coupon.

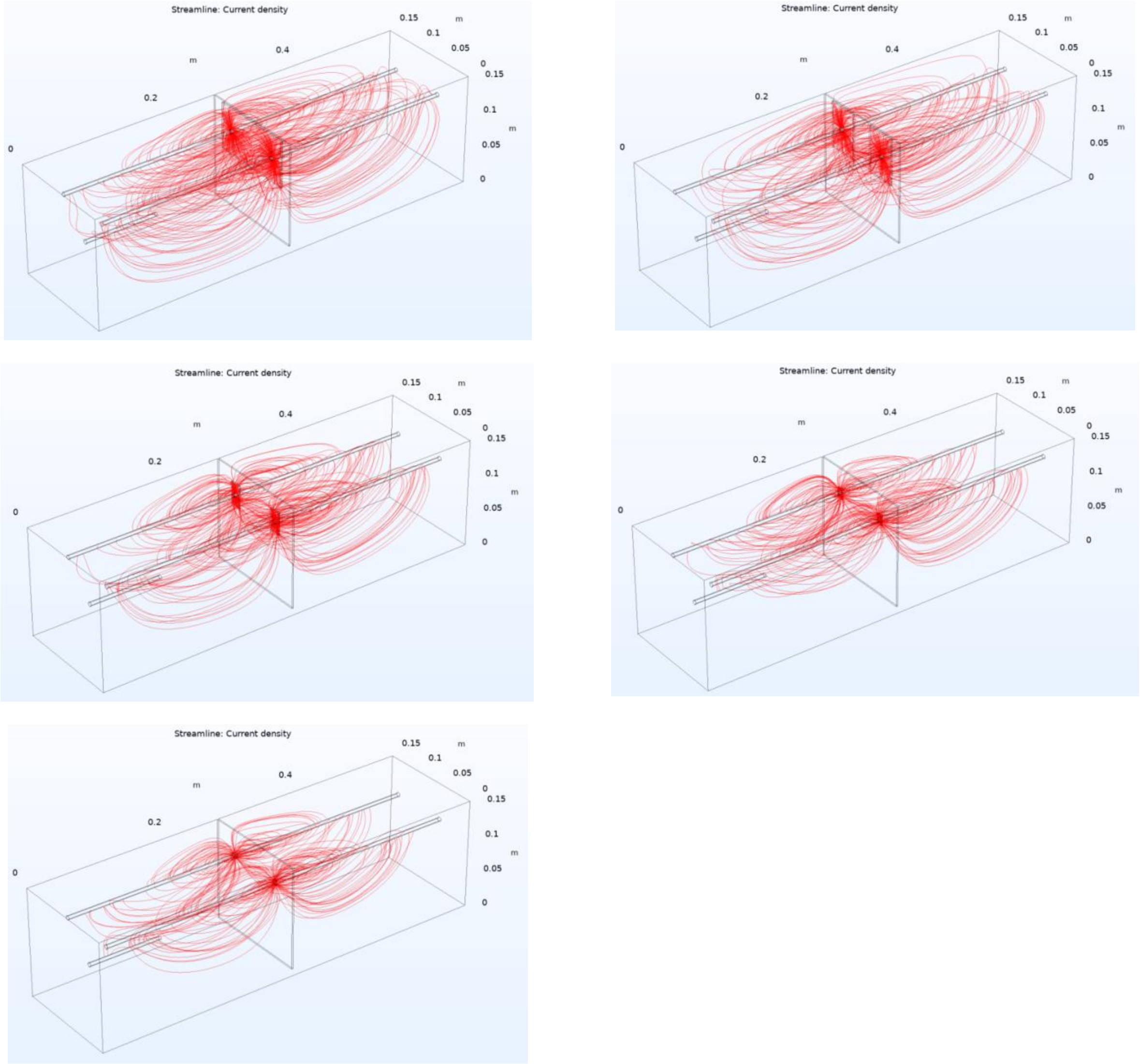

Figure 132 : anodic current distribution versus the drying of the crack

Because of lower resistivity of water in the crack path, the ionic current spread in the whole crack path fill by water to then diffuse in the concrete (Figure 132).

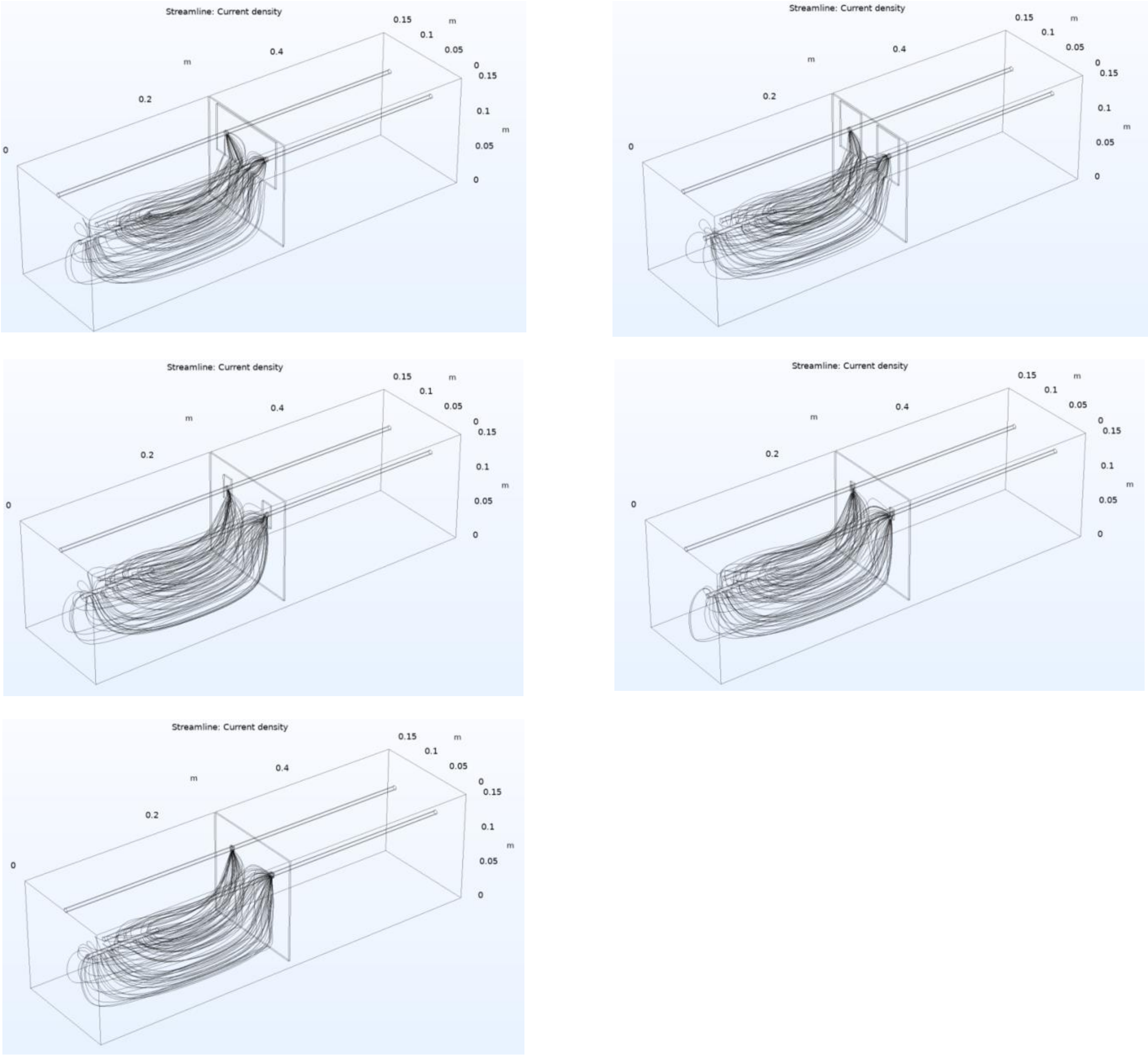

Figure 133 : Cathodic current distribution on the steel coupon versus the drying of the crack

In Figure 133, only the part of cathodic current flux generated by the metallic coupon is shown.

Finally, there is a decrease in the corrosion current versus the desaturation time which is shown on Figure 134.

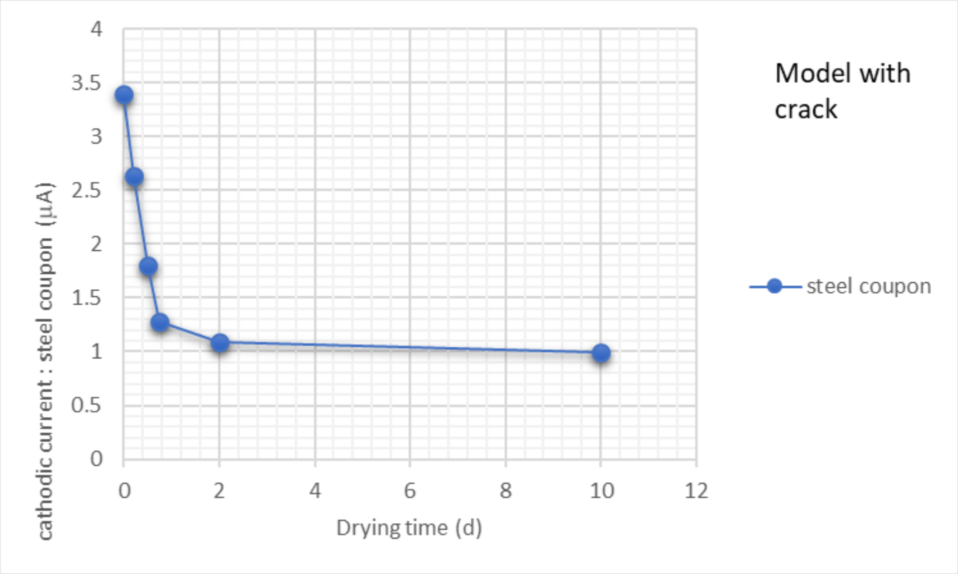

Figure 134 : Decrease of the cathodic current measured by the coupon as a function of desaturation time

Comparison between the real behavior (Figure 130) and the simulated one (Figure 134) is quite notable and shows that the peak values, experimentally recorded, corresponds to a full wetting of the crack path and the decrease in current is due to the desaturation of crack.

It is interesting to notice that the k ratio is not affected by the desaturation process as shown in Figure 135. This result allows calculate the total corrosion current by multiplying the cathodic current by a single coefficient versus time.

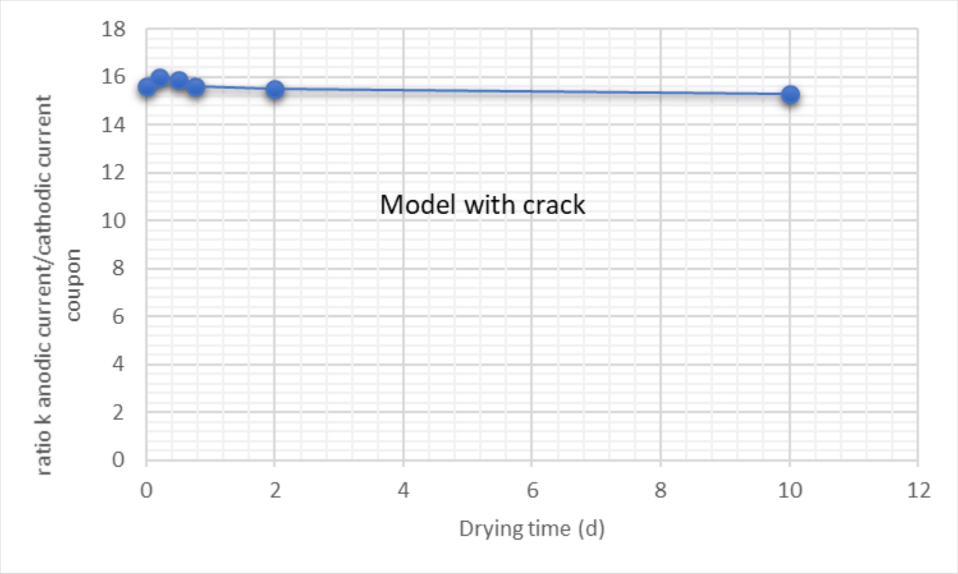

Figure 135 : Evolution of k ratio versus the desaturation time

The effect of desaturation of the crack path versus time allows also to predict the corrosion behavior in the case of a permanently cracks filled by water (Figure 136).

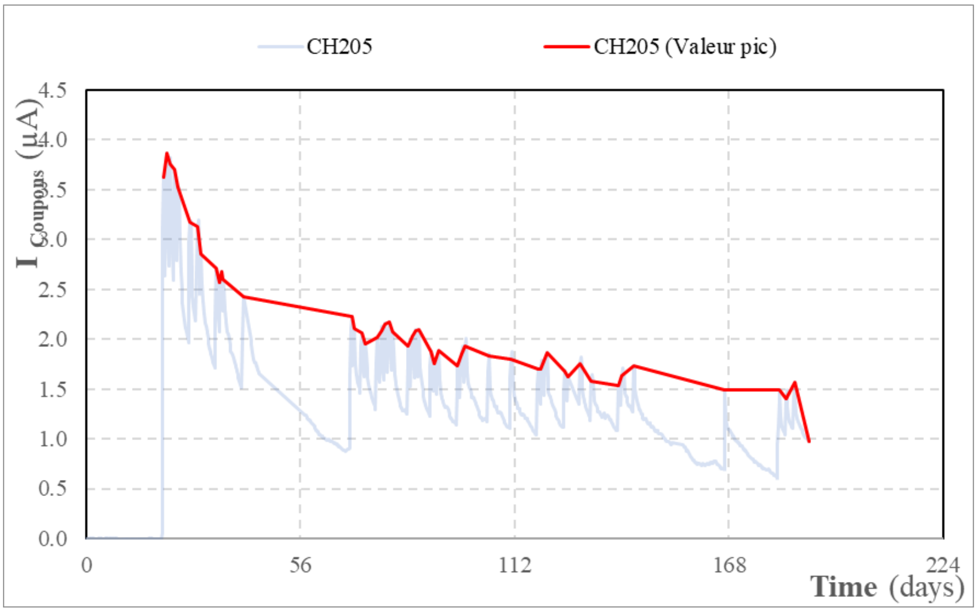

Figure 136 : Visualization of the cathodic current variation with time in case of permanently crack filled by water.

It is then possible to see that cracks permanently filled by water increased the macro-cell corrosion process, and it is also possible to see that there is a continuous decrease in the cathodic current versus time, but that this cathodic current cannot be considered as neglected for all the duration of the testing.

Based on the results shown in Figure 134, it is possible to consider that the difference in macro cell current between a permanently wet crack path and a wetting-drying cycle of 1 day is 3.5/1.25 = 2.8.

On Figure 136, it is possible to see that there is a decrease in corrosion macro-cell current during the test but there is still a non-neglected macro cell current at the end of the testing.

3.3.2.4. Macro-cell current and density according to the length of the anodic zone

The length of anodic zone is highly influence by the quality of concrete at the steel concrete interface. For top bars, the quality is poorer and leads to an increase of the anodic length at the level of the load-induced cracks.

The numerical model allows predict the corrosion current and the macro cell corrosion current density (or corrosion rate) according to the anodic length.

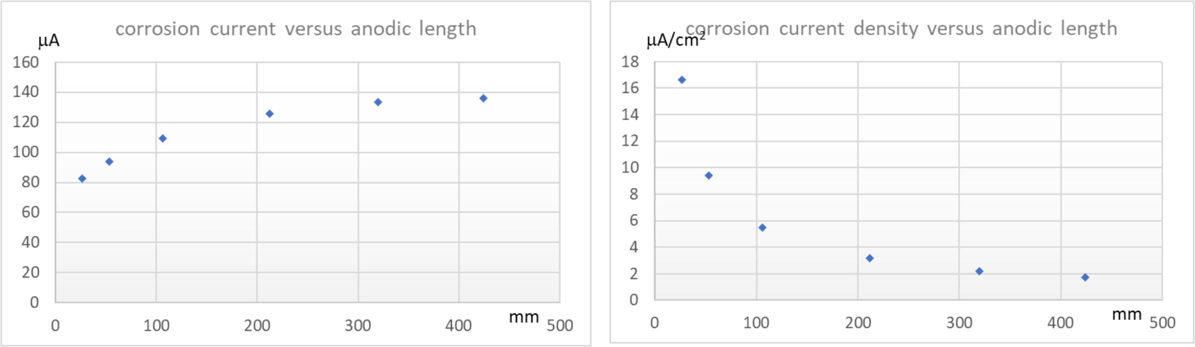

Figure 137 : macro cell corrosion current and corrosion rate according the length of the anodic site

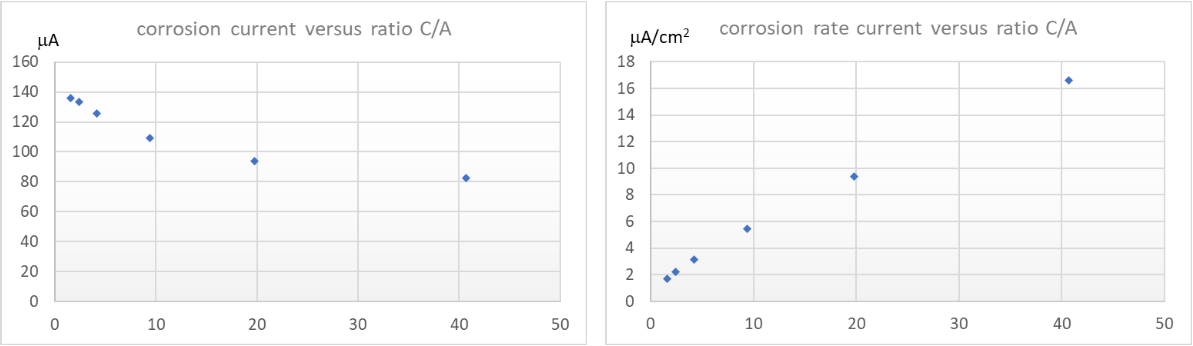

Figure 138 : Macro cell corrosion current and corrosion rate according to the ratio C/A

According to Figure 137 and Figure 138, it appears that the macro cell corrosion rate is highly dependent of the anodic site length and then C/A ratio. It is quite interesting to see that the values predict by the model are quite comparable with those found in chapter 3 for the CEM I concrete (i.e. around 6µA/cm^2) (Figure 77) if we consider the effect of the resistivity. Indeed, for low C/A ratio the macro cell corrosion rate is close to 2µA/cm^2 (Figure 138) but with a resistivity which is higher than the one on the CEM I concrete in chapter 3.

3.3.3. Results from corrosion current monitoring

The measured current during time is shown on the following pictures. Figure 139 and Figure 140 show respectively the macro cell current recorded by the metallic coupon and the total macro cell current calculated according to the k ratio (Table 17) for the specimen ref1. This specimen was subjected to wetting and drying cycles for 380 days.

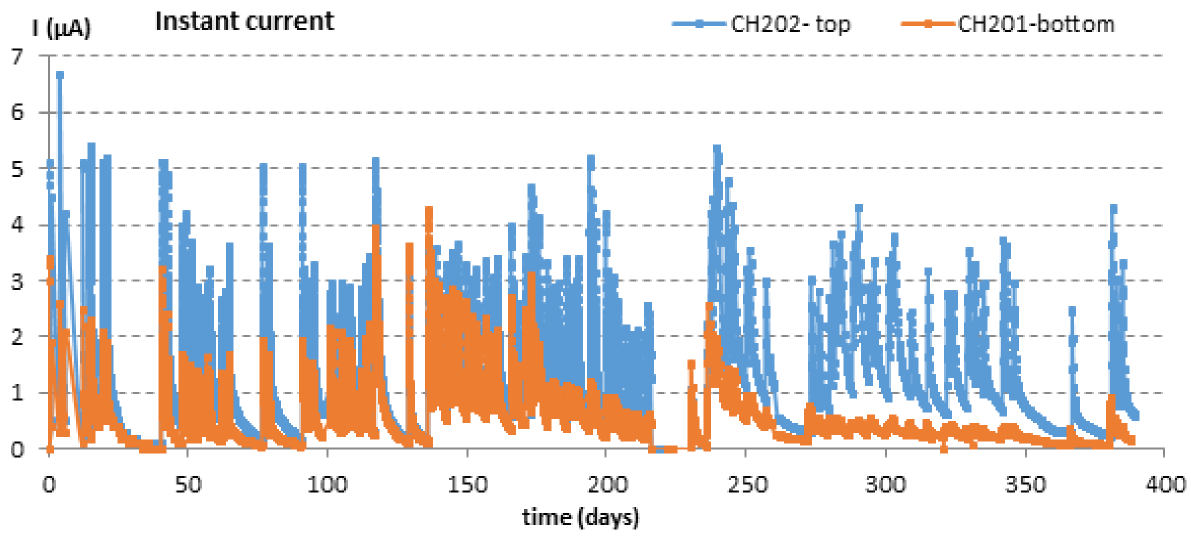

Figure 139. Evolution of I coupon during time of ref 1

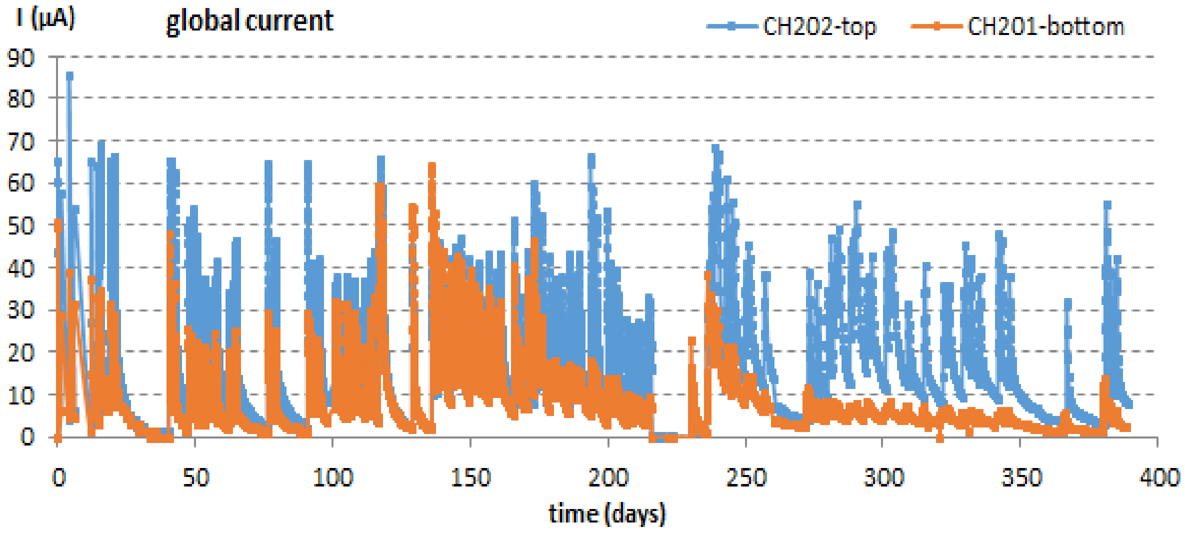

Figure 140. Evolution of global current during time of ref 1

From the value of total macro cell current, it is possible to calculate the cumulated electrical charge (Figure 141).

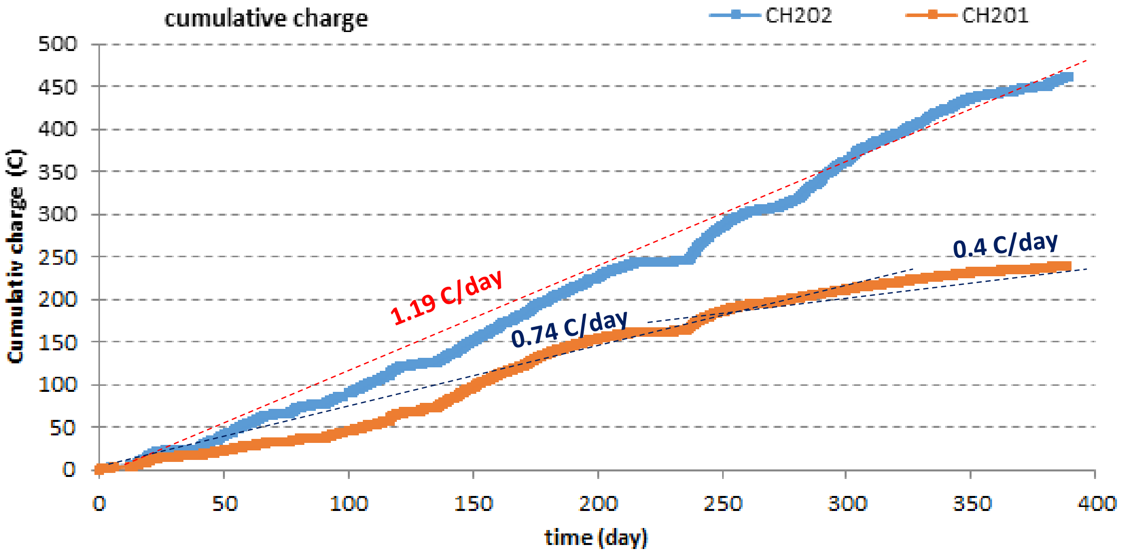

Figure 141. Cumulative electrical charge of ref 1

The cumulative electrical charge is higher for top bar than for bottom bar despite the fact that the C/A ratio is higher for bottom bar than top bar. For the sample ref 1, it appears that there is no change in the slope of cumulative electrical charge for top bar, but there is a decrease in slope for bottom bars at about 200 days (Figure 141). The decrease in cumulative electrical charge for bottom bar could be associated to an induction phase (or dormant phase) in the corrosion phenomenological process. It is then coherent with the results of Ghantous [2]and Timhadjelt [53] for reinforcing bars not affected by top-bar effect.

Figure 142 and Figure 143 show respectively the macro cell current recorded by the metallic coupon and the total macro cell current calculated according to the k ratio (Table 17) for the specimen ref2. This specimen was subjected to wetting and drying cycles for 380 days.

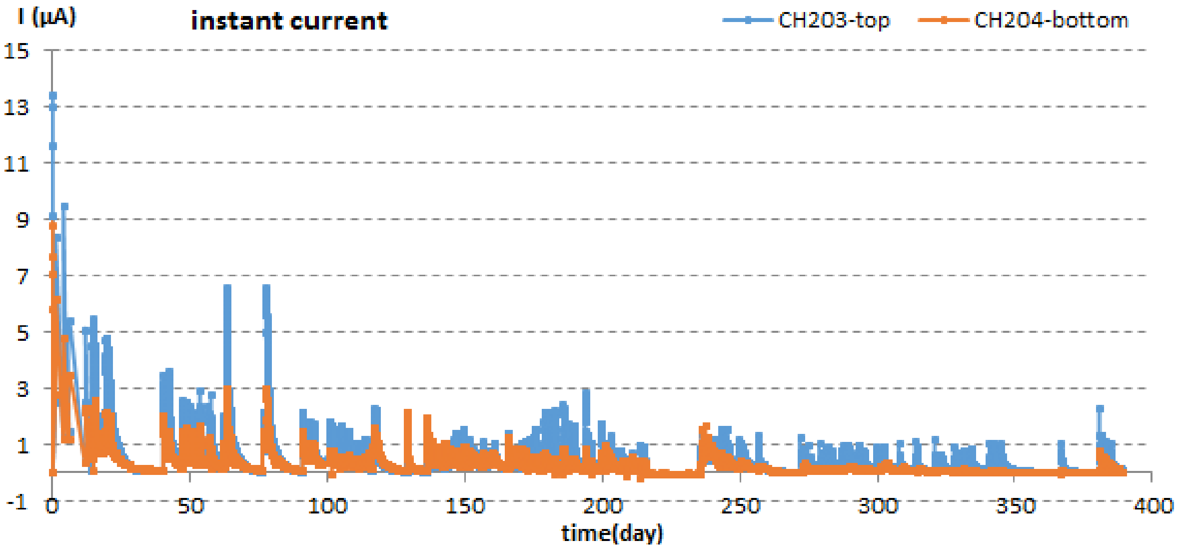

Figure 142. Evolution of I coupon during time of ref 2

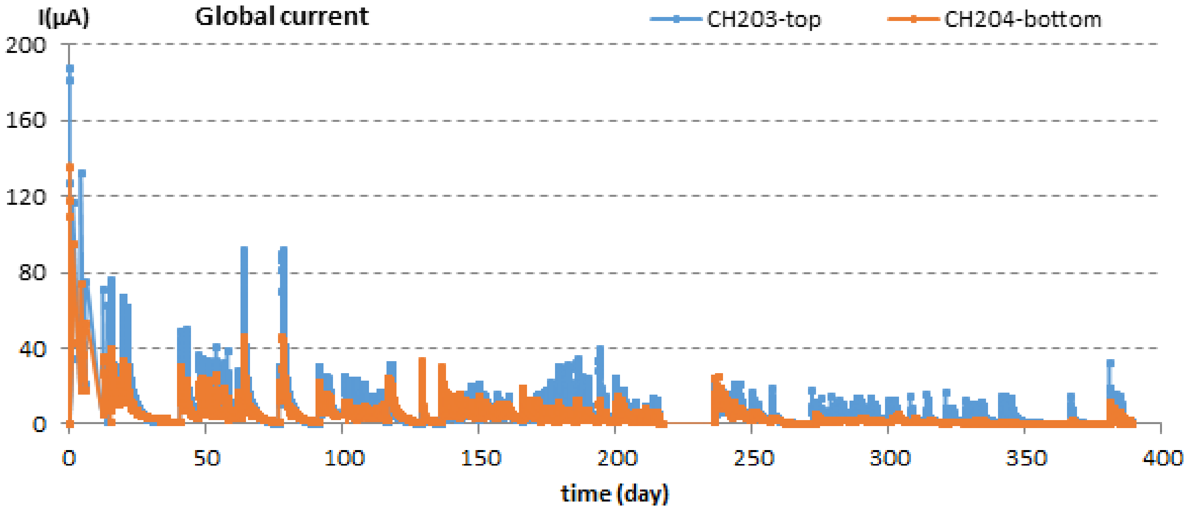

Figure 143. Evolution of global current during time of ref 2

From the value of total macro cell current, it is possible to calculate the cumulated electrical charge (Figure 144).

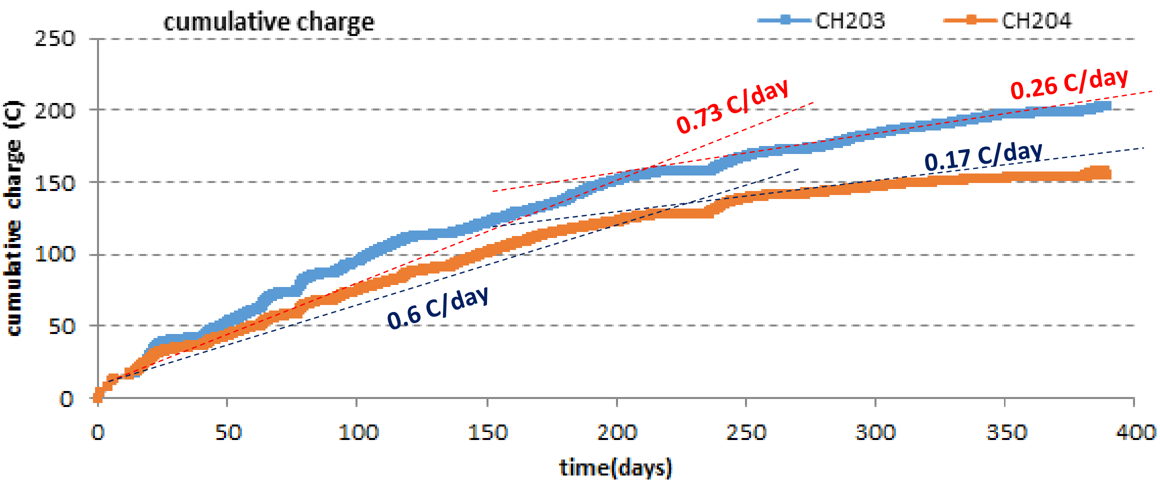

Figure 144. Cumulative electrical charge of ref 2

As in the case of ref 1 specimen, the cumulative electrical charge is higher for top bar than for bottom bar. Similarly, also with specimen ref 1, there is a decrease in cumulative electrical charge for bottom bar (around 200 days) which could be associated to an induction phase (or dormant phase) in the corrosion phenomenological process. For top bar, it seems also that there is a decrease in the slope of cumulative charge (around 200 days) which could indicate the beginning a dormant phase.

Figure 145 and Figure 146 show respectively the macro cell current recorded by the metallic coupon and the total macro cell current calculated according to the k ratio (Table 17) for the specimen ref3. This specimen was subjected to wetting and drying cycles for 160 days.

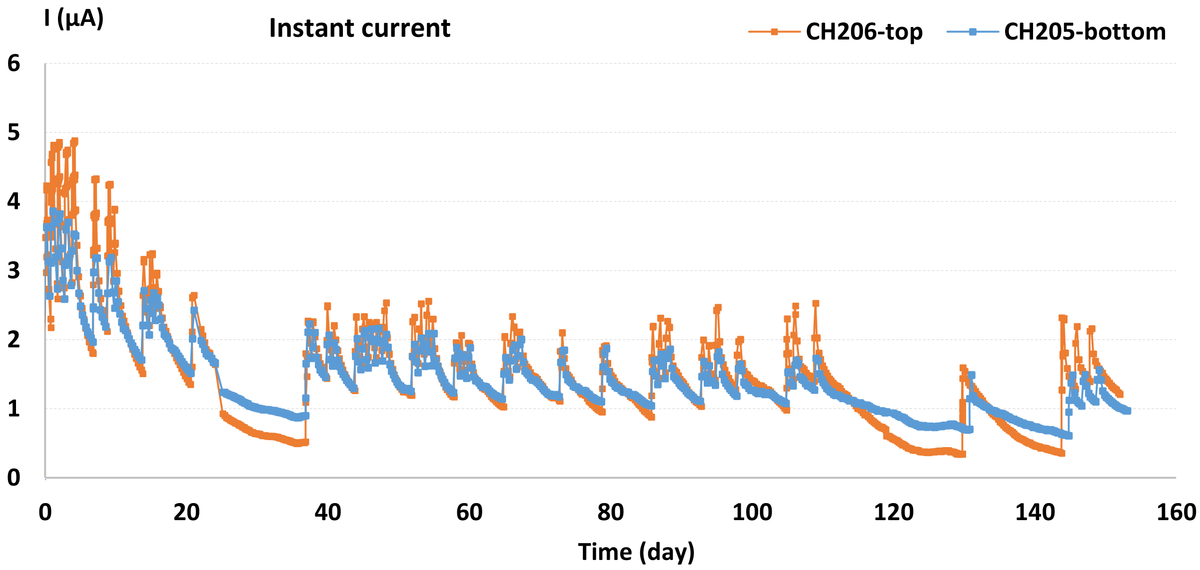

Figure 145. Evolution of I coupon during time of ref 3

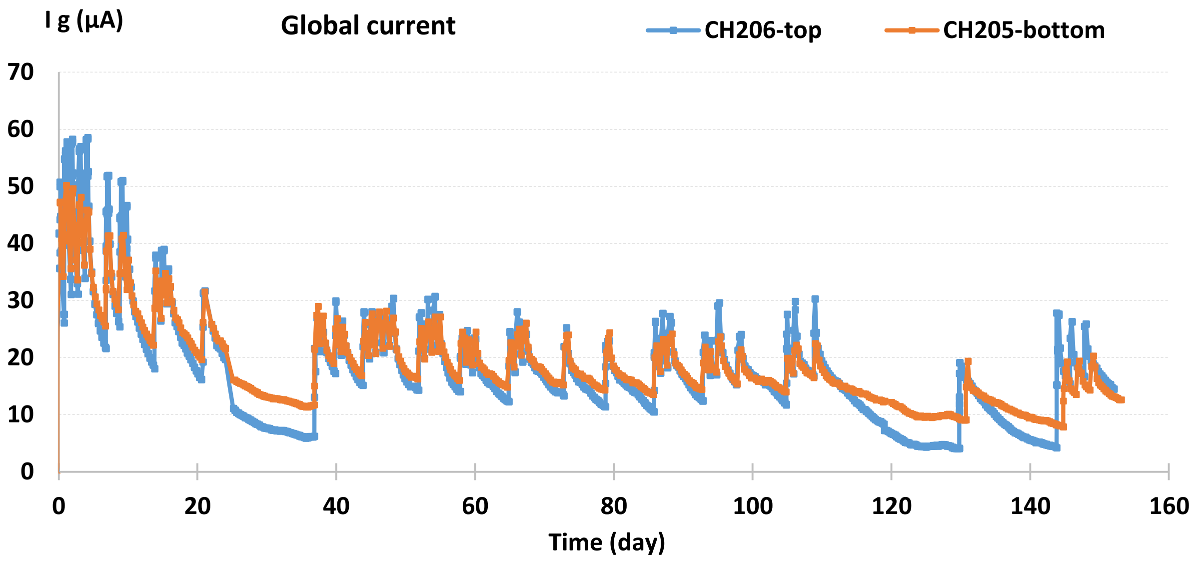

Figure 146. Evolution of global current during time of ref 3

From the value of total macro cell current, it is possible to calculate the cumulated electrical charge (Figure 147).

For sample ref 3, it is worth noting that the length of carbonated zone and then corroded zone is important for the bottom bars: it corresponds to the value of top bars for other specimens (Figure 112). As a result, it is not surprising that the macro cell corrosion current versus time for bottom bars is not so different of the one recorded on the top bars.

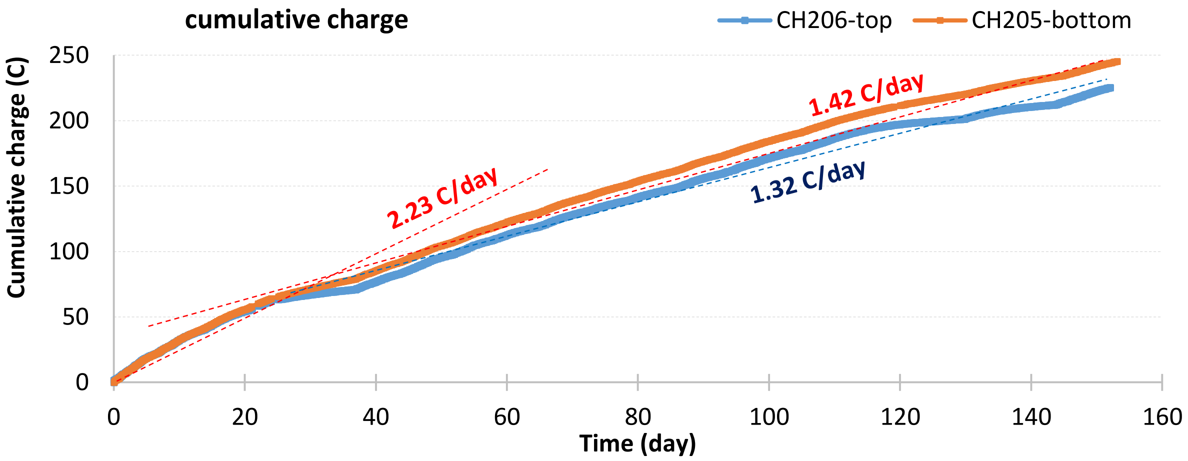

Figure 147. Cumulative electrical charge of ref 3

For specimen ref 3, and despite a change in slope at about 25 days, the cumulative electrical charge for bottom bar and top bar is quite linear. It is difficult to compare with the behavior of ref 1 and ref 2, since the change in slope for cumulative charge was after 200 days, which is more important that the total duration of the test for ref 3.

Figure 148 and Figure 149 show respectively the macro cell current recorded by the metallic coupon and the total macro cell current calculated according to the k ratio (Table 17) for the specimen ref4. This specimen was subjected to wetting and drying cycles for 160 days as specimen ref 3.

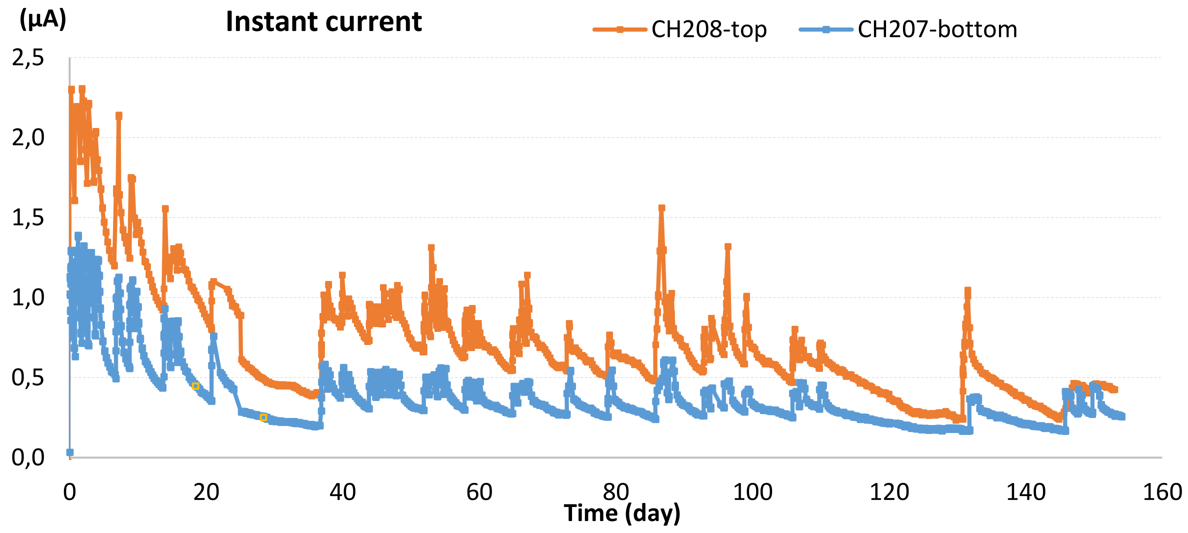

Figure 148. Evolution of I coupon during time of ref 4

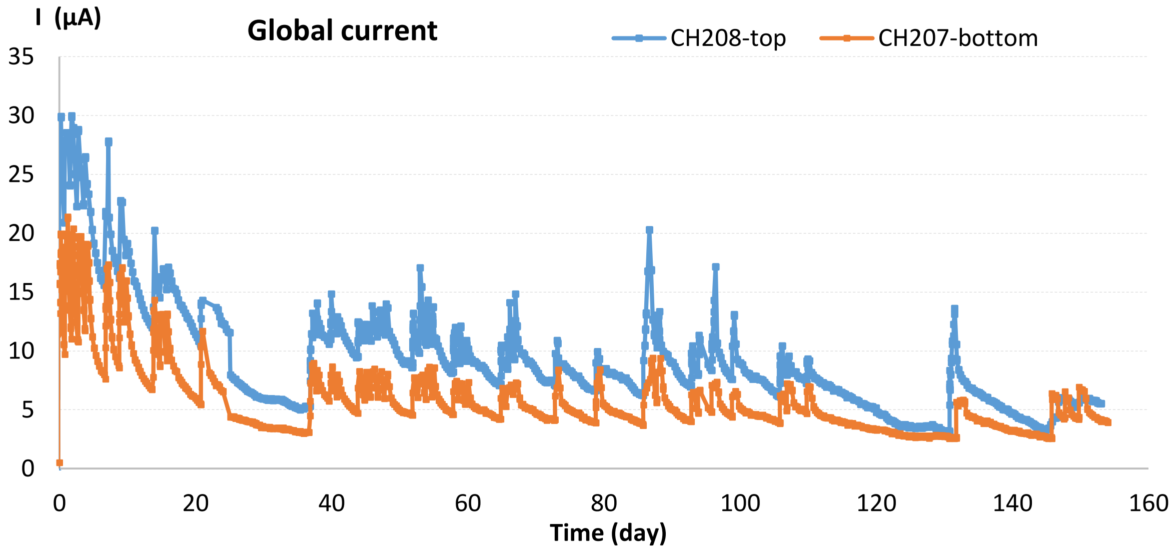

Figure 149. Evolution of global current during time of ref 4

From the value of total macro cell current, it is possible to calculate the cumulated electrical charge (Figure 150).

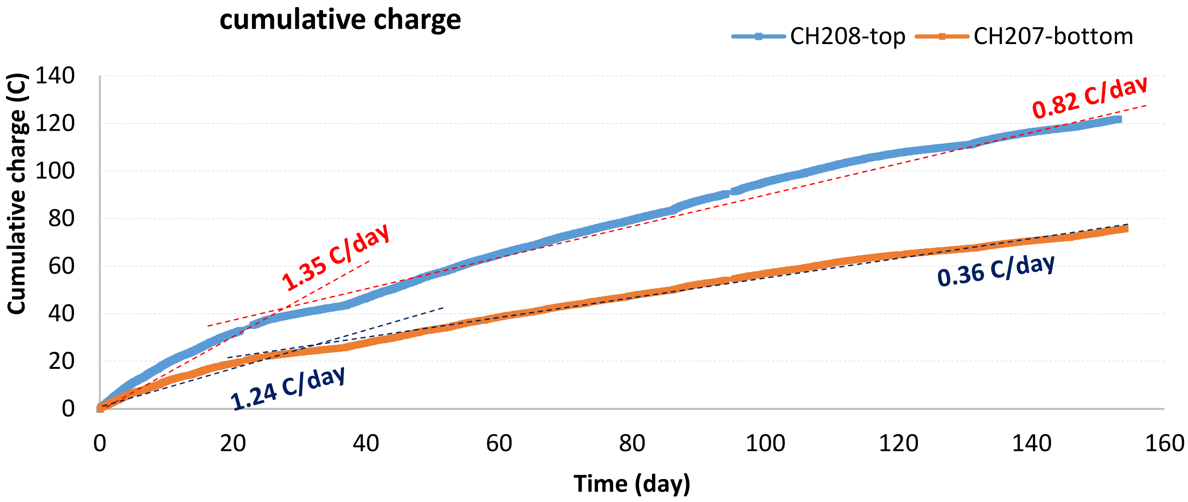

Figure 150. Cumulative electrical charge of ref 4

Similarly, to specimen ref 3, ref 4 shows a change in slope at about 25 days, but after that the cumulative electrical charge for bottom bar and top bar is quite linear. On contrary to ref 3 specimen, the cumulative charge for bottom bar is significantly weaker than top bar.

Finally, Figure 151 and Figure 152 show respectively the macro cell current recorded by the metallic coupon and the total macro cell current calculated according to the k ratio (Table 17) for the specimen ref5. This specimen was subjected to wetting and drying cycles for 380 days as ref 1 and ref 2 specimens.

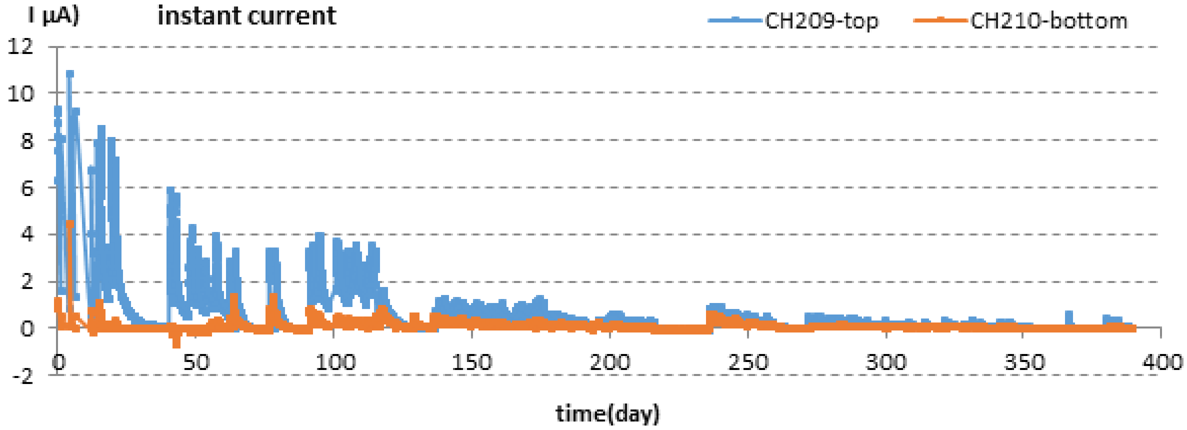

Figure 151. Evolution of I coupon during time of ref 5

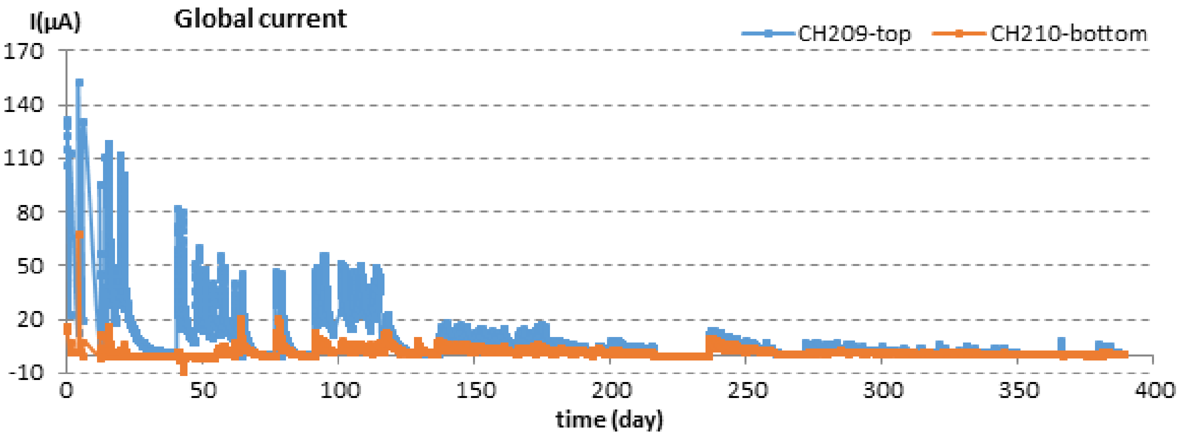

Figure 152. Evolution of global current during time of ref 5

From the value of total macro cell current, it is possible to calculate the cumulated electrical charge (Figure 153).

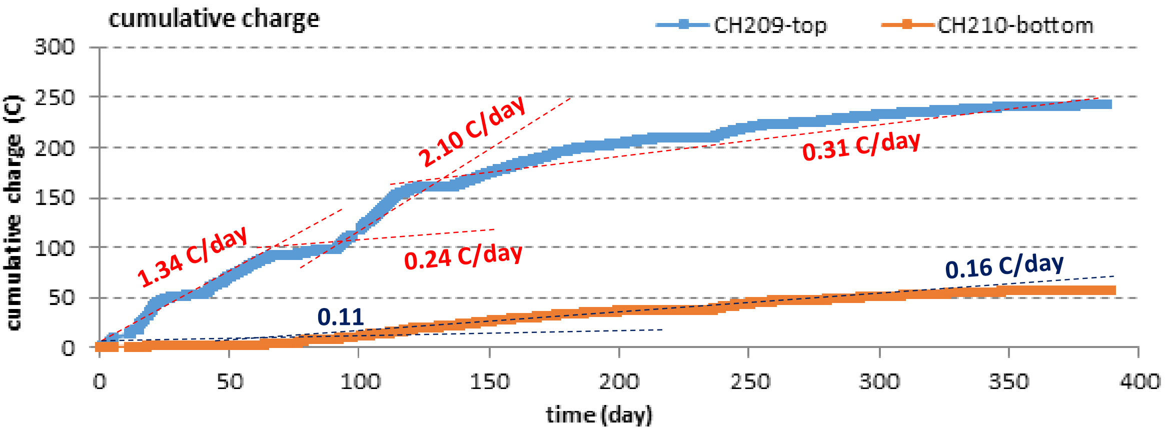

Figure 153. Cumulative electrical charge of ref 5

For ref 5 specimen, the cumulative electrical charge is significantly higher for top bar than for bottom bar. Similarly, also with specimen ref 2, there is a decrease in cumulative electrical charge for top bar which could be associated to an induction phase (or dormant phase) in the corrosion phenomenological process. Nevertheless, it seems that the change in slope correspond to a duration about 120 days for the top bar. For the bottom bar, the slope is always weak and is comparable with the slope of ref 2 during the induction phase.

From the cumulative electrical charge, the loss of steel mass was calculated according to Faraday's law as in Equation 21. The evolution of the mass of loss of steel bars in concrete beams then was performed in Figure 154 and Figure 155, for respectively the test duration of 380 days and 60 days.

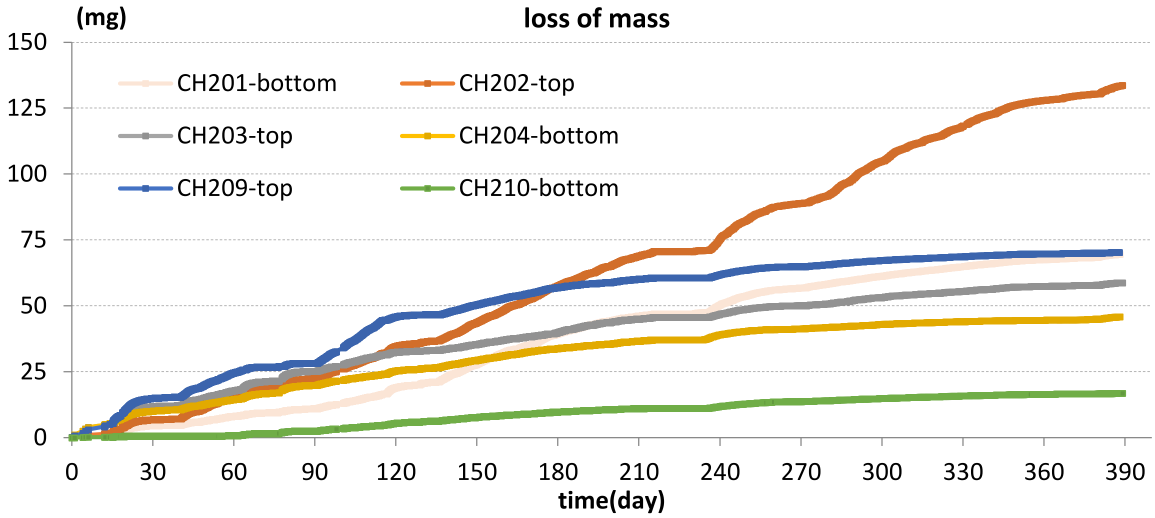

Figure 154. Evolution of loss of mass as a function of time (ref1,2 and 5)

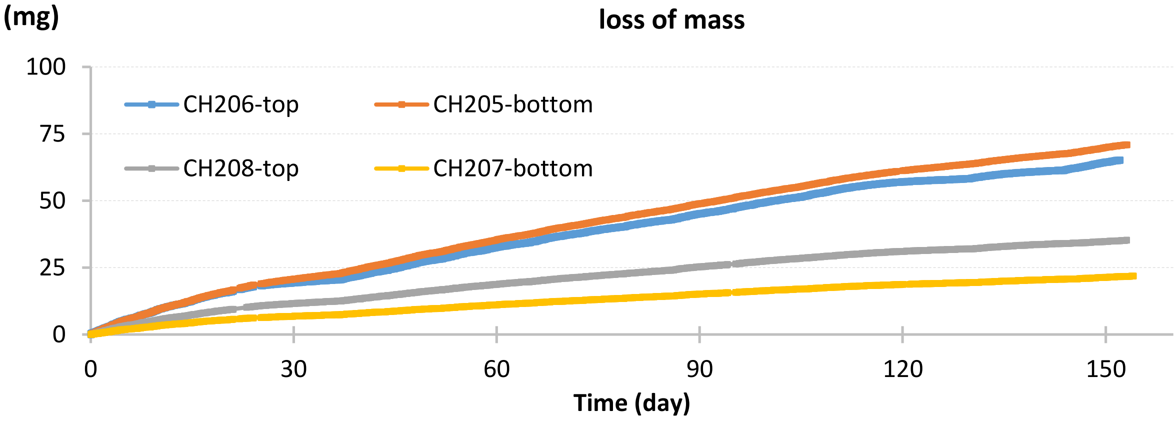

Figure 155. Evolution of loss of mass as a function of time (Ref 3 and 4)

As described by François et al. [19], the phenomenological process of corrosion in case of load-induced cracked concrete could be divided in 4 stages (Figure 156):

- Incubation: time for depassivation of re-bars at crack tip → here it is a short period: 1 wetting-drying cycle
- Initiation: corrosion have started at the crack tip and along the damage zone along the SCI
- Incubation: corrosion kinetic decreased → could be link to healing of the load-induced cracks or damage zone of SCI by corrosion products
- Propagation: corrosion re-starts; after a given time in propagation period there is the appearance of corrosion-induced cracks → in this case, corrosion process change since there is a mixed between corrosion in concrete and atmospheric corrosion (zones in front of load-induced cracks including further delamination).

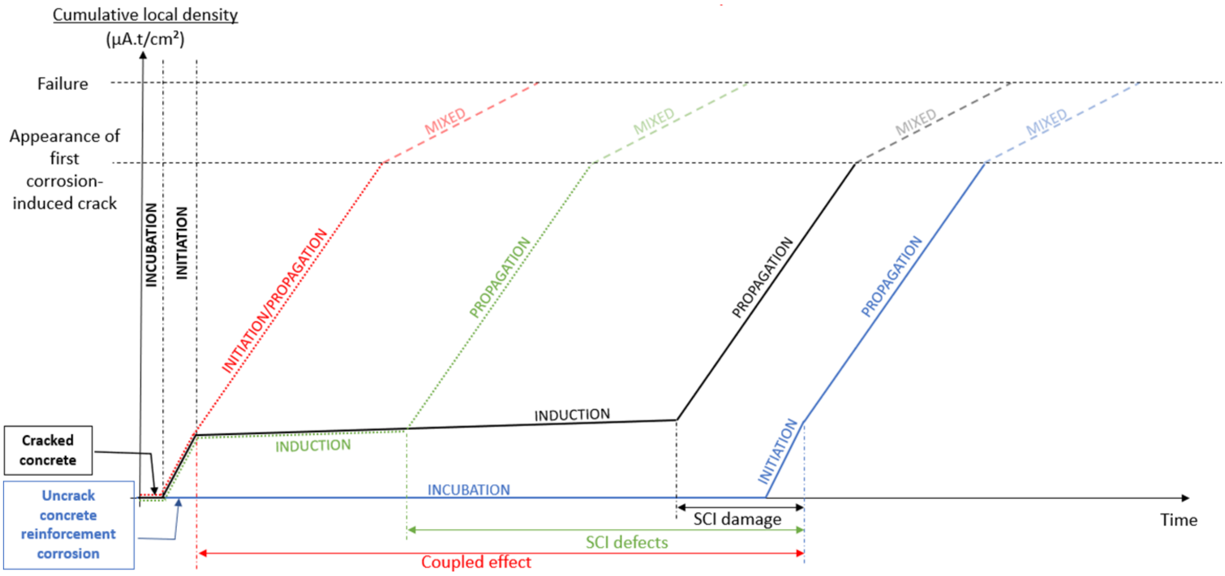

Figure 156 : Corrosion phenomenological process for both cracked or un-cracked reinforced concrete adapted from François et al. [19]

By comparing Figure 154 to Figure 156, it is clear that all the rebars except CH 202, are in the so-called induction phase. The corrosion kinetic is not null but is quite weak, which correspond to a dormant phase. Moreover, no corrosion-induced cracks were visible of the concrete surface of all samples during the full duration of the experiments.

By comparing Figure 155 to Figure 156, it seems that two re-bars, CH 205 and CH 206, are still in the initiation stage while for the two others rebars, CH 207 and CH 208, the corrosion kinetic is already weak and representative of a dormant phase. We could probably expect that the induction phase would be visible if the experiments were longer as it is the case for the samples shown in Figure 154.

As a result, it seems that top bar effect does not lead to an absence of induction (or dormant) phase in the corrosion process at load-induced crack location. Of course, there is one top re-bar which do not exhibit a dormant phase but it could be considered as an exception.

This result could be quite surprising, but in Figure 156, the corrosion phenomenological model do not proposed an absence of induction phase in case of SCI defect (such as top bar effect) but a reduction of the duration of induction phase: probably the experimental duration is not enough to have a conclusion on this phenomenon.

As shown in the Figure 154 and Figure 155, the iron mass loss is always higher for the top bars than the bottom bars.

Comparison between the loss of mass calculated in current measurement and the loss of mass from gravimetric can be seen in Figure 157.

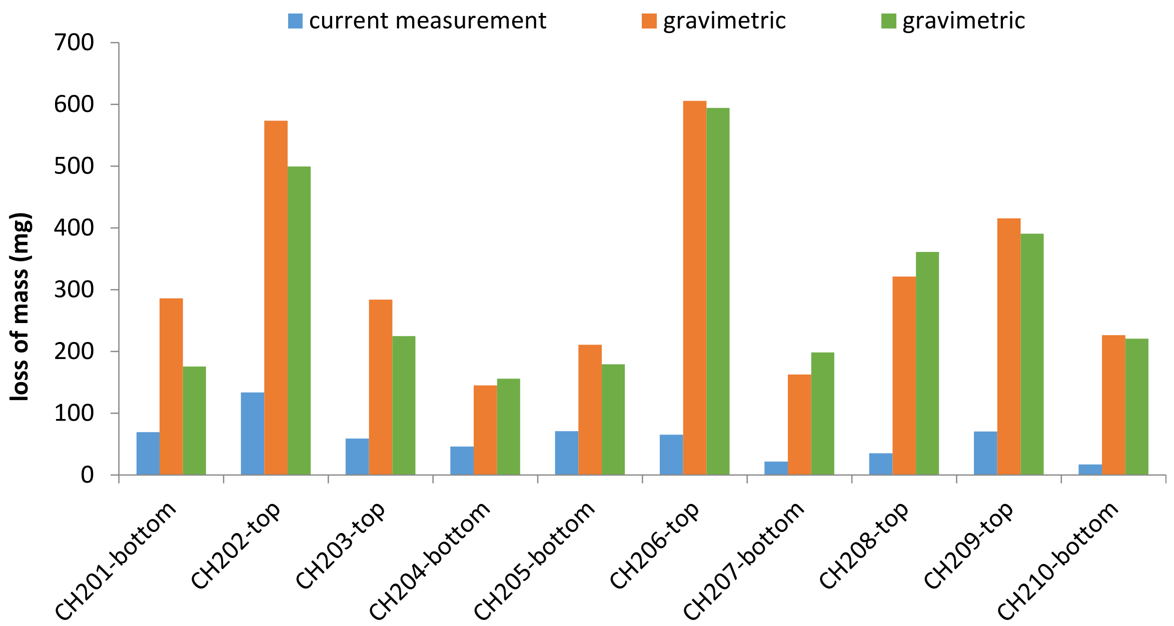

Figure 157. Loss of mass from current measurement and gravimetric

It is observed that the loss of mass measured in current monitoring method exhibited a significantly lower value than the one determined by gravimetric measurement. It is probably due to the fact that the wet period duration is small in comparison with the dry period duration.

The comparison between the loss of mass due to macro cell (current measurement) and the loss of mass due to macro cell and uniform corrosion (in gravimetric measurement) is showed in this following picture (Figure 158).

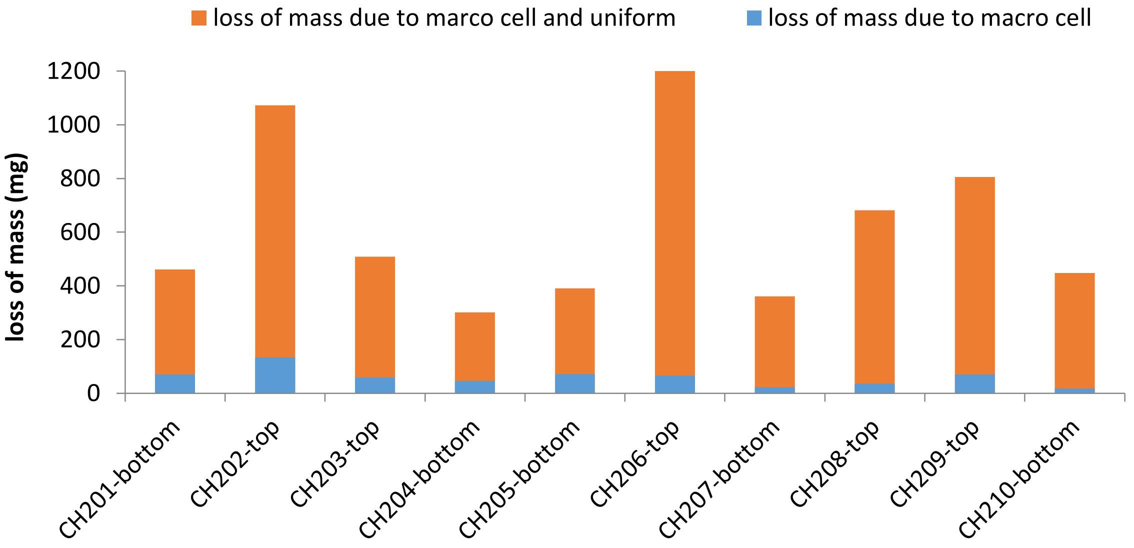

Figure 158. Comparison between loss of mass due to macro cell and uniform and loss of mass due to macro cell

The ratio between uniform and macro cell can be seen in Figure 159.

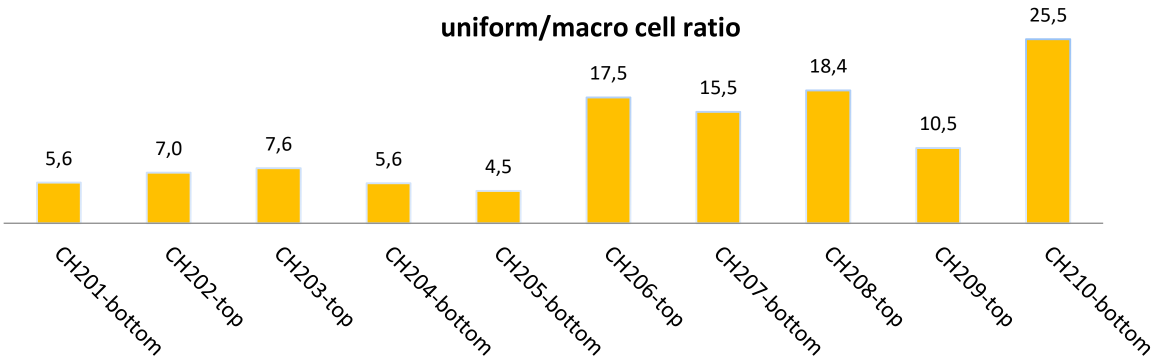

Figure 159. Ratio of uniform and macro cell

It was observed that for some samples macro cell plays a very small part (eg CH210- bottom, CH 208 top or CH 206-top) corresponding to very high ratio between uniform and macro cell (more than 20 times) while other samples (eg CH 205 bottom, CH 201 bottom or CH 204 bottom) showed a lower ratio (approximately 5 or 6 times).

It is worth noting that if the wetting exposure is longer, the role of macro cell then is more important. We have shown previously that without drying in the crack path, the macro cell would be almost 3 times higher (Figure 134). Then a comparison between uniform corrosion and 3 times macro cell corrosion is performed to simulate the case of permanent wetting of the crack as in Figure 160. A shown in Figure 160, a decrease of the ratio between uniform and macro cell was recorded and for some samples (eg in CH 201, 202, 203, 204 and 205 bottom) the ratio could be below 2 times and even macro cell current could be higher than uniform corrosion current (specimen CH 205 bottom).

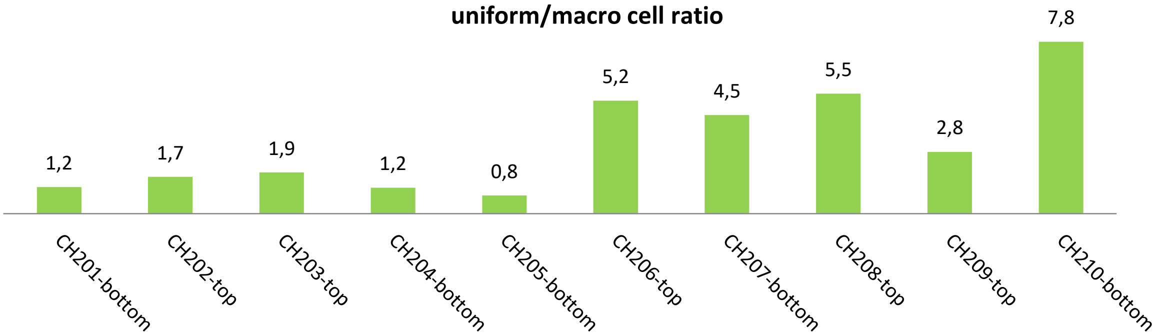

Figure 160. Ratio of uniform and macro cell in case of permanent wetting of the crack

By using Equation 13, corrosion kinetics was calculated in Figure 161 (for a duration about a year) and in Figure 162 (for a duration about six months).

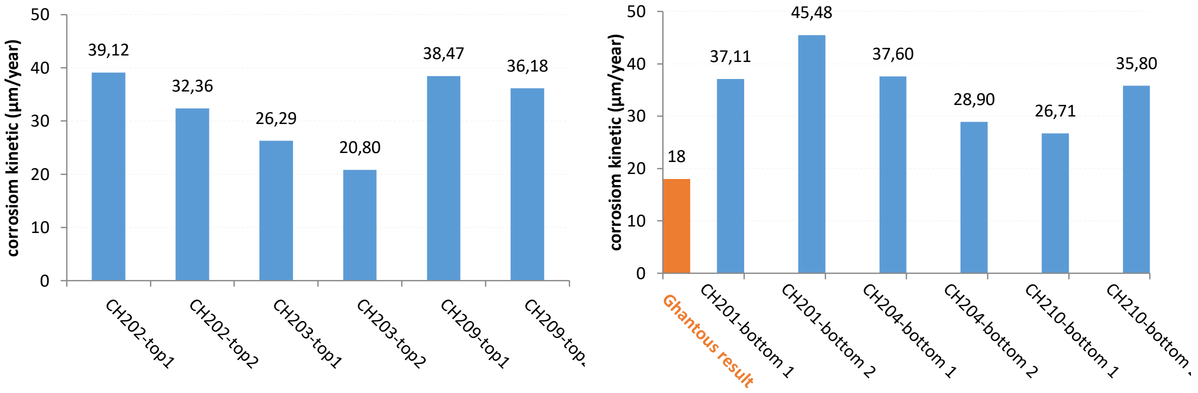

Figure 161. Corrosion kinetic in one year

For a corrosion period of 1 year (Figure 161), it appears that the corrosion kinetic found by Ghantous [2] is weaker that those we calculated. The value could be closed (CH203 – but it corresponds to top bar with longer corrosion length) but it is generally to a value twice the one found by Ghantous [2] in case of bottom bars. This difference could be linked to the fact that in Ghantous the wetting-drying cycle is 3 days, and in our case the wetting-drying is daily for the first 6 months and twice a day for the last 6 months.

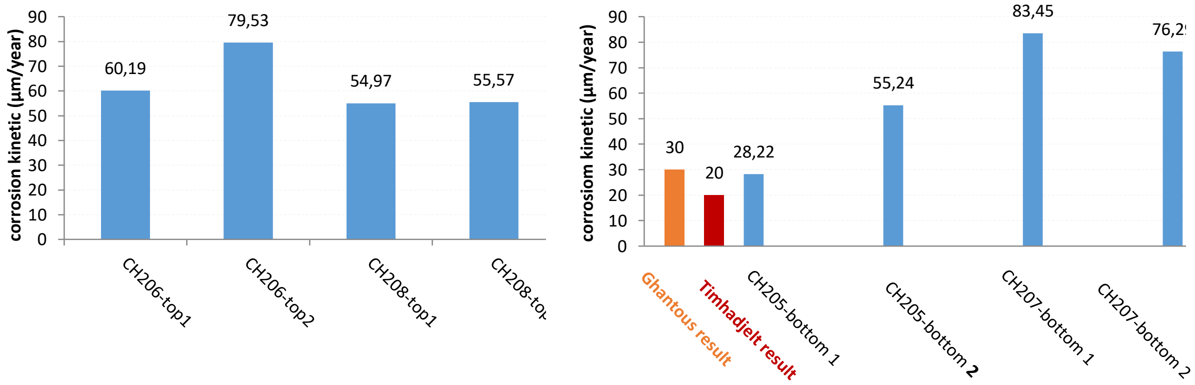

Figure 162. Corrosion kinetic in six months

For a corrosion period of six months year (Figure 162), it appears that the corrosion kinetic found by Ghantous [2] is weaker that those we calculated. The value could be closed (CH 205) but it corresponds generally to a value twice or three times the one found by Ghantous [2] in case of bottom bars. This difference could be linked to the fact that in Ghantous the wetting-drying cycle is 3 days, and in our case the wetting-drying is twice a day for the 6 month duration of experiments on ref 3 and ref 4 specimens. Same comments could be done with Timhadjelt [53] results, since in Timhadjelt, the wetting-drying cycle is the same as Ghantous while it is twice a day in our experiments.

The corrosion kinetics deduced from monitoring measurement current is presented in Figure 163. In general, it expressed the same tendency with a decrease by time. Nevertheless, CH 210 bottom and

CH 202 top seem to have a quite constant behavior versus time and CH 201 bottom exhibits a high scatter.

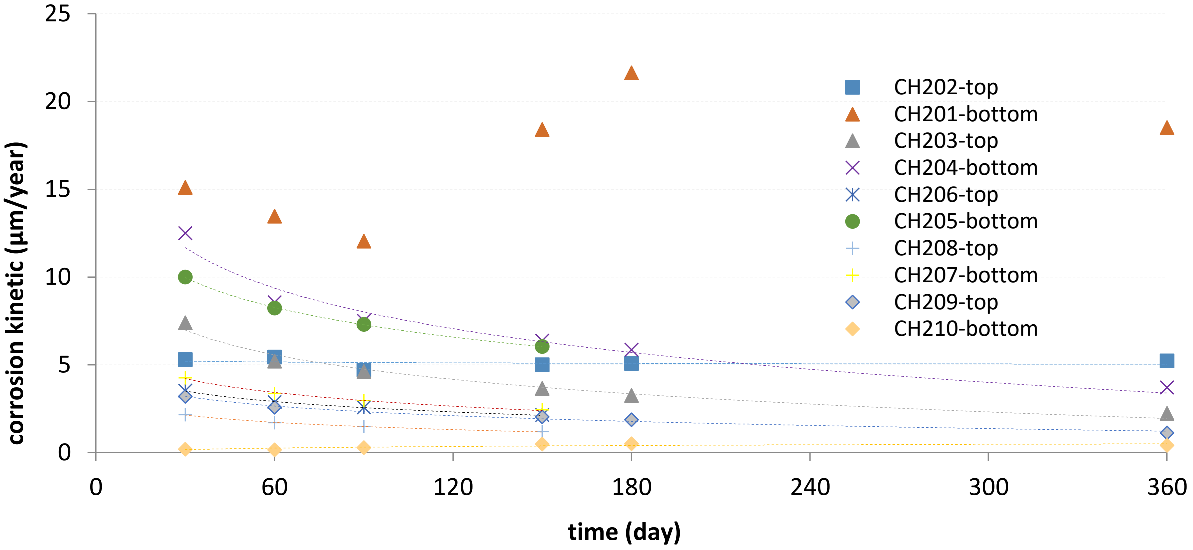

Figure 163. Corrosion kinetic from monitoring measurement current

By assuming a constant corrosion kinetic versus time, it is possible to calculate the total corrosion current density, i.e. the sum of uniform and macro-cell corrosion. For the 160 days long experiment, the corrosion current density is closed to 4µA/cm^2. In chapter 3, we found that uniform corrosion current density was closed to 1.5 µa/cm^2 and that the macro cell corrosion current density could be more significant in the case of CEM I. From Figure 138, it can be seen that macro cell corrosion current density is closed to 2µA/cm^2 for C/A ratio about 1 and slightly higher if C/A is more important. It corresponds then to a total corrosion current density about 3.5µA/cm^2. As a result, the values of corrosion current densities plot in Figure 164 are coherent with the results from the chapter 3.

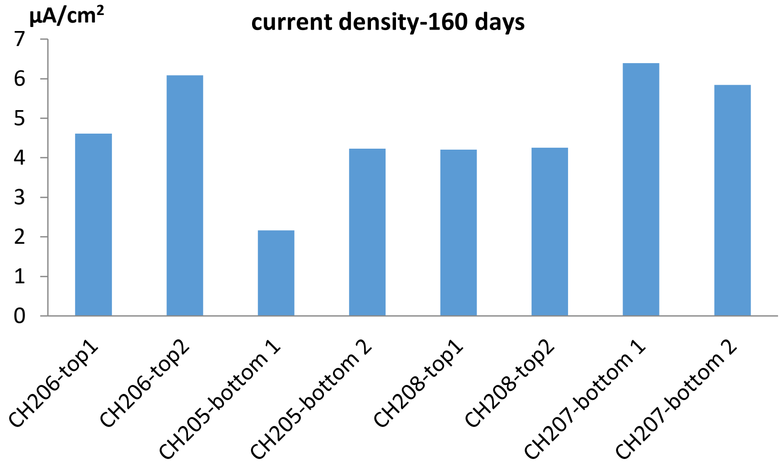

Figure 164. Total corrosion current density after 160 days

The total corrosion current density after 380 days is shown on Figure 165, from this picture it is clear that there is a reduction in corrosion current density between 160 days (Figure 164) and 380 days. This is consistent with the reduction of the macro cell current corrosion found versus time and especially after the period of 160 days.

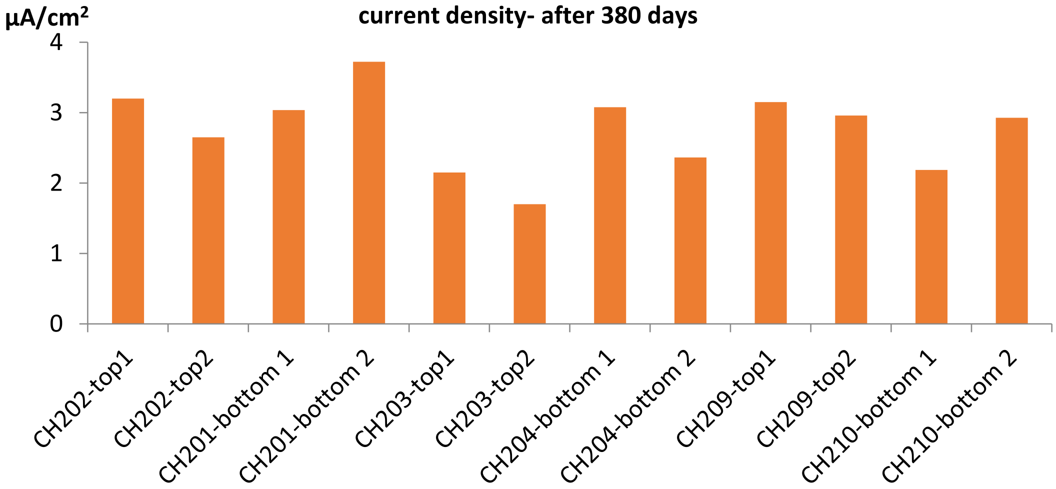

Figure 165. Total corrosion current density after 380 days

- **Discussion:**

Ghantous and Timhadjelt also studied the effect of load-induced cracks on corrosion induced by carbonation in their PhD. Experiments in Ghantous and Timhadjelt were based on 7x7x28 cm sample with only one rebar and a wetting period of 30 mn followed by 72 h drying (1 wetting drying cycle each 3 days).

On “small” samples 7x7x28 cm, with one rebar and no top bar effect, Ghantous found that there is an induction period before 180 days (from gravimetric measurement) (Figure 166) whatever the crack width. It is likely that the beginning of induction period could be 90 days since the difference between loss of steel mass at 90 days and 180 days is quite small. The calculation of the corrosion rate leads to value around 50 µm/year at 90 days and around 25 µm/year at 180 days (Figure 167), whatever also the crack width.

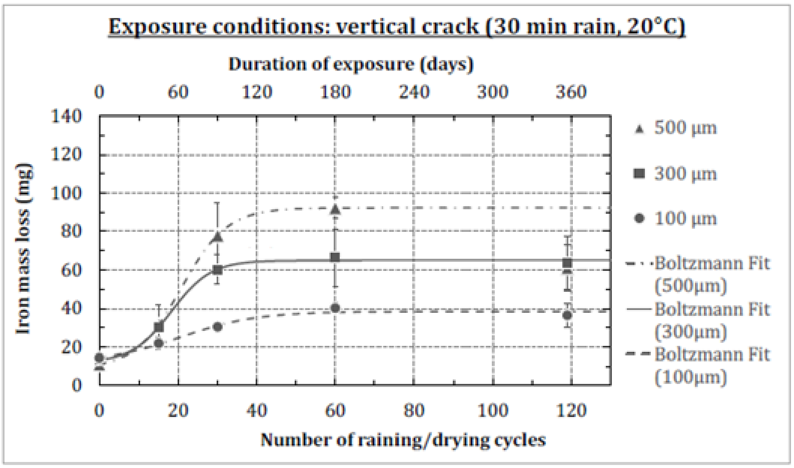

Figure 166: Loss of mass due to corrosion versus time in Ghantous [2]

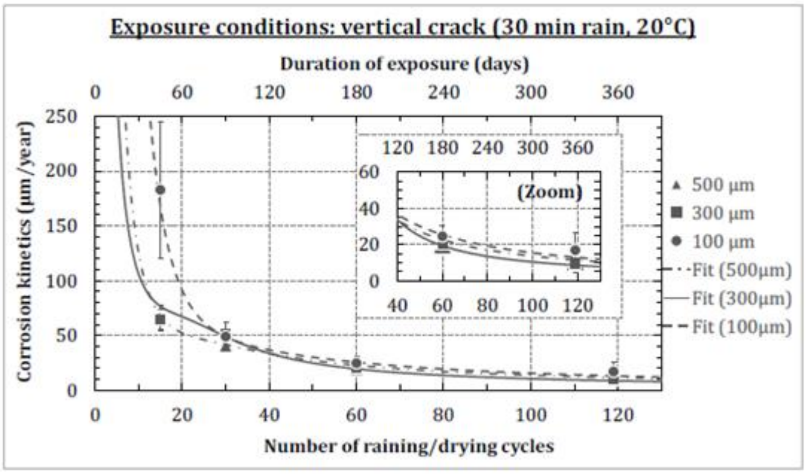

Figure 167 : corrosion kinetics versus time in Ghantous[2]

On same “small” samples 7x7x28 cm, with one rebar and no top bar effect, Nassim Timhadjelt found that there is also an induction period at 90days whatever the crack width (from gravimetric measurement) (Figure 168) and the corrosion rate was around 25-30 µm/year at 90 days and around 15-20 µm/year at 180 days (whatever crack width).

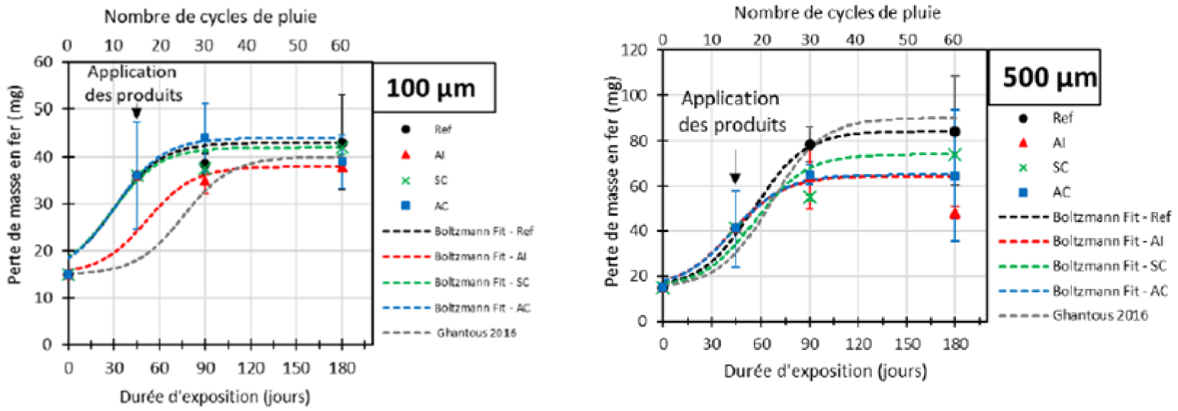

Figure 168 : loss of mass due to corrosion versus time in Timhadjelt [53]

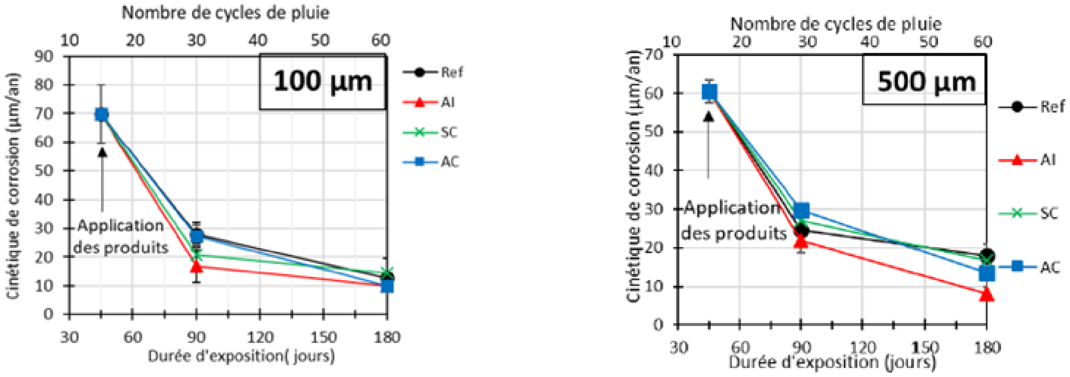

Figure 169 : corrosion kinetics versus time in Timhadjelt [53]

It appears that in both studies of Ghantous and Timhadjelt, there is an induction period in the corrosion process whatever the crack width, after an exposure time about 90 days. Nevertheless, the corrosion kinetics is slightly lower in the case of Timhadjelt study in comparison with Ghantous.

It is worth noting that in the results of Timhadjelt, there was both gravimetric measurements versus time and macro cell corrosion current versus time. It is then quite interesting to compare gravimetric loss of mass and calculated loss of mass from macro cell corrosion current measurement versus time.

From gravimetric measurement, as mentioned previously, it appears that an induction period begins at approximately 90 days whatever crack width (Figure 168). From macro cell current measurement, it appears that an induction period begins after 40 days (Figure 170) whatever crack width. In Figure 170, there is a change in the slope of cumulative charge versus time which allows to propose the 40 days duration before the beginning of the induction period. There is no contradiction between this beginning of induction period after 40 days and the results found in case of gravimetric measurement: beginning of induction period at 90 days. Indeed, the change in slope of macro cell current allow to continue to have an increase in loss of steel mass after 40 days of corrosion process during induction period. Nevertheless, it should be recall that gravimetric measurement corresponded to the whole corrosion scenario: uniform and macro cell corrosion. As a result, it is possible to assume that both uniform and macro cell corrosion follow the same phenomenological process: i.e. an initiation phase followed by an induction phase. There is only a remaining question about the beginning of the induction phase: is it simultaneous for both corrosion process or not?

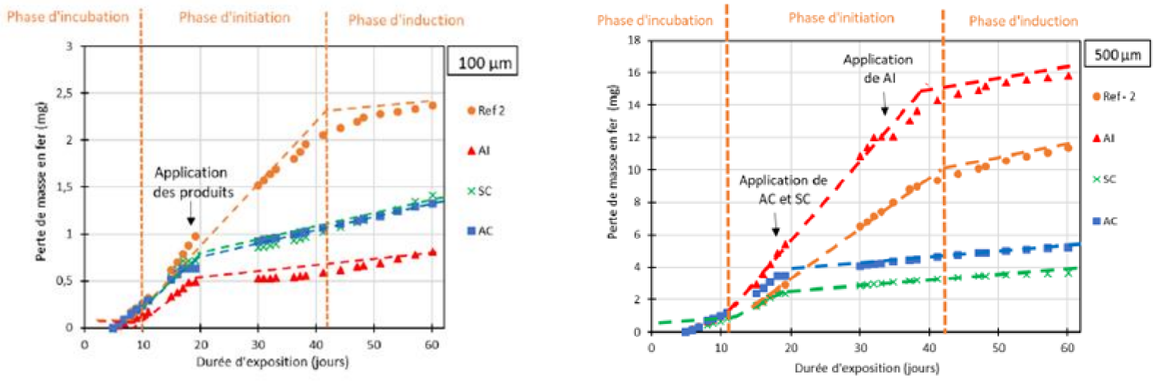

Figure 170 : loss of mass from macro cell corrosion current measurement versus time in Timhadjelt [53]

The work done by Timhadjelt allows also to have an idea about the relative ratio between uniform corrosion and macro cell corrosion. Indeed, from Figure 170, the loss of mass calculated from macro cell current measurement is, respectively, at 60 days: 2.4 mg and 12 mg for 100 µm crack and 500 µm crack. From Figure 168, the loss of mass at 60 days is respectively, 40 mg and 60 mg for 100 µm crack and 500 µm crack.

The ratio between total gravimetric loss of mass versus macro cell loss of mass is then, respectively, 16.7 and 5 for µm crack and 500 µm crack.

There is then an important difference between the ratios of gravimetric loss of steel mass/macro cell loss of steel mass, between the two specimens. Despite the large variation: 5 and 16.7, it is clear from this result that uniform corrosion is significantly higher than macro cell corrosion. One explanation could be the short wetting period (30 mn) followed by a long drying period (3 days) because macro cell corrosion needs a saturated crack path to be effective.

But in Timhadjelt, there is also some experiments on larger samples with 2 layers of rebars to study the influence of water bleed defect which is likely to occur on top bars: specimens were 15x15x55 cm as it is the case in our thesis. For these specimens, Timhadjelt has performed macro cell corrosion measurement but there is no gravimetric measurement. The wetting drying cycles is supposed to be 30 mn wetting each day.

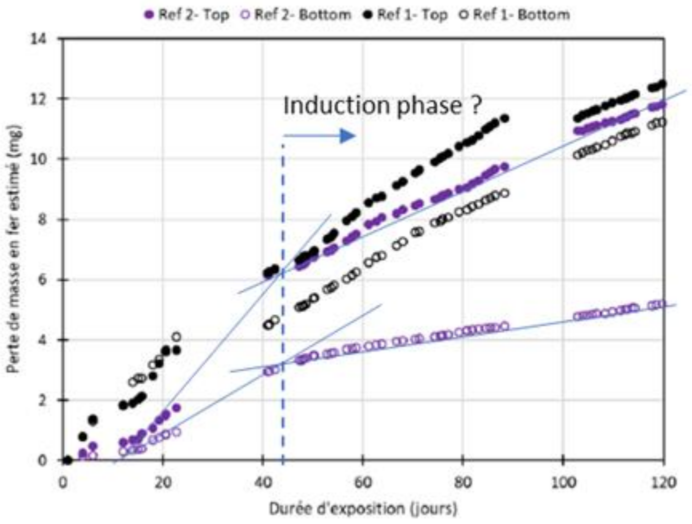

Figure 171 : loss of mass due to macro cell corrosion for both bottom and top bars versus time from Timhadjelt [53]

From Figure 171, it seems that the 2 specimens studied do not exhibit the same behavior. For ref-2 specimen, it is clear that there is a change in slope after about 40 days. For ref2-bottom, it could be assumed that there is an induction phase since the slope is significantly reduced. For ref2-Top, there is also a change in slope but it is difficult to assume that corresponds to an induction phase since the corrosion is still significant. For ref-1 specimen, bottom and top bars seems to have a similar behavior.

The comparison between our results and previous results from Ghantous and Timhadjelt is not easy. Indeed, in Ghantous, all the experimental results versus time correspond only to gravimetric measurement of loss of steel mass due to corrosion, while in our experiments the experimental results versus time correspond to loss of steel mass extrapolated from macro cell current measurement on steel coupon. As a result, in Ghantous loss of steel mass correspond to the sum of uniform corrosion and macro cell corrosion, while in our results it is only macro cell corrosion. Corrosion kinetic is not very different in your experiment from the one of Ghantous at 90 days; the difference could be linked to the different time between two consecutive wetting periods: 3 days in the case of Ghantous and 1 day or half a day in our experiments. Nevertheless, what is non-intuitive is that corrosion kinetic is weaker for top bar that for bottom bar.

Finally, both Ghantous and Timhadjelt experimental results show that whatever the crack width, there is a reduction in corrosion kinetics after a period of time in the range of 40-90 days, corresponding to the appearance of an induction phase.

Nevertheless, this conclusion is linked to a wetting drying process of 30 mn followed by 3 days of drying. As a result, as shown in the macro cell corrosion current versus time, only the wetting period lead to a significant corrosion current, there is then a decrease in corrosion current during the drying.

It is quite sure that uniform corrosion in also reduced during drying period since there is no corrosion in dry concrete.

4. Conclusion

In this chapter the effect of top-bar casting on carbonation induced corrosion in concrete in presence of load induced crack was studied.

Specimens were made only from CEM I cement. It corresponds to small beams (15x15x55 cm) with 2 layers of rebars (Top and bottom), each layer with 2 rebars.

Carbonation is due to ingress of CO_2 (3% CO_2 chamber) in the load-induced crack path.

A part of the macro cell corrosion rate was recorded by using a steel coupon. The total macro cell corrosion rate was then estimated thanks to a numerical modeling of the macro cell corrosion in the small beams. By computing the total electrical charge during the experiments, it was then possible to calculate the loss of mass due to macro cell corrosion.

A gravimetric measurement of loss of mass due to corrosion was performed at the end of the experiments.

The difference between the gravimetric loss of mass and the macro cell loss of mas, allows to calculate to part of uniform corrosion.

Surprisingly, results show that loss of mass due to uniform corrosion is largely higher to the one due to macro cell corrosion. The difference is between 2 to 10 according to the different sample and rebars which corresponds to a high scatter.

Nevertheless, it was shown that the duration of the drying period in the wetting-drying cycles are not favorable for macro cell corrosion since the current decrease quickly during the drying process. Then to compare with the saturated conditions at anode, it is necessary to use the maximum macro cell corrosion current recorded during the wetting process: it corresponds to an increase by 3 times. In virtual fully saturated conditions, the difference between uniform corrosion and macro cell corrosion appears to be positive or negative: in some case the macro cell process is more important; in most cases the uniform process is more important.

Influence of load-induced cracks of carbonation-induced corrosion for both top bars and bottom bars

In Ghantous, the influence of the crack opening on the carbonation-induced corrosion process is tested on specimens subjected to corrosion under raining/drying cycles at 20°C for 30 minute rain duration in each cycle. After a certain number of raining/drying cycles, a decrease in the corrosion rate is detected. This is attributed to rebar repassivation which is due to the corrosion products that seal the cracks and act as a protective layer for the rebar by limiting the access of aggressive agents. Moreover, the corrosion process appears to be independent from the residual crack opening.

One objective of our works was to study the effect of defects at the SCI interface: in particular, are water bleed defects able to modify the conclusions drawn by Ghantous?

First of all, it is worth noting that top bars exhibit a longer carbonation length along the SCI interface from the crack tip. The carbonation length appears to be between 2 times to up to times higher for top bars than bottom bars. Nevertheless, quite surprisingly, carbonation length does not reach the whole length of the top rebars.

Our results are most contrasted than the one from Ghantous. For bottom bars, the final corrosion kinetic at 400 days appears to be comparable to the one of Ghantous at 90 days, which means that the rebar repassivation is not fully achieved. Nevertheless, cumulative electrical charge from macro cell measurement shows a tendency to a reduction of corrosion, corresponding to an induction phase after about 180 days.

For top bars, the corrosion is more important in term of loss of mass in comparison with bottom bars, but the corrosion kinetic is in most case weaker than for bottom bars. In term of only macro cell corrosion, the same conclusions could be drawn, the cumulative electrical charge is always more important for top bars than bottom bars.

Because corrosion kinetic in case of top bars is lower than corrosion kinetic in case of bottom bars, it is assumed that water bleed defects are not detrimental for carbonation-induced corrosion from a load-induced crack.

CHAPTER V. CHLORIDE-INDUCED CORROSION IN PRESENCE OF ARTIFICIAL CRACKS: INFLUENCE OF FIBERS IN PRESENCE OF TOP BAR EFFECT

1. Introduction

Zhang [4] have tested the effect of artificial cracks on the corrosion development due to chlorides, on reinforced concrete. Artificial crack is used to separate the effect of crack path for chlorides to reach quickly the steel re-bars, from the effect of Steel Concrete Interface (SCI) damage due to load-induced cracks. For the sample used by Zhang, the artificial crack is induced on the top bars to study the effect of SCI damage due to water bleeding.

This chapter aims to study the influence of top-bar effect on chloride-induced corrosion, in presence of artificial crack. The new parameter studied in comparison with the work of Zhang [4] is the used of fibers concrete. The idea was to study the effect of fibers on the resistance to corrosion-induced cracking which could increase the acceptable pressure due to corrosion products of covercrete. It was supposed that a higher confinement of corrosion products could help to get an anodic control of corrosion, leading to a decrease in corrosion kinetics. Material of specimens and experiment process is introduced followed the results and discussion on these results. Finally, is the conclusion.

2. Experimental program

2.1. Preparing of reinforced concrete specimens

Twelve samples of reinforced concrete with dimension of 210x150x280 mm in length, width and height, respectively, named G3-1 ÷ G3-12 were prepared. Each specimen contained a frame work consisting of two stirrups with diameter of 6mm and four main steel bars with 12mm in diameter and 160mm in length. Two reinforcements were embedded in the top were named top-front (TF) or top-back (TB) and two reinforcements were placed in the bottom of the concrete named bottom-front (BF) or bottom-back (BB). They were numbered according to the specimens. Also a steel bar with the same dimension was embedded in the center of the framework playing the role of steel coupon in the following corrosion measurement. The cover depths of the stirrups and main bars were 16mm and 21mm, respectively while it was about 69mm to the steel coupon. It should be noted that there were also two others groups (labeled group A and B in Zhang [4]) with similar dimension but different formulation of concrete exposed to the same wetting/drying cycles.

For six samples (G3-4, G3-5, G3-6, G3-10, G2-11 and G3-12) an artificial crack with a width of 1mm and a length of 27mm was applied. A shim was fixed at the middle location of the steel frame work before concrete casting and was removed after initial setting of concrete. No artificial cracks were made on the six remaining specimens including G3-1, G3-2, G3-3, G3-7, G3-8 and G3-9. In several researches [169, 173, 182] concerning the effect of load-induced cracks on corrosion, it was indicated that for long term studies crack width less than 0.5 mm did not affect the corrosion development.

Instead of it, top casting defects was determined to play a more significant role. In addition in presence of small crack width self-healing was observed [155-157]. The object of using an artificial crack is to eliminate the presence of mechanical damage at steel concrete surface due to load-induced crack as well as the mechanisms of self-healing.

Electrical wires were soldered onto the mains bars and the central bar in order to measure a part of the macro cell corrosion current. In addition, the stirrups and main bars were also insulated to prevent the electrical connections between all the bars. The long distance from the central bar to the up and bottom surface (69mm) remains it in passive state during the experiment on corrosion. Neither a pollution due to chlorides nor carbonation could occur at the location of the steel coupon). The electrical current obtained in the following measurement between the main steel bar and the coupon steel is a part of the cathodic corrosion current. For samples G3-1, G3-2, G3-3, G3-4, G3-5 and G3-6, there was a unique wire to connect all mains bar while there were 4 wires connecting each main bar in the samples G3-7, G3-8, G3-8, G3-10, G3-11 and G3-12 (Figure 172, Figure 173). In this last case, each main bar is electrically isolated from the reinforcement lay out.

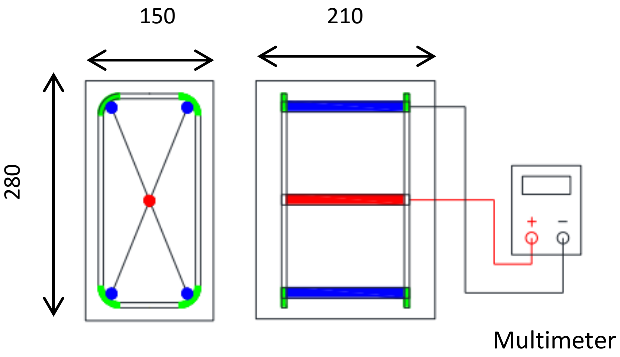

Figure 172. Sample without artificial crack

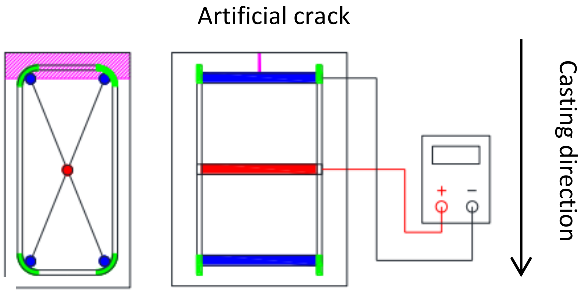

Figure 173. Sample in presence of artificial crack

2.2. Materials

The formulation of the concrete block G3 is summarized in Table 18.

Materials	Quantity (kg/m^3)
CEM I 52.5 R (Lafarge)	435
Sand 0-5 mm	895.3
Gravel 4-10 mm	726.2
Water	217.5
Fibre Dramix 65-35	58.5
Slump	
70 mm	

Table 18. Formulation of concrete

The concrete was added fiber in the compositions. It is known that fibers can help to have a higher tensile strength and then to delay the appearance of corrosion induced crack or in the other words a possibility of inducing a dormant phase of corrosion [228-230]. The autopsy of block at the end of the experiments indicated that there was no corrosion of the fibers in the concrete, which confirms that the chloride threshold initiating corrosion is significantly higher in case of metallic fibers than in case of reinforcing bars.

2.3. Casting and curing

The casting direction is defined from the top bar to the bottom bar as in Figure 172, Figure 173. After casting the blocks were covered with a plastic sheet to avoid shrinkage induced crack. The curing was performed in a standard curing room with a temperature of (20±2)°C and relative humidity of higher than 95% during 28 days followed exposing to chloride environment.

2.4. Exposure conditions

After curing process, all the samples were exposed to a chloride environment by applying a system of wetting-drying cycles (Figure 174). The procedure took place in a wooden chamber. Each cycle included two days of wetting followed by five days of drying. During the wetting period, a salt fog (35g/l of NaCl, corresponding to the salt concentration of seawater) was generated by four spray nozzles located at each upper corner of the chamber. The direction of exposure to chloride environment is from upper to lower surface. The temperature is the same as the natural outdoor environment of southwest of France, with monthly average temperatures ranging from 5.1°C to 21.3 °C and relative humidity varied from 50% to 84%.

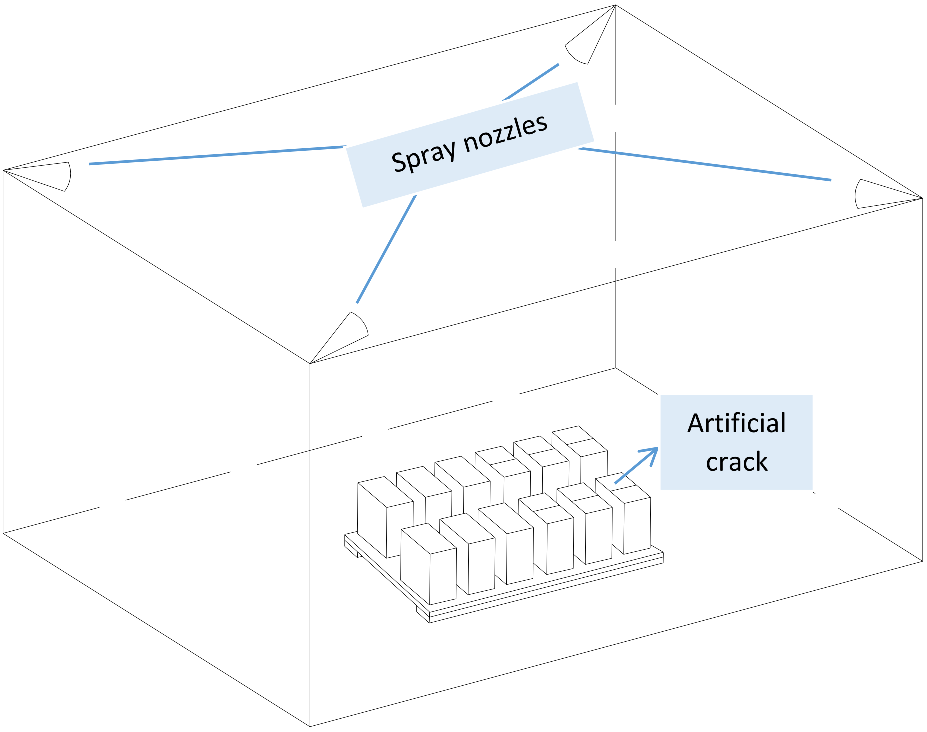

Figure 174. Image of exposure conditions

2.5. Measurement of macro cell corrosion current

The measurement of macro cell corrosion current was based on ASTM G71, utilizing a multi-meter with an accuracy of 0.01 µA. The metallic coupon was connected to the positive pole of the equipment while the main bar was linked to the negative pole. The received data indicated the macro cell current which resulted from the potential decrease of the steel bar. The measurement was carried out weekly, on the first day of the drying period.

3. Results and discussions

3.1. Cracking map

The specimens with and without artificial crack were submitted to 85 and 94 wetting-drying cycles, respectively. Corrosion induced cracks were observed after 64th wetting-drying cycles of wetting-drying, but the widths of corrosion-induced crack were only measured at the end of the experiments by using a portable microscope with an accuracy of 0.01 mm. Following is drawn the cracking map Table 19.

The cracks which were induced by corrosion were found on the surfaces of several blocks including both samples in presence of artificial crack (G3-01, G3-02 and G3-03) or not (G3-04, G3-06, and G3-11). Most of the longitudinal cracks appeared at the location of the upper steel bars.

In samples with artificial crack, the presence of corrosion-induced crack was recorded only on the back side of the block. On the other hands, in the sample without artificial crack, the observation of corrosion-induced crack was found on the front, back and left surface of the block.

The width of corrosion-induced crack was in the range of 20 to 500 µm.

Sample	Location	Width of corrosion-induced crack (µm)
G3-01(no AC)	Front side	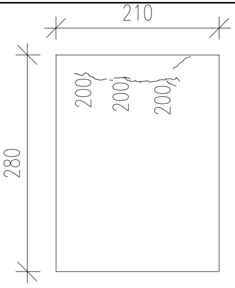
	Left	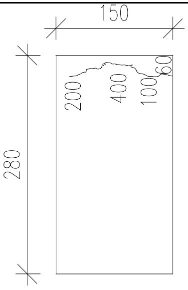
G3-02 (no AC)	Back	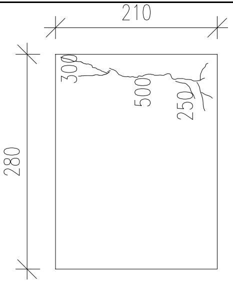
	Left	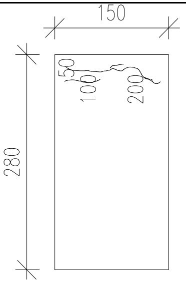
G3-03 (no AC)	Front	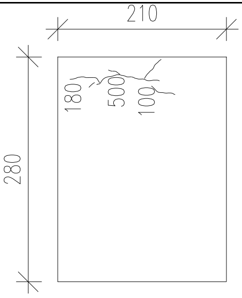

G3-04 (AC)	Back	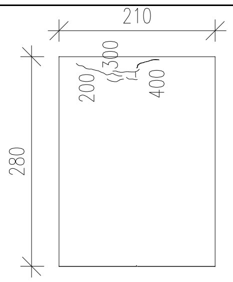
G3-06 (AC)	Back	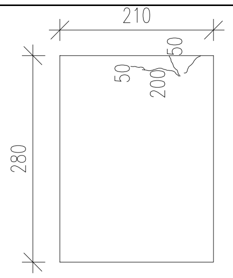
G3-11 (AC)	Back	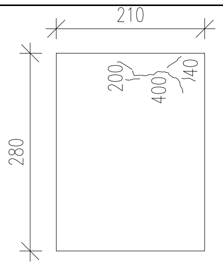

Table 19. Cracking map of specimens

- *81st wetting/drying cycle in case sample with AC*
- *90th wetting/drying cycle in case sample without AC*

It is really interesting and quite surprising that corrosion-induced cracks were recorded at about the same period of time for samples with or without artificial cracks. One reason for this result could be that the artificial cracks act as an expansion tank: artificial crack is filled by corrosion products without any pressure on the concrete cover, and only when corrosion propagated along the rebar and crack path is filled, there is enough pressure to induce cracking. Another surprising result is the fact that only the main rebar of the samples with Artificial Crack was concerned by the appearance of the corrosion induced crack. On the contrary, there is the appearance of corrosion-induced cracks on the end faces of the concrete blocks without artificial cracks: it corresponds to the presence of the stirrups (Figure 175).

Figure 175 : Example of corrosion on stirrup

It is also very interesting to see that some samples do not exhibit any corrosion induced cracks during the experiments. When comparing with the results from Zhang, it appears that there is a delay in the appearance of the corrosion-induced cracking in case of concrete reinforced by fibers: at least fourth time difference to induce the first corrosion induced crack. Moreover, for fibers reinforced samples which do not exhibit corrosion-induced cracking before the end of the experiment, this difference in time is then higher than fourth time. This result shows that fibers could play a role to control the corrosion-induced cracking.

The development and appearance of corrosion induced crack were also found one year after stopping the wetting/drying cycles (Table 20). In addition of the widening of existed cracks, there was recorded the presence of new longitudinal crack on surface of other specimens (G3-08, G3-09). Nevertheless, the position remained mainly adjacent to the bottom side of upper steel bar.

Sample	Location	Width of corrosion-induced crack (µm)
G3-01 (No AC)	Front	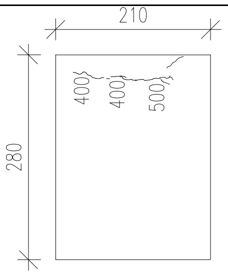
G3-02 (No AC)	Back	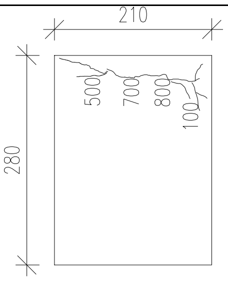

G3-03 (No AC)	Back	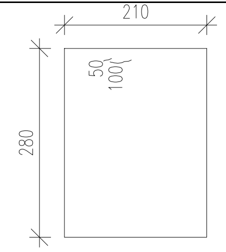
	Front	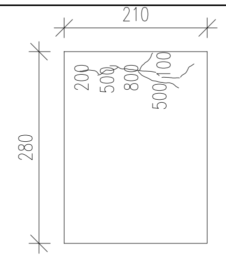
G3-04 (AC)	Back	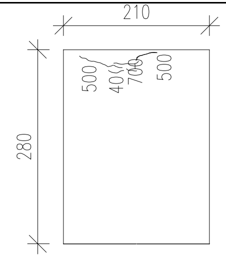
G3-06 (AC)	Back	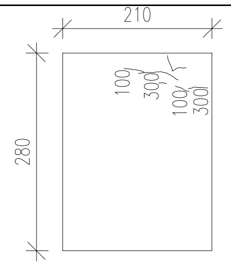
G3-08 (No AC)	Back	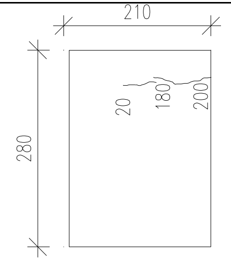
G3-09 (No AC)	Front	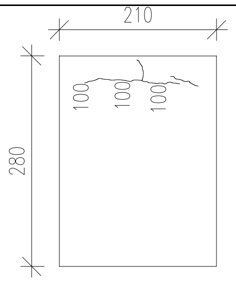

	Back	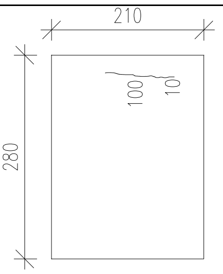
G3-11 (AC)	Back	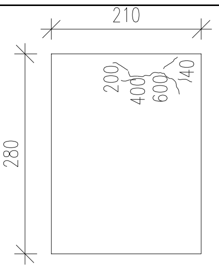
	Front	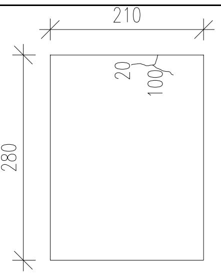

Table 20. Cracking map of specimens (one year after stop the measurement of macro cell current)

It can be observed the presence of corrosion induced crack in both specimens with or without artificial crack. In addition, longitudinal corrosion-induced cracks were found longer in the samples without artificial crack. Indeed, there was presence of new corrosion-induced cracks on G3-08 and G3-09, specimens without artificial crack, besides the growth of previous crack on old samples (G3-01, G3-02, G3-03, G3-04, G3-06 and G3-11). It seems that the existence of pre-crack is not the main reason for the development of corrosion induced crack in this case.

In case of specimens with artificial crack, corrosion induced cracks were observed to commence at the location near the artificial crack. The description of corrosion induced crack widths for all the specimens is resumed in Table 21.

Sample	Before stop wetting/drying cycle	One year after stop wetting/drying cycles	Location of corrosion induced crack
G3-01 (no AC)	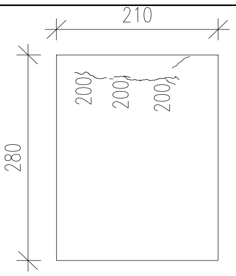	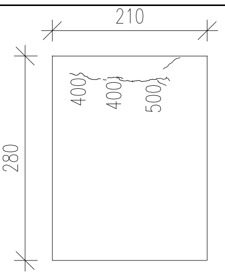	Front side
G3-02 (no AC)	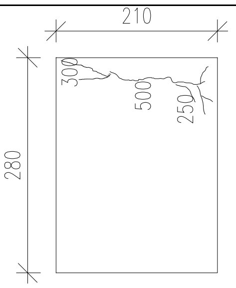	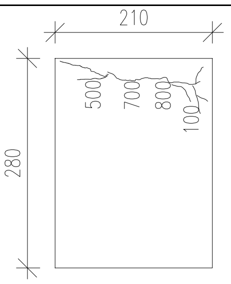	Back side
G3-03 (No AC)	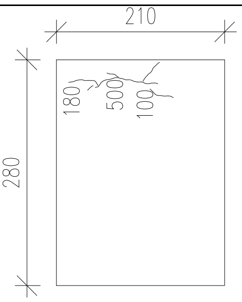	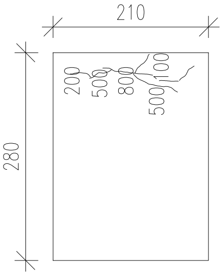	Front side
		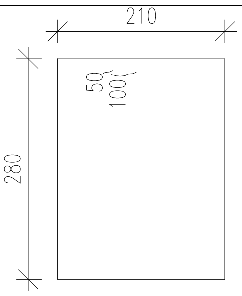	Back side
G3-04 (with AC)	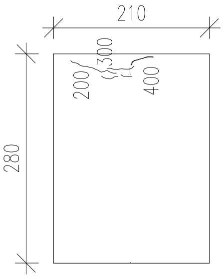	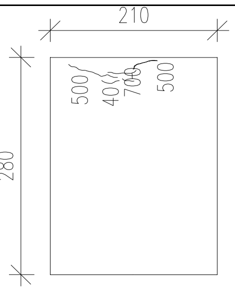	Back side

G3-05 (with AC)			No corrosion induced crack
G3-06 (with AC)	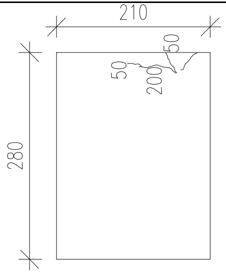	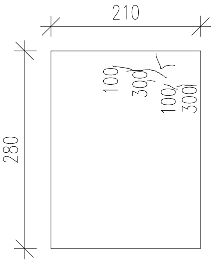	Back side
G3-07 (NO AC)			No corrosion induced crack
G3-08 (No AC)		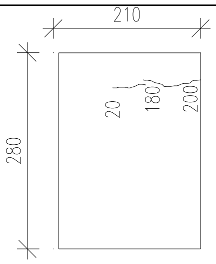	Back side
G3-09 (No AC)		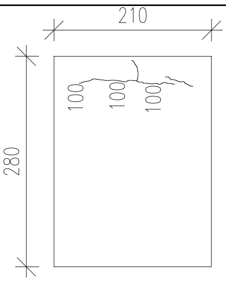	Front side
G3-10 (with AC)			No corrosion induced crack
G3-11 (with AC)	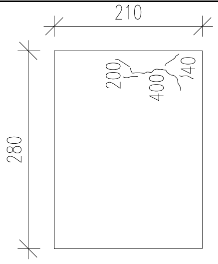	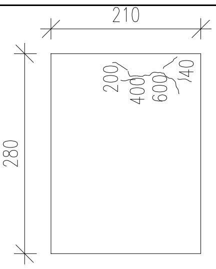	Back side

		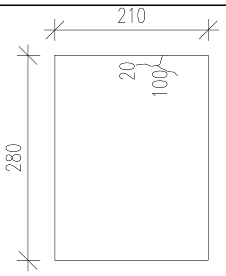	Front side
G3-12 (with AC)			No corrosion induced crack

Table 21. Description of corrosion induced crack

For the samples tested by Zhang [4] without fibers, the first corrosion-induced cracks appears after 16 wetting-drying cycles on the specimens B-1.

Zhang indicated in his PhD thesis that after 45 wetting-drying cycles (about 1 year of exposure) all the samples with artificial cracks exhibited corrosion-induced cracks.

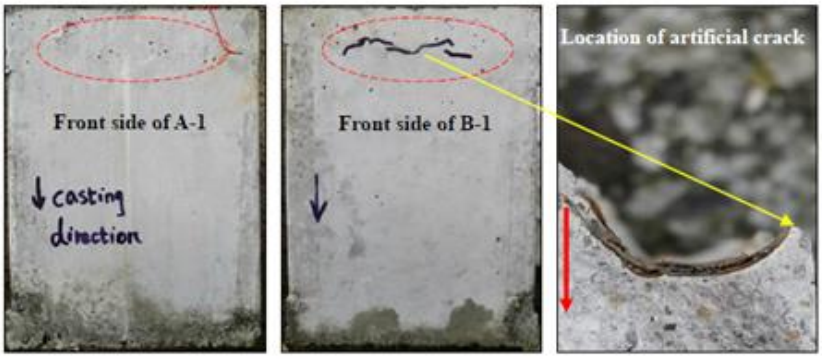

(a) Front side of A-1 (b) Front side of B-1 (c) Cross-section of B-1 at artificial crack

Figure 176 : appearance of first corrosion-induced crack from Zhang [4]

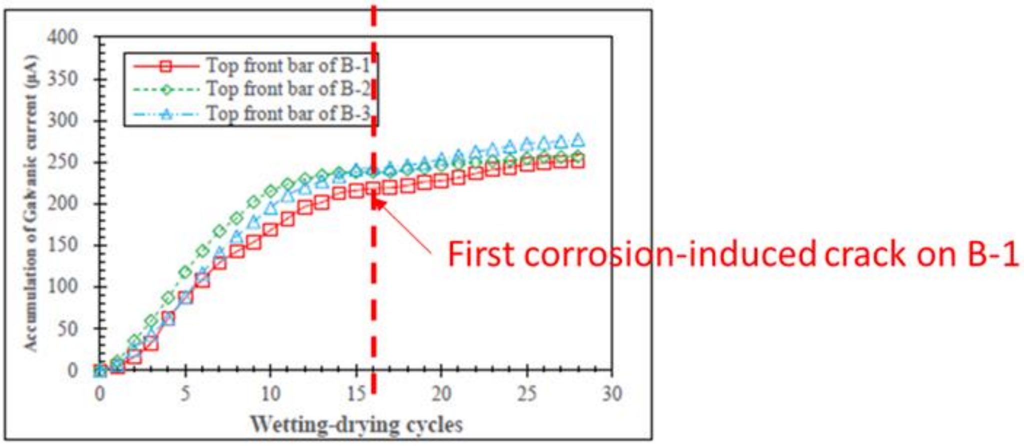

Figure 177 : the first corrosion-induced cracks appears quickly after the change in slope on B-1 samples (from Zhang [4])

3.2. Autopsy of specimens to analyze the corrosion along the reinforced steel bar

After monitoring the corrosion current, the block concrete was cut into smaller prisms (number 1-2-3-4 in Figure 178 and Figure 179), including two located in the upper side and two located in the lower side of the concrete. Each small block contained a main steel bar thereafter was split along the bar to obtain the top and bottom of steel concrete interface.

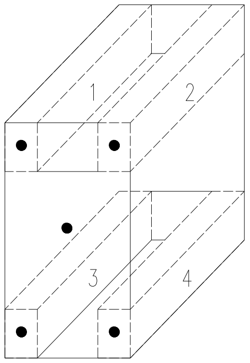

Figure 178. Illustration of position of the prism (block without AC)

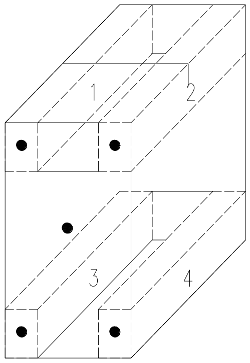

Figure 179. Illustration of position of the prism (block with AC)

After splitting the smaller specimens and extracting the reinforcement, several visual inspections were found.

The concrete color of the top was observed deeper than of the bottom bar in all steels interface (Figure 180, Figure 181). The reason is that during the bleeding and settlement of fresh concrete, a loose and porous layer of cement hydration products formed at the lower side of steel due to the top casting effect in compare to a denser layer in the upper side.

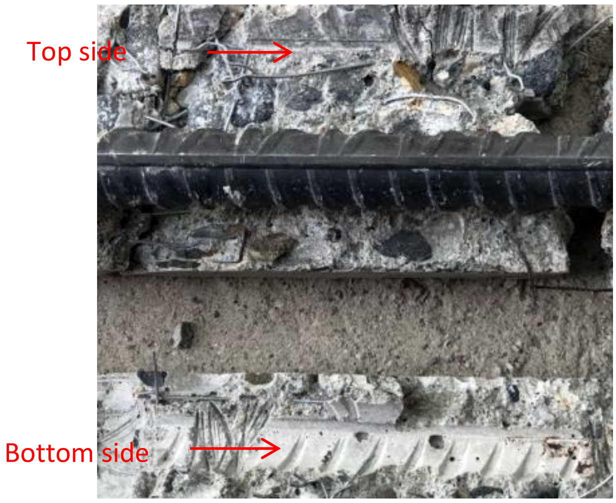

Figure 180. Picture of the color in the SCI of a bottom bar

Figure 181. Picture of the color in the SCI of a top bar

For all concrete block, the SCI exhibited more corroded zone in two top bars than in the bottom bars. However, it was more clear visualization with the upper steel bars embedded. Also in a steel bar, the upper sides showed less imprint of corrosion than the lower side (Figure 182, Figure 183, Figure 184 and Figure 185).

Figure 182. Picture of imprint of corrosion in the SCI of a bottom bar (with AC)

Figure 183. Picture of imprint of corrosion in the SCI of a top bar (with AC)

Figure 184. Picture of imprint of corrosion in the SCI of a bottom bar (without AC)

Figure 185. Picture of imprint of corrosion in the SCI of a top bar (without AC)

About the location of corrosion products, it was observed that rust stains mainly existed at the rib foot zone rather than the voids zone. Indeed, corrosion products could be found in the position of rib zone and with presence of voids or no presence of voids while no corrosion could be recorded in the position of voids without presence of rib. This observation is in accordance with research by Zhang et al [231].

Following the reinforcement was cleaned to remove the corrosion products on the surface. After that the reinforcement was weighed utilizing a balance with a precision of 0.01g. The loss of mass of steel bar for top bar and bottom bar were exhibited in Figure 186 and Figure 187.

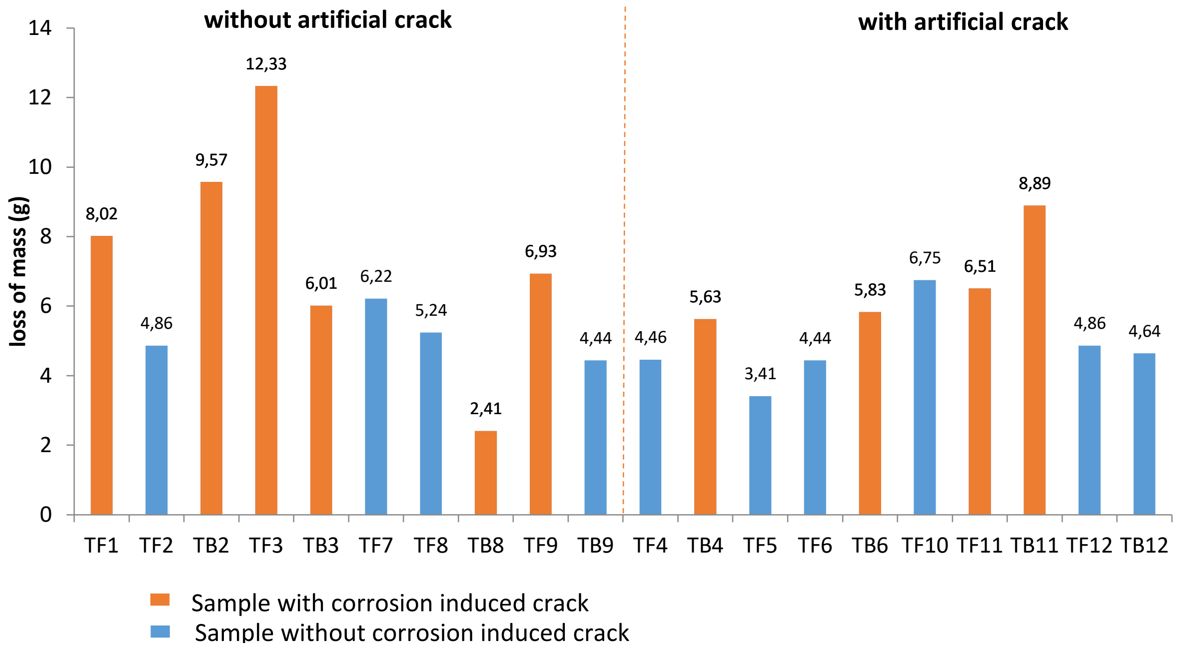

Figure 186. Loss of mass in case of top bars

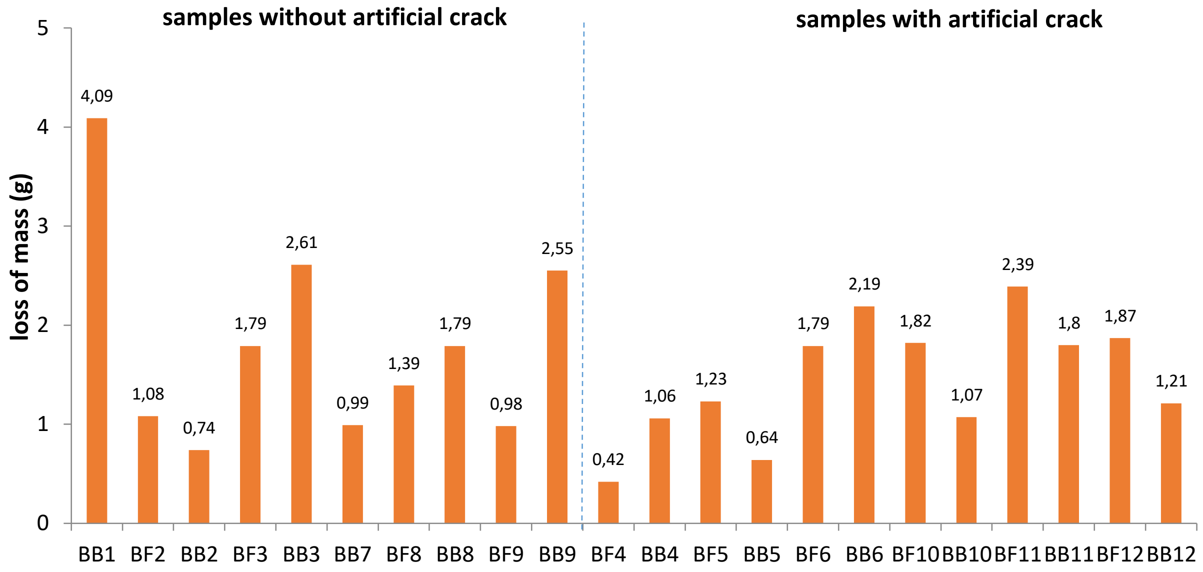

Figure 187. Loss of mass in case of bottom bars

From the measurement of the loss of mass due to corrosion (Figure 186 and Figure 187) it is possible to draw some remarks. Firstly, despite some scatters between the different re-bars, there is no effect of the presence of the artificial crack on the loss of mass, on top bars, at the end of the experiments. This result confirms that top surface exposure to chloride spray and top bar effect are more important parameters than for corrosion development cracks (even artificial crack) in case of weak concrete cover: only 21 mm for this study. Same conclusions were drawn, in case of load-induced cracks, by François et al. [182] and Yu et al. [169]. Secondly, bottom bars with the same concrete cover as top bars, exhibit a significantly lower loss of mass due to corrosion in comparison with top bars. In this case, the difference of corrosion level is linked to the difference in concrete porosity and SCI quality: top part of concrete specimens is more porous than bottom part and there are no macroscopic defects at SCI for bottom bars as shown in Soylev and François [191, 200]. It is worth noting that the level of corrosion found on bottom bars is not sufficient to induce cracks due to corrosion.

Finally, it is also interesting to see that the loss of mass measured on top bars are generally higher in presence of corrosion-induced cracks (Figure 186), and the threshold value of loss of mass leading to the appearance of corrosion-induced cracks is about 6 g.

It is interesting to compare the visual damage due to corrosion for the samples using concrete reinforced by fibers in terms of corrosion-induced cracks width, with the existing models built on concrete without fibers, such as the one of Vidal et al. [232] and Khan et al. [233].

Correlation with corrosion-induced crack width and corrosion of the re-bars

The local cross section loss initiating cracking is determined by equation proposed by Vidal et al. [232]:

$$\Delta A_{s0} = A_s \left[1 - \left[1 - \frac{2 pf_g}{\Phi_0} \left(7.53 + 9.32 \frac{c}{\Phi_0} \right) 10^{-3} \right]^2 \right]$$

Equation 25

Where:

- Δ A_{s0} (mm2) is the local cross section loss leading to the occurrence of corrosion induced crack,
- As (mm^2) is the nominal cross-section of the steel bars,
- $Ø_0$ (mm) is the nominal diameter of the reinforcement,
- c (mm) is the distance between the reinforcement and the outer concrete surface,
- pf_g is the geometric pitting factor, taken as equal to 4 for chloride induced corrosion.

From Equation 25, the local loss of cross section which could initiate the first corrosion induced crack is then 3.56 mm^2, which correspond to 3.1% of loss of cross-section. If we supposed a full corrosion along the rebar, this percentage of loss of cross-section would correspond to 4.4 g of loss of mass. It is worth noting that this value is never reach for bottom bars (Figure 187), which is coherent with the fact that no corrosion-induced cracks are visible on the concrete surface on front of bottom bars.

From this result, and considering the scatters in the results, it seems that the presence of fibers increases slightly the minimal local loss of cross section which initiated the first corrosion-induced crack which is closed to 6 g. It is not necessary a surprising result since the pressure induced by corrosion products could sharply increase for a small amount of loss of mass, since the available space in porosity of at SCI defects is already full of corrosion products.

The local cross section loss is then calculated (from François at al. [19] adapted from Khan et al. and Vidal et al.):

$$\Delta A_s = \frac{w_{eq}}{K} + \Delta A_{s0}$$

Equation 26

Where:

- ΔA_s (mm2) is the local cross section loss,
- ΔA_{s0} (mm2) is the local cross section loss leading to the occurrence of corrosion induced crack,
- W_{eq} (mm) is the equivalent of crack opening,
- K=0.0575 a proportionality coefficient.

The distribution of cross section loss along the length of reinforcement in block concrete with presence of corrosion induced crack was performed as in Figure 188, Figure 189.

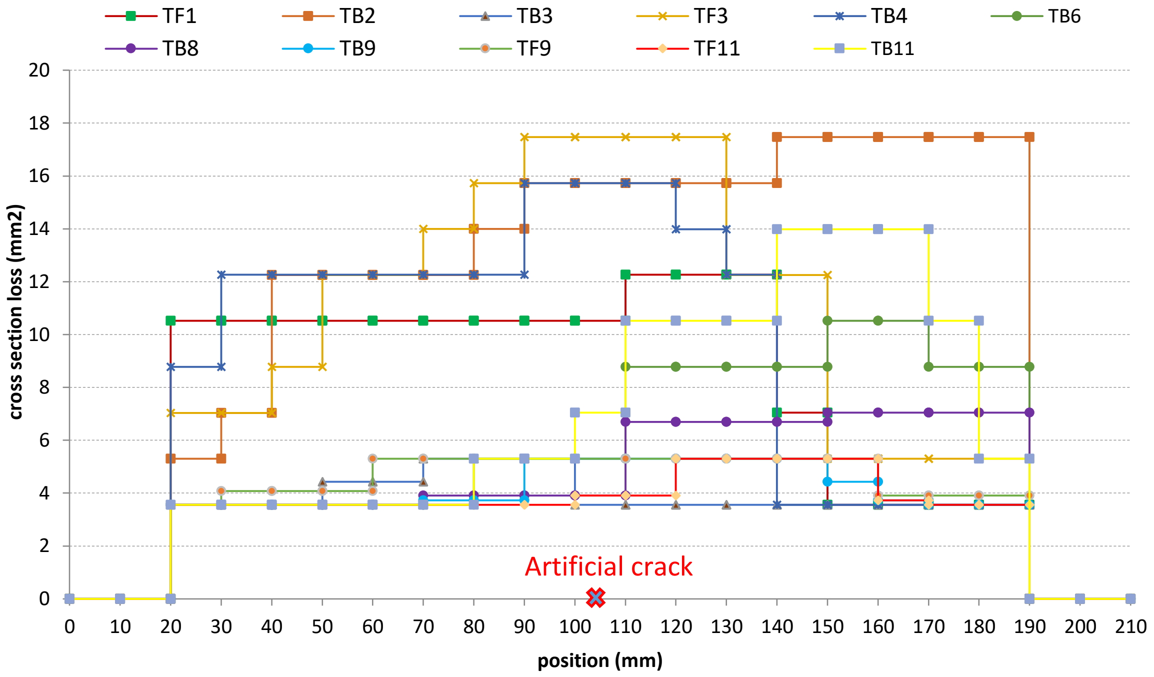

Figure 188. Cross section loss (mm) of samples

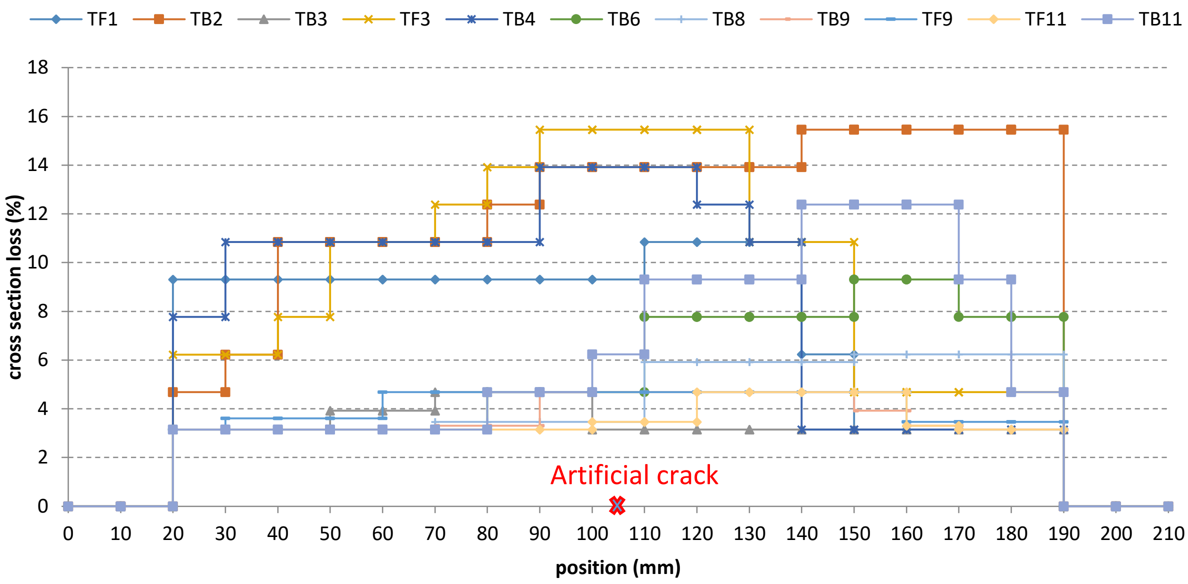

Figure 189. Cross section loss (%) of samples

The mass of loss then was calculated and displayed in Figure 190. It is important to notice that loss of mass corresponds to the maximal values of local loss of cross-section, which by definition could not be constant all along the re-bars, since it is local loss of cross-section: i.e. the distribution of pitting corrosion along the re-bars.

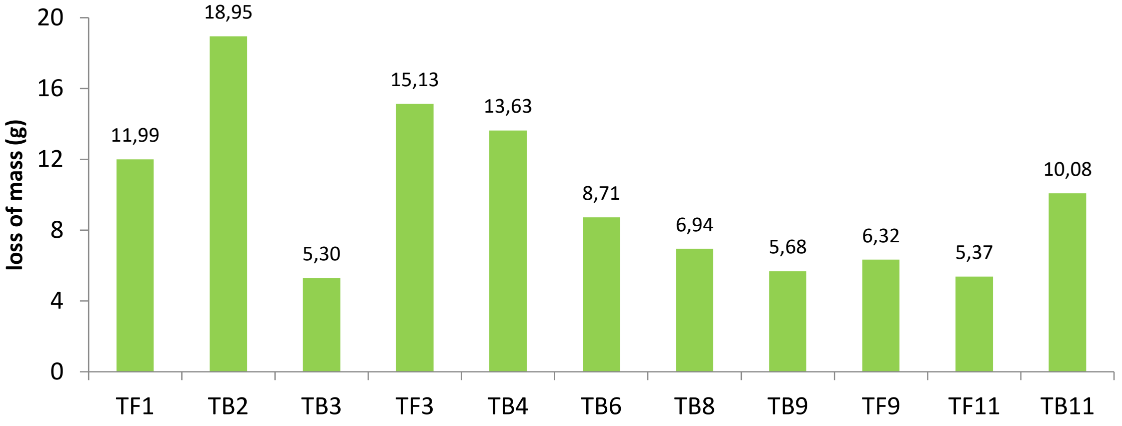

Figure 190. Local Loss of mass according to Vidal et al. equation

There is another model to predict the average (or generalized) loss of cross-section due to corrosion. The average cross section loss is calculated using this equation proposed in [233, 234] and exhibited in Figure 191.

$$\Delta A_{sm} = 5.22\frac{c}{\varphi}\left(w_{eq} - 0.164\right) \qquad \textit{Equation 27}$$

Where:

- W_{eq} (mm) is the equivalent crack opening in mm
- C (mm) is the reinforcement concrete cover
- Ø (mm) is the reinforcement diameter
- ΔA_{sm} (mm^2) is the average cross section loss

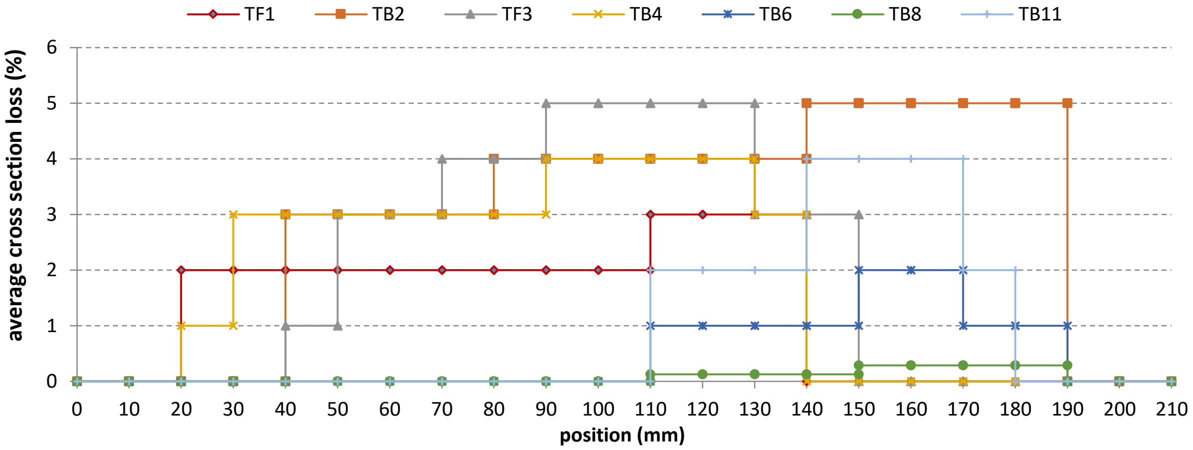

Figure 191. Average cross section loss of samples

The loss of mass calculated from average cross section loss are shown in Figure 192. Because this loss of mass corresponds to an average value of corrosion along the reinforcement, it could be compare with the value recorded by gravimetric measurement and presented in Figure 186.

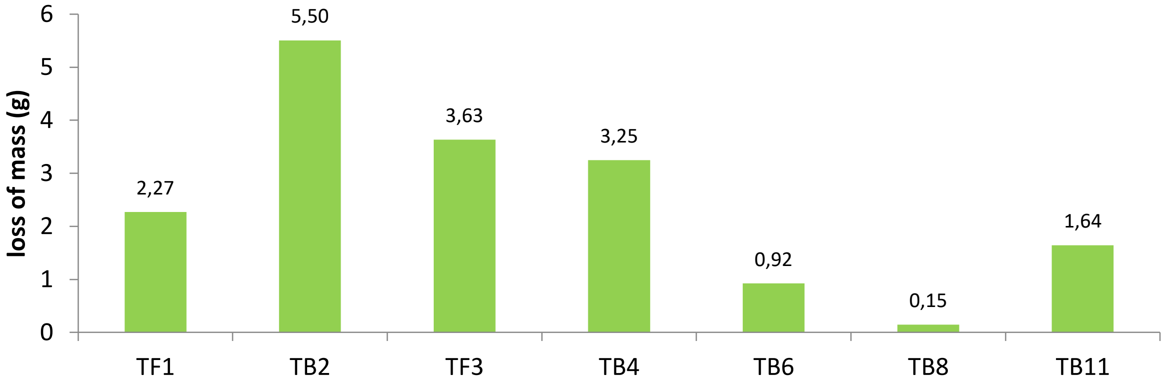

Figure 192. Generalized Loss of mass from average cross section loss

By comparing the results from gravimetric measurement and the predicted values from Khan et al. model (Figure 193), it is clear that the real loss of mass is significantly higher than the predicted one. As a result, that means that fibers allow to reduce the opening of corrosion-induced cracks. This result is not surprising, since when corrosion-induced cracks already exist, the corrosion products could fill the crack path and the increase in pressure could lead to both an increase of crack opening, which is controlled by fibers, and to an exit of corrosion products outside the concrete and the end of the crack path.

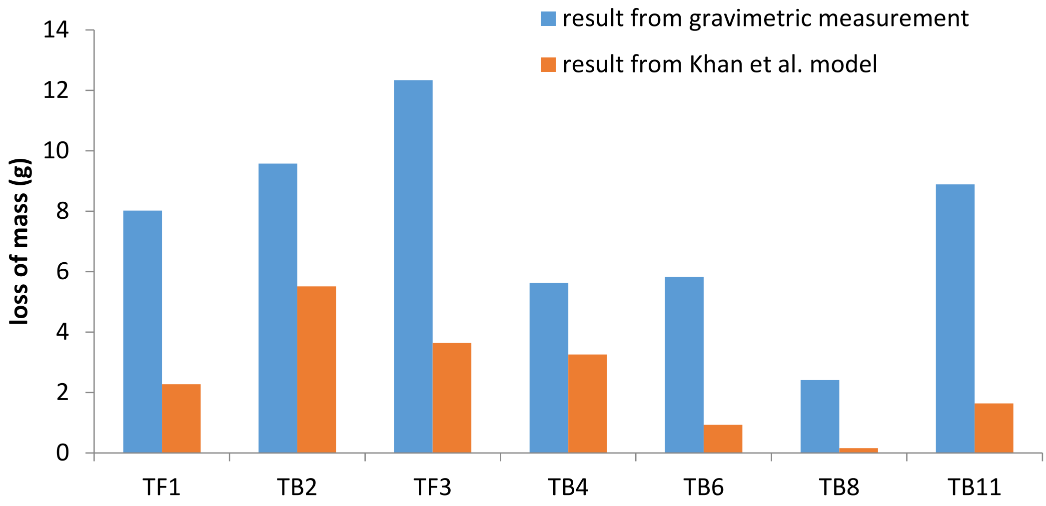

Figure 193. Comparison between the results from gravimetric measurement and the predicted values from Khan et al. model

It is interesting to check the corrosion pattern along the rebars: top or bottom, and according to the presence or not of artificial crack. Corrosion of steel bars at the end of the experiments then was shown in Figure 194, Figure 195.

- In the case with presence of artificial crack on the concrete block, but only in front of top bars:

Top bar

Bottom bar

TB4- top side

BB4-top side

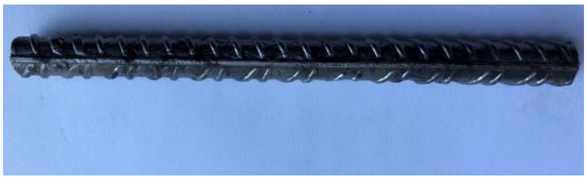

TB4- bottom side

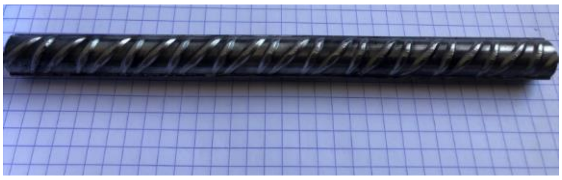

BB4-bottom side

TF4- top view

BF4-top view

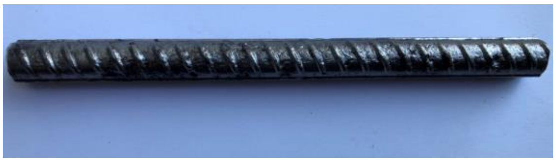

TF4- bottom side

BF4-bottom side

TF5-top side

BB5- top side

TF5- bottom side

BB5-bottom side

BF5-top side

BF5-bottom side

TB6-top side

BF6-top side

TB6-bottom side

BF6-bottom side

TF6-top side

BB6- top side

TF6- bottom side

BB6-bottom side

TF10-top side

BB10-top side

TF10- bottom side

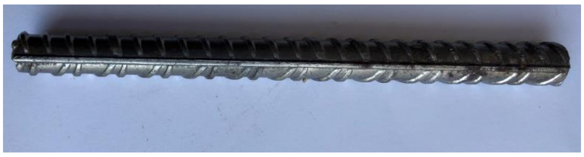

BB10-bottom side

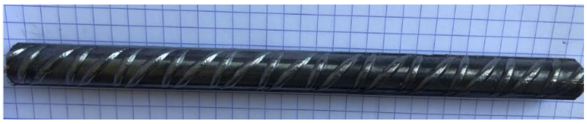

BF10-top side

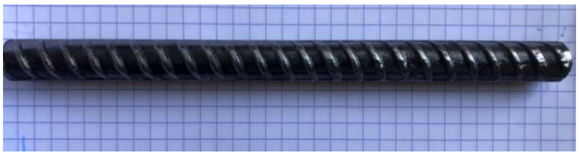

BF10-bottom side

TB11-top side

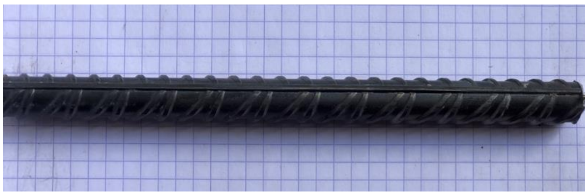

BB11-top side

TB11-bottom side

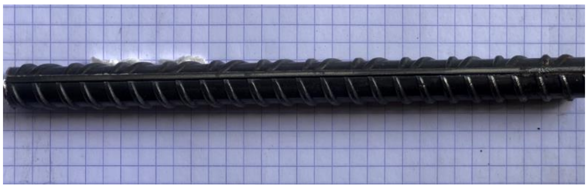

BB11- bottom side

TF11-top side

BF11- top side

TF11- bottom side

BF11- bottom side

TB12-top side

BB12-top side

TB12-bottom side *BB12-bottom side*

TF12-top side *BF12-top side*

TF12- bottom side *BF12-bottom side*

Figure 194. Corrosion of rebar in specimens with artificial crack

- In the case without presence of artificial crack on the concrete block:

Top bar Bottom bar

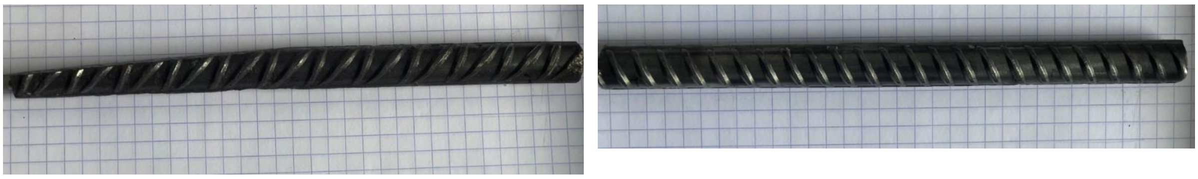

TB1-top side *BB1- top side*

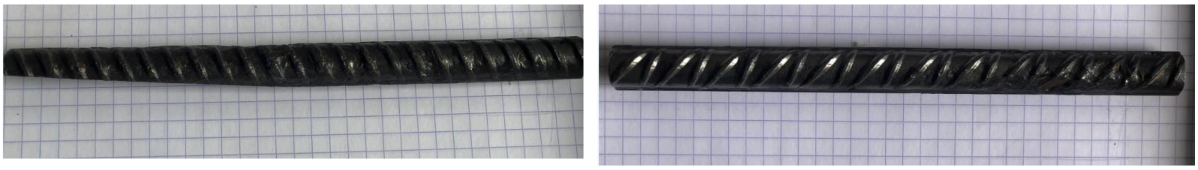

TB1-bottom side *BB1-bottom side*

TF1-top side

BF1-top side

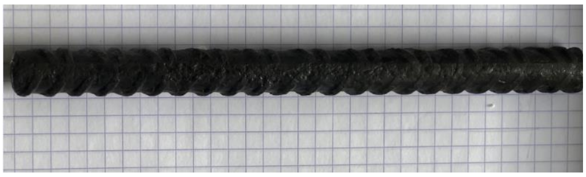

TF1- bottom side

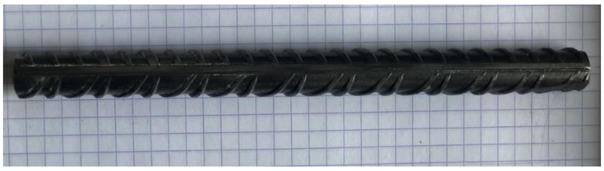

BF1-bottom side

TB2-top side

BB2-top side

TB2-bottom side

BB2-bottom side

TF2-top side

BF2- top side

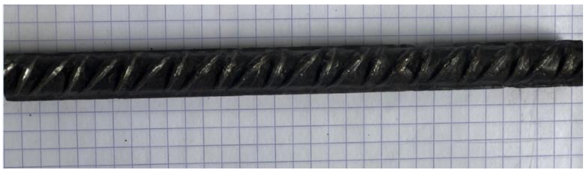

TF2- bottom side

BF2-bottom side

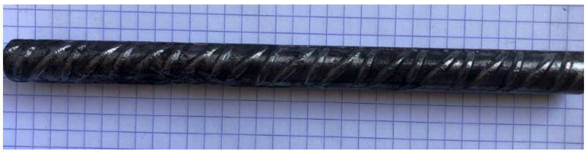

TB3-top side

BB3-top side

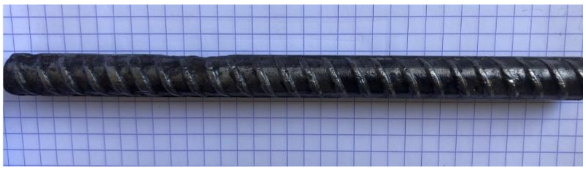

TB3-bottom side

BB3-bottom side

TF3-top side

BF3- top side

TF3- bottom side

BF3- bottom side

TB7-top side

BB7-top side

TB7-bottom side

BB7-bottom side

TB8-top side

BF8-top side

TB8-bottom side

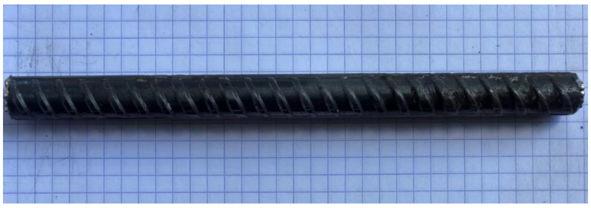

BF8-bottom side

TF8-top side

BB8- top side

TF8- bottom side

BB8- bottom side

TB9-top side

BB9-top side

TB9-bottom side

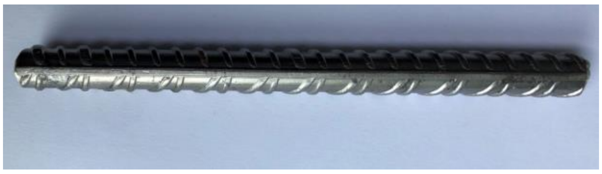

BB9-bottom side

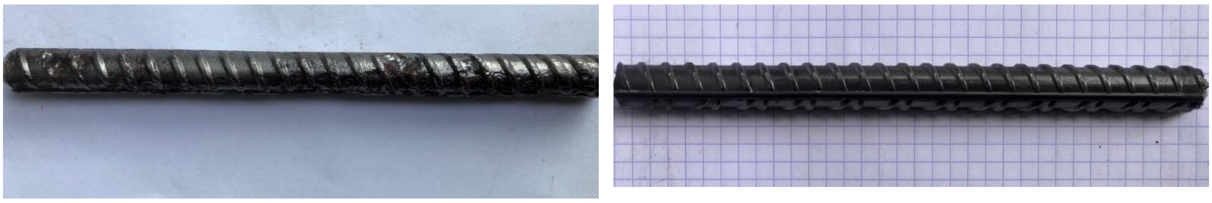

TF9-top side *BF9-top side*

TF9- bottom side *BF9-bottom side*

Figure 195. Corrosion of rebar in specimens without artificial crack

It could be observed that all the top bars were much corroded than the bottom bars. For each top bar, the bottom side recorded more corrosion than the top side.

Corrosion maps of top steel bars in the samples where each bar was connected to the coupon after being cleaned were drawn to study the distribution of pitting corrosion along the length. Each rebar was divided into the top surface and bottom surface according to the casting direction. The red line indicates the location of corrosion.

- In the case with artificial crack:

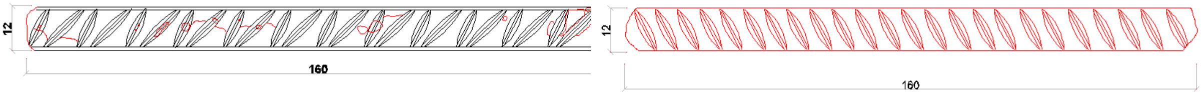

TB12- top side- corrosion *TB12- bottom side- corrosion*

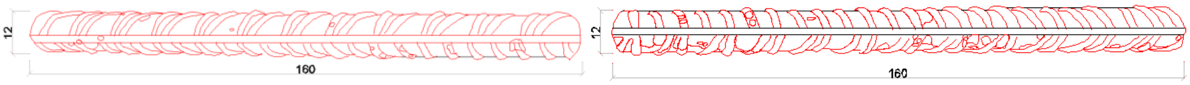

TF12- top side- corrosion *TF12- bottom side- corrosion*

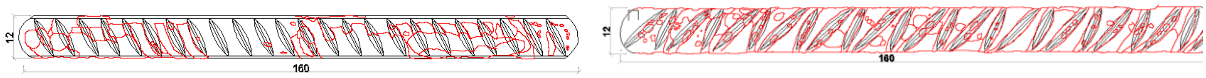

TF11-top side- corosion *TF11- bottom side – corrosion*

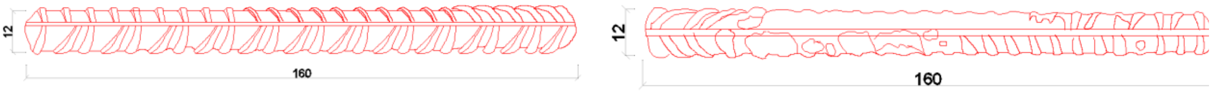

TB11- top side- corrosion *TB11- bottom side – corrosion*

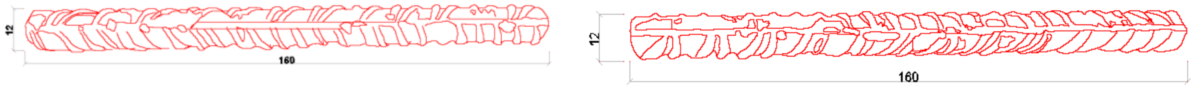

TF10- top side- corrosion *TF10- bottom side- corrosion*

Figure 196. Corrosion maps of top bar in samples with artificial crack.

It is worth noting that despite the presence of an artificial crack, the corrosion is not located in front of the crack path. On the contrary, the corrosion spread all along the rebar, especially of the bottom side. This is indeed a huge difference with the result of Lucas Hess [3] and this difference is due to the presence of SCI defects at the bottom side of rebar resulting from the top bar effect.

- In the case without artificial crack:

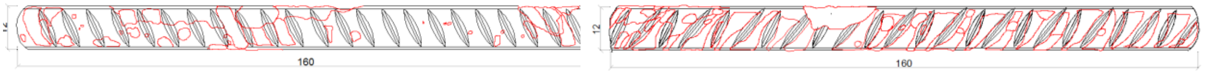

TB7- top side- corrosion *TB7- bottom side- corrosion*

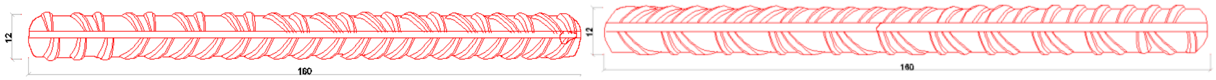

TF8- top side- corrosion *TF8- bottom side- corrosion*

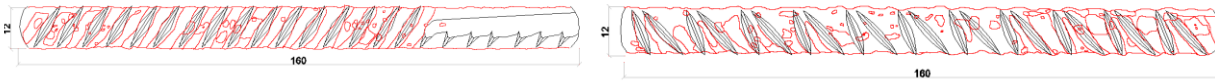

TB8- top side- corrosion *TB8- bottom side- corrosion*

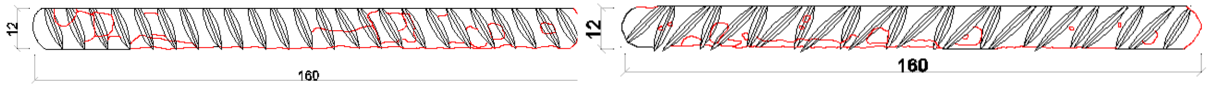

TF9- top side- corrosion *TF9- bottom side- corrosion*

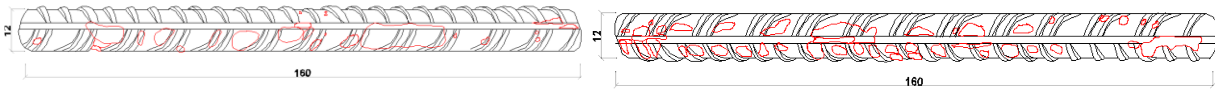

TB9- top side- corrosion *TB9-bottom side- corrosion*

Figure 197. Corrosion maps of top bar in samples without artificial crack.

Without the presence of an artificial crack, the corrosion also spread all along the rebar, especially of the bottom side. This is also due to the presence of SCI defects at the bottom side of rebar resulting from the top bar effect.

Concerning the corrosion pattern: corrosion was found almost along all the top reinforcements with a thin layer dominate and small pitting (1-2 mm in length) mainly on the top side for example TB7, TF8 or thin layer and huger pitting (up to 2-3 cm in length for example TF9, TF 11). Corrosion width was up to more than 1mm in TF11, TF9.

3.3. Effect of top-bar effect and presence of artificial crack on corrosion process

3.3.1. Corrosion process in presence of artificial crack: specimens G3-10, G3-11 and G3-12

According to the 4-phases phenomenological corrosion model (Figure 198) the duration of incubation was observed too short to be recorded: corrosion occurs at the first wetting-drying cycles.

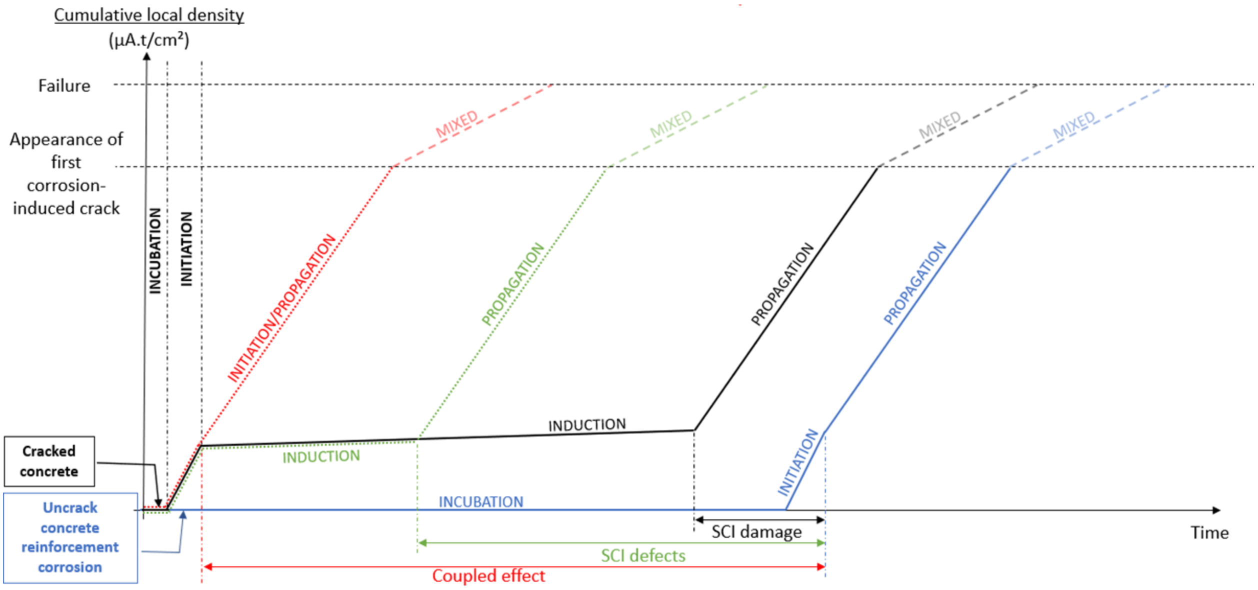

Figure 198 : phenomenological model of corrosion: 2-phases without cracks, 4-phases with cracks adapted from [19]

It could be explained by the contact of chloride to top side of steel bar by the preferable penetration via the crack path. The initiation phase occurred until the 10-20th wetting-drying cycle followed by the propagation phase. Corrosion induced crack was identified in several samples including G3-4 (front side), G3-6 (back side) and G3-11 (back side and front side). No crack induced by corrosion was detected in the others (G3-5, G3-10 and G3-12).

Macro cell (or galvanic) current measurement

The 3 specimens G3-10, G3-11 and G3-12 are detailed: each specimen has 2 top bars which are in contact with the artificial crack, and 2 bottom bars (without any cracks).

It is quite interesting to notice that for the 6 top bars in contact with the artificial crack, the behavior is comparable.

There is a quick increase in the cathodic current measured by the steel coupon which reaches a value close to 40 µA. Then after 5 to 10 wetting drying cycles, the cathodic current decrease to be almost neglectable: it corresponds then probably to the spreading of corrosion along the rebar thanks to the SCI defects. It corresponds then to the propagation period.

Specimens with artificial cracks: G3 -12 (Figure 199)

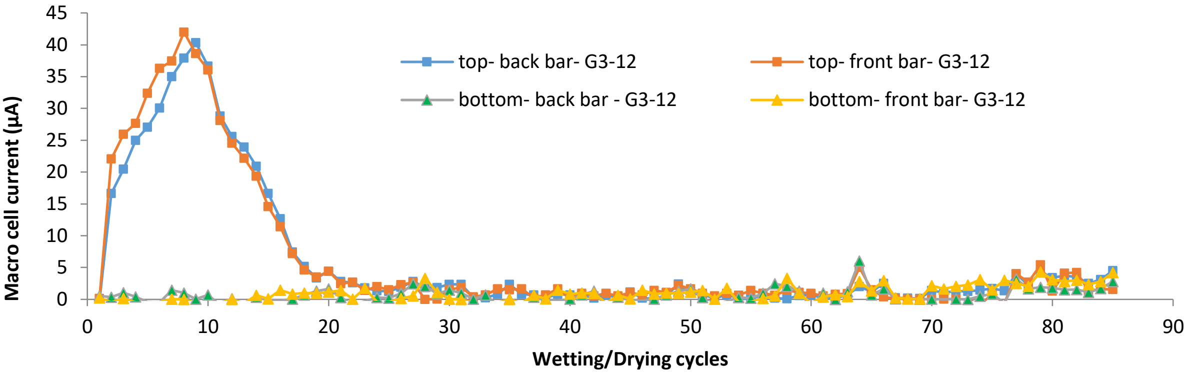

Figure 199 : macro cell corrosion current between all bars and the steel coupon (specimen G3-12): top bars are in contact with the artificial crack

Specimens with artificial cracks: G3 -11 (Figure 200)

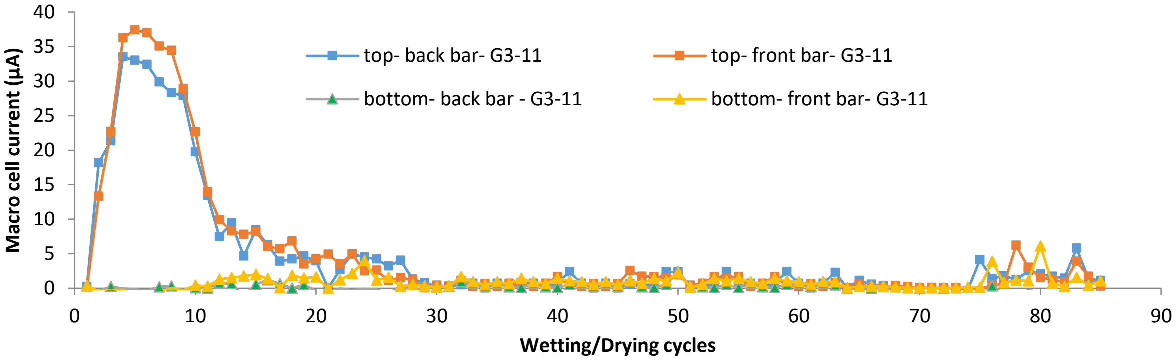

Figure 200 : macro cell corrosion current between all bars and the steel coupon (specimen G3-11): top bars are in contact with the artificial crack

Specimens with artificial cracks: G3 -10 (Figure 201)

For the specimen G3-10, the top back bar was extracted after 4 cycles of wetting and drying.

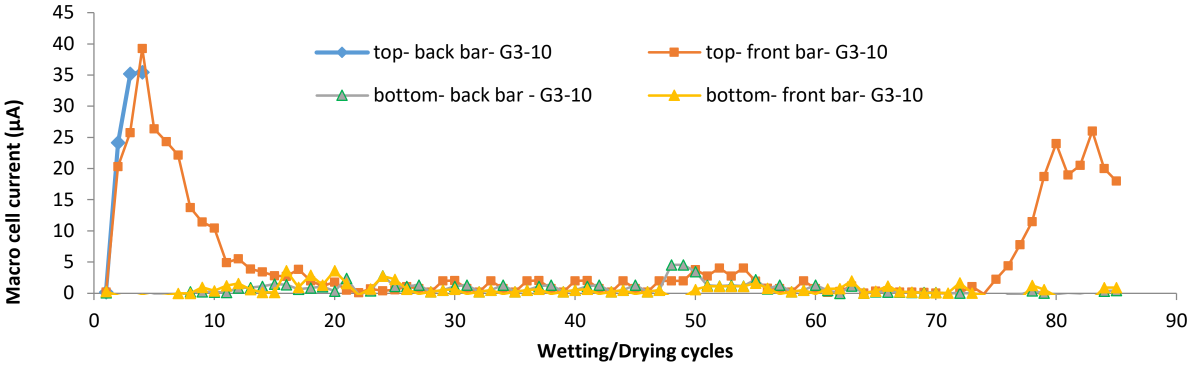

Figure 201 : macro cell corrosion current between all bars and the steel coupon (specimen G3-10): top bars are in contact with the artificial crack

Autopsy of top bar of G3-10 specimen after 4 wetting drying cycles:

After 4 cycles of exposure and because exhibiting a high corrosion current, one top bar of the G3-10 was extracted. Corrosion can be seen at the level of the artificial crack, but only on the bottom part (Figure 202). A zoom is available on Figure 204.

Figure 202 : top back bar of G3-10 specimen extracted after 4 cycles : bottom view

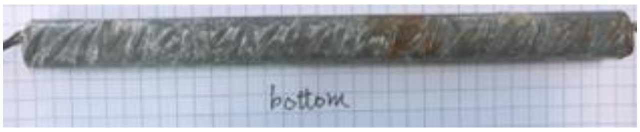

Figure 203 : top back bar of G3-10 specimen extracted after 4 cycles: top view

Surprisingly, no corrosion is visible on the top part of the re-bar which is just in front of the chlorides ingress (Figure 203). Nevertheless, it is clear from the pictures that corrosion current is really related to corrosion at the crack location.

Figure 204 : Zoom of the corrosion at the location of the artificial crack after 4 cycles (top back bar of G3-10 specimen)

The autopsy of the top back bar of the G3-10 specimens confirms that the high current recorded during 10 wetting-drying cycles is associated with the corrosion in front of the artificial crack

(Figure 204). Then the spreading of corrosion along the rebar, which correspond to the propagation period, is associated to a weaker corrosion current, probably associated to the decrease in C/A ratio.

For samples with artificial crack, there are also 2 bottom bars in each which are not concerned by the artificial crack. For theses bottom bars, the cathodic current recorded by the steel coupons appears to be null only during the first 10 wetting cycles. It corresponds then to an incubation period which is quite short but significantly more important than in the case of top bars without artificial cracks as we will see later. The difference between top bars and bottom bars must be in relation with the higher porosity at the top part of the concrete specimens and also to the fact that the upper surface was receiving the salt fog, which is not the case for the bottom surface of the specimens. This unfavorable effect of horizontal surface in contact or not with the salt spray was also mentioned by François [235] and Yu et al. [169] and Zhang et al. [173].

Cumulative charges result for G3-10, G3-11 and G3-12:

The cumulative charges for top-bars in front of the artificial crack are presented Figure 205. It is clear from (Figure 205) that all the top-bars show a propagation period which begins between 10 to 20 cycles of wetting-drying cycles. On top bar (top front bar of G3-10 sample) exhibit an onset of propagation period after 80 cycles.

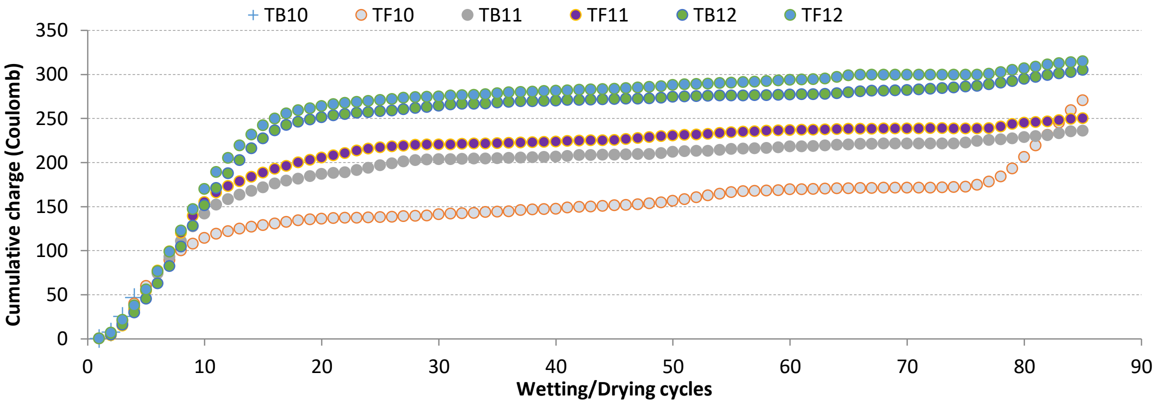

Figure 205 : cumulative charge in Coulomb (C) for the 6 top-bars of sample G3-10, G3-11 and G3-12. Back bar of G3-10 was extracted after 4 cycles to check the corrosion

During the propagation phase, corrosion-induced cracks were visible after 64th wetting-drying cycles for G3-11 specimen. It does not correspond to any change in macro cell current and cumulative charge. On the contrary, there is an increase of macro cell current for G3-10 sample after about 80th wetting-drying cycles and then a change in the slope of cumulative electrical charge. No corrosion induced cracks were recorded on G3-12 samples. According to the shape of the cumulative charges, it seems that the appearance of corrosion-induced cracks does not modify the corrosion behavior. This result is probably logical for a short period after the appearance of corrosion-induced cracks, but it seems that this behavior would exhibit some changes, as corrosion-induced cracks could modify the ionic flux depending of wetting or drying conditions, since corrosion products which induced the crack formation are not electronic conductor and are ionic conductor only if wet.

For bottom bars of the G3-10, G3-11 and G3-12 samples, the cumulative charge is presented Figure 206.

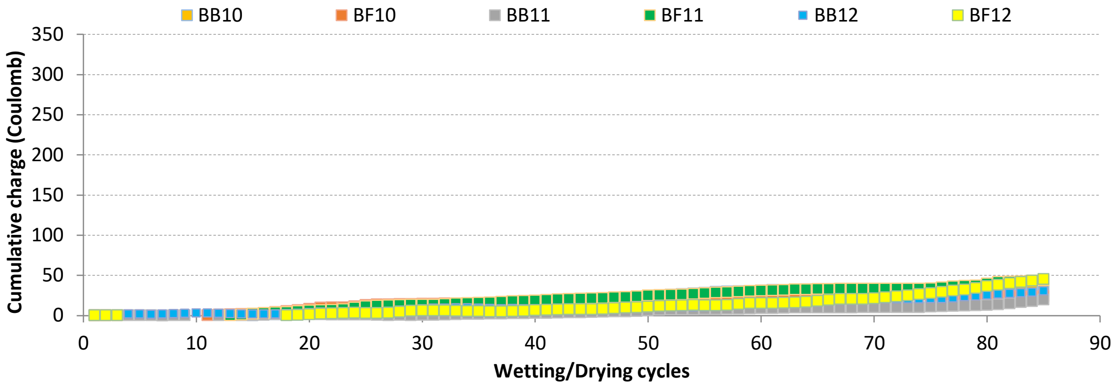

Figure 206 : cumulative charge in Coulomb (C) for the 6 bottom-bars of sample G3-10, G3-11 and G3-12.

The cumulative charges for bottom bars appear to be very weak in comparison with those of top bars with artificial cracks. Nevertheless, the slope of cumulative charge is similar with the one in propagation phase for top bars.

When making a zoom (Figure 207) of the Figure 206, it can be seen that the incubation period was limited at 10 wetting drying cycles for almost all bottom bars: only the bottom back bar of G3-12 specimens seems to get earlier corrosion, probably due to a defect during casting.

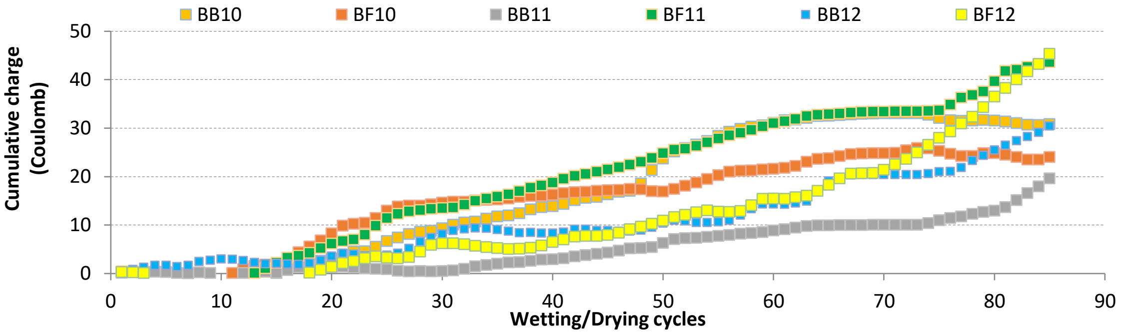

Figure 207 : zoom at cumulative charge in Coulomb (C) for the 6 bottom-bars of sample G3-10, G3-11 and G3-12.

All the cumulative charges for all bottom bars are in the same order of magnitude which is 5 to 8 times lower that the one on top bars. For these levels of corrosion, and despite the absence of expansion tank allowed by artificial cracks, corrosion-induced cracks were not visible on the concrete surface in front of all the bottom bars. The low porosity at the bottom part of reinforced concrete sample is also a parameter which could favor the formation of corrosion induced cracks because limiting the available space for corrosion products. As a result, the pressure exerted by corrosion products on the covercrete could be high, but it appears to be not sufficient probably thanks to the presence of fibers.

3.3.2. Corrosion process without artificial crack: specimens G3-7, G3-8 and G3-9

In Figure 208 and Figure 209 and Figure 210, the incubation periods appear to be very short and without any correlation with the location of the re-bars top or bottom. This result is coherent with the results from bottom bars in case of presence of artificial cracks where induction period could be very short (bottom back G3-12) or limited at 10 wetting drying cycles (others bottom bars). The presence of fibers lead to a reduction of incubation period if we compare with the research [4] by Zhang, in which the duration of the initiation was approximately 14 wetting/drying cycles then followed the propagation.

Indeed, the presence of fibers could lead to preferential path for aggressive agents and induced earlier corrosion initiation. As soon as corrosion is initiated, it would be then interesting to see if the corrosion process in term of cumulative charge is identical or not in presence of fibers.

Macro cell current measurement

The 3 short-beams cast without artificial crack: G3-7, G3-8 and G3-9 are detailed. 4 bars are concerned for each sample: 2 top bars (front and back) and 2 bottom bars (front and back).

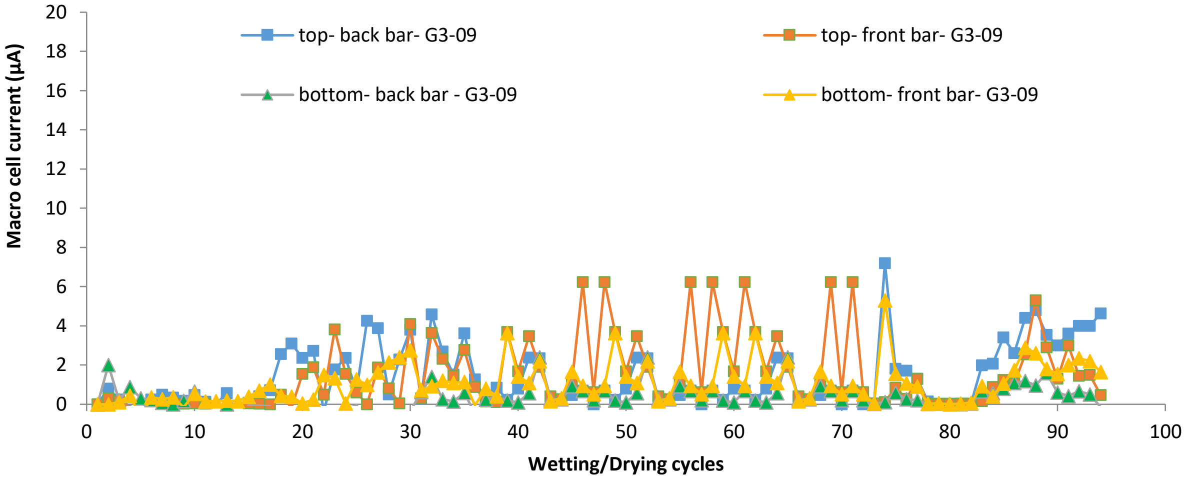

Figure 208 : macro cell corrosion current between all bars and the steel coupon (specimen G3-09)

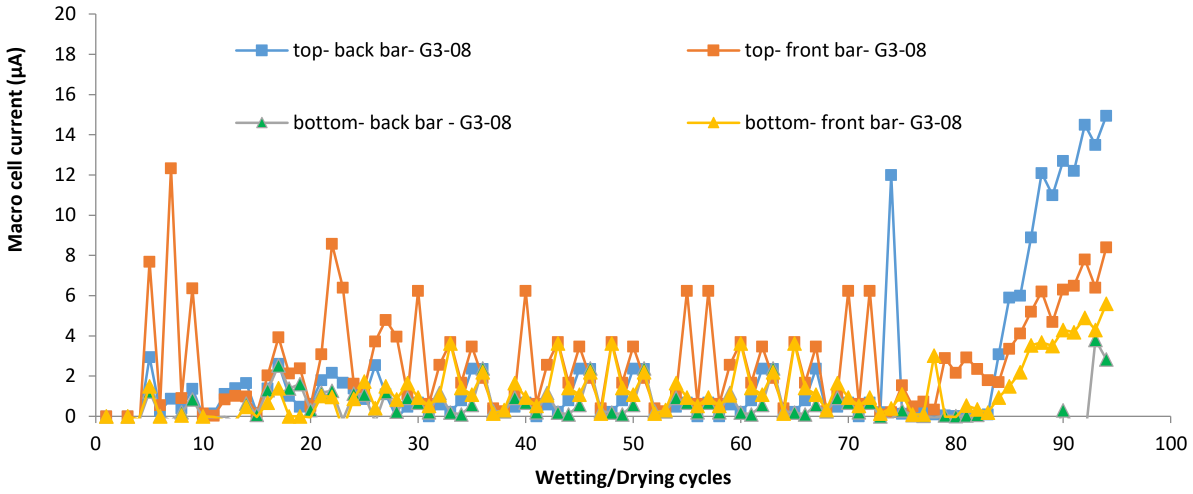

Figure 209: macro cell corrosion current between all bars and the steel coupon (specimen G3-08)

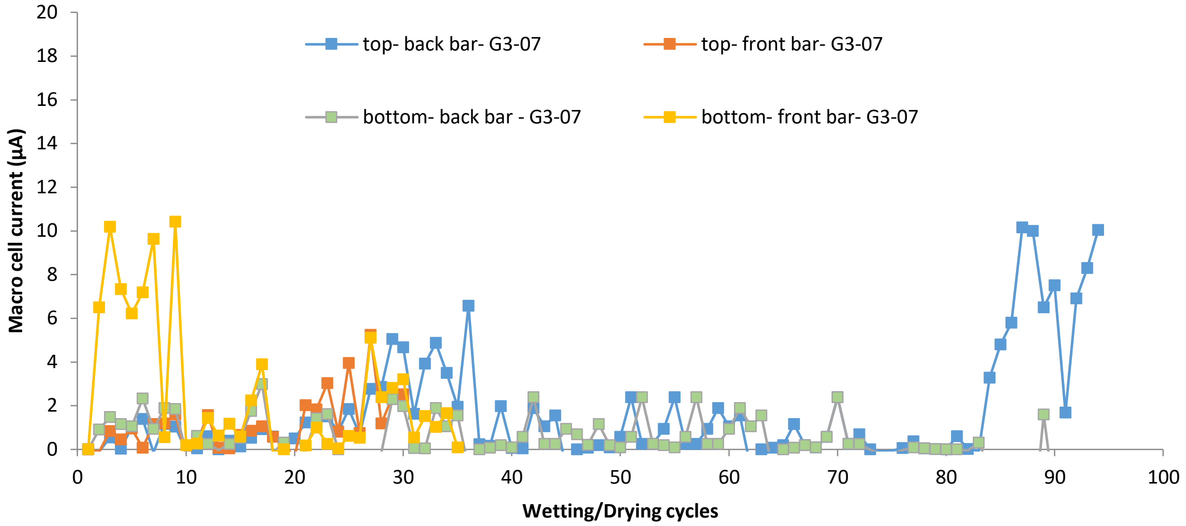

Figure 210 : macro cell corrosion current between all bars and the steel coupon (specimen G3-07)

We can notice some macro cell current measured between the re-bars and the coupon: it is generally more pronounce on the top bars than the bottom bars. It was not the case for the bottom bar of G3-07 sample which exhibited a high current from the beginning of the experiment: this is the reason why we decide to perform an autopsy after 30 cycles of wetting drying cycles.

Autopsy of the Bottom front bar of G3-07 sample after 30 cycles of wetting-drying:

Quite surprisingly, only two small sites of corrosion are visible at the foot of 2 ribs (Figure 211 and Figure 213). But there is also a rust stain which is visible on Figure 212 and Figure 214 which could correspond also to an onset of corrosion. As a result, there is some corrosion which could explain the macro cell current which is measured, but the corrosion level is very weak.

Figure 211 : bottom front bar of G3-07 sample after 30 cycles of wetting-drying cycles

Figure 212 : bottom front bar of G3-07 sample after 30 cycles of wetting-drying cycles

Figure 213 : corrosion visible at the foot of 2 ribs on bottom front bar G3-07 after 30 cycles

Figure 214 : corrosion stain visible between 2 ribs on top front bar G3-07 after 30 cycles

Macro cell charge for samples without artificial crack (top bars and bottom bars):

The cumulative charges for top-bars of samples without artificial crack are presented Figure 215. It is clear from Figure 215 that all the top-bars show an onset of propagation period which begins before 20th wetting-drying cycles). This value is closed to the beginning of the propagation period for top bars of samples with artificial cracks. It is quite remarkable that the kinetic of propagation period expressed in Coulomb/day is not so different between the case of the presence of artificial crack and the absence of artificial crack. As a result, the reduction of corrosion kinetic observed in case of the presence of artificial crack after a high corrosion kinetic during initiation period, seems to correspond to the kinetic of corrosion without artificial cracks, and then to a mechanism of spreading of corrosion along the rebar due to the presence of SCI defects.

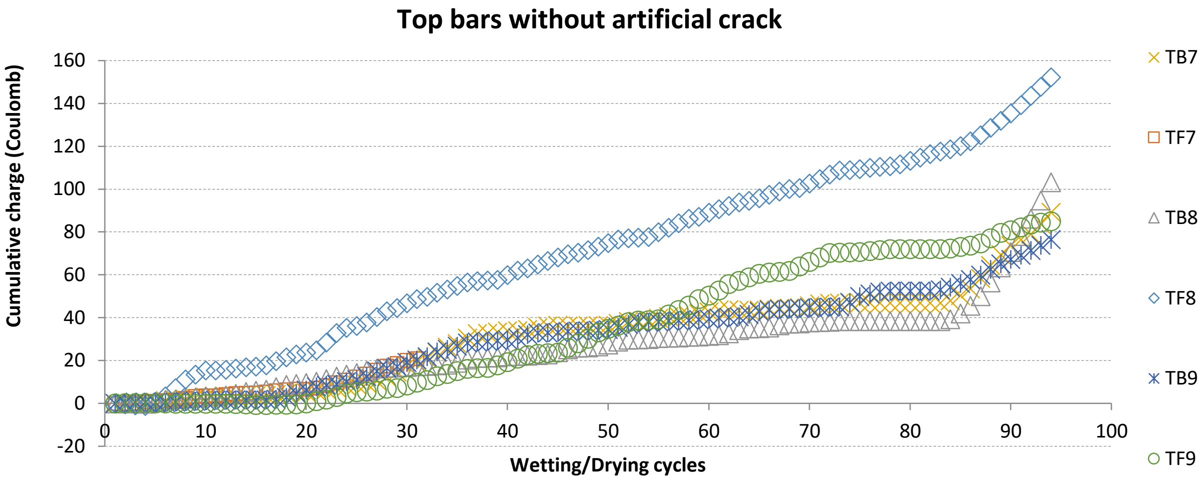

Figure 215 : cumulative charge in Coulomb (C) for the 6 top-bars of sample G3-7, G3-8 and G3-9. Top front bar of G3-07 was extracted after 30 cycles to check the corrosion

The cumulative charges for bottom-bars for samples without artificial crack are presented:

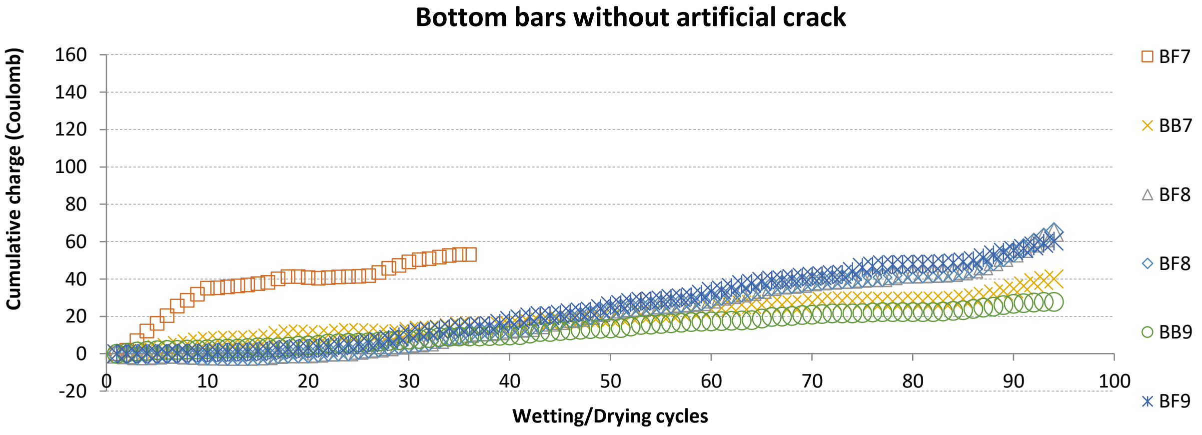

Figure 216 : Cumulative charge in Coulomb (C) for the 6 bottom-bars of sample G3-7, G3-8 and G3-9.

The cumulative charges for bottom-bars for samples without artificial crack are presented Figure 216. It is coherent with the results of bottom bars of sample with artificial cracks (Figure 206). It is clear from Figure 215 and Figure 216 that bottom bars exhibit a corrosion kinetic which is not very different from the one of the top bars. Nevertheless, it seems that the corrosion current is slightly higher in case of top bars in comparison with bottom bars; one explanation could be the higher porosity of the concrete near the top bars and also the defects at the interface which give more space for corrosion products.

3.3.3. Summary of the corrosion process with or without artificial crack

Figure 217, Figure 218, Figure 219 and Figure 220 illustrate the cumulative charge value for the top steel bars of specimens in presence of artificial crack or without artificial crack. It is clear that the results are quite consistent with model 2-phase introduced by Tuutti [84] for un-cracked concrete and clearly consistent with model 4-phase proposed by François et al. [182] for cracked concrete.

Firstly, we plot the cumulative electrical charge for the samples where each longitudinal rebar could be connected to the steel coupon. In this case, it is possible to separate the behavior of top (Figure 217) and bottom bars (Figure 218).

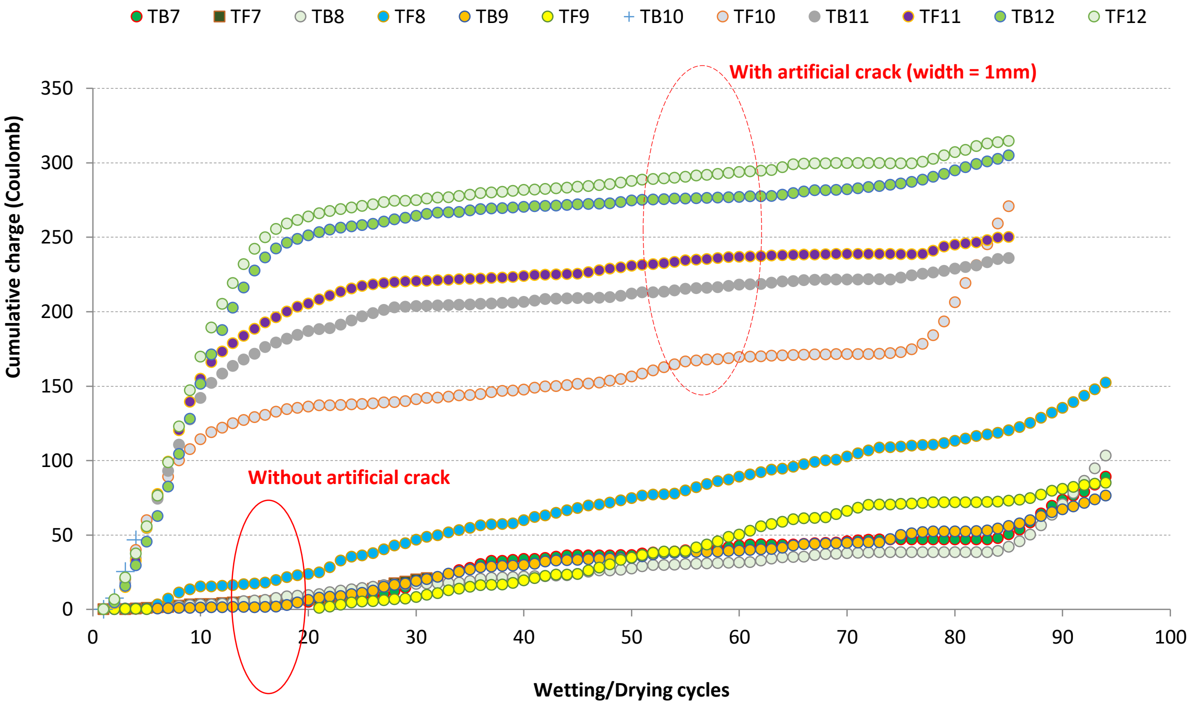

Figure 217. Cumulative charge for the top bars

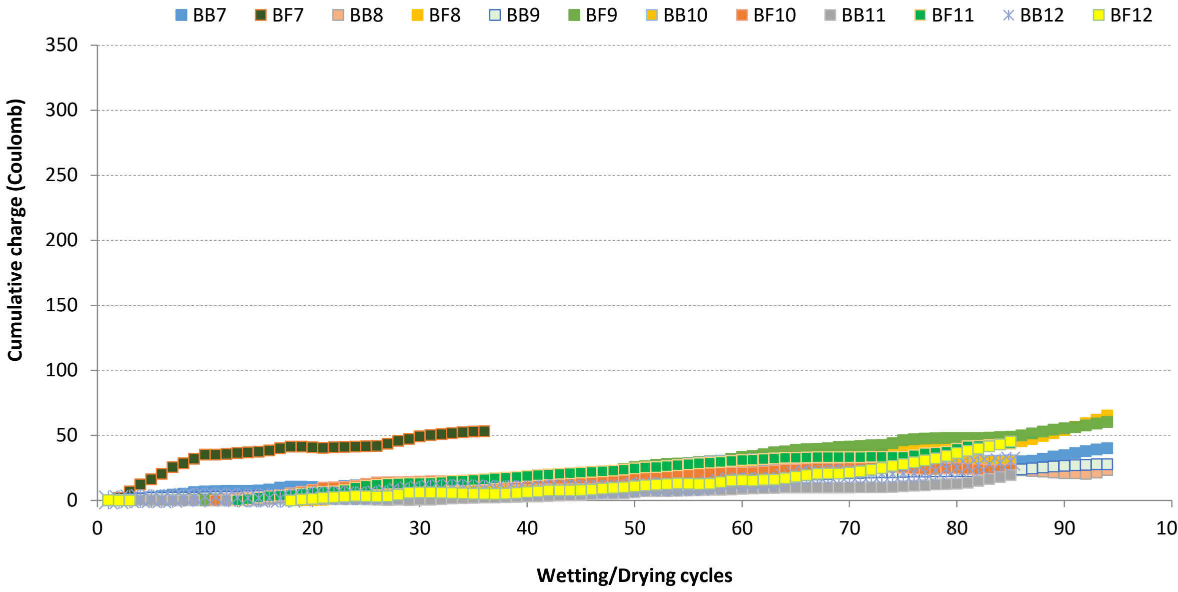

Figure 218. Cumulative charge for the bottom bars

Then we plot the cumulative charge for the samples where all the 4 rebars (both bottom and both top) are connected simultaneity to the steel coupon (Figure 219).

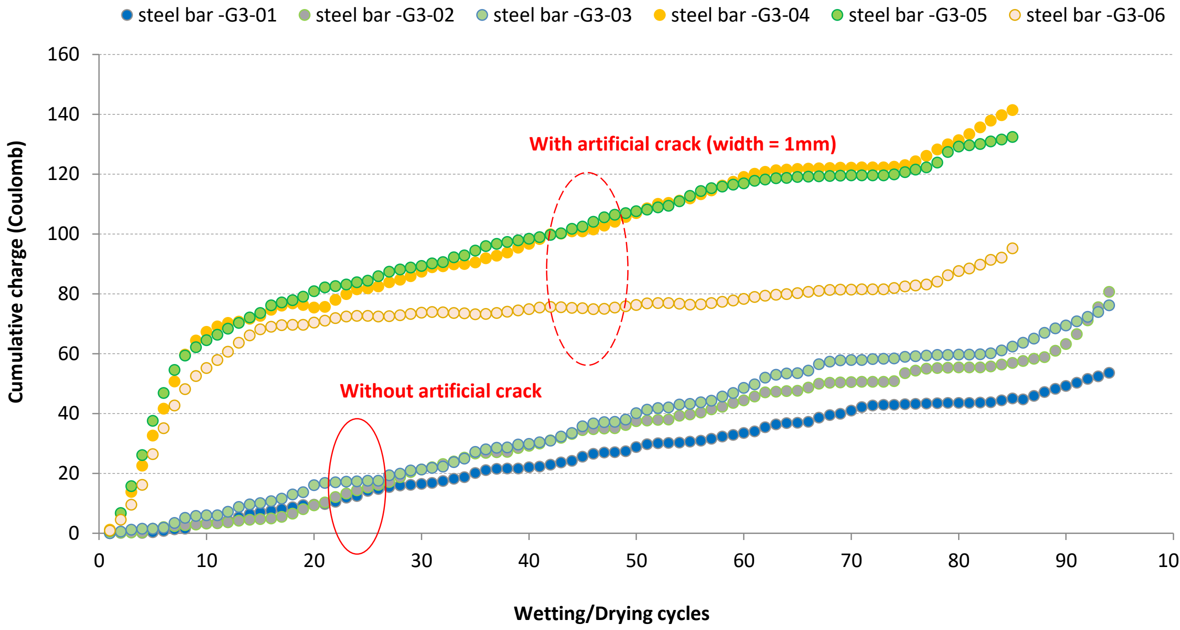

Figure 219. Cumulative charge for the steel bars in electrical continuity

Figure 220 shows the comparison between the cumulative charge measured when all main rebars are electrically connected, and the average value of the 4 bars when they are electrically disconnected.

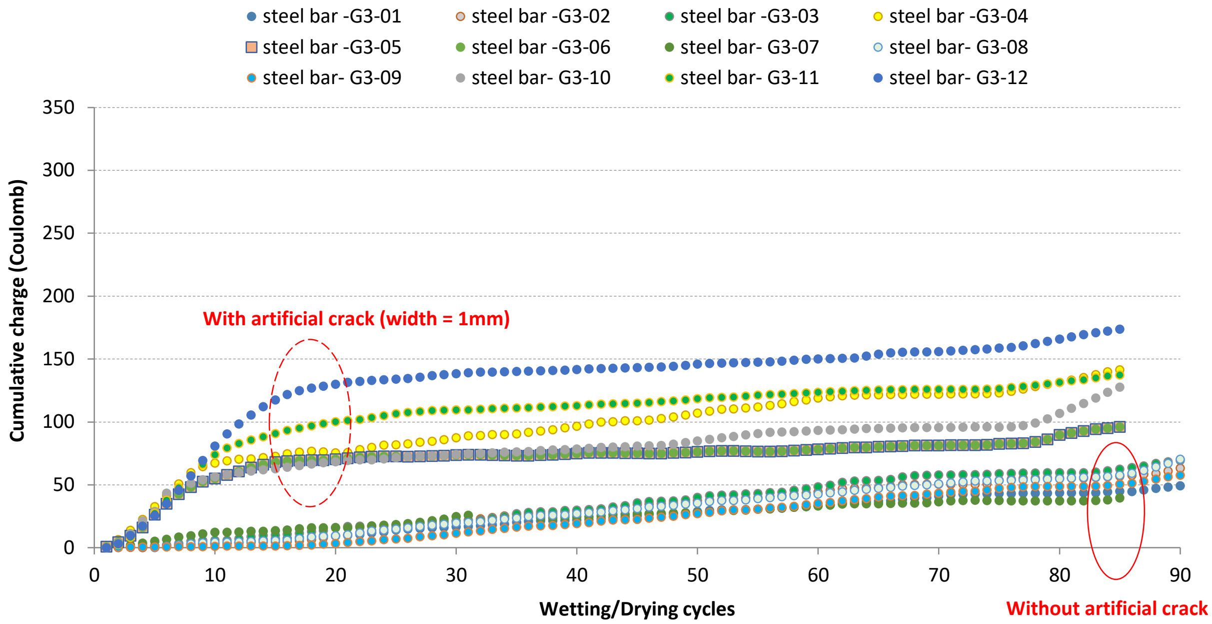

Figure 220. Cumulative charge for the steel bars of samples in electrical continuity and current average of other samples

From Figure 220, it appears that all the results in term of corrosion current monitoring are coherent. The presence of artificial crack gives a quicker onset of corrosion development, but in absence of artificial crack, the corrosion current slope is at least comparable with the one with artificial crack.

In presence of artificial cracks, the incubation period is very short and during initiation period, the corrosion current is important. After about 10 wetting/drying cycles, the initiation period finished for cracked specimens, corresponding to the propagation period since the corrosion rate have a quite similar value (Figure 217 and Figure 218) with the one of uncracked specimens or for bottom bars. The same observation can be also found in a study by Zhang [4].

It should be notice that the change in slope at the end of the initiation phase could be interpreted as a kind of dormant phase which would then correspond to the induction period of the 4-phases phenomenological model of corrosion. But the slope is quite similar to the one recorded for samples without artificial crack and also for bottom bars. Moreover, during this phase, some corrosion-induced cracks appear on both samples with or without artificial crack. Because induction phase in the 4-phases model cannot be associated with the creation of corrosion-induced cracks, the phase which follow the initiation phase could only be the propagation phase.

Because the corrosion rate corresponds to macro cell measurement, it seems surprising that this corrosion rate appears to be constant in the propagation period for cracked specimens and also constant for uncracked specimen. Indeed, due to the extension of the corroded zone, there is a reduction of the ratio Cathode/Anode, which will normally lead to a reduction of the corrosion rate.

As a result, the reduction of corrosion current due to the decrease of C/A ratio is compensated by an increase of the anodic activity in the corroded zone.

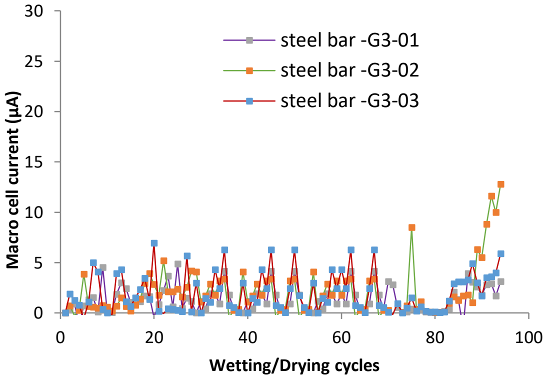

Figure 221. Macro cell current in steel bar (without AC)

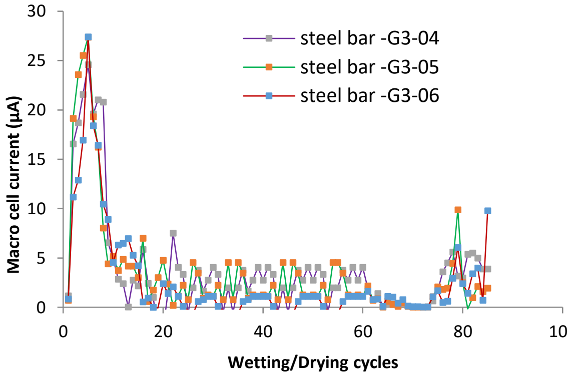

Figure 222. Macro cell current in steel bar (with AC)

In Figure 221 and Figure 222, it is clear that the instantaneous corrosion current is strongly higher for cracked specimens during the first 10 wetting-drying cycles: then the instantaneous corrosion current is in the same order of magnitude of uncracked specimens.

From Figure 221, it seems that there is some macro cell current after only 1 or 2 wetting-drying cycles. Nevertheless, it corresponds to the specimens where all rebars are electrically connected, and then the corrosion current could correspond to any rebars, and even to stirrups which have a weaker cover than the main bars. For specimens corresponding to electrically isolated main bars, and without artificial crack (Figure 223), it appears that some rebar does not exhibit any macro cell current before 15-20 wetting-drying cycles as TF9 rebar, but some rebars show already non-null macro cell current after 2-4 wetting-cycles.

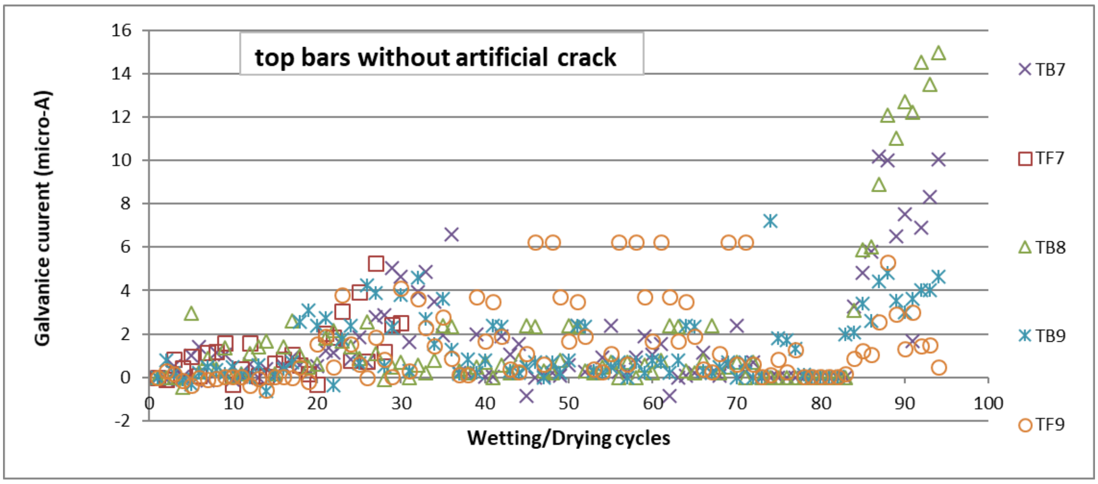

Figure 223 : macro cell current versus time for specimens without artificial crack and each main bar electrically isolated from the reinforcement lay-out

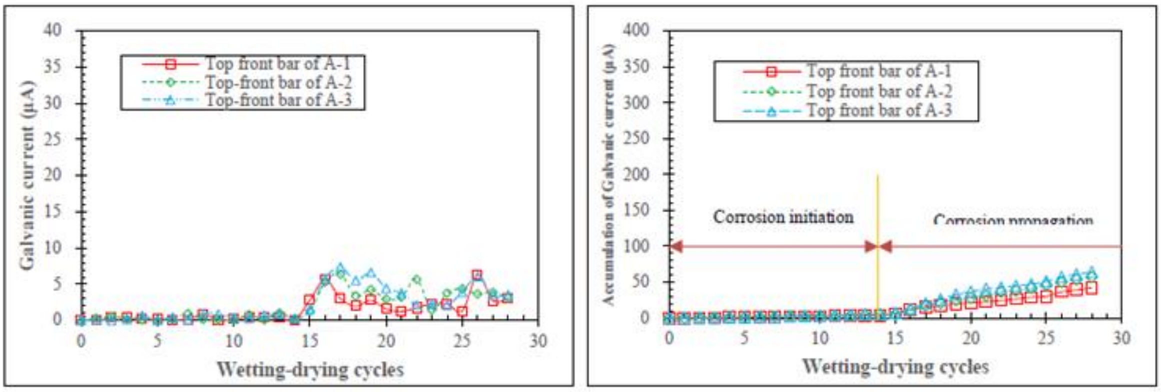

(a) Galvanic current (b) Accumulation of galvanic current

Figure 224 : Macro cell corrosion current on samples A tested by Zhang [4]

If we compare, the duration of the incubation period with the one found by Zhang [4] it can be seen on Figure 224, that the incubation period for samples A tested by Zhang during his PhD, is about 14 wetting-drying cycles. It corresponds to the duration necessary for chlorides to reach the SCI through the concrete cover, and to reach the chloride threshold value. In the case of G3 samples with fibers, the fact that the incubation could be very short (2 wetting-drying cycles) or could have the same duration of the one of samples A and B (in Zhang [4] is probably due to the preferential path for chlorides or CO2 along the fibers. Indeed, it was shown by Al-Almad et al. in [80] or Sassine in [236] that CO_2 is able to progress along SCI or wires very quickly to induce corrosion. Chlorides could also ingress along SCI or wires or fibers to quickly depassivate the steel: it was shown by François [235] or Geiker et al. [237] in the case of spacers of reinforcement lay-out, but also in [3] were very small crack openings measured by X-Ray CT, allows the quick initiation of corrosion.

As a result, it appears that fibers, even if they are not concerned by corrosion (because of a higher chloride threshold) could decreases the time for corrosion initiation of reinforcing steel due to the preferential path for aggressive species along the fibers.

3.4. Numerical determination of the k factor between the current measured by the metallic coupon

Table 22 shows the electrochemical parameters used for the numerical simulation. These parameters are based on the work done by Chalhoub [27]. The concrete composition in Chalhoub corresponds to the use of a CEM I, which is also the case in our experiments. Chalhoub has shown that the cathodic behavior is highly influenced by the cement, in term of resulting porosity at SCI and also in term of oxygen depletion which could occurred in case of the use CEM III.

baa (V/dec)	bca (V/dec)	bap (V/dec)	bcp (V/dec)	corr-a (A/m^2	corr-p (A/m^2	Ecorr-a (V)	Ecorr-p (V)
0.125	0.13	0.24	0.13	5.00E-02	6.00E+05	-0.5 (V)	-0.138 (V)

Table 22 : electrochemical parameter used for the numerical simulation

Because the specimens are submitted to wetting and drying period in a salt fog chamber, it is considered that the resistivity is quite low: 150 Ohm.m. Resistivity cannot be checked on site since the composition involved metallic fibers which are preferential paths for the electronic current when measuring the resistivity.

Numerical modeling with artificial crack filled by salt water:

The model (Figure 225) corresponds to the presence of an artificial crack. It allows estimate the total anodic current for top bars from the cathodic current measured on the steel coupon.

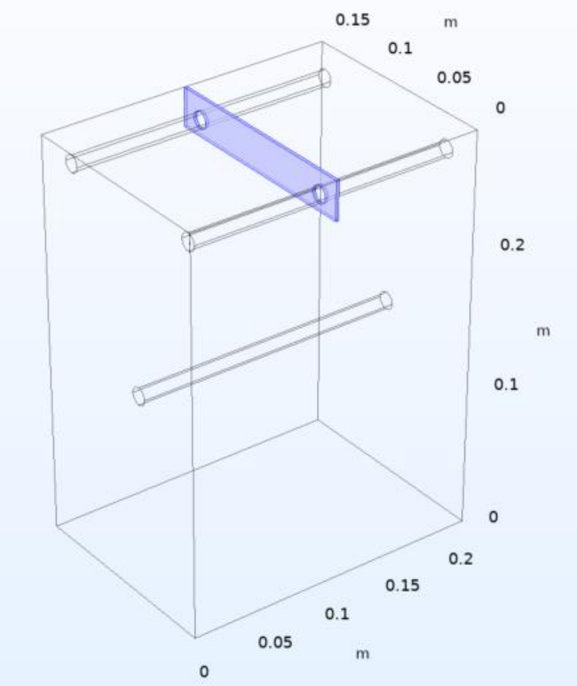

Figure 225 : numerical model to predict the macro cell corrosion current

Different sizes of the anodic site are studied. The total corrosion current on the anodic site located in front of the artificial crack appears to be hardly influence by the anodic length. For anodic length between 2 mm to 8 mm, the corrosion current is about 100 µA (Figure 226). On the other hand, the corrosion rate (or corrosion current density) decrease strongly with the length of the anodic site (Figure 227).

This result is due to the decrease of C/A ratio: indeed the Figure 228 shows that the corrosion current is almost linear as a function of the C/A ratio.

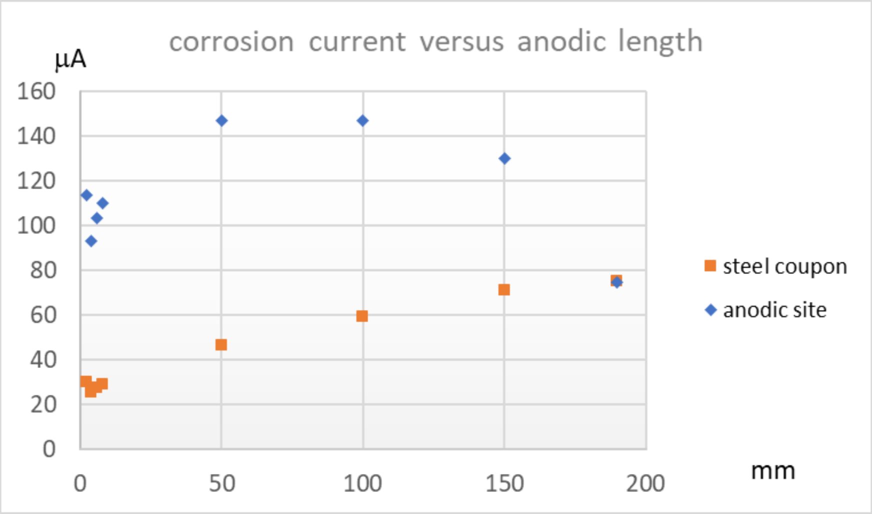

Figure 226 : numerical value of corrosion current and cathodic current on the steel coupon according to the length of the anodic site.

From Figure 226, it can be seen that the corrosion current measured by the steel coupon is closed to 30 µA at the beginning of the corrosion process when only anodic sites are located in front of the artificial crack. It is then coherent with the experimental results shown Figure 199, Figure 200 and Figure 201. On the contrary, with the extension of the anodic sites along the rebar, the numerical modeling shows that the corrosion current recorded by the steel coupon increase, which is not the case for the experimental results. Nevertheless, it is necessary to consider the fact that the numerical model is based on a continuous connection between the steel coupon and the rebar, which is not the case during the experiments. Indeed, the steel coupon is only connected to the main bar during 1 mn to make a measurement of the cathodic current exchange between the 2 bars: it is supposed that it allows to have an idea of the anodic activity on the main bar, but probably the transient behavior is not fully understood.

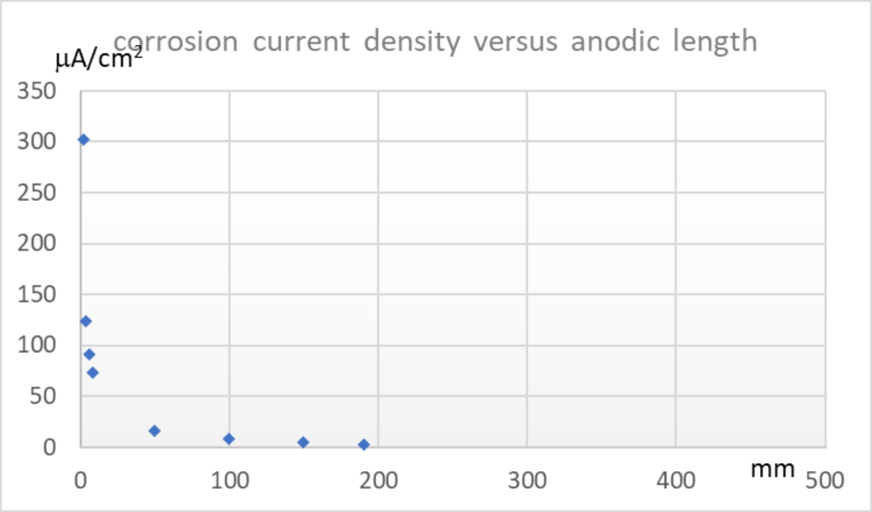

Figure 227 : corrosion rate (corrosion current density) according to the length of the anodic site.

Logically, the corrosion current density decreases with the increase of anodic length (Figure 227). This result is coherent and similar to the one found by Hess [3].

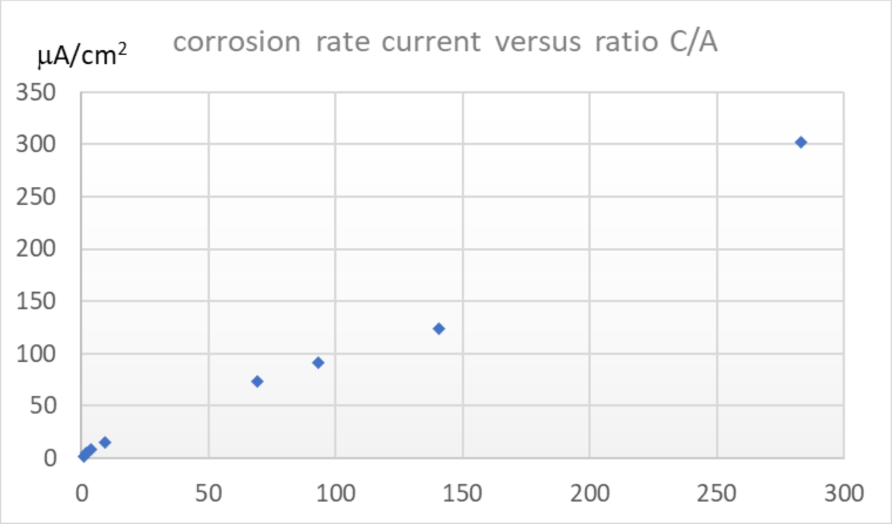

Figure 228 : corrosion rate versus the ratio C/A

Logically also, the corrosion current density increases with the increase of C/A ratio (Figure 228), which correspond for the main bar to a higher corrosion density at the beginning of the corrosion process when corrosion is only effective in front of the artificial crack.

Figure 229 shows the k ratio between the cathodic current measured by the steel coupon and the total corrosion current: at the beginning of the corrosion process the k factor is closed to 3.8. When all the length of the top bars is corroded the ratio is then 1 since the only residual cathodic site corresponds to the steel coupon.

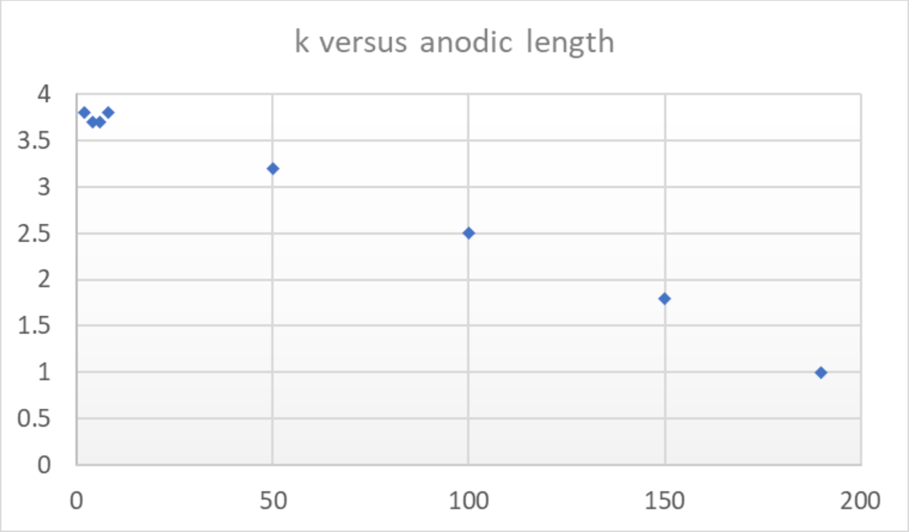

Figure 229 : ratio k between the cathodic current measured by the coupon and the total anodic current, versus the anodic length

As a result, increase the length of anodic site leads to a decrease in the corrosion current and also in the corrosion rate. It could lead to an apparent decrease of the corrosion rate during the experimental testing.

The numerical modeling is performed in steady state behavior, while the experimental measurements are performed in transient behavior. Probably, there is not a huge effect when C/A is high, because the presence or not of the steel coupon do not change significantly the C/A ratio: it is the case for the initiation period of corrosion in case of artificial crack, since the anodic site is limited to the size of the crack as shown in Figure 204.

On the contrary during the propagation phase, the extension of the anodic site along the rebar corresponds to a corrosion process which cannot be represented by an instantaneous connection to the steel coupon.

4. Conclusion

As previously found by Zhang[4] in presence of artificial crack, the incubation period is very short, since corrosion current is recorded after the first wetting-drying cycle. The initiation period before a reduction in slope is around 10 wetting-drying cycles, then the cumulative charge, for all samples, exhibit a significant change in slope corresponding to a strong reduction of corrosion kinetic. In Zhang [4] this change in slope is associated to the beginning of the propagation phase which correspond to the absence of induction phase, in the 4-phases model of François [19]. This assumption is associated to the comparison between specimens with or without artificial crack. Indeed, as shown in Figure 230, the slope of the cumulative charge is the same in the propagation phase for both un-cracked and cracked specimen. Corrosion propagation is also associated to a large extension of the corroded zone, especially at the bottom part of top bars as shown in Figure 231. This large corroded zone leads to get a small C/A ratio and then a corrosion rate which is significantly reduced by comparison with the initiation phase in case of artificial crack, where C/A ratio is important as shown by the numerical modeling.

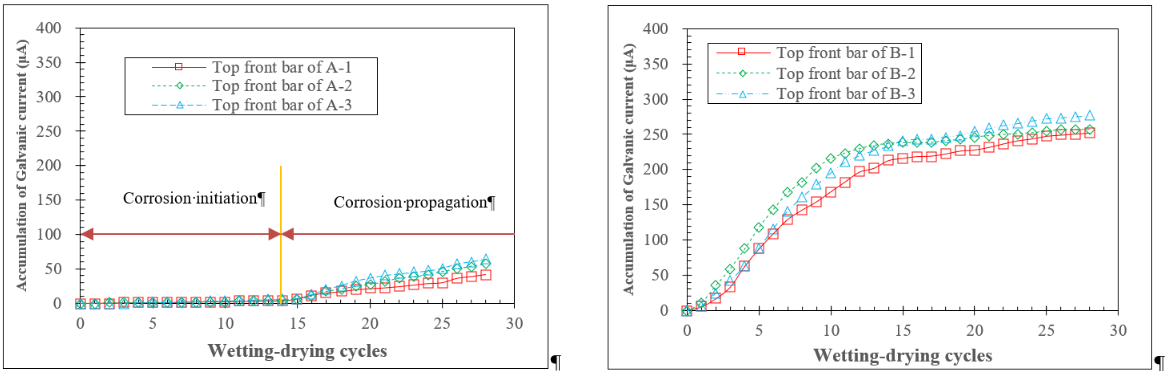

(b) Accumulation of galvanic current (b) Accumulation of galvanic current

Figure 230 : comparison with the electrical charge versus time for samples without (left) or with (right) artificial crack from Zhang et al. [231]

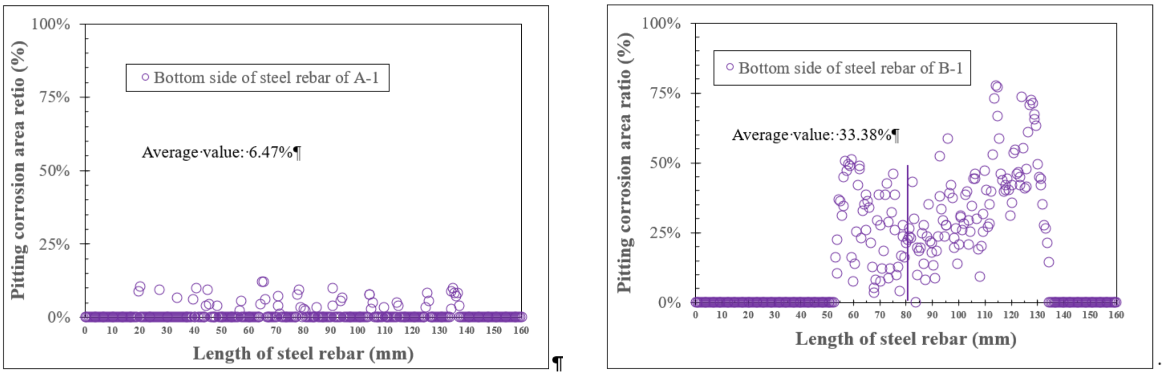

(b) Bottom surface of steel rebar of A-1 (b) Bottom surface of steel rebar of B-1

Figure 231 : comparison between the length of corroded zone at bottom face of top rebars for sample without (left) or with (right) artificial crack from Zhang et al. [231]

Our results are coherent with the one of Zhang [4] indeed autopsy performed at the end of the experiments show that corrosion spread all along the steel bar preferentially at the bottom part of the top re-bars. It is assumed that the extension of the corroded length along the reinforcement begins at the end of the initiation phase: i.e. about 10 wetting-drying cycles. As a result, the propagation phase visible on cumulative charge versus time is explained by the extension of the anodic activity all along the rebar. This extension of anodic activity reduce the C/A ratio and then reduce the corrosion current which is then identical for specimen with artificial crack (Figure 232) and specimen without artificial crack (Figure 233).

Moreover, the fact that corrosion-induced cracks appears during the experiments confirms that all specimens were in propagation phase: i.e. the 4-phases corrosion phenomenological model for cracked concrete assumes that corrosion-induced cracks could only appear during the propagation stage.

This result is in accordance with the one from [3] who found that no induction phase was visible in chloride-induced corrosion in presence of load-induced crack, since their width were higher or equal to 0.5 mm. Induction phase could be only visible for crack width lower of equal to 0.3 mm.

If we accept the idea that large load-induced cracks could be represented by artificial crack, the main difference between Hess experimental program and our experimental program is the presence or not of SCI defects due to top bar effect. As a result, without top-bar effect, corrosion concentrate of a small area and the corrosion density is high due to high C/A ratio which does not allow a change in slope for corrosion process versus time. In this case, Hess considered that there is only one phase after the incubation, which is call initiation/propagation. On the contrary, with top bar effect, the corrosion spread on a long distance which reduce C/A and reduce the corrosion density which lead to a change in slope after initiation of corrosion at crack tip.

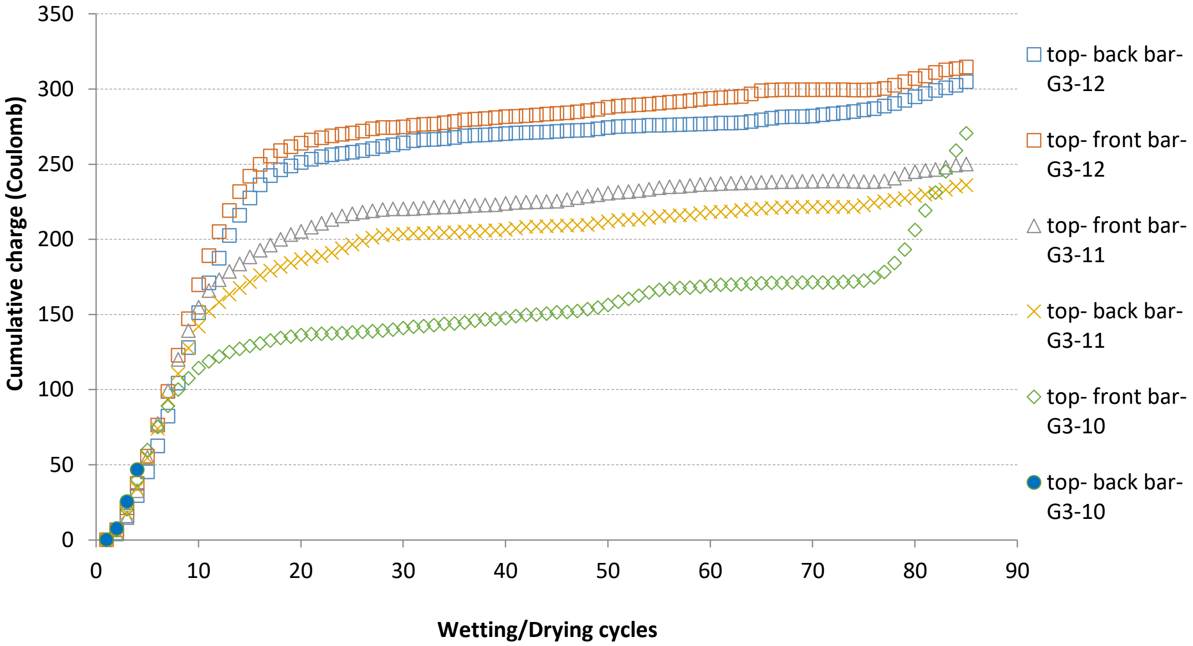

Figure 232 : cumulative electrical charge versus time for sample with artificial crack

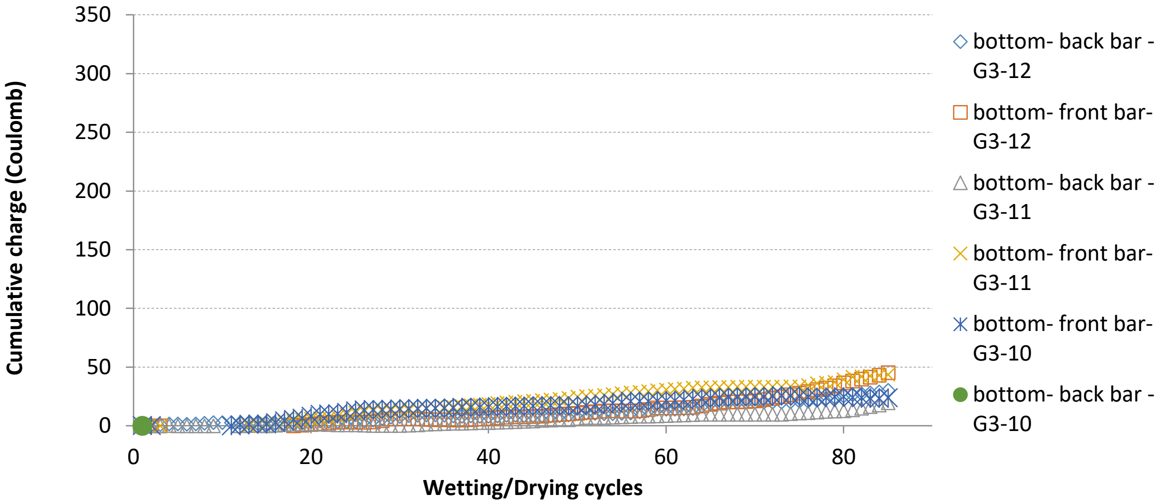

Figure 233 : cumulative electrical charge versus time for sample without artificial crack

Effect of fibers on the corrosion process

Comparison between the samples from Zhang [4] (Figure 230) made of concrete without fibers and our specimens made with fibers (Figure 232) do not show any difference in the phenomenological process, and also no difference in term of cumulative charge. It is quite logical since the corrosion process is linked to the presence of the artificial crack and water bleed defects at SCI which are the same in Zhang experiments and in our experiments.

Nevertheless, the initial goal was to check if an anodic control could occur in case of fibers concrete due to the higher resistance to cracking. In this case the pressure around corrosion products would be higher and could limit the anodic process by lack of space for corrosion products.

A delay in time to induce the first corrosion-induced crack was found between Zhang experiments and our experiments. Zhang found that the corrosion-induced crack appears after 17 wetting drying cycles, then only after a short period in the propagation phase; while we found that the first corrosion-induced crack appears after 64 wetting drying cycles.

As a result, it can be argued that the increase of the acceptable pressure induced by the corrosion products which is given by the presence of fibers can delay the appearance of the first corrosion induced crack. The presence of fibers allows also for a control of the increase of the corrosion-induced crack width visible on the concrete surface. Nevertheless, these effects are only “visible” effects and do not give a better resistance versus the spreading of corrosion all along the reinforcement in case of top-bar effect.

Finally, contrary to the assumption made at the beginning of the thesis, it is not possible to achieve an anodic control by increasing the acceptable pressure before concrete cracking.

CONCLUSIONS AND RECOMMENDATIONS

1. Conclusions

In this thesis, the effect of top casting induced defects and cracks on the corrosion behavior were investigated. Both carbonation-induced corrosion and chlorides-induced corrosion were studied. If the macro cell predominant behavior is well established now for chlorides-induced corrosion, it was an open question concerning the carbonation-induced corrosion and was the subject of chapter 3. The effect of top-bar defects on carbonation-induced corrosion in presence of load-induced cracks was studied in chapter 4: it allows to complete the results concerning the presence of load-induced cracks on carbonation-induced corrosion already studied by Ghantous [2]. Finally, the presence of top bar defects associated with the use of concrete reinforced by fibers and the presence of artificial cracks was studied in chapter 5: it allows to study the possibility of anodic control of corrosion by increasing the confinement of corrosion products, and to complete the results from Zhang [4] concerning the effect of top bar defects associated with an artificial crack. According to the experimental and numerical study the following conclusions can be drawn.

Uniform and macro cell corrosion for carbonation-induced corrosion

The ratio between uniform and macro cell corrosion was studied in saturated conditions: i.e. anode fully immerged in solution. Both Uniform corrosion rate and macro cell corrosion rate were measured on steel rebar embedded in carbonated concretes. 3 Concretes were studied, one based on CEM I and 2 based on CEM III: all concretes were also studied in Perfdub project. Anode samples were fully carbonated in a 50% CO_2 concentration chamber.

- The uniform corrosion rate does not depend of the concrete resistivity. (Resistivity in this research varies from 69 to 718 Ωm before carbonation and from 240 to 2000 Ωm after carbonation)
- The macro cell corrosion rate is highly dependent of the resistivity, and especially on the resistivity at the anode.
- On-site corrosion rate, which is the sum of the uniform part and the galvanic part, is then likely to depend of the resistivity of concrete.
- The macro cell corrosion rate is highly dependent of the C/A ratio. In practice, C/A ratio could be limited or important. In the case of local defects or presence of cracks, the macro cell part of corrosion rate could be the most important contribution to the total corrosion rate. Without local defects, the uniform corrosion current is suitable to be the more important part of corrosion process. During a corrosion diagnosis on a reinforced concrete structure, it is then important to take into both local and global phenomena.

- the use of CEM III concrete, which corresponds to high resistivity concrete, leads to a significant limitation in the galvanic corrosion rate on-site.
- for a Cathode/Anode ratio C/A=1, macro cell corrosion is 6 times higher than uniform corrosion rate for CEM I concrete, while for CEM III concrete, the uniform corrosion current is higher than the macro cell corrosion current.

Contrary to the chloride-induced corrosion, the ratio between macro cell corrosion current and uniform corrosion current is variable and depend mostly of the concrete resistivity. For high resistivity, macro cell corrosion current could be weaker than the uniform corrosion current. Saturated conditions at the anode lead to the higher macro cell corrosion current.

Effect of top bar defects on carbonation-induced corrosion in presence of load-induced cracks

Wetting-drying cycles were used at the load-induced crack location to study the influence of top-bar defects on corrosion development. Indeed, in case of carbonation-induced corrosion, the load-induced cracked zone cannot be always saturated, since carbonation process need dry period. Nevertheless, we need to be aware than macro cell process in strongly affected by the wetness at the crack location, which do not correspond to the conditions of chapter 3. Specimens were made only from CEM I cement. It corresponds to small beams (15x15x55 cm) with 2 layers of rebars (Top and bottom), each layer with 2 rebars. Carbonation is due to ingress of CO_2 (3% CO_2 chamber) in the load-induced crack path. A part of the macro cell corrosion rate was recorded by using a steel coupon. The total macro cell corrosion rate was then estimated thanks to a numerical modeling of the macro cell corrosion in the small beams. By computing the total electrical charge during the experiments, it was then possible to calculate the loss of mass due to macro cell corrosion. A gravimetric measurement of loss of mass due to corrosion was performed at the end of the experiments. The difference between the gravimetric loss of mass and the macro cell loss of mas, allows to calculate to part of uniform corrosion. Surprisingly, results shows that loss of mass due to uniform corrosion is largely higher to the one due to macro cell corrosion. The difference is between 2 to 10 according to the different sample and rebars which corresponds to a high scatter. Nevertheless, it was shown that the wetting-drying cycles are not favorable for macro cell corrosion since the current decrease quickly during the drying process. Then to compare with the saturated conditions at anode, it is necessary to use the maximum macro cell corrosion current recorded during the wetting process: it corresponds to an increase by 3 times. In virtual fully saturated conditions, the difference between uniform corrosion and macro cell corrosion appears to be positive or negative: in some case the macro cell process is more important; in most cases the uniform process is more important.

Influence of load-induced cracks of carbonation-induced corrosion for both top bars and bottom bars

In Ghantous [2] the influence of the crack opening on the carbonation-induced corrosion process is tested on specimens, without top bar defects, subjected to corrosion under raining/drying cycles at 20°C for 30 minutes rain duration in each cycle. After a certain number of raining/drying cycles, a decrease in the corrosion rate is detected. This is attributed to rebar repassivation which is due to the corrosion products that seal the cracks and act as a protective layer for the rebar by limiting the access of aggressive agents. Moreover, the corrosion process appears to be independent from the residual crack opening. Our results are most contrasted than the one from Ghantous. For bottom bars, the final corrosion kinetic at 400 days appears to be comparable to the one of Ghantous at 90 days, which means that the rebar repassivation is not fully achieved. Nevertheless, cumulative electrical charge from macro cell measurement shows a tendency to a reduction of corrosion, corresponding to an induction phase after about 180 days. For top bars, the corrosion is more important in term of loss of mass in comparison with bottom bars, but the corrosion kinetic is in most case weaker than for bottom bars. In term of only macro cell corrosion, the same conclusions could be drawn, the cumulative electrical charge is always more important for top bars than bottom bars.

- For load-induced cracked specimens, the carbonation process lead to a significantly longer carbonation length along the SCI interface from the crack tip in case of top bar defects, than in case of no top bar defects . The carbonation length appears to be between 2 times to up to times higher for top bars than bottom bars.
- Because corrosion kinetic in case of top bars is lower than corrosion kinetic in case of bottom bars, it is assumed that water bleed defects are not detrimental for carbonation-induced corrosion from a load-induced crack.
- For carbonation-induced corrosion, the presence of load-induced cracks lead to a quick initiation of corrosion, but after less than one year there is a decrease of corrosion rate, whatever the presence of not of top bar defects. At crack location, uniform corrosion is predominant in comparison with macro cell corrosion.

Effect of top bar effects and presence of fibers on the macro cell corrosion in case of chloride-induced corrosion:

On contrary with carbonation-induced corrosion, chlorides-induced corrosion is mostly macro cell corrosion, even in the case of the corrosion at crack tip: this was recently confirms in Hess thesis [3]. In presence of load-induced cracks, Hess [3] shows that the corrosion at crack tip could corresponds to a continuous propagation stage after the quick initiation at crack tip; but he also found that initiation of corrosion could be followed by an induction phase. No explanation could be found to explain this different scenario. As in Ghantous, Hess does not study the effect of defects at SCI such as water bleed defects. To study the effect of water bleed defects from the chloride ingress in a crack, it was chosen to have top bars effect on rebars with a sufficient height of concrete > 250 mm, and then the cracks are not induced by load but correspond to artificial cracks created by a plastic sheet. The most important difference between load-induced cracks are firstly, the fact there is no possible restriction of chloride ingress in the crack path, such as self-healing, and secondly, that there is no mechanical damage at the interface. Nevertheless, for this last point it is expected that water bleed defects at interface are significantly more important that mechanical damage and then the absence of mechanical damage do not affect the conclusions of the study. In addition to the study of top bar effect on corrosion development, the effect of fibers is also studied. Fibers allow to have a better tensile strength for concrete: the goal was to see if fibers allow effectively a delay in the appearance of corrosion-induced cracks; and also if the confinement of corrosion products allowed by a higher tensile strength of covercrete could allow to obtain a reduction of the anodic process (anodic control of corrosion).

Corrosion process in presence of artificial crack and top bar effect

In presence of artificial crack, the incubation period is very short, since corrosion current is recorded after the first wetting-drying cycle. The initiation period before a reduction in slope is around 10 wetting-drying cycles, then the cumulative charge, for all samples, exhibit a significant change in slope corresponding to a strong reduction of corrosion kinetic. This change in slope is associated to the beginning of the propagation phase which corresponds to the absence of induction phase, in the 4-phases model of François [19]. This assumption is associated to the comparison between specimens with or without artificial crack. These conclusions are coherent with the one of Zhang [4], indeed autopsy performed at the end of the experiments show that corrosion spread all along the steel bar at the bottom part of the top rebars. It is assumed that the extension of the corroded length along the reinforcement is already achieved at the end of the initiation phase. As a result, the propagation phase visible on cumulative charge versus time is explained by the extension of the anodic activity all along the rebar. This extension of anodic activity reduces the C/A ratio and then reduces the corrosion current which is then identical for specimen with artificial crack and specimen without artificial crack.

Top bar defects will lead to an absence of induction (or dormant) phase of corrosion in presence of cracks.

Effect of fibers on the corrosion process

Comparison between the samples from Zhang [4] made of concrete without fibers and our specimens made with fibers do not show any difference in the phenomenological process, and also no difference in term of cumulative charge. It is quite logical since the corrosion process is linked to the presence of the artificial crack and water bleed defects at SCI which are the same in Zhang and in our experiments. A delay in time to induce the first corrosion-induced crack was found between Zhang experiments and our experiments. Zhang found that the corrosion-induced crack appears after 17 wetting drying cycles, then only after a short period in the propagation phase; while we found that the first corrosion-induced crack appears after 64 wetting drying cycles.

- Fibers allow to have a slight increase of corrosion degree before the appearance of the first load-induced crack. Fibers allow also to control the opening the corrosion-induced cracks during the corrosion process.
- Nevertheless, the initial goal was to check if an anodic control could occur in case of fibers concrete due to the higher resistance to cracking. The conclusion is that fibers do not allow to give an anodic control of corrosion and then the possibility of induction period is not linked to a confinement of the corrosion products.
- The presence of top bar defects is associated with an important height of concrete and a concrete formulation which have an important water bleeding. In this case, there is also a higher porosity of concrete closed to the top surface. This higher porosity leads to premature corrosion development even in absence of artificial crack. As a result, the corrosion development in absence of artificial crack is not different of the one with the presence of crack if the concrete cover is not sufficient : this conclusions was already drawn by François [235] and Yu et al. [169] and Zhang et al. [173].

2. Recommendations

Based on the results of this thesis, it appears necessary to perform the study of chlorides-induced corrosion in presence of cracks and top bar defects, on samples with a covercrete at least equal to 5 cm to avoid premature corrosion due to the increase of chlorides through the concrete cover.

REFERENCES

[1] A. Nasser, A. Clément, S. Laurens, and A. Castel, "Influence of steel–concrete interface condition on galvanic corrosion currents in carbonated concrete," *Corrosion Science,* vol. 52, pp. 2878-2890, 2010.

[2] R. M. Ghantous, "Initiation and propagation of rebar corrosion in carbonated and cracked concrete," 2016.

[3] L. Hess, "Etude du mécanisme de corrosion en fond de fissure du béton armé en présence de chlorures," Toulouse, INSA, 2024.

[4] W. Zhang, "Influence des défauts de mise en place du béton et des fissures fonctionnelles transversales sur la corrosion des armatures des structures en béton exposées aux chlorures," Toulouse, INSA, 2020.

[5] J. González, S. Feliu, P. Rodríquez, W. López, E. Ramírez, C. Alonso*, et al.*, "Some questions on the corrosion of steel in concrete. Part II: Corrosion mechanism and monitoring, service life prediction and protection methods," *Materials and Structures,* vol. 29, pp. 97-104, 1996.

[6] H. Böhni, *Corrosion in reinforced concrete structures*: Elsevier, 2005.

[7] M. Pourbaix, "Atlas dEquilibres Electrochimiques, Gauthier-Villars and C," *Editeur, Paris,* vol. 286, 1963.

[8] A. Carnot, I. Frateur, S. Zanna, B. Tribollet, I. Dubois-Brugger, and P. Marcus, "Corrosion mechanisms of steel concrete moulds in contact with a demoulding agent studied by EIS and XPS," *Corrosion science,* vol. 45, pp. 2513-2524, 2003.

[9] L. Freire, X. Nóvoa, M. Montemor, and M. Carmezim, "Study of passive films formed on mild steel in alkaline media by the application of anodic potentials," *Materials Chemistry and Physics,* vol. 114, pp. 962-972, 2009.

[10] F. Miserque, B. Huet, G. Azou, D. Bendjaballah, and V. L'Hostis, "X-ray photoelectron spectroscopy and electrochemical studies of mild steel FeE500 passivation in concrete simulated water," in *Journal de Physique IV (Proceedings)*, 2006, pp. 89-97.

[11] R. Chen, J. Hu, Y. Ma, W. Guo, H. Huang, J. Wei*, et al.*, "Characterization of the passive film formed on the reinforcement surface in alkali activated fly ash: Surface analysis and electrochemical evaluation," *Corrosion Science,* vol. 165, p. 108393, 2020.

[12] P. Ghods, O. Isgor, J. Brown, F. Bensebaa, and D. Kingston, "XPS depth profiling study on the passive oxide film of carbon steel in saturated calcium hydroxide solution and the effect of chloride on the film properties," *Applied Surface Science,* vol. 257, pp. 4669-4677, 2011.

[13] B. Huet, V. L'Hostis, F. Miserque, and H. Idrissi, "Electrochemical behavior of mild steel in concrete: Influence of pH and carbonate content of concrete pore solution," *Electrochimica Acta,* vol. 51, pp. 172-180, 2005.

[14] F. Glasser and K. Sagoe-Crentsil, "Steel in concrete: Part II Electron microscopy analysis," *Magazine of Concrete Research,* vol. 41, pp. 213-220, 1989.

[15] C. Andrade, M. Keddam, X. R. Nóvoa, M. Pérez, C. Rangel, and H. Takenouti, "Electrochemical behaviour of steel rebars in concrete: influence of environmental factors and cement chemistry," *Electrochimica Acta,* vol. 46, pp. 3905-3912, 2001.

[16] L. Chomat, V. L'Hostis, E. Amblard, and L. Bellot-Gurlet, "Long term study of passive corrosion of steel rebars in Portland mortar in context of nuclear waste disposal," *Corrosion engineering, science and technology,* vol. 49, pp. 467-472, 2014.

[17] V. L'Hostis, E. Amblard, C. Blanc, F. Miserque, C. Paris, and L. Bellot-Gurlet, "Passive corrosion of steel in concrete in context of nuclear waste disposal," *Corrosion engineering, science and technology,* vol. 46, pp. 177-181, 2011.

[18] L. Bertolini, B. Elsener, P. Pedeferri, E. Redaelli, and R. B. Polder, *Corrosion of steel in concrete: prevention, diagnosis, repair*: John Wiley & Sons, 2013.

[19] R. François, S. Laurens, and F. Deby, *Corrosion and its consequences for reinforced concrete structures*: Elsevier, 2018.

[20] C. Hansson, A. Poursaee, and A. Laurent, "Macrocell and microcell corrosion of steel in ordinary Portland cement and high performance concretes," *Cement and concrete research,* vol. 36, pp. 2098-2102, 2006.

[21] S. Laurens, P. Hénocq, N. Rouleau, F. Deby, E. Samson, J. Marchand*, et al.*, "Steady-state polarization response of chloride-induced macrocell corrosion systems in steel reinforced concrete—numerical and experimental investigations," *Cement and concrete research,* vol. 79, pp. 272-290, 2016.

[22] M. Raupach, "Chloride-induced macrocell corrosion of steel in concrete—theoretical background and practical consequences," *Construction and building materials,* vol. 10, pp. 329-338, 1996.

[23] R. Zhang, "Phase d'initiation et de propagation de la corrosion dans les structures en béton armé et leurs conséquences sur la durée de vie," Toulouse, INSA, 2008.

[24] M. B. Otieno, "The development of empirical chloride-induced corrosion rate prediction models for cracked and uncracked steel reinforced concrete structures in the marine tidal zone," 2014.

[25] Y. Linwen, "Etude du développement de la corrosion dans le béton armé fissuré et de la performance mécanique de poutres en béton armé corrodées," Polytechnique Montréal, 2016.

[26] D. Garcia, "Études exploratoires dédiées au diagnostic de corrosion assisté par ordinateur des structures de génie civil," Université Paul Sabatier-Toulouse III, 2020.

[27] C. Chalhoub, "Study of the initiation and propagation phases of chloride induced corrosion in reinforced concrete structures," Université Paul Sabatier-Toulouse III, 2020.

[28] S. Kranc and A. A. Sagüés, "Computation of reinforcing steel corrosion distribution in concrete marine bridge substructures," *Corrosion,* vol. 50, pp. 50-61, 1994.

[29] C. Chalhoub, R. Francois, and M. Carcasses, "Effect of cathode–anode distance and electrical resistivity on macrocell corrosion currents and cathodic response in cases of chloride induced corrosion in reinforced concrete structures," *Construction and Building Materials,* vol. 245, p. 118337, 2020.

[30] T. D. Marcotte, "Characterization of chloride-induced corrosion products that form in steel-reinforced cementitious materials," 2001.

[31] D. J. Naus, "Primer on durability of nuclear power plant reinforced concrete structures-A review of pertinent factors," 2007.

[32] I. G. Markeset, "Modelling of reinforcement corrosion in concrete-State of the art."

[33] M. Thiery, "Modélisation de la carbonatation atmosphérique des matériaux cimentaires: prise en compte des effets cinétiques et des modifications microstructurales et hydriques," *ETUDES ET RECHERCHES DES LABORATOIRES DES PONTS ET CHAUSSEES-SERIE OUVRAGES D'ART,* 2006.

[34] A. Dunster, "An investigation of the carbonation of cement paste using trimethylsilylation," *Advances in Cement Research,* vol. 2, pp. 99-106, 1989.

[35] M. Gougar, B. Scheetz, and D. Roy, "Ettringite and C⍰ S⍰ H Portland cement phases for waste ion immobilization: A review," *Waste management,* vol. 16, pp. 295-303, 1996.

[36] H. F. Taylor, *Cement chemistry* vol. 2: Thomas Telford London, 1997.

[37] P. Castro, M. Sanjuán, and J. Genescá, "Carbonation of concretes in the Mexican Gulf," *Building and Environment,* vol. 35, pp. 145-149, 2000.

[38] C. Cheng-Feng and C. Jing-Wen, "Strength and elastic modulus of carbonated concrete," *ACI materials journal,* vol. 102, p. 315, 2005.

[39] M. Auroy, S. Poyet, P. Le Bescop, J.-M. Torrenti, T. Charpentier, M. Moskura*, et al.*, "Impact of carbonation on unsaturated water transport properties of cement-based materials," *Cement and concrete research,* vol. 74, pp. 44-58, 2015.

[40] S. P. Burg, *Postharvest physiology and hypobaric storage of fresh produce*: Cabi, 2004.

[41] M. Stefanoni, U. Angst, and B. Elsener, "Corrosion rate of carbon steel in carbonated concrete–A critical review," *Cement and Concrete Research,* vol. 103, pp. 35-48, 2018.

[42] I. Galan, C. Andrade, and M. Castellote, "Natural and accelerated CO2 binding kinetics in cement paste at different relative humidities," *Cement and Concrete Research,* vol. 49, pp. 21-28, 2013.

[43] P. Liu, Y. Chen, and Z. Yu, "Effects of temperature, relative humidity and carbon dioxide concentration on concrete carbonation," *Magazine of Concrete Research,* vol. 72, pp. 936-947, 2020.

[44] G. Verbeck, *Carbonation of hydrated Portland cement*: ASTM International West Conshohocken, PA, USA, 1958.

[45] M. Castellote, L. Fernandez, C. Andrade, and C. Alonso, "Chemical changes and phase analysis of OPC pastes carbonated at different CO 2 concentrations," *Materials and Structures,* vol. 42, pp. 515-525, 2009.

[46] N. Hyvert, A. Sellier, F. Duprat, P. Rougeau, and P. Francisco, "Dependency of C–S–H carbonation rate on CO2 pressure to explain transition from accelerated tests to natural carbonation," *Cement and Concrete Research,* vol. 40, pp. 1582-1589, 2010.

[47] D. Ho and R. Lewis, "Carbonation of concrete and its prediction," *Cement and Concrete Research,* vol. 17, pp. 489-504, 1987.

[48] T. Al-Kadhimi, P. Banfill, S. Millard, and J. Bungey, "An accelerated carbonation procedure for studies on concrete," *Advances in Cement Research,* vol. 8, pp. 47-59, 1996.

[49] G. W. Groves, A. Brough, I. G. Richardson, and C. M. Dobson, "Progressive changes in the structure of hardened C3S cement pastes due to carbonation," *Journal of the American Ceramic Society,* vol. 74, pp. 2891-2896, 1991.

[50] G. Groves, D. Rodway, and I. Richardson, "The carbonation of hardened cement pastes," *Advances in Cement research,* vol. 3, pp. 117-125, 1990.

[51] P. Faucon, B. Gerard, J. Jacquinot, and J. Marchand, "Water attack of a cement paste: towards an improved accelerated test?," *Advances in cement research,* vol. 10, pp. 67-73, 1998.

[52] T. A. Harrison, M. R. Jones, M. D. Newlands, S. Kandasami, and G. Khanna, "Experience of using the prTS 12390-12 accelerated carbonation test to assess the relative performance of concrete," *Magazine of Concrete Research,* vol. 64, pp. 737-747, 2012.

[53] N. Timhadjelt, "Efficacité et comportement à long terme des produits colmateurs pour bétons," INSA de Toulouse, 2021.

[54] H. Hornain, *GranDuBé: grandeurs associées à la durabilité des bétons*: Presses des Ponts, 2007.

[55] V. Shah, K. Scrivener, B. Bhattacharjee, and S. Bishnoi, "Changes in microstructure characteristics of cement paste on carbonation," *Cement and Concrete Research,* vol. 109, pp. 184-197, 2018.

[56] M. A. Baccay, N. Otsuki, T. Nishida, and S.-i. Maruyama, "Influence of cement type and temperature on the rate of corrosion of steel in concrete exposed to carbonation," *Corrosion,* vol. 62, 2006.

[57] L. Liu, J. Ha, T. Hashida, and S. Teramura, "Development of a CO2 solidification method for recycling autoclaved lightweight concrete waste," *Journal of materials science letters,* vol. 20, pp. 1791-1794, 2001.

[58] E. Drouet, "Impact de la température sur la carbonatation des matériaux cimentaires: prise en compte des transferts hydriques," École normale supérieure de Cachan-ENS Cachan, 2010.

[59] A. Younsi, P. Turcry, A. Aït-Mokhtar, and S. Staquet, "Accelerated carbonation of concrete with high content of mineral additions: effect of interactions between hydration and drying," *Cement and concrete research,* vol. 43, pp. 25-33, 2013.

[60] V. G. Papadakis, "Effect of supplementary cementing materials on concrete resistance against carbonation and chloride ingress," *Cement and concrete research,* vol. 30, pp. 291-299, 2000.

[61] H.-W. Song, S.-J. Kwon, K.-J. Byun, and C.-K. Park, "Predicting carbonation in early-aged cracked concrete," *Cement and Concrete Research,* vol. 36, pp. 979-989, 2006.

[62] N. Hyvert, "Application de l'approche probabiliste à la durabilité des produits préfabriqués en béton," Toulouse 3, 2009.

[63] N. Short, C. Page, and G. Glass, "A galvanic sensor for monitoring corrosion of steel in carbonated concrete," *Magazine of concrete research,* vol. 43, pp. 149-154, 1991.

[64] G. K. Glass, C. L. Page, and N. Short, "Factors affecting the corrosion rate of steel in carbonated mortars," *Corrosion Science,* vol. 32, pp. 1283-1294, 1991.

[65] C. D. Atiş, "Accelerated carbonation and testing of concrete made with fly ash," *Construction and Building Materials,* vol. 17, pp. 147-152, 2003.

[66] A. Castel and A. Nasser, "Influence of pre-existing oxides layer and interface condition with carbonated concrete on active reinforcing steel corrosion," *Materials and Corrosion,* vol. 66, pp. 206-214, 2015.

[67] B. Huet, "Comportement à la corrosion des armatures dans un béton carbonaté. Influence de la chimie de la solution interstitielle et d'une barrière de transport," INSA Lyon, 2005.

[68] F. Lollini and E. Redaelli, "Service life of reinforced concrete structures made with blended cements and exposed in urban environment," *Structural Concrete,* vol. 23, pp. 694-705, 2022.

[69] S. Goto and D. M. Roy, "The effect of w/c ratio and curing temperature on the permeability of hardened cement paste," *Cement and concrete research,* vol. 11, pp. 575-579, 1981.

[70] K. Kobayashi and K. Shuttoh, "Oxygen diffusivity of various cementitious materials," *Cement and Concrete Research,* vol. 21, pp. 273-284, 1991.

[71] H. Gurdián, E. García-Alcocel, F. Baeza-Brotons, P. Garcés, and E. Zornoza, "Corrosion behavior of steel reinforcement in concrete with recycled aggregates, fly ash and spent cracking catalyst," *Materials,* vol. 7, pp. 3176-3197, 2014.

[72] A. M. Arachchige, "Influence of cement content on corrosion resistance," *Proceedings of the Institution of Civil Engineers-Construction Materials,* vol. 161, pp. 31-39, 2008.

[73] L. Parrott, "Some effects of cement and curing upon carbonation and reinforcement corrosion in concrete," *Materials and Structures,* vol. 29, pp. 164-173, 1996.

[74] E. I. Moreno and A. A. Sagues, "Carbonation-induced corrosion of blended cement concrete mix designs for highway structures," in *CORROSION 98*, 1998.

[75] R. Dhir, M. Jones, and M. McCarthy, "PULVERIZED-FUEL ASH CONCRETE: CARBONATION-INDUCED REINFORCEMENT CORROSION RATES," *Proceedings of the Institution of Civil Engineers-Structures and Buildings,* vol. 94, pp. 335-342, 1992.

[76] C. Alonso, C. Andrade, and J. González, "Relation between resistivity and corrosion rate of reinforcements in carbonated mortar made with several cement types," *Cement and concrete research,* vol. 18, pp. 687-698, 1988.

[77] K. Hornbostel, C. K. Larsen, and M. R. Geiker, "Relationship between concrete resistivity and corrosion rate–A literature review," *Cement and concrete composites,* vol. 39, pp. 60-72, 2013.

[78] B. Huet, V. L'hostis, G. Santarini, D. Feron, and H. Idrissi, "Steel corrosion in concrete: Determinist modeling of cathodic reaction as a function of water saturation degree," *Corrosion science,* vol. 49, pp. 1918-1932, 2007.

[79] M. Raupach, "Models for the propagation phase of reinforcement corrosion–an overview," *Materials and Corrosion,* vol. 57, pp. 605-613, 2006.

[80] S. Alahmad, A. Toumi, J. Verdier, and R. François, "Effect of crack opening on carbon dioxide penetration in cracked mortar samples," *Materials and Structures,* vol. 42, pp. 559-566, 2009.

[81] V. H. Dang, R. François, and V. L'Hostis, "Effects of pre-cracks on both initiation and propagation of re-bar corrosion in pure carbon dioxide," in *EPJ Web of Conferences*, 2013, p. 06006.

[82] P. Bamforth, "Probabilistic performance based durability design of concrete structures," in *Management of Concrete Structures for Long-Term Serviceability*, ed: Thomas Telford Publishing, 1997, pp. 33-44.

[83] V. H. Dang, R. François, V. L'Hostis, and D. Meinel, "Propagation of corrosion in pre-cracked carbonated reinforced mortar," *Materials and structures,* vol. 48, pp. 2575-2595, 2015.

[84] K. Tuutti, *Corrosion of steel in concrete*: Cement-och betonginst., 1982.

[85] R. François, "Béton armé: corrélation entre fissuration et corrosion," Toulouse 3, 1987.

[86] A. Nasser, "La corrosion des aciers dans le béton à l'état passif et par carbonatation: prise en compte des courants galvaniques et des défauts d'interface acier-béton," Toulouse 3, 2010.

[87] Z. Zhang, P. Studer, and U. Angst, "A multi-technique study of corrosion products at the steel–concrete interface under two exposure conditions," *Journal of Microscopy,* vol. 286, pp. 191-197, 2022.

[88] J. Smith and Y. P. Virmani, "Materials and methods for corrosion control of reinforced and prestressed concrete structures in new construction," United States. Federal Highway Administration2000.

[89] M. Ormellese, L. Lazzari, S. Goidanich, G. Fumagalli, and A. Brenna, "A study of organic substances as inhibitors for chloride-induced corrosion in concrete," *Corrosion Science,* vol. 51, pp. 2959-2968, 2009.

[90] G. Glass and N. Buenfeld, "Chloride-induced corrosion of steel in concrete," *Progress in Structural Engineering and Materials,* vol. 2, pp. 448-458, 2000.

[91] U. M. Angst, O. B. Isgor, C. M. Hansson, A. Sagüés, and M. R. Geiker, "Beyond the chloride threshold concept for predicting corrosion of steel in concrete," *Applied Physics Reviews,* vol. 9, p. 011321, 2022.

[92] A. Neville, "Chloride attack of reinforced concrete: an overview," *Materials and Structures,* vol. 28, pp. 63-70, 1995.

[93] M. Montemor, A. Simoes, and M. Ferreira, "Chloride-induced corrosion on reinforcing steel: from the fundamentals to the monitoring techniques," *Cement and concrete composites,* vol. 25, pp. 491-502, 2003.

[94] J. Kropp, "Chlorides in concrete," *Performance criteria for concrete durability,* pp. 139-164, 1995.

[95] V. Q. Tran, "Contribution à la compréhension des mécanismes de dépassivation des armatures d'un béton exposé à l'eau de mer: théorie et modélisation thermochimique," Ecole Centrale de Nantes, 2016.

[96] L. Tang, L.-O. Nilsson, and P. M. Basheer, *Resistance of concrete to chloride ingress: Testing and modelling*: CRC Press, 2011.

[97] B. Martın-Pérez, H. Zibara, R. Hooton, and M. Thomas, "A study of the effect of chloride binding on service life predictions," *Cement and concrete research,* vol. 30, pp. 1215-1223, 2000.

[98] A. Guerrero, S. Goni, and V. Allegro, "Durability of class C fly ash belite cement in simulated sodium chloride radioactive liquid waste: Influence of temperature," *Journal of hazardous materials,* vol. 162, pp. 1099-1102, 2009.

[99] M. Maslehuddin, C. Paget, and Rasheeduzzafar, "Temperature effect on the pore solution chemistry in contaminated cements," *Magazine of Concrete Research,* vol. 49, pp. 5-14, 1997.

[100] G. K. Glass and N. R. Buenfeld, "The presentation of the chloride threshold level for corrosion of steel in concrete," *Corrosion science,* vol. 39, pp. 1001-1013, 1997.

[101] H. Justnes, "A review of chloride binding in cementitious systems," *Nordic Concrete Research-Publications-,* vol. 21, pp. 48-63, 1998.

[102] Q. Yuan, C. Shi, G. De Schutter, K. Audenaert, and D. Deng, "Chloride binding of cement-based materials subjected to external chloride environment–a review," *Construction and building materials,* vol. 23, pp. 1-13, 2009.

[103] T. Luping and L.-O. Nilsson, "Chloride binding capacity and binding isotherms of OPC pastes and mortars," *Cement and concrete research,* vol. 23, pp. 247-253, 1993.

[104] C. Arya, N. Buenfeld, and J. Newman, "Factors influencing chloride-binding in concrete," *Cement and Concrete research,* vol. 20, pp. 291-300, 1990.

[105] U. Angst, B. Elsener, C. K. Larsen, and Ø. Vennesland, "Critical chloride content in reinforced concrete—A review," *Cement and concrete research,* vol. 39, pp. 1122-1138, 2009.

[106] P. V. Nygaard and M. R. Geiker, "A method for measuring the chloride threshold level required to initiate reinforcement corrosion in concrete," *Materials and Structures,* vol. 38, pp. 489-494, 2005.

[107] V. Garcia, R. François, M. Carcasses, and P. Gegout, "Potential measurement to determine the chloride threshold concentration that initiates corrosion of reinforcing steel bar in slag concretes," *Materials and structures,* vol. 47, pp. 1483-1499, 2014.

[108] C. Chalhoub, R. François, and M. Carcasses, "Critical chloride threshold values as a function of cement type and steel surface condition," *Cement and Concrete Research,* vol. 134, p. 106086, 2020.

[109] D. P. Bentz, E. J. Garboczi, Y. Lu, N. Martys, A. R. Sakulich, and W. J. Weiss, "Modeling of the influence of transverse cracking on chloride penetration into concrete," *Cement and Concrete Composites,* vol. 38, pp. 65-74, 2013.

[110] C. Andrade and C. Alonso, "Test methods for on-site corrosion rate measurement of steel reinforcement in concrete by means of the polarization resistance method," *Materials and Structures,* vol. 37, pp. 623-643, 2004.

[111] C. Chalhoub, R. François, and M. Carcasses, "Determination of chloride threshold initiating corrosion: A new set-up taking the localized aspect of corrosion into account," *Cement and Concrete Research,* vol. 124, p. 105825, 2019.

[112] R. François, "A discussion on the order of magnitude of corrosion current density in reinforcements of concrete structures and its link with cross-section loss of reinforcement," *RILEM Technical Letters,* vol. 6, pp. 158-168, 2021.

[113] B. Yu, L. Yang, M. Wu, and B. Li, "Practical model for predicting corrosion rate of steel reinforcement in concrete structures," *Construction and Building Materials,* vol. 54, pp. 385-401, 2014.

[114] A. Scott and M. Alexander, "The influence of binder type, cracking and cover on corrosion rates of steel in chloride-contaminated concrete," *Magazine of Concrete Research,* vol. 59, pp. 495-505, 2007.

[115] A. Scott and M. Alexander, "Effect of supplementary cementitious materials (binder type) on the pore solution chemistry and the corrosion of steel in alkaline environments," *Cement and Concrete Research,* vol. 89, pp. 45-55, 2016.

[116] B. Pradhan and B. Bhattacharjee, "Performance evaluation of rebar in chloride contaminated concrete by corrosion rate," *Construction and building materials,* vol. 23, pp. 2346-2356, 2009.

[117] V. Sirivivatnanon, L. Bucea, E. Meck, S. Yozghatlian, and H. Cao, "Influence of fly ash, ground granulated blast furnace slag and silica fume on chloride induced corrosion of steel reinforcement [Keynote paper]," 1994.

[118] C. Arya and Y. Xu, "Effect of cement type on chloride binding and corrosion of steel in concrete," *Cement and Concrete Research,* vol. 25, pp. 893-902, 1995.

[119] A. A. Busari, W. K. Kupolati, J. M. Ndambuki, E. R. Sadiku, J. Snyman, L. Tolulope*, et al.*, "Response surface analysis of the corrosion effect of metakaolin in reinforced concrete," *Silicon,* vol. 13, pp. 2053-2061, 2021.

[120] A. M. Aguirre-Guerrero, R. A. Robayo-Salazar, and R. M. de Gutiérrez, "A novel geopolymer application: Coatings to protect reinforced concrete against corrosion," *Applied Clay Science,* vol. 135, pp. 437-446, 2017.

[121] K. Kupwade-Patil and E. N. Allouche, "Examination of chloride-induced corrosion in reinforced geopolymer concretes," *Journal of materials in civil engineering,* vol. 25, pp. 1465-1476, 2013.

[122] P. Chindaprasirt and W. Chalee, "Effect of sodium hydroxide concentration on chloride penetration and steel corrosion of fly ash-based geopolymer concrete under marine site," *Construction and building materials,* vol. 63, pp. 303-310, 2014.

[123] C. Tennakoon, A. Shayan, J. G. Sanjayan, and A. Xu, "Chloride ingress and steel corrosion in geopolymer concrete based on long term tests," *Materials & design,* vol. 116, pp. 287-299, 2017.

[124] M. Raupach, "Investigations on the influence of oxygen on corrosion of steel in concrete—Part 2," *Materials and structures,* vol. 29, pp. 226-232, 1996.

[125] M. Otieno, "Sensitivity of chloride-induced corrosion rate of steel in concrete to cover depth, crack width and concrete quality," *Materials and Structures,* vol. 50, pp. 1-10, 2017.

[126] H. Lopez-Calvo, P. Montes-García, V. Jiménez-Quero, H. Gómez-Barranco, T. Bremner, and M. Thomas, "Influence of crack width, cover depth and concrete quality on corrosion of steel in HPC containing corrosion inhibiting admixtures and fly ash," *Cement and Concrete Composites,* vol. 88, pp. 200-210, 2018.

[127] T. Liu and R. Weyers, "Modeling the dynamic corrosion process in chloride contaminated concrete structures," *Cement and Concrete research,* vol. 28, pp. 365-379, 1998.

[128] D. Vořechovská, J. Podroužek, M. Chromá, P. Rovnanikova, and B. Teplý, "Modeling of chloride concentration effect on reinforcement corrosion," *Computer-Aided Civil and Infrastructure Engineering,* vol. 24, pp. 446-458, 2009.

[129] C. Chalhoub, R. François, D. Garcia, S. Laurens, and M. Carcasses, "Macrocell corrosion of steel in concrete: Characterization of anodic behavior in relation to the chloride content," *Materials and Corrosion,* vol. 71, pp. 1424-1441, 2020.

[130] W. López, J. González, and C. Andrade, "Influence of temperature on the service life of rebars," *Cement and Concrete Research,* vol. 23, pp. 1130-1140, 1993.

[131] N. Otsuki, M. S. Madlangbayan, T. Nishida, T. Saito, and M. A. Baccay, "Temperature dependency of chloride induced corrosion in concrete," *Journal of Advanced Concrete Technology,* vol. 7, pp. 41-50, 2009.

[132] A. Michel, P. Nygaard, and M. Geiker, "Experimental investigation on the short-term impact of temperature and moisture on reinforcement corrosion," *Corrosion science,* vol. 72, pp. 26-34, 2013.

[133] B. Yu, J. Liu, and B. Li, "Improved numerical model for steel reinforcement corrosion in concrete considering influences of temperature and relative humidity," *Construction and Building Materials,* vol. 142, pp. 175-186, 2017.

[134] V. Bouteiller, J.-F. Cherrier, V. L'Hostis, N. Rebolledo, C. Andrade, and E. Marie-Victoire, "Influence of humidity and temperature on the corrosion of reinforced concrete prisms," *European journal of environmental and civil engineering,* vol. 16, pp. 471-480, 2012.

[135] C. Andrade, C. Alonso, and J. Sarria, "Influence of relative humidity and temperature on-site corrosion rates," *Materiales De Construccion,* vol. 48, pp. 5-17, 1998.

[136] J. Ahlström, J. Tidblad, B. Sederholm, and L. Wadsö, "Influence of chloride and moisture content on steel rebar corrosion in concrete," *Materials and Corrosion,* vol. 67, pp. 1049-1058, 2016.

[137] J. R. Lliso-Ferrando, I. Gasch, A. Martínez-Ibernón, and M. Valcuende, "Macrocell Corrosion Currents in Simulated Concrete Pore Solution and Reinforced Concrete," *International Journal of Concrete Structures and Materials,* vol. 17, p. 15, 2023.

[138] J. Warkus and M. Raupach, "Modelling of reinforcement corrosion–geometrical effects on macrocell corrosion," *Materials and Corrosion,* vol. 61, pp. 494-504, 2010.

[139] C. Arya and P. Vassie, "Influence of cathode-to-anode area ratio and separation distance on galvanic corrosion currents of steel in concrete containing chlorides," *Cement and Concrete Research,* vol. 25, pp. 989-998, 1995.

[140] P. Cavalier, P. Vassie, and TRRL, "Investigation and repair of reinforcement corrosion in a bridge deck," *Proceedings of the Institution of Civil Engineers,* vol. 70, pp. 461-480, 1981.

[141] J. Warkus and M. Raupach, "Modelling of reinforcement corrosion–Corrosion with extensive cathodes," *Materials and Corrosion,* vol. 57, pp. 920-925, 2006.

[142] S. Y. Jang, B. S. Kim, and B. H. Oh, "Effect of crack width on chloride diffusion coefficients of concrete by steady-state migration tests," *Cement and Concrete Research,* vol. 41, pp. 9-19, 2011.

[143] S.-S. Park, S.-J. Kwon, and S. H. Jung, "Analysis technique for chloride penetration in cracked concrete using equivalent diffusion and permeation," *Construction and Building Materials,* vol. 29, pp. 183-192, 2012.

[144] M. Ismail, A. Toumi, R. François, and R. Gagné, "Effect of crack opening on the local diffusion of chloride in cracked mortar samples," *Cement and concrete research,* vol. 38, pp. 1106-1111, 2008.

[145] L. Marsavina, K. Audenaert, G. De Schutter, N. Faur, and D. Marsavina, "Experimental and numerical determination of the chloride penetration in cracked concrete," *Construction and Building Materials,* vol. 23, pp. 264-274, 2009.

[146] K. Audenaert, L. Marsavina, and G. De Schutter, "Influence of cracks on the service life of concrete structures in a marine environment," in *Key Engineering Materials*, 2009, pp. 153-160.

[147] A. Poursaee and B. Ross, "The Role of Cracks in Chloride-Induced Corrosion of Carbon Steel in Concrete," *Corrosion and Materials Degradation,* vol. 3, pp. 258-269, 2022.

[148] A. Al-Ameeri, M. Rafiq, and O. Tsioulou, "Influence of cracks on the carbonation resistance of concrete structures," in *Proceedings of the Sixth International Conference on the Durability of Concrete Structures, University of Leeds, Woodhouse, Leeds, UK*, 2018, pp. 18-20.

[149] L. E. Sullivan-Green, "Effect of Crack Width on Carbonation: Implications for Crack-Dating," Northwestern University Evanston, IL, USA, 2005.

[150] S.-J. Kwon and U.-J. Na, "Prediction of durability for RC columns with crack and joint under carbonation based on probabilistic approach," *International Journal of Concrete Structures and Materials,* vol. 5, pp. 11-18, 2011.

[151] A. S. Al-Ameeri, M. I. Rafiq, O. Tsioulou, and O. Rybdylova, "Impact of climate change on the carbonation in concrete due to carbon dioxide ingress: Experimental investigation and modelling," *Journal of Building Engineering,* vol. 44, p. 102594, 2021.

[152] B. Stitmannaithum, H. Q. Vu, and M. Tran, "Chloride penetration into reinforced concrete structures," in *Proceedings of 3rd international conference on sustainable construction materials and technologies*, 2013.

[153] A. Konin, R. François, and G. Arliguie, "Penetration of chlorides in relation to the microcracking state into reinforced ordinary and high strength concrete," *Materials and structures,* vol. 31, pp. 310-316, 1998.

[154] S. Jacobsen, J. Marchand, and L. Boisvert, "Effect of cracking and healing on chloride transport in OPC concrete," *Cement and Concrete Research,* vol. 26, pp. 869-881, 1996.

[155] S. Mu, G. De Schutter, and B.-g. Ma, "Non-steady state chloride diffusion in concrete with different crack densities," *Materials and structures,* vol. 46, pp. 123-133, 2013.

[156] T. U. Mohammed, T. Yamaji, T. Aoyama, and H. Hamada, "Marine Durability of 15-Year Old Uncracked and Precracked Concrete Made with Different Cements," *Doboku Gakkai Ronbunshu,* vol. 2002, pp. 201-214, 2002.

[157] H.-W. Reinhardt and M. Jooss, "Permeability and self-healing of cracked concrete as a function of temperature and crack width," *Cement and concrete research,* vol. 33, pp. 981-985, 2003.

[158] T. Nishiwaki, S. Kwon, D. Homma, M. Yamada, and H. Mihashi, "Self-healing capability of fiber-reinforced cementitious composites for recovery of watertightness and mechanical properties," *Materials,* vol. 7, pp. 2141-2154, 2014.

[159] T. U. Mohammed, N. Otsuki, and H. Hamada, "Corrosion of steel bars in cracked concrete under marine environment," *Journal of materials in civil engineering,* vol. 15, pp. 460-469, 2003.

[160] M. Otieno, M. Alexander, and H.-D. Beushausen, "Corrosion in cracked and uncracked concrete–influence of crack width, concrete quality and crack reopening," *Magazine of Concrete Research,* vol. 62, pp. 393-404, 2010.

[161] O. G. Rodriguez, "Influence of cracks on chloride ingress into concrete," 2003.

[162] P. P. Win, M. Watanabe, and A. Machida, "Penetration profile of chloride ion in cracked reinforced concrete," *Cement and concrete research,* vol. 34, pp. 1073-1079, 2004.

[163] N. Gowripalan, V. Sirivivatnanon, and C. Lim, "Chloride diffusivity of concrete cracked in flexure," *Cement and Concrete research,* vol. 30, pp. 725-730, 2000.

[164] S.-i. Miyazato and N. Otsuki, "Steel corrosion induced by chloride or carbonation in mortar with bending cracks or joints," *Journal of Advanced Concrete Technology,* vol. 8, pp. 135-144, 2010.

[165] U. M. Angst, "Durable concrete structures: Cracks & corrosion and corrosion & cracks," in *Proceedings of the 10th International Conference on Fracture Mechanics of Concrete and Concrete Structures; Pijaudier-Cabot, G., Grassl, P., La Borderie, C., Eds*, 2019.

[166] A. Boschmann Käthler, U. M. Angst, M. Wagner, C. Larsen, and B. Elsener, "Effect of cracks on chlorideinduced corrosion of steel in concrete-a review: Etatsprogrammet Varige konstruksjoner 2012-2015," 2017.

[167] R. Francois and G. Arliguie, "Durability of loaded reinforced concrete in chloride environment," *Special Publication,* vol. 145, pp. 573-596, 1994.

[168] G. De Schutter, "Quantification of the influence of cracks in concrete structures on carbonation and chloride penetration," *Magazine of Concrete Research,* vol. 51, pp. 427-435, 1999.

[169] L. Yu, R. François, V. H. Dang, V. l'Hostis, and R. Gagné, "Development of chloride-induced corrosion in pre-cracked RC beams under sustained loading: Effect of load-induced cracks, concrete cover, and exposure conditions," *Cement and Concrete Research,* vol. 67, pp. 246-258, 2015.

[170] R. Zhang, A. Castel, and R. François, "The corrosion pattern of reinforcement and its influence on serviceability of reinforced concrete members in chloride environment," *Cement and Concrete Research,* vol. 39, pp. 1077-1086, 2009.

[171] R. Francois, I. Khan, N. A. Vu, H. Mercado, and A. Castel, "Study of the impact of localised cracks on the corrosion mechanism," *European journal of environmental and civil engineering,* vol. 16, pp. 392-401, 2012.

[172] S. Jaffer and C. Hansson, "The influence of cracks on chloride-induced corrosion of steel in ordinary Portland cement and high performance concretes subjected to different loading conditions," *Corrosion science,* vol. 50, pp. 3343-3355, 2008.

[173] W. Zhang, R. François, and L. Yu, "Influence of load-induced cracks coupled or not with top-casting-induced defects on the corrosion of the longitudinal tensile reinforcement of naturally corroded beams exposed to chloride environment under sustained loading," *Cement and Concrete Research,* vol. 129, p. 105972, 2020.

[174] R. Francois and J. Maso, "Effect of damage in reinforced concrete on carbonation or chloride penetration," *Cement and Concrete Research,* vol. 18, pp. 961-970, 1988.

[175] R. M. Ghantous, S. Poyet, V. l'Hostis, N.-C. Tran, and R. François, "Effect of crack openings on carbonation-induced corrosion," *Cement and Concrete Research,* vol. 95, pp. 257-269, 2017.

[176] R. M. Ghantous, R. François, S. Poyet, V. L'hostis, F. Bernachy-Barbe, D. Meinel*, et al.*, "Relation between crack opening and extent of the damage induced at the steel/mortar interface," *Construction and Building Materials,* vol. 193, pp. 97-104, 2018.

[177] M. Şahmaran and İ. Ö. Yaman, "Influence of transverse crack width on reinforcement corrosion initiation and propagation in mortar beams," *Canadian Journal of Civil Engineering,* vol. 35, pp. 236-245, 2008.

[178] M. Otieno, H. Beushausen, and M. Alexander, "Chloride-induced corrosion of steel in cracked concrete–Part I: Experimental studies under accelerated and natural marine environments," *Cement and Concrete Research,* vol. 79, pp. 373-385, 2016.

[179] W. Li, W. Liu, and S. Wang, "The effect of crack width on chloride-induced corrosion of steel in concrete," *Advances in Materials Science and Engineering,* vol. 2017, 2017.

[180] K. Pettersson, O. Jorgenson, and P. Fidjestoll, "The effect of cracks on reinforcement corrosion in high-performance concrete in a marine environment," *Special Publication,* vol. 163, pp. 185-200, 1996.

[181] R. Francois and G. Arliguie, "Effect of microcracking and cracking on the development of corrosion in reinforced concrete members," *Magazine of Concrete Research,* vol. 51, pp. 143-150, 1999.

[182] R. François and G. Arliguie, "Influence of service cracking on reinforcement steel corrosion," *Journal of Materials in Civil Engineering,* vol. 10, pp. 14-20, 1998.

[183] R. François, A. Castel, T. Vidal, and N.-A. Vu, "Long term corrosion behavior of reinforced concrete structures in chloride environnement," in *Journal de Physique IV (Proceedings)*, 2006, pp. 285-293.

[184] T. U. Mohammed, N. Otsuki, M. Hisada, and T. Shibata, "Effect of crack width and bar types on corrosionof steel in concrete," *Journal of Materials in Civil Engineering,* vol. 13, pp. 194-201, 2001.

[185] A. Blagojevic, "The influence of cracks on the durability and service life of reinforced concrete structures in relation to chloride-induced corrosion," *Technical University of Delft, Delft, The Netherlands,* 2016.

[186] P. Schießl and M. Raupach, "Laboratory studies and calculations on the influence of crack width on chloride-induced corrosion of steel in concrete," *Materials Journal,* vol. 94, pp. 56-61, 1997.

[187] F. U. A. Shaikh, "Effect of cracking on corrosion of steel in concrete," *International Journal of Concrete Structures and Materials,* vol. 12, pp. 1-12, 2018.

[188] A. Poursaee and C. M. Hansson, "The influence of longitudinal cracks on the corrosion protection afforded reinforcing steel in high performance concrete," *Cement and Concrete Research,* vol. 38, pp. 1098-1105, 2008.

[189] U. M. Angst, M. R. Geiker, A. Michel, C. Gehlen, H. Wong, O. B. Isgor*, et al.*, "The steel–concrete interface," *Materials and Structures,* vol. 50, pp. 1-24, 2017.

[190] T. U. Mohammed, N. Otsuki, H. Hamada, and T. Yamaji, "Chloride-induced corrosion of steel bars in concrete with presence of gap at steel-concrete interface," *Materials Journal,* vol. 99, pp. 149-156, 2002.

[191] T. A. Söylev and R. François, "Corrosion of reinforcement in relation to presence of defects at the interface between steel and concrete," *Journal of materials in civil engineering,* vol. 17, pp. 447-455, 2005.

[192] U. M. Angst, M. R. Geiker, M. C. Alonso, R. Polder, O. B. Isgor, B. Elsener*, et al.*, "The effect of the steel–concrete interface on chloride-induced corrosion initiation in concrete: a critical review by RILEM TC 262-SCI," *Materials and Structures,* vol. 52, pp. 1-25, 2019.

[193] K. Ann and N. Buenfeld, "The effect of calcium nitrite on the chloride-induced corrosion of steel in concrete," *Magazine of Concrete Research,* vol. 59, pp. 689-697, 2007.

[194] B. Reddy, "Influence of the steel-concrete interface on the chloride threshold level," University of London, 2001.

[195] T. Yonezawa, V. Ashworth, and R. Procter, "Pore solution composition and chloride effects on the corrosion of steel in concrete," *Corrosion,* vol. 44, pp. 489-499, 1988.

[196] J.-G. Nam, W. H. Hartt, and K. Kim, "Effects of air void at the steel-concrete interface on the corrosion Initiation of reinforcing steel in concrete under chloride exposure," *Journal of the Korea Concrete Institute,* vol. 17, pp. 829-834, 2005.

[197] J. Ryou and K. Ann, "Variation in the chloride threshold level for steel corrosion in concrete arising from different chloride sources," *Magazine of Concrete Research,* vol. 60, pp. 177-187, 2008.

[198] C. B. Käthler, U. M. Angst, and B. Elsener, "Towards understanding corrosion initiation in concrete–influence of local concrete properties in the steel-concrete interfacial zone," in *MATEC Web of Conferences*, 2018, p. 04002.

[199] U. M. Angst and B. Elsener, "The size effect in corrosion greatly influences the predicted life span of concrete infrastructures," *Science advances,* vol. 3, p. e1700751, 2017.

[200] T. A. Soylev and R. François, "Quality of steel–concrete interface and corrosion of reinforcing steel," *Cement and Concrete Research,* vol. 33, pp. 1407-1415, 2003.

[201] T. U. Mohammed, H. Hamada, and T. Yamaji, "Performance of seawater-mixed concrete in the tidal environment," *Cement and concrete research,* vol. 34, pp. 593-601, 2004.

[202] A. Castel, T. Vidal, R. François, and G. Arliguie, "Influence of steel–concrete interface quality on reinforcement corrosion induced by chlorides," *Magazine of Concrete Research,* vol. 55, pp. 151-159, 2003.

[203] T. Vidal, A. Castel, and R. Francois, "Corrosion process and structural performance of a 17 year old reinforced concrete beam stored in chloride environment," *Cement and Concrete Research,* vol. 37, pp. 1551-1561, 2007.

[204] R. Zhang, A. Castel, and R. François, "Influence of steel–concrete interface defects owing to the top-bar effect on the chloride-induced corrosion of reinforcement," *Magazine of concrete research,* vol. 63, pp. 773-781, 2011.

[205] W. Zhang, L. Yu, and R. Francois, "Influence of top-casting-induced defects on the corrosion of the compressive reinforcement of naturally corroded beams under sustained loading," *Construction and Building Materials,* vol. 229, p. 116912, 2019.

[206] L. Yu, R. François, and R. Gagné, "Influence of steel–concrete interface defects induced by top-casting on development of chloride-induced corrosion in RC beams under sustained loading," *Materials and structures,* vol. 49, pp. 5169-5181, 2016.

[207] R. M. Ghantous, S. Poyet, V. L'Hostis, N.-C. Tran, and R. François, "Effect of accelerated carbonation conditions on the characterization of load-induced damage in reinforced concrete members," *Materials and structures,* vol. 50, pp. 1-10, 2017.

[208] M. Stefanoni, U. Angst, and B. Elsener, "Innovative Sample Design for Corrosion Rate Measurements in Carbonated Blended Concrete," in *2016 International Concrete Sustainability Conference*, 2016.

[209] P. F. Marques, C. Chastre, and Â. Nunes, "Carbonation service life modelling of RC structures for concrete with Portland and blended cements," *Cement and Concrete Composites,* vol. 37, pp. 171-184, 2013.

[210] C. A. Hendriks, E. Worrell, D. De Jager, K. Blok, and P. Riemer, "Emission reduction of greenhouse gases from the cement industry," in *Proceedings of the fourth international conference on greenhouse gas control technologies*, 1998, pp. 939-944.

[211] M. Baccay, N. Otsuki, T. Nishida, and S. Maruyama, "Influence of cement type and temperature on the rate of corrosion of steel in concrete exposed to carbonation," *Corrosion,* vol. 62, pp. 811-821, 2006.

[212] C. Andrade and R. Buják, "Effects of some mineral additions to Portland cement on reinforcement corrosion," *Cement and Concrete Research,* vol. 53, pp. 59-67, 2013.

[213] J. M. Chi, R. Huang, and C. Yang, "Effects of carbonation on mechanical properties and durability of concrete using accelerated testing method," *Journal of marine science and technology,* vol. 10, pp. 14-20, 2002.

[214] J. A. Gonzalez, J. Algaba, and C. Andrade, "Corrosion of reinforcing bars in carbonated concrete," *British Corrosion Journal,* vol. 15, pp. 135-139, 1980.

[215] C. Alonso and C. Andrade, "Effect of cement type and cement proportion in the corrosion rate of rebars embedded in carbonated mortar," *Materiales de Construcción,* vol. 37, pp. 5-15, 1987.

[216] G. Glass, C. Page, and N. Short, "Factors affecting the corrosion rate of steel in carbonated mortars," *Corrosion Science,* vol. 32, pp. 1283-1294, 1991.

[217] J. Gulikers, "Theoretical considerations on the supposed linear relationship between concrete resistivity and corrosion rate of steel reinforcement," *Materials and Corrosion,* vol. 56, pp. 393-403, 2005.

[218] P. Marques and A. Costa, "Service life of RC structures: Carbonation induced corrosion. Prescriptive vs. performance-based methodologies," *Construction and Building Materials,* vol. 24, pp. 258-265, 2010.

[219] M. Khadra, J.-F. Lataste, N. Burlion, T. Rougelot, and J.-P. Carlier, "Carbonation effect on measurements of electrical resistivity tomography," in *Conference: 2nd International Conference on Civil, Structural and Transportation Engineering (ICCSTE'16)*, 2016.

[220] I.-S. Yoon and J.-W. Nam, "Influence of chloride content of on electrical resistivity in concrete," *Journal of the Korea institute for structural maintenance and inspection,* vol. 18, pp. 90-96, 2014.

[221] M. T. Walsh and A. A. Sagüés, "Steel corrosion in submerged concrete structures—Part 1: field observations and corrosion distribution modeling," *Corrosion,* vol. 72, pp. 518-533, 2016.

[222] C. Chalhoub, R. François, and M. Carcasses, "Effect of Cathode–Anode distance and electrical resistivity on macrocell corrosion currents and cathodic response in cases of chloride induced corrosion in reinforced concrete structures," *Construction and Building Materials,* vol. 245, p. 118337, 2020.

[223] C. Andrade and C. Alonso, "Corrosion rate monitoring in the laboratory and on-site," *Construction and building materials,* vol. 10, pp. 315-328, 1996.

[224] K. M. Smith, A. J. Schokker, and P. J. Tikalsky, "Performance of supplementary cementitious materials in concrete resistivity and corrosion monitoring evaluations," *Materials Journal,* vol. 101, pp. 385-390, 2004.

[225] E. Chávez-Ulloa, R. Camacho-Chab, M. Sosa-Baz, P. Castro-Borges, and T. Pérez-López, "Corrosion process of reinforced concrete by carbonation in a natural environment and an accelerated test chamber," *Int. J. Electrochem. Sci,* vol. 8, pp. 9015-9029, 2013.

[226] R. Polder, C. Andrade, B. Elsener, O. Vennesland, J. Gulikers, R. Weidert*, et al.*, "RILEM TC 154-EMC: electrochemical techniques for measuring metallic corrosion," *Materials and structures,* vol. 33, pp. 603-611, 2000.

[227] C. Boschmann Käthler, U. M. Angst, G. Ebell, and B. Elsener, "Chloride-induced reinforcement corrosion in cracked concrete: The influence of time of wetness on corrosion propagation," *Corrosion Engineering, Science and Technology,* vol. 56, pp. 1-10, 2021.

[228] G. Naidu Gopu and S. A. Joseph, "Corrosion Behavior of Fiber-Reinforced Concrete—A Review," *Fibers,* vol. 10, p. 38, 2022.

[229] S. Kakooei, H. M. Akil, A. Dolati, and J. Rouhi, "The corrosion investigation of rebar embedded in the fibers reinforced concrete," *Construction and Building Materials,* vol. 35, pp. 564-570, 2012.

[230] A. S. El-Dieb, "Mechanical, durability and microstructural characteristics of ultra-high-strength self-compacting concrete incorporating steel fibers," *Materials & Design,* vol. 30, pp. 4286-4292, 2009.

[231] W. Zhang, R. Francois, Y. Cai, J.-P. Charron, and L. Yu, "Influence of artificial cracks and interfacial defects on the corrosion behavior of steel in concrete during corrosion initiation under a chloride environment," *Construction and Building Materials,* vol. 253, p. 119165, 2020.

[232] T. Vidal, A. Castel, and R. François, "Analyzing crack width to predict corrosion in reinforced concrete," *Cement and concrete research,* vol. 34, pp. 165-174, 2004.

[233] I. Khan, R. François, and A. Castel, "Prediction of reinforcement corrosion using corrosion induced cracks width in corroded reinforced concrete beams," *Cement and concrete research,* vol. 56, pp. 84-96, 2014.

[234] R. Zhang, A. Castel, and R. François, "Concrete cover cracking with reinforcement corrosion of RC beam during chloride-induced corrosion process," *Cement and Concrete Research,* vol. 40, pp. 415-425, 2010.

[235] R. François and J. Maso, "Effect of damage in reinforced concrete on carbonation or chloride penetration," *Cement and Concrete Research,* vol. 18, pp. 961-970, 1988.

[236] E. Sassine, "Protection cathodique du béton armé par revêtement electro-conducteur autonome," Toulouse, INSA, 2018.

[237] M. Geiker, S. Robuschi, K. Lundgren, C. Paraskevoulakos, C. Gundlach, T. Danner*, et al.*, "Concluding destructive investigation of a nine-year-old marine-exposed cracked concrete panel," *Cement and Concrete Research,* vol. 165, p. 107070, 2023.